GEOCHEMISTRY AND METAMORPHISM OF METABASITES, AND SPATIAL VARIATION OF P-T PATHS ACROSS THE BHUTAN HIMALAYA: IMPLICATIONS FOR THE EXHUMATION OF THE GREATER HIMALAYAN SEQUENCE

by

Joyia Chakungal

Submitted in partial fulfilment of the requirements
for the degree of Doctor of Philosophy

at

Dalhousie University
Halifax, Nova Scotia
December 2006

DALHOUSIE UNIVERSITY

DEPARTMENT OF EARTH SCIENCES

The undersigned hereby certify that they have read and recommend to the Faculty of Graduate Studies for acceptance a thesis entitled "GEOCHEMISTRY AND METAMORPHISM OF METABASITES AND SPATIAL VARIATION OF P-T PATHS ACROSS THE BHUTAN HIMALAYA: IMPLICATIONS FOR THE EXHUMATION OF THE GREATER HIMALAYAN SEQUENCE" by Joyia Chakungal in partial fulfillment of the requirements for the degree of Doctor of Philosophy.

Dated: December 8. 2006

External Examiner:

Research Supervisor:

Examining Committee:

Departmental Representative:

DALHOUSIE UNIVERSITY

DATE: December 8, 2006

AUTHOR: Joyia Chakungal

TITLE: GEOCHEMISTRY AND METAMORPHISM OF METABASITES, AND SPATIAL VARIATION OF P-T PATHS ACROSS THE BHUTAN HIMALAYA: IMPLICATIONS FOR THE EXHUMATION OF THE GREATER HIMALAYAN SEQUENCE

DEPARTMENT OR SCHOOL: Department of Earth Sciences

DEGREE: PhD CONVOCATION: October YEAR: 2007

Distribution License

DalSpace requires agreement to this non-exclusive distribution license before your item can appear on DalSpace.

NON-EXCLUSIVE DISTRIBUTION LICENSE

You (the author(s) or copyright owner) grant to Dalhousie University the non-exclusive right to reproduce and distribute your submission worldwide in any medium.

You agree that Dalhousie University may, without changing the content, reformat the submission for the purpose of preservation.

You also agree that Dalhousie University may keep more than one copy of this submission for purposes of security, back-up and preservation.

You agree that the submission is your original work, and that you have the right to grant the rights contained in this license. You also agree that your submission does not, to the best of your knowledge, infringe upon anyone's copyright.

If the submission contains material for which you do not hold copyright, you agree that you have obtained the unrestricted permission of the copyright owner to grant Dalhousie University the rights required by this license, and that such third-party owned material is clearly identified and acknowledged within the text or content of the submission.

If the submission is based upon work that has been sponsored or supported by an agency or organization other than Dalhousie University, you assert that you have fulfilled any right of review or other obligations required by such contract or agreement.

Dalhousie University will clearly identify your name(s) as the author(s) or owner(s) of the submission, and will not make any alteration to the content of the files that you have submitted.

If you have questions regarding this license please contact the repository manager at dalspace@dal.ca.

Grant the distribution license by signing and dating below.

Name of signatory	Date

TABLE OF CONTENTS

LIST OF FIGURES

LIST OF TABLES

ABSTRACT

This study was designed to investigate the provenance and metamorphic history of metabasites and metasediments in the GHS of western Bhutan, with the aim of improving our understanding of the tectonic evolution of this poorly known part of the Himalaya. In so doing, a secondary aim was to use the results of this study to test the applicability of the channel flow-extrusion models as viable hypotheses for the tectonic evolution of this segment of the orogen.

Metabasites found in the high- and 'mid'-structural levels of the GHS are within-plate basalts that were intruded into the distal parts of the North Indian margin during a period of Paleo-Mesoproterozoic magmatism, long before the onset of Himalayan orogenesis. Temperature estimates made on the metabasites and the encompassing metasediments reveals that peak-T conditions decrease with structural position from ~ 900 °C immediately below the STD down to ~ 650-700 °C proximal to the MCT zone. Associated pressures show a slight increase ranging from 9 kbar at the STD to 11 kbar at the MCT, consistent with observations across the orogen. U-Pb ages on zircon rims from the 'high' and 'mid'-structural levels suggest peak-T conditions in the GHS persisted to at least 21 Ma. Amphibole and biotite argon ages imply cooling through 500 °C and 350 °C by 15 Ma and 13 Ma respectively. The associated P-T-t paths vary with structural position and display marked similarities with paths predicted by thermomechanical model HT111 of Beaumont et al. (2004). The similarity between model results and the data suggests exhumation of the GHS as two hot-channels or domes that have been superimposed upon one another. The absence of a marked time gap in the geochronological data suggests extrusion and exhumation of the domes did not occur in pulses but was a continuous process. At the base of the GHS, the Jaishidanda Formation comprises protomylonities and corresponds with a zone of intense top-to-the-south shearing, probably correlating with the MCT zone. Isotopic data and the intercalation of rocks of varying metamorphic grade reveals that the zone of intense penetrative shear developed over a metamorphic discontinuity between GHS material that was subjected to high-T for protracted periods (homogeneous garnets) versus rocks that were not. Thus, the MCT zone in south-western Bhutan has developed in rocks entirely of GHS affinity implying that not everywhere in the Himalaya does the MCT zone correlate with a protolith boundary between the LHS and GHS.

LIST OF ABBREVIATIONS USED

Acc	Accessory
Alm	Almandine
Amp	Amphibole
Ap	Apatite
Bt	Biotite
Cpx	Clinopyroxene
Crd	Cordierite
Grs	Grossular
Grt	Garnet
Herc	Hercinite
Ilm	Ilmenite
Kfs	Potassium feldspar
Ky	Kyanite
Mag	Magnetite
Ms	Muscovite
Oamp	Orthoamphibole
Opx	Orthopyroxene
Pl	Plagioclase
Py	Pyrope
P-T	Pressure-temperature
Qtz	Quartz
Ru	Rutile
Sil	Sillimanite
Sp	spinel
Sps	Spessartine
Ti	Titanite
Tour	Tourmaline
Zr	Zircon

ACKNOWLEDGEMENTS

This study would not have been possible without the support and assistance of our colleagues at the Geological Survey of Bhutan. My utmost gratitude extends to Etho Metho Tours and Treks for all of their logistical support in the field, we would not have made it without them and the hard work and determination of our most excellent field crews. Financial support for the fieldwork and isotope analyses was graciously provided by the NSERC grant of D. Grujic. Financial support for geochemical analyses was provided by the NSERC grant of J. Dostal. To S. Duchêne and everyone at the Centre de Recherches Pétrographiques et Géochimiques in Vandœuvre lès Nancy who assisted me with the isotope geochemistry and U-Pb geochronology, thank you very much. And last but not least, to all of my family and friends, your unfailing encouragement and support was most appreciated and will forever be remembered. Thank you.

CHAPTER I: INTRODUCTION

1.1 INTRODUCTION

The metamorphic core of the Himalayan-Tibetan orogen, known as the Greater Himalayan Sequence (GHS), is a package of deformed, pervasively sheared, high-grade metamorphic rocks and leucogranites bounded at its margins by two parallel, north-dipping shear zones. Though the sense of displacement was opposite, movement along the shear zones was coeval (Burchfiel and Royden 1985; Searle and Rex 1989; Godin et al. 2006b). This observation combined with the evidence for pervasive ductile deformation throughout the metamorphic core of the orogen has led to the view that GHS material developed at mid-crustal levels in a low viscosity channel that extends beneath the Tibetan plateau to the north, which was subsequently exhumed as a southward extruding slab over lower grade rocks of the Lesser Himalayan Sequence (LHS), between two north dipping shear zones. This model for the exhumation of the GHS is widely known as the channel flow-extrusion hypothesis (Beaumont et al. 2001; 2004; 2006; Medvedev and Beaumont 2006), which has successfully reproduced many of the geophysical and geological field observations that have been summarized by Hodges (2006), and include: i) presence of low viscosity material bounded by relatively higher viscosity rocks at mid-crustal levels; ii) a plateau of variable crustal thickness which results in a horizontal lithostatic pressure gradient thereby driving the low viscosity material to flow; iii) extrusion and exhumation of the channel resulting in coeval thrust sense movement at its base and normal-sense kinematics at its upper margin; iv) inversion from an earlier top-to-the-south kinematics due to underthrusting of the Indian slab, to top-to-the-north kinematics along the upper shear zone due to back flow of the channel; v) pervasive shearing throughout the extruded channel block with strain concentrated along its margins; and vi) development of an inverted metamorphic field gradient at the base of the extruded material, and right-way-up metamorphic sequences at the top.

As noted by Jamieson et al. (2004), in order to assess the validity of a model it is important to compare experimental results with real data. For the purposes of this study the area of interest is the relatively poorly studied eastern Himalaya, in particular the Kingdom of Bhutan. The GHS is the lithotectonic unit of interest, the primary focus being to test model results with respect to four issues. First is the matter of provenance, which is discussed in chapter 2. Structural restoration of the LHS, GHS and Tethyan Sedimentary Sequence (TSS) suggests the metasediments that comprise them were deposited on the north Indian continental margin, which may have been continuous with little to no topographic relief prior to the onset of orogenesis (Myrow et al. 2003). However, isotopic provenance studies across the orogen have revealed that though the sediments were deposited onto the same margin, the source for each unit was paleogeographically different (Parrish and Hodges 1996; DeCelles et al. 2000; Miller et al. 2000; Argles et al. 2003; Gehrels et al. 2003; Myrow et al. 2003; DeCelles et al. 2004; Martin et al. 2005). Numerical modelling has yielded similar results and predicts the protolith of material presently at the top of the GHS to have been derived from a source that was outboard of the Indian craton relative to rocks at the bottom and in the LHS which were probably sourced by the Archean craton itself (Jamieson et al. 2006). A detailed geochemical and geochronological study of metabasic rocks in the highest structural levels of the GHS in north-western Bhutan reveals that though sparse, material of similar provenance to the LHS was present in the distal portions of the margin, potentially supporting a continuous margin reconstruction for the paleo-Indian continental shelf.

The second issue is that the metasedimentary rocks throughout the GHS generally do not preserve prograde, peak-pressure mineral assemblages, which has been attributed to metamorphic overprinting during high temperature metamorphism (Brunel and Kienast 1986; Swapp and Hollister 1991; Davidson et al. 1997; Neogi et al. 1998; Ganguly et al. 2000; Dasgupta et al. 2004; Harris et al. 2004). Subsequent chemical modifications of the peak temperature assemblage by late diffusive exchange between garnet and the matrix minerals on decompression and cooling has also made it difficult to resolve the peak conditions of high temperature metamorphism. It is well established, however, that relative to metasedimentary rocks, mineral assemblages in metabasites are less sensitive to changes in pressure and temperature except at very low grades (Yardley 1989). The implications for this are that assemblages in metabasic rocks are stable over a broader range of P-T conditions. With this in mind, the metamorphic history of the metabasites in north-western Bhutan were a focus for this study for the purpose of trying to resolve the earlier, high-temperature history of rocks in the GHS, as discussed in chapter 3.

The structural thickness of the GHS is highly variable, ranging from 2-3 km in the west-central portions to > 30 km in the east (Edwards et al. 1996; 1999; Grujic et al. 2002; Searle and Godin 2003). The channel-flow model predicts it should be ~ 10-20 km thick (Royden et al. 1997; Beaumont et al. 2004; Godin et al. 2006b). The observed thickness variations may be the result of post-extrusion modifications, and/or the consequence of pulsed flow and doming of the low viscosity channel due to instabilities in the upper crust resulting in out-of-sequence thrusting within the main body of the GHS (Godin et al. 2006b). In Bhutan, evidence for pulsed channel activity causing duplication of the GHS and development of the North Himalayan gneiss domes has been found (Grujic et al. 1996; 2002; Hollister and Grujic 2006; Lee et al. 2006). Based on model results (Jamieson et al. 2006), superposition of a younger channel structurally above an earlier one would result in a thick exposure of the GHS at the surface. Jamieson et al (2006) note that the identification of the two channel packages would undoubtedly be difficult in the field however, with sufficiently detailed observations structural, metamorphic, and age discontinuities should be detectable. Chapter 3 provides a comparison of the microtextural and thermochronological data, and P-T paths of metasediments and metabasites from the highest and mid-structural levels of the GHS, to test the hypothesis for out-of-sequence thrusting in north-western Bhutan.

Finally, along the length of the orogen, an inverted metamorphic field gradient, and a zone of high strain mark the base of the GHS and top of the LHS. Since south-directed thrusting is not confined to a single surface but is distributed over a broad zone of protomylonites with both LHS and GHS affinities (Brunel 1986; Grujic et al. 2002), the zone of intense south-directed shearing is most commonly known as the MCT Zone (Grujic et al. 1996) and may be correlated with the Jaishidanda Formation in Bhutan. Largely due to the lack of outcrop exposure, the exact location of the boundary between the LHS and GHS (i.e. the MCT) has been a source of confusion (Searle et al. 2006a). Some workers place the boundary between the GHS and LHS at the kyanite-in isograd (Le Fort et al. 1986; Pêcher 1989), while others place it within the zone of condensed thrust sense shearing below the last appearance of ortho- and paragneisses of GHS affinity (Mohan et al. 1989; Searle et al. 1992; Metcalfe 1993; Stephenson et al. 2001). The channel flow model predicts the MCT zone as a metamorphic boundary and zone of high strain that develops between low-grade metasediments of the LHS and high-grade rocks for the GHS (Beaumont et al. 2001). In chapter 4, isotope and P-T data reveal that the MCT zone in southwestern Bhutan is a zone of high strain that has overprinted a metamorphic discontinuity that does not encompass the boundary between the LHS and GHS.

1.2 GEOLOGY OF THE HIMALAYA

The Himalaya is defined as the 2500 km long arc of mountain ranges that extend between the Nanga Parbat syntaxis in Pakistan and the Namche Barwa syntaxis in southeastern Tibet. It developed as a consequence of continent-continent collision between the Indian and Eurasian plates beginning ~ ca. 55 Ma (Pognante and Spencer 1991; Guillot et al. 1995; de Sigoyer et al. 2000; Leech et al. 2005). Based initially on detailed mapping of well-exposed outcrops in the Punjab and Kumaun regions of the Indian Himalaya, the orogen has been divided into six lithotectonic units that are bounded by major ductile and brittle fault systems and can be traced along the length of the orogen (Figure 1.1; Hodges 2000 and references therein). From south to north, in order of increasing structural level they include the Subhimalayan Zone; Lesser Himalayan Sequence; Greater Himalayan Sequence; Tethyan Sedimentary Sequence; Indus-Tsangpo Suture, and Transhimalayan Zone (Figures 1.1 and 1.2).

The Subhimalayan Zone constitutes foreland sediments that were deposited between the Miocene and Pliocene, and lie above the active thrust front of the orogen known as the Main Frontal Thrust (MFT). The unit comprises Paleocene – Miocene sediments of the Rawalpindi Group and Miocene – Pleistocene sediments of the Siwalik Group (Najman and Garzanti 2000 and references therein), which dominate the Subhimalayan Zone in the eastern segment of the orogen. Structurally up-section is the Lesser Himalayan Sequence (LHS), which comprises Paleoproterozoic to early Cambrian greenschist to lower-amphibolite facies meta-igneous and metasedimentary cover sequence rocks that were deposited on the north Indian continental margin prior to the onset of Himalayan orogenesis. Thrust over the LHS are rocks of the Greater Himalayan Sequence (GHS), which comprises lower amphibolite to granulite grade Neoproterozoic

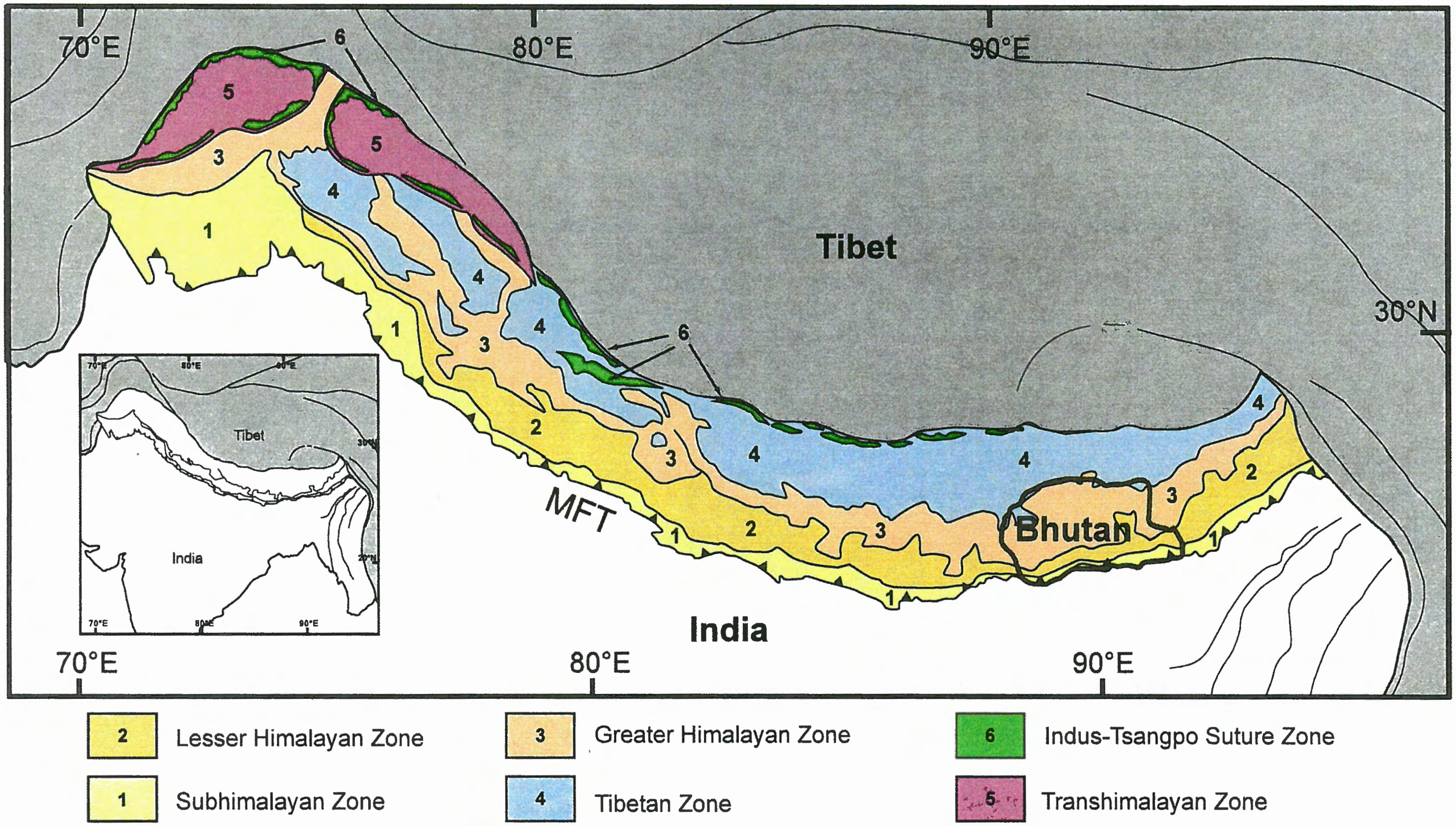

Figure 1.1: Regional map of the Himalaya modified from Gansser (1983), highlighting the major lithotectonic units of the Himalaya and the location of the Kingdom of Bhutan. ***MFT,*** Main Frontal Thrust.

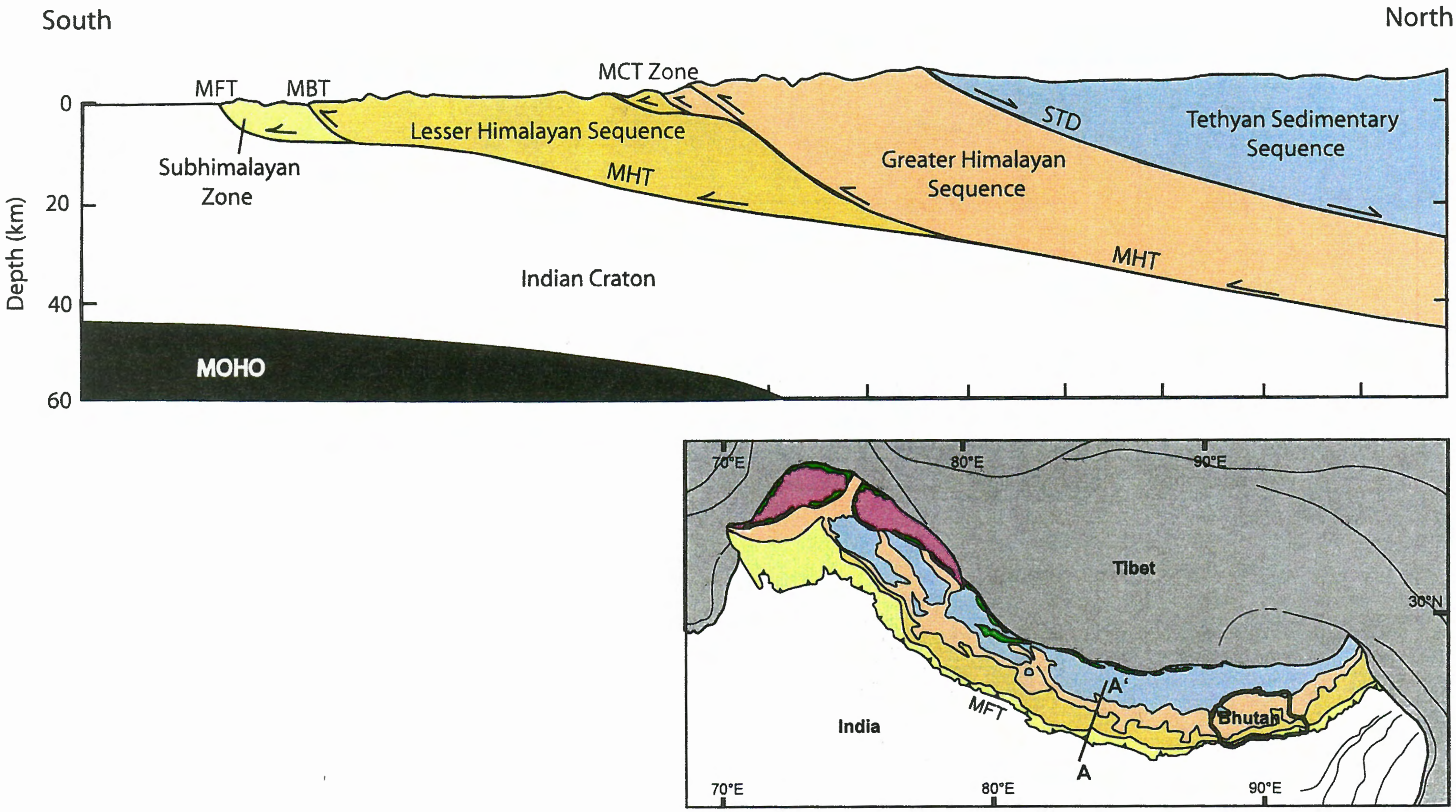

Figure 1.2: General cross section of the Himalaya modified from Hodges et al. (2001), illustrating the principal tectonostratigraphic zones of the Himalaya along A-A'. **Legend:** ***MFT,*** Main Frontal Thrust; ***MBT,*** Main Boundary Thrust; ***MCT Zone,*** Main Central Thrust zone; ***MHT,*** Main Himalayan Thrust; ***STD,*** South Tibetan Detachment.

to Ordovician metasediments and meta-igneous rocks, and Miocene leucogranites. The Tethyan Sedimentary Sequence (TSS), which overlies the metamorphic core of the orogen, constitutes an unmetamorphosed, near-complete Paleozoic – Eocene stratigraphic record of the north Indian continental margin. Marking the boundary between the Indian and Eurasian plates is the Indus-Tsangpo Suture Zone, which can be discontinuously traced along the entire length of the orogen between Myanmar and Afghanistan. It includes ophiolites of the Neo-Tethys Ocean and turbidites of both the Indian and Eurasian continental margins. Finally, the northernmost Transhimalayan Zone comprises volcanic, plutonic and associated volcaniclastic and sedimentary rocks related to the continental arc complex that marked the southern, active margin of Eurasia prior to the onset of Himalayan orogenesis.

1.2.1 ESTABLISHED PROVENANCE OF THE GHS AND LHS

Based on isotope provenance studies throughout the western and central Himalaya it has been established that the source regions of the GHS and LHS are geochemically different. Whole rock Sm-Nd data reveal that metasediments of the LHS are characterized by Nd model ages ranging between 2.3 - 2.8 Ga, while metasediments of the GHS yield model ages ranging between 1.4 - 2.4 Ga (Parrish and Hodges 1996; DeCelles et al. 2000; Miller et al. 2000; Robinson et al. 2001; Argles et al. 2003; Gehrels et al. 2003; Myrow et al. 2003; DeCelles et al. 2004; Martin et al. 2005). Epsilon neodymium values (εNd) for the two units also vary, with low εNd(500) values between -21 and -14 characterizing the LHS, while higher values ranging between -13 and -1 are common to rocks of the GHS (Martin et al. 2005, and references therein). Together, the Nd model ages and epsilon values suggest a Late Archean to Paleoproterozoic source for the metasediments of the LHS versus a Meso- to Neoproterozoic source for the GHS.

The conclusions drawn from the Nd data are supported by U-Pb detrital zircon ages obtained from both tectonic units. Detrital zircons in the LHS preserve a spectrum of ages ranging from 2.6-1.9 Ga with peaks at 2.5 and 1.9 Ga, while ages from the GHS range between 2.5 – 0.5 Ga with two prominent peaks at 1.5 and 1.0 Ga and a minor peak at 2.5 Ga (Martin et al. 2005, and references therein). From the published data, it is apparent that there is overlap between the Sm-Nd and U-Pb ages obtained from the LHS and GHS however, the preservation of a population of Neoproterozoic and Paleozoic detrital zircons in the GHS is what distinguishes it from the LHS.

In terms of igneous units, intermediate fine-grained metavolcanic rocks and the Ulleri augengneiss in the LHS yield magmatic zircon ages ranging from ~ 2.0 – 1.8 Ga (DeCelles et al. 2004), implying magmatic activity along the proto-Indian margin during that time. In the GHS, one igneous age of ~ 823 Ma has been reported (Singh et al. 2002), while the Tso Morari eclogite, granitic gneisses and undeformed granites yield zircon ages between ~ 490 – 400 Ma (DeCelles et al. 2004 and references therein.), thus implying periods of magmatic activity along the Indian margin between the Neoproterozoic and early Devonian. The age variations between the igneous rocks in the two units, and the fact that the LHS contains a greater population of Precambrian detrital zircons, suggests that the basement rocks from which sediments of the LHS and GHS were derived are variable in age. Metasediments of the LHS appear to have been derived from older, Archean – Paleoproterozoic rocks while the metasediments of the GHS are derived from a basement predominantly comprised of Neoproterozoic – Ordovician rocks.

1.2.2 STRUCTURAL EVOLUTION OF THE HIMALAYA

Three broad stages of deformation have been identified throughout the orogen, the transition between each marked by a major change in the style of deformation (Hodges 2000). From oldest to most recent the three stages include the Protohimalayan (~ 75 Ma? ~ 55 Ma); the Eohimalayan (55 Ma ~ 23 Ma); and Neohimalayan (23 Ma – present) stages of deformation and metamorphism. Evidence for the first stage is largely based on field observations from the Zanskar and Ladakh regions in the western Himalaya (Hodges 2000 and references therein), while evidence for the Eohimalayan and Neohimalayan stages are observed throughout the orogen.

As defined by Hodges (2000), the Protohimalayan stage of deformation took place prior to the onset of continent-continent collision between India and Eurasia. It has been attributed to subduction of the Tethys Ocean beneath the Eurasian craton, development of a south-verging Cretaceous fold-and-thrust belt throughout the Transhimalayan Zone; thrusting of the Kohistan arc southward over the north Indian margin; and obduction of ophiolites within the Indus-Tsangpo suture. Subsequent to the complete subduction of the intervening Tethys Ocean, the Eohimalayan stage of deformation is defined by the transition from marine to non marine sedimentation within the suture zone (Rowley 1996; Searle et al. 1997) and has been associated with under-plating of Indian continental material (D_1) to high- and ultra-high pressure eclogite conditions beneath the Eurasian continent and Transhimalayan Zone (Pognante and Spencer 1991; Guillot et al. 1995). Associated with the late Eohimalayan – early Neohimalayan deformational phase (D_2, ca. 23 - 16 Ma) is the continued development of south-directed thrusts and isoclinal folds throughout the GHS and TSS, as the GHS was being exhumed to the surface from midcrustal depths. The pervasive east-west trending foliation (S_2) observed throughout the GHS defines the axial plane of the isoclinal folds. Most prominent of the D_2 structures are the east-west striking, north-dipping MBT, MCT, and STD. Finally, deformation of the D_2 structures and the development of broad east-west trending open folds and shear bands (S_3) that cross cut the pervasive S_2 foliation occurred during the most recent, Neohimalayan phase of deformation (D_3) which is associated with continued exhumation and decompression of the GHS.

1.3 GEOLOGY OF BHUTAN

Of the six lithotectonic units that comprise the orogen, four are exposed in the Kingdom of Bhutan (Figures 1.2 and 1.3). From south to north, in order of increasing structural level, the units include the Siwaliks, LHS, GHS and TSS (Gansser 1964; 1983). The Tertiary foreland basin sediments of the Siwaliks are separated from the LHS along the north-dipping Main Boundary Thrust (MBT). At its upper boundary, the LHS is bounded by the north-dipping Main Central Thrust (MCT) along which migmatites of the GHS were thrust beginning in the early Miocene (Hodges 2000 and references therein; Daniel et al. 2003). At its uppermost boundary, the GHS is bounded by the north-dipping South Tibetan Detachment (STD), a broad ductile shear zone with normal shear sense (Burchfiel et al. 1992; Edwards et al. 1996; Edwards et al. 1999; Wiesmayr et al. 2002), which separates high grade GHS rocks from the overlying low-grade to unmetamorphosed sediments of the TSS (Gansser 1983; Burg and Chen 1984; Burchfiel et al. 1992; Garzanti 1999).

In addition to the four lithotectonic units discussed above, klippen of low-grade Neoproterozoic metasediments of the Chekha Formation are observed structurally above

Figure 1.3: a) Geological map of Bhutan modified from Grujic et al. (2002). Line A-A' indicates the position of the cross-section presented in Figure 1.3b. **b)** Geological cross-section through western Bhutan along line A-A' illustrating the nature of the boundaries between units, and the relative locations of the three structural levels that are discussed in this study. Information was compiled from Gansser (1983), Burchfiel et al. (1992), Wu et al. (1998), and this study. The position of the Main Himalayan Thrust (MHT) has been extrapolated from the INDEPTH results (Hauck et al. 1998). ***HSL,*** highest structural level; ***MSL,*** mid-structural level; ***LSL,*** lower structural level; ***LHS,*** Lesser Himalayan Sequence; ***GHS,*** Greater Himalayan Sequence; ***TSS,*** Tethyan Sedimentary Sequence; ***MFT,*** Main Frontal Thrust; ***MBT,*** Main Boundary Thrust; ***MCTl,*** lower Main Central Thrust; ***MCTu,*** upper Main Central Thrust;***KT,*** Kakhtang Thrust; ***STDl,*** lower South Tibetan Detachment; ***STDu,*** upper South Tibetan Detachment. Slivers of green illustrate the structural positioning of garnet-amphibolite bearing horizons at the 'mid'– and higher – structural levels of the GHS. Slivers of red serve to remind that though the cross-section does not intersect a major Miocene leucogranitic body, leucogranite sills are observed throughout the GHS.

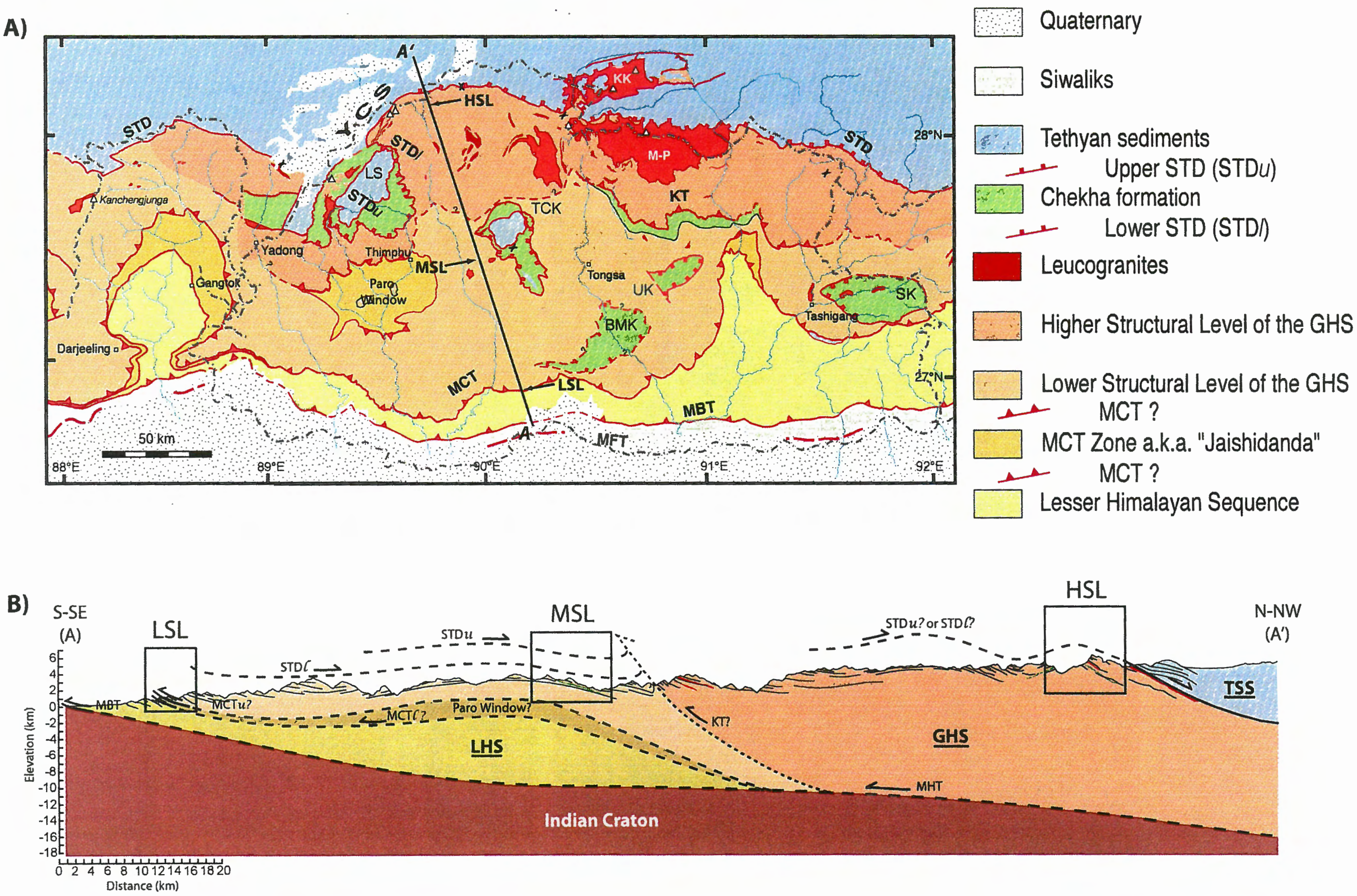
A)
A'
A
HSL
MSL
LSL
STD
STDl
STDu
YCS
LS
KK
M-P
KT
TCK
UK
BMK
SK
MCT
MBT
MFT
Kanchenjunga
Yadong
Thimphu
Gangtok
Paro Window
Darjeeling
Tongsa
Tashigang
28°N
27°N
88°E
89°E
90°E
91°E
92°E
50 km
Quaternary
Siwaliks
Tethyan sediments
Upper STD (STDu)
Chekha formation
Lower STD (STDl)
Leucogranites
Higher Structural Level of the GHS
Lower Structural Level of the GHS
MCT ?
MCT Zone a.k.a. "Jaishidanda"
MCT ?
Lesser Himalayan Sequence
B)
S-SE (A)
N-NW (A')
LSL
MSL
HSL
STDu
STDl
STDu? or STDl?
MBT
MCTu?
MCTl?
Paro Window?
KT?
MHT
LHS
GHS
TSS
Indian Craton
Elevation (km)
6
4
2
0
-2
-4
-6
-8
-10
-12
-14
-16
-18
0 2 4 6 8 10 12 14 16 18 20
Distance (km)

the GHS along what is here referred to as the lower STD (STDl; Figure 1.2; Gansser 1983; Bhargava 1995; Grujic et al. 2002). Locally, the sediments of the TSS are observed structurally above the Chekha Formation along what will here be referred to as the upper STD (STDu; Figure 1.3). Two levels of the STD have also been observed in the Annapurna-Manaslu region (Searle and Godin 2003; Godin et al. 2006a) and the Mount Everest massif (Searle et al. 2003; 2006b).

Of particular interest in this study is the GHS, which represents the metamorphic core of the orogen. The unit predominantly comprises intensely metamorphosed Proterozoic basement and overlying sedimentary cover rocks that formed the distal part of the northern proto-Indian margin prior to the onset of continent-continent collision at ca. 55 Ma. It is generally accepted that the GHS comprises material from the mid- and upper crust of the proto-Indian margin, which was underplated, accreted to the orogen and subsequently metamorphosed and migmatized prior to and during exhumation between the MCT and STD beginning ca. 23 Ma (Hodges 2000; Daniel et al. 2003; Harris et al. 2004).

Metamorphic grade within the GHS ranges from upper greenschist to lower amphibolite facies within the MCT zone and immediately above it, to granulite facies at the top where high grade metamorphism is spatially associated with large Miocene leucogranite intrusions (Gansser 1983; Swapp and Hollister 1991; Grujic et al. 1996; Davidson et al. 1997; Daniel et al. 2003). Across the lower STD, metamorphic grade decreases steeply from granulite to upper amphibolite-facies, and to greenschist-facies across the upper STD and into the TSS (Grujic et al. 2002). Thus, throughout the LHS and into the lower parts of the GHS metamorphic isograds are inverted, whereas throughout the uppermost part of the GHS and into the Chekha Formation isograds are right way up, a pattern that is observed along the length of the Himalaya (Gansser 1983; Hodges 2000; Searle et al. 2003). In central Bhutan the inverted metamorphic sequence in the GHS is locally repeated (Swapp and Hollister 1991; Grujic et al. 1996; Davidson et al. 1997; Daniel et al. 2003), where garnet-staurolite grade schists are observed both above and below garnet – sillimanite-bearing granulite facies gneisses and migmatites. The relatively lower-grade rocks are confined to the footwall of the major out-of-sequence Kakhtang Thrust, while the garnet – sillimanite-bearing migmatites and the largest bodies of leucogranite define the hanging wall (Gansser 1983; Grujic et al. 1996; Davidson et al. 1997; 2002). Pressure-temperature estimates from footwall rocks of the Kakhtang Thrust reveals that rocks at mid-structural levels of the GHS were not subjected to temperatures above 650 °C (Davidson et al. 1997; Ritchie 2004). The preservation of growth zoning profiles in garnets at this structural level supports the conclusion made from the P-T estimates.

Throughout the GHS rocks show evidence for three metamorphic stages: i) M_1 corresponds to the growth of garnet and kyanite during prograde, peak-pressure metamorphism, probably associated with underthrusting of the proto-Indian continental margin beneath the Eurasian continental margin at ca. 44 ~ 30 Ma (Vance and Harris 1999; Foster et al. 2000); ii) M_2, a peak temperature event that took place at ca. 30 ~ 20 Ma and corresponds to melting at midcrustal levels, and development of the peak metamorphic mineral assemblage (garnet and sillimanite) that defines the regionally pervasive foliation observed throughout the GHS (Brunel and Kienast 1986; Neogi et al. 1998; Ganguly et al. 2000; Catlos et al. 2004; Dasgupta et al. 2004); and iii) M_3, which is associated with the breakdown of garnet and sillimanite to cordierite and biotite during the decompression at relatively moderate temperatures (Swapp and Hollister 1991; Neogi et al. 1998; Ganguly et al. 2000).

Except for the rare occurrence of kyanite as inclusions in garnet and/or pseudo-morphing of kyanite by high temperature sillimanite, rocks from the highest structural levels of the GHS generally do not preserve the prograde, peak-pressure mineral assemblage. Absence of the prograde assemblage is likely the consequence of metamorphic overprinting during M_2, when rocks were subjected to peak temperatures in excess of 750 °C during isobaric heating, followed by isothermal decompression from pressures > 12 kbar (Swapp and Hollister 1991; Davidson et al. 1997; Dasgupta et al. 2004). It is also difficult to resolve from the metasedimentary rocks the absolute peak temperature of M_2 metamorphism as a consequence of chemical modifications of the peak temperature assemblage by late diffusive exchange between garnet and the matrix minerals on decompression and cooling of the GHS (Swapp and Hollister 1991; Daniel et al. 2003).

In this study, metasedimentary and metabasic rocks were collected from three localities along a north-south transect across the GHS of western Bhutan (Figure 1.3). The first group of samples that will be discussed were taken from locations in the relatively higher structural levels of the GHS, ~ 1-2 km below the STD. A second and smaller group was collected further south, from the apparently mid-structural level of the unit, while the third and final group of samples were collected from the base of the GHS at the lowest structural levels. The following sections provide descriptions of the sampled and surrounding rocks at each of the levels, in the context of their structural relationship between one another.

1.3.1 Higher Structural Level (HSL)

During his pioneer mapping of the geology of Bhutan, Augusto Gansser (1983), identified a major northwest trending anticline and syncline in the higher structural levels of the GHS in north - western Bhutan (Figure 1.4). Within the anticline Gansser (1983) also recognized the presence of three apparently continuous mafic layers. Geological observations made at the base of Masang Kang (this study) revealed that mafic and ultramafic rocks in fact form discontinuous layers and boudins in an ~ 2 km thick zone that forms the core of the anticline (Figure 1.5). Boudins are variable in size ranging from one to several metres in diameter. For simplicity, in the following discussions the suite of metabasic and ultramafic rocks collected from this structural level will be referred to as the higher structural level (HSL) suite. For a detailed list of sample numbers and corresponding GPS co-ordinates, refer to Appendix A.

Structural observations made along two river valleys at the base of Masang Kang indicate that the pervasive, penetrative foliation strikes northwest – southeast, dipping to the northeast within the northern limb of the antiform and to the southwest in the southern limb, the fold axis trending northwest – southeast (Figure 1.6a,b). Stretching and mineral lineations measured within the foliation planes trend to the east – southeast (Figure 1.6c). The main, penetrative foliation corresponds to the regional S_2 fabric that is interpreted to have developed during the late Eohimalayan – early Neohimalayan stage of deformation. Most of the information pertaining to the early Eohimalayan phase of deformation appears to be absent at this structural level.

Approximately 1 km below the STD, at the structurally highest levels of the GHS,

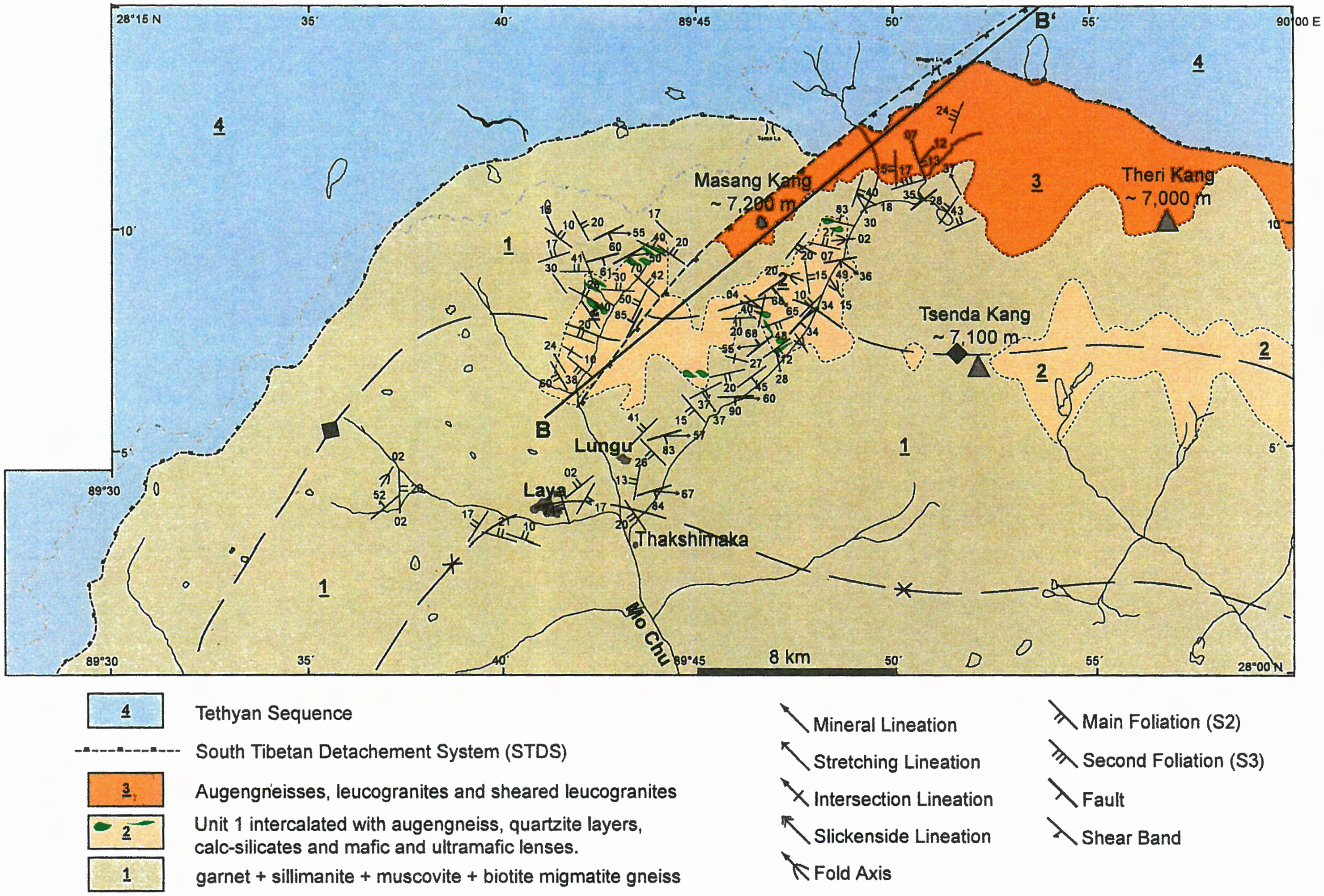

Figure 1.4: Geological map of north - western Bhutan on which locations of metasedimentary and metabasic samples from the HSL have been marked. Information was compiled from Gansser, (1983), Burchfiel et al. (1992), Wu et al. (1998) and this study. The heavy, grey, dash-dot line marks the Bhutanese border. B-B', marks the position of the cross-section in Figure 1.5.

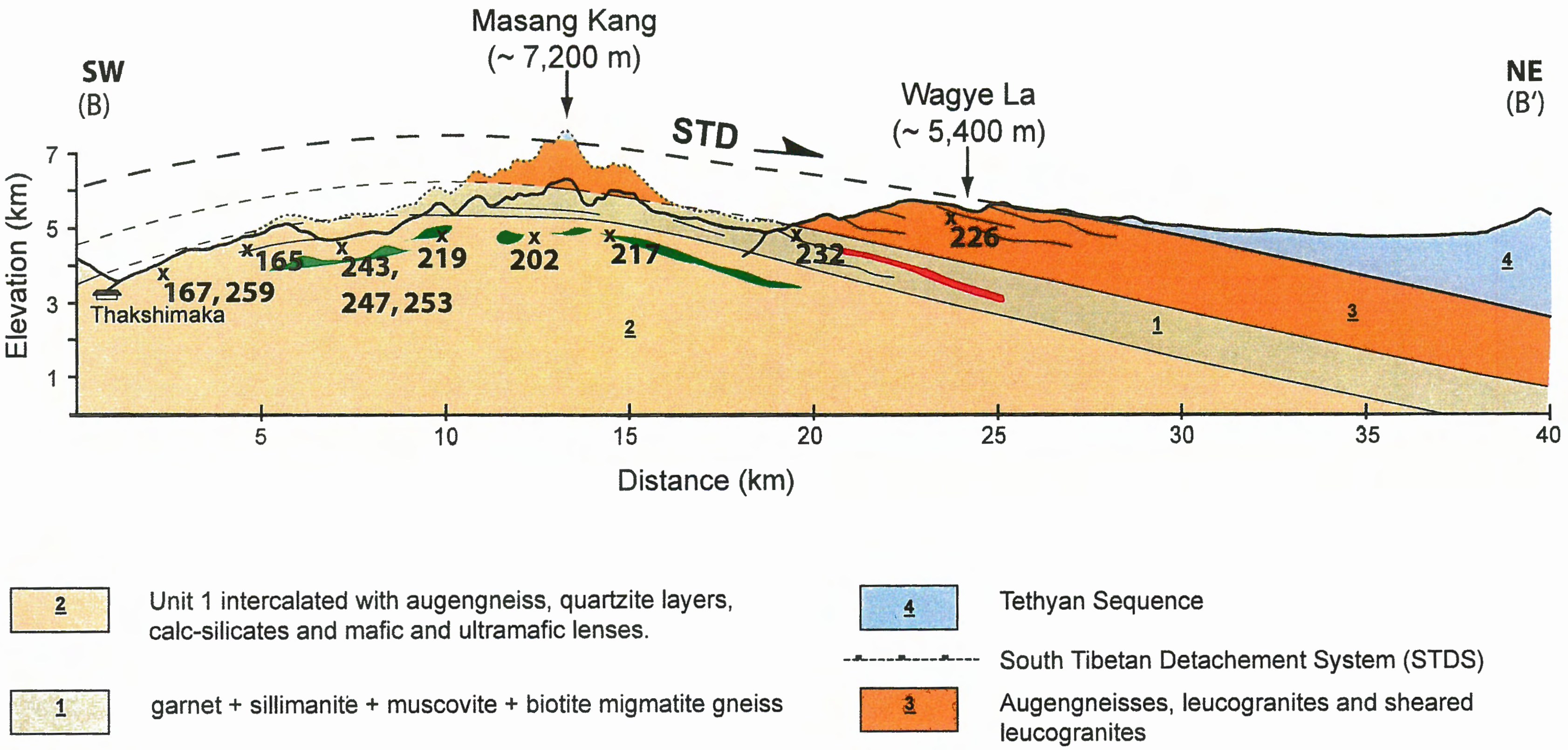

Figure 1.5: Geological cross-section through Masang Kang and into southern Tibet along line B-B' in figure 1.4. ***Solid, heavy line:*** the topographic profile based on SRTM data; ***dashed, heavy line:*** topographic profile to the true elevation; ***green layers and boudines:*** position of metabasic rocks; ***red:*** late Miocene leucgranites.

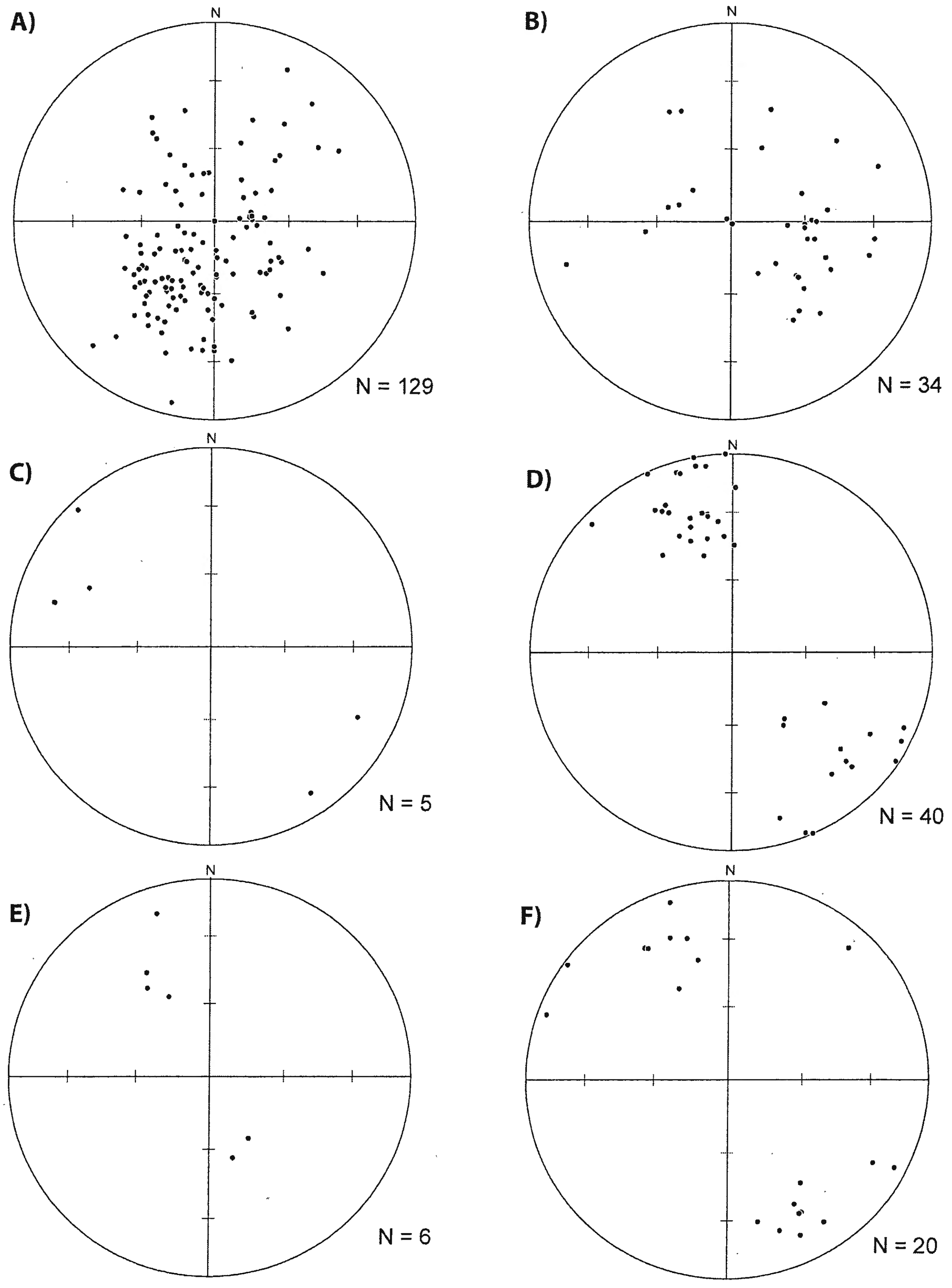

Figure 1.6: Equal area projections of structural data from the higher structural level (HSL) of the GHS in north - western Bhutan. A) main foliation; b) stretching lineation measured on foliation planes; c) fold axes; d) fault planes; e) shear bands; f) stretching lineations measured on fault planes and within shear bands. Tick marks spacing on stereonet is 30 degrees.

the NW-SE trending S_2 foliation is obliquely overprinted by a penetrative C-type fabric that is visible on the outcrop scale and dips to the north (Figure 1.6), offsetting the main foliation. N-NW trending stretching lineations are associated with NW dipping shear bands and faults, while S-SE trending stretching lineations are associated with southeast trending structures (Figure 1.6). Development of these structures coincides with concomitant normal-and thrust-sense shearing related to the exhumation of the GHS between the STD and MCT respectively, during Neohimalayan deformation.

A cross-section through the area (Figure 1.5) illustrates that biotite + muscovite + sillimanite + garnet gneisses and migmatites (Unit 1) comprise the SW portion of the transect followed by a narrow ~ 0.5 km zone of the same gneiss intercalated with augengneiss, quartzite and calc-silicates with minor mafic lenses. This narrow zone grades into biotite + muscovite + sillimanite + garnet gneiss with both mafic and ultramafic lenses, which form the core of the antiform (Unit 2). Dikes, sills and irregular lenses of Miocene muscovite + tourmaline + beryl leucogranite are locally observed within the migmatites. To the northeast, structurally above the gneisses and migmatites, is a ~ 3 km thick package of augen gneisses, leucogranites and sheared leucogranites (Unit 3) that extend to the base of the STD.

All rocks have undergone recrystallization at granulite facies conditions, followed by a retrograde overprint at amphibolite facies conditions, both presumably during Himalayan orogenesis. Due to the intense metamorphic overprint and discontinuous nature in outcrop, it was impossible to distinguish primary contacts between the metabasic rocks and the surrounding metasediments. On the outcrop scale three mineralogically different types of metabasic rocks were distinguishable. The three types include i) coarse to medium grained garnet (± pyroxene) bearing amphibolites; ii) coarse to medium-grained pyroxene-bearing amphibolites; and iii) medium to fine-grained biotite amphibolites. The ultramafic rocks are coarse-grained cumulate rocks containing relict olivine, pyroxene and chrome spinel. At the outcrop scale, a weakly developed foliation can be observed in the fine-grained lithologies. With the exception of the ultramafic rocks, primary igneous textures and minerals are not preserved in the mafic rocks. The foliation within the boudins is discordant with the main, planar, north-west – south-east trending planar fabric observed in the surrounding migmatites.

1.3.2 Mid-Structural Level (MSL)

In the mid-structural levels (labelled as such as a consequence of the relative ground position in the unit) of the GHS in western Bhutan, a unit of migmatites and minor leucogranites structurally overlies a zone, perhaps a few hundred metres thick, of intercalated mica schists, quartzites, garnet – amphibolites, and minor migmatites. Three garnet amphibolite samples were collected from a metabasic boudin hosted by biotite + muscovite + sillimanite + garnet gneisses and migmatites that are virtually identical to the gneisses and migmatites hosting the HSL suite. The penetrative foliation at this level also strikes east - west and dips shallowly to the north (Figure 1.7). Stretching mineral lineations measured on the foliation surfaces trend north – northwest.

The contact between the intercalated muscovite bearing metasedimentary and metabasic rock package with the overlying migmatites was not actually observed, and according to the geological map of Grujic et al (2002; Figure 1.3a), may be the western extension of the out-of-sequence Kakhtang Thrust (KT). In this case, the mafic boudins that were sampled at this level are situated in the footwall of the thrust. However, as is indicated by the dotted line on the map, the position of the KT in western Bhutan is uncertain and has only been inferred. In central Bhutan, the type locality for the KT, garnet – staurolite grade metasedimentary rocks are overlain by garnet – sillimanite grade migmatites (Davidson et al. 1997; Grujic et al. 2002). Unfortunately the marked variation in metamorphic grade observed in the type locality for the KT has not been observed in the field along the transect discussed here. Swapp and Hollister (1991), who conducted a preliminary study of the metasedimentary rocks exposed along the same transect described here, postulated the presence of a thrust shear-zone of considerable cumulative displacement between rocks of the MSL and HSL based on spatial variations between mineral reactions and deformation textures they observed in thin-section. Thus, it remains unclear whether or not the KT is present in the north-western part of Bhutan. If it does exist, then the exact location of the structure is uncertain.

1.3.3 Lower Structural Level (LSL)

Early mapping carried out by the Geological Survey of India across much of Bhutan revealed the presence of a group of mylonitized metasedimentary rocks that can be traced, almost continuously, between the lowest structural levels of the GHS and

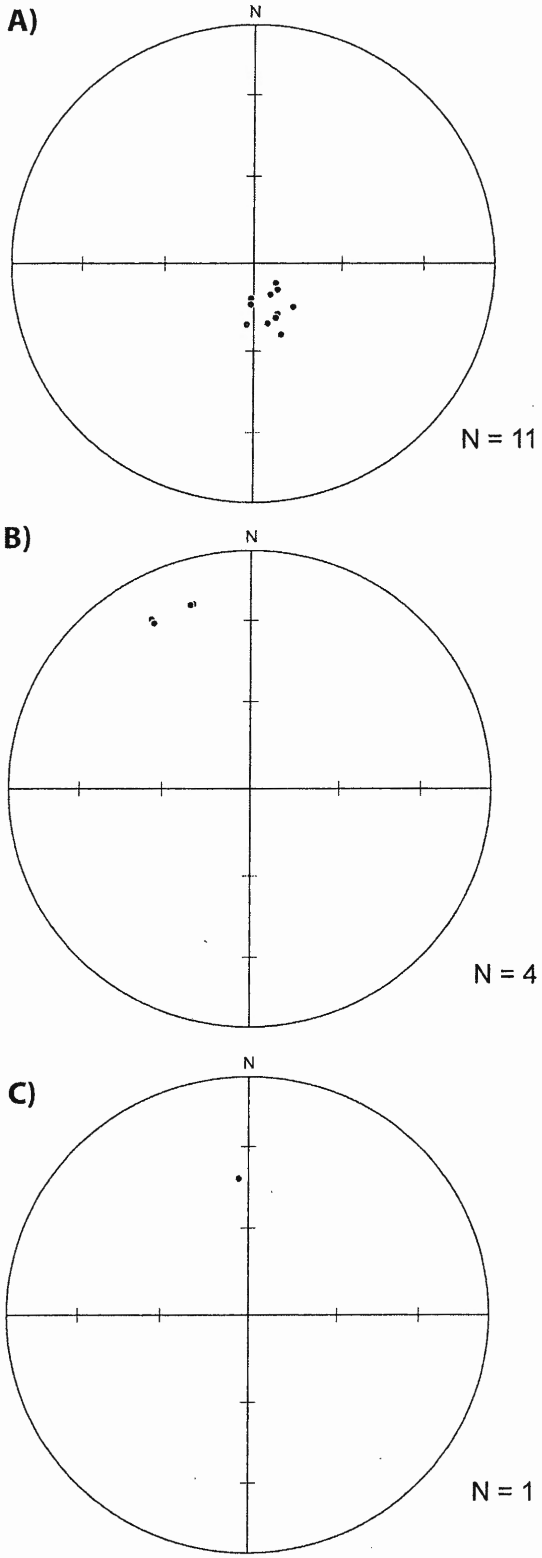

Figure 1.7: Equal area projections of structural data from the mid-structural level (MSL) of the GHS in north - western Bhutan. A) main foliation; b) stretching lineation measured on foliation planes; c) Shear bands related that cut the main foliation. Tick marks spacing on stereonet is 30 degrees.

highest structural levels of the LHS (Dasgupta 1995). They described the package as predominantly comprising of garnet-mica schists that are intercalated with micaceous quartzite, rare carbonate bands and local lenses of carbonaceous schist. The mylonitized and metamorphic nature of the package, combined with its persistent occurrence between the GHS and LHS led geologists at the Geological Survey of India to classify the group of rocks as the Jaishidanda Formation. Structural observations made along the Surey-Jigmecholing (northeast of Gelephu) and Sarpang – Damphu sections in this study (Figure 1.8), where the unit is thickest (~ 400 m), reveals that the Jaishidanda Formation comprises intercalated and intensely mylonitized garnet-mica schists, micaceous quartzites, rare carbonate bands, orthogneisses, augen gneisses and leucogranites. Based on contrasting metamorphic grade of the rocks comprising the package, the micaceous schists, quartzites and carbonate bands are assumed to be of LHS affinity while the gneisses and leucogranites were interpreted to be of GHS affinity.

Detailed structural observations (Figure 1.9) also reveal the presence of a north - south trending antiform between the two transects (Figure 1.8). Along the Surey-Jigmecholing section, the main penetrative foliation dips to the northeast while further west, the same foliation dips to the north – northwest along the Sarpang – Damphu section (Figure 1.9). Stretching lineations along both transects trend to the north – northwest (Figure 1.9c). As was the case in the HSL and MSL, the penetrative foliation observed at the lower structural level may also correspond to the regional S_2 fabric that developed during the late Eohimalayan – early Neohimalayan phase of deformation.

1.4 EXHUMATION OF THE GHS: THE CHANNEL FLOW-EXTRUSION HYPOTHESIS

A number of models have been proposed to account for ductile deformation and exhumation of the GHS along with several other geological features observed throughout the Himalayan-Tibetan orogen, including the presence of an inverted metamorphic sequence at the base of the GHS and upper reaches of the LHS, within the MCT zone. The models explain the inverted sequence of isograds as the consequence of either syn-post metamorphic deformation (i.e. shearing of a previously right-way up metamorphic sequence; Brunel and Kienast 1986; Searle and Rex 1989; Jain and Manickavasagam 1993; Hubbard 1996), or as a product of a heat source (i.e. hot-over-cold thrusting, shear heating, intrusion of leucogranites; Le Fort 1975; Hodges and Silverberg 1988; Molnar

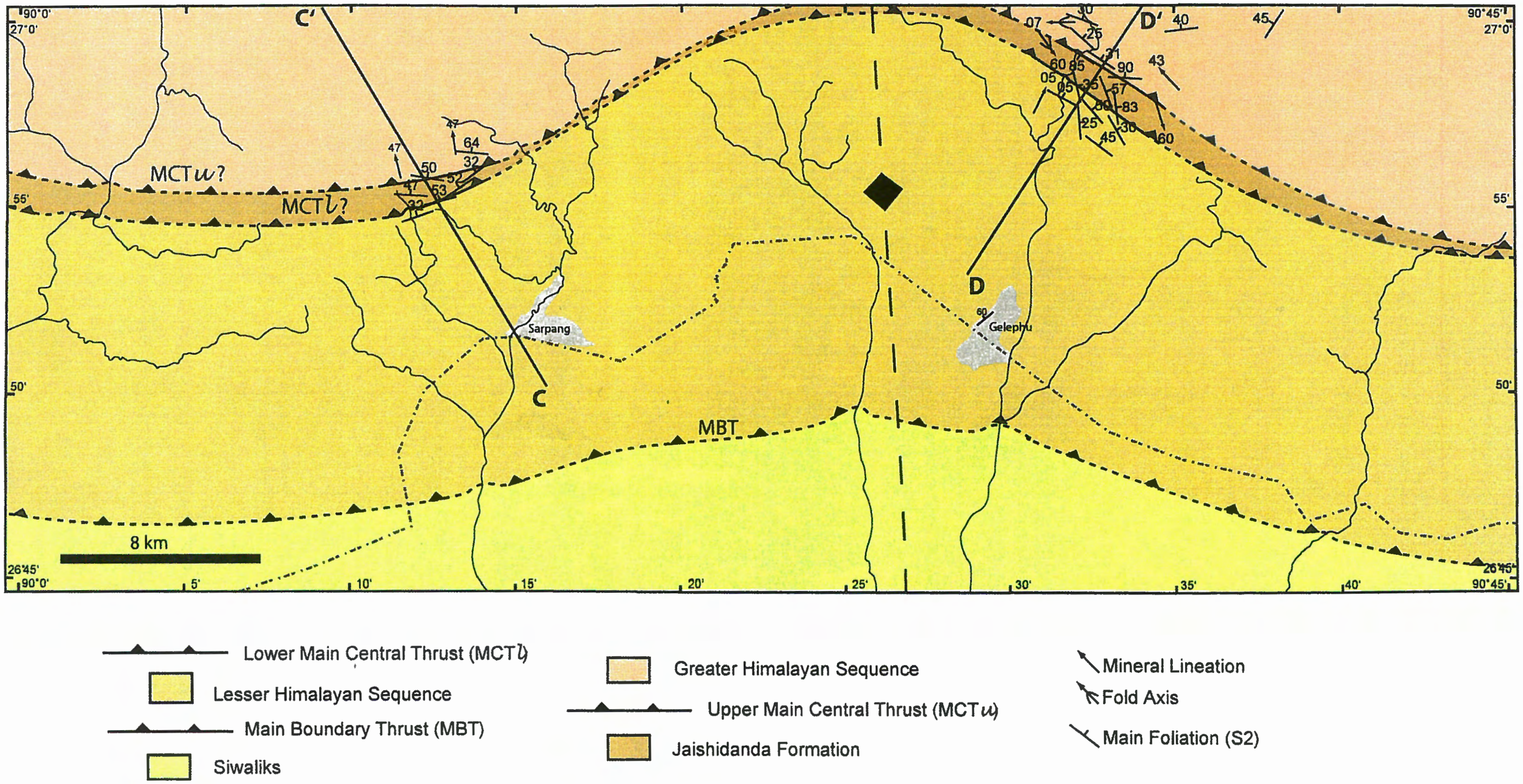

Figure 1.8: Geological map of southern Bhutan. Information was compiled from Gansser (1983), Bhargava (1995), and this study. The heavy, grey, dash-dot line is the Bhutanese border. Line C-C' and line D-D' indicate the position of the Sarpang-Damphu and Gelephu-Surey transects presented in figure 1.9.

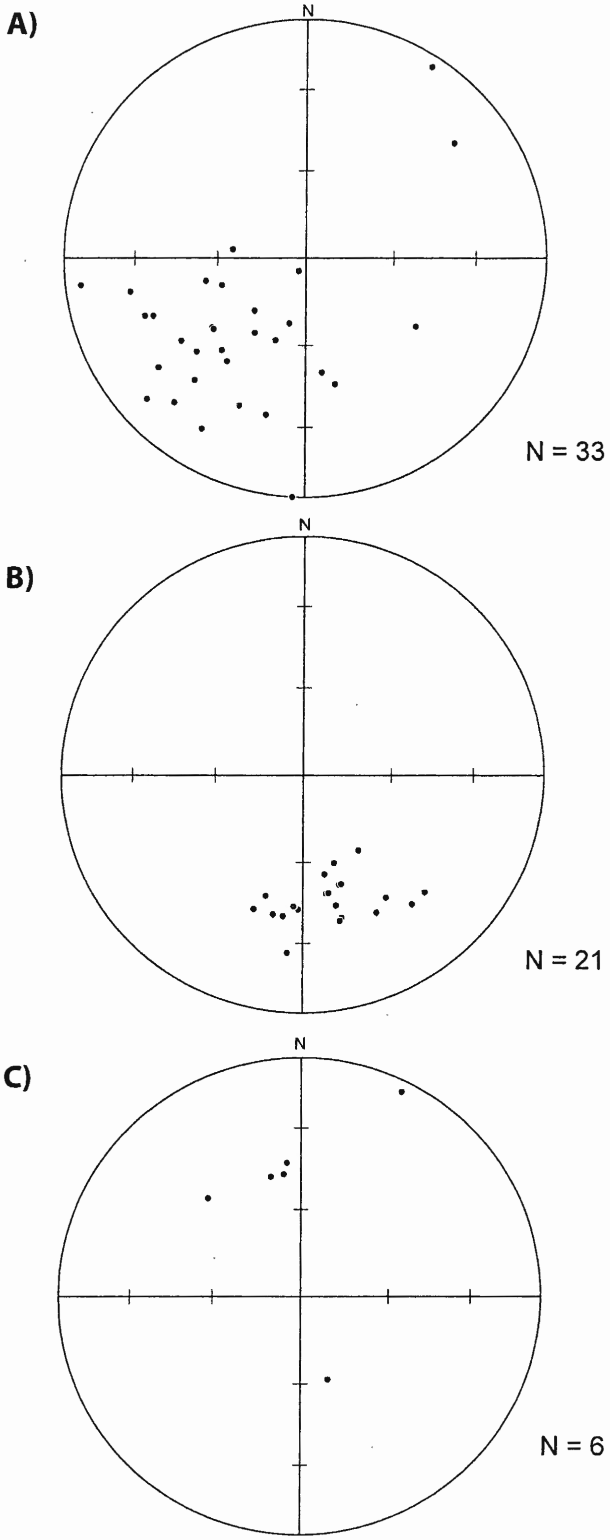

Figure 1.9: Equal area projections of structural data from the Jaishidanda Formation in southern Bhutan. A) main foliation measured along the Surey-Jigmecholing section; b) main foliation measured along the Sarpang - Damphu section; c) stretching lineations measured in both sections.

and England 1990). None of the models account for the development of the STD at the top of the GHS, along which normal-sense movement was contemporaneous with thrust-sense displacement on the MCT. It is this critical observation that has led to the development of the channel flow-extrusion hypothesis which currently, is the most popular thermo-mechanical model to explain the development and exhumation of the GHS (Figure 1.10; Grujic et al. 1996; Royden 1996; Beaumont et al. 2001; Beaumont et al. 2004; Jamieson et al. 2004).

The model predicts the formation of a low-viscous channel at mid-crustal levels in a thickened crust, as mantle lithosphere is subducted. Melting and the associated decrease in viscosity of mid-crustal rocks is invoked at temperatures in excess of 700°C, broadly corresponding to muscovite dehydration conditions. Potential heat sources for the increase in temperature include asthenospheric, strain, and/or radiogenic heating. The models by Beaumont et al. (2001) assumes a radiogenic heat source from a tectonically thickened crust (Jamieson et al. 2004). Pressure gradients in the upper crust lead the low viscosity material to flow laterally and as erosion is induced along the orogenic front, the channel is exhumed between two shear zones with thrust-sense movement confined to the base and normal-sense movement to the upper margin (Figure 1.10). As the channel material migrates through the crust, advection of heat forces deformation of the isotherms resulting in the development of an inverted metamorphic field gradient at the base, and right-way-up at the top. Depending on the strength and geometry of the over- and underlying crust, and the degree of erosion at the surface, exhumation of the viscous material is not confined to a single channel but may give rise to a second channel above the first (Figure 1.10; Hollister and Grujic 2006), and/or doming to the north of the active orogenic front.

Geochemical, geochronological and mineral chemical data for GHS rocks from western Bhutan are presented in chapters 2-4 of this thesis. A comparison of the data in the context of the thermomechanical models presented above, and how they compare with studies conducted elsewhere in the orogen is provided in the final discussion chapter (Chapter 5).

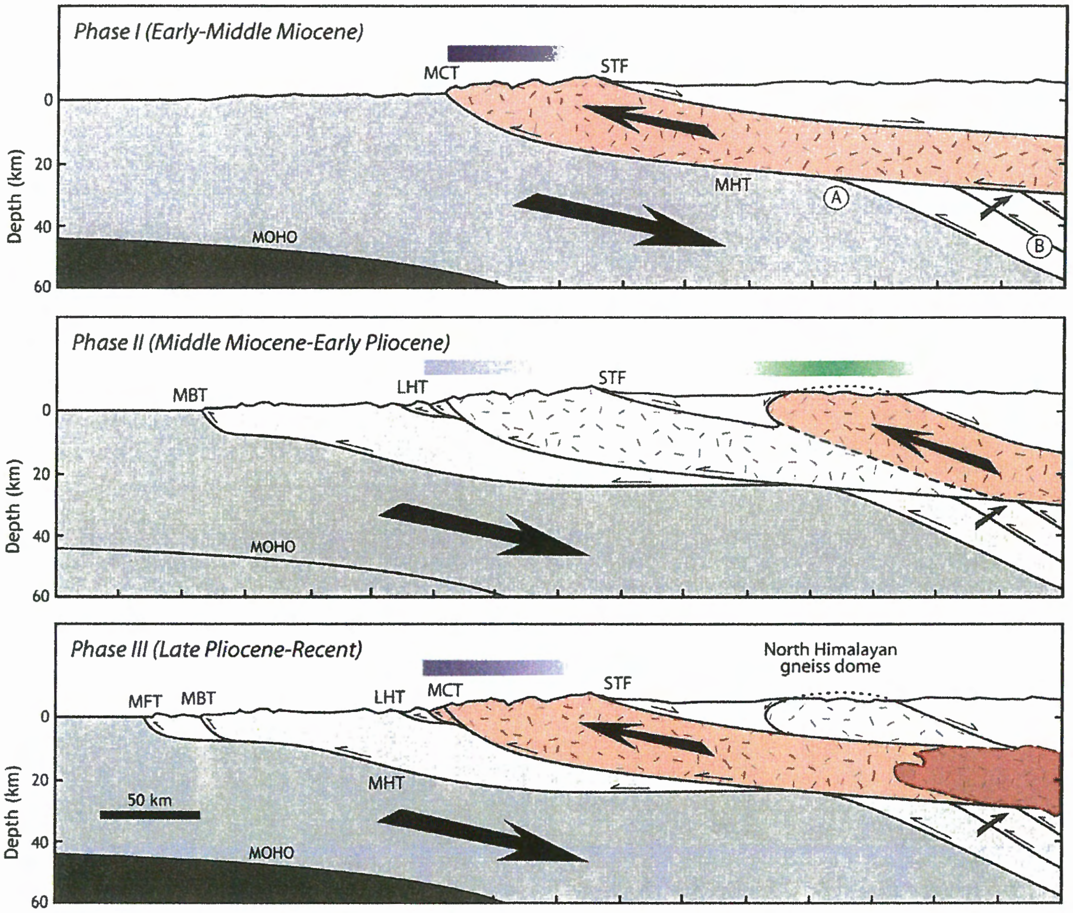

Figure 1.10: Schematic channel flow cross-sections taken directly from Hodges (2006) illustrating the three phases of channel extrusion at the Himalayan front since the Early Miocene. Dark-grey shading designates the Indian craton which is being underthrust below the Eurasian plate to the north. Fields with light-grey shading, random-dash patterning, and no shading represents Indian crustal material that has been accreted to the Eurasian plate. Unpatterned material corresponds to the un- to weakly metamorphosed TSS. Material with random dash patterning includes high-grade metamorphic rocks of extruded channels. The actively extruding material in each frame has a light-red overlay pattern. Previously extruded material has no overlay shading. Note the development of a ductile shear zone (dashed heavy line) at the base of the actively extruding material in the frame for Phase II. The dark-red shading in the Phase III frame indicates partially molten material as imaged in the INDEPTH seismic reflection experiment (Nelson et al. 1996). The blue bars in each frame represent the zone of orographic rainfall, with the colour gradient representing the rainfall gradient in a schematic way – lighter colours indicate lighter rainfall. Note that average rainfall is much lower during Phase II, a speculation based on sedimentological evidence for lower erosion rates. The green bar indicates a zone of extension over the North Himalayan gneiss domes, with the gradient representing intensity of extensional strain in upper crustal material. **Legend:** LHT, Lesser Himalayan thrust system; MBT, Main Boundary thrust system; MCT, Main Central thrust system; MFT, Main Frontal thrust system; MHT, Main Himalayan thrust; STF, South Tibetan fault system.

CHAPTER II: PROVENANCE

2.1 INTRODUCTION

The Greater Himalayan Sequence (GHS) is a continuous belt of metamorphic rocks extending along the entire length of the Tibet-Himalayan orogenic front. Detrital zircon U-Pb ages and Sm-Nd whole rock data (e.g. Parrish and Hodges 1996; Miller et al. 2000; Argles et al. 2003; DeCelles et al. 2004; Martin et al. 2005) indicates that the GHS comprises migmatized Proterozoic orthogneisses, and metasediments derived predominantly from Neoproterozoic to Cambrian rocks which formed the sedimentary cover of the north Indian continental margin prior to Himalayan orogenesis. Rocks of the Lesser Himalayan Sequence (LHS), on the other hand are comprised of Paleoproterozoic orthogneisses (DeCelles et al. 2000) and metasediments derived mainly from Archean to Cambrian igneous and metamorphic basement material (Parrish and Hodges 1996; DeCelles et al. 2000; Myrow et al. 2003; Martin et al. 2005). According to the field data upon which the numerical, thermo-mechanical channel flow models of Beaumont et al. (2001; 2004) and Grujic et al. (2002) are based, the basement and sedimentary cover rocks of the Indian margin were underthrust to mid-crustal levels at the onset of continent-continent collision (ca. 55 Ma). The models predict that the rocks were metamorphosed and underwent partial melting at mid-crustal levels prior to exhumation to their present day positions between the Main Central Thrust (MCT) and South Tibetan Detachment (STD). The models also suggest that the exhumed material is of Indian affinity (Jamieson et al. 2005).

In this chapter geochronological and geochemical data from metabasic and ultramafic rocks are presented. Samples were collected from the apparent mid- and highest structural levels of the GHS in north-western Bhutan (Figure 2.1), where they were recognized by Gansser (1983). However, despite their known presence in outcrop, the metamorphic history and relationship of metabasites with the surrounding metasediments remain poorly understood. The primary aim of this chapter is to constrain the provenance of the metabasic and ultramafic rocks in the GHS of Bhutan in order to understand the tectonic nature of the north Indian margin prior to the onset of Himalayan orogenesis. The study demonstrates that fragments of Precambrian igneous rocks, though apparently sparse, are preserved within the GHS suggesting that Paleo - Mesoproterozoic

Figure 2.1: Geological map and cross-section for Bhutan. **a)** Geological map of Bhutan modified from Grujic et al. (2002). Line A-A' indicates the position of the cross-section presented in Figure 2.1b. **b)** Geological cross-section through western Bhutan along line A-A' illustrating the nature of the boundaries between units, and the relative locations of the three structural levels that are discussed in this study. Information was compiled from Gansser (1983), Burchfiel et al. (1992), Wu et al. (1998), and this study. The position of the Main Himalayan Thrust (MHT) has been extrapolated from the INDEPTH results (Hauck et al. 1998). ***HSL,*** highest structural level; ***MSL,*** mid-structural level; ***LSL,*** lower structural level; ***LHS,*** Lesser Himalayan Sequence; ***GHS,*** Greater Himalayan Sequence; ***TSS,*** Tethyan Sedimentary Sequence; ***MFT,*** Main Frontal Thrust; ***MBT,*** Main Boundary Thrust; ***MCTl,*** lower Main Central Thrust; ***MCTu,*** upper Main Central Thrust;***KT,*** Kakhtang Thrust; ***STDl,*** lower South Tibetan Detachment; ***STDu,*** upper South Tibetan Detachment.

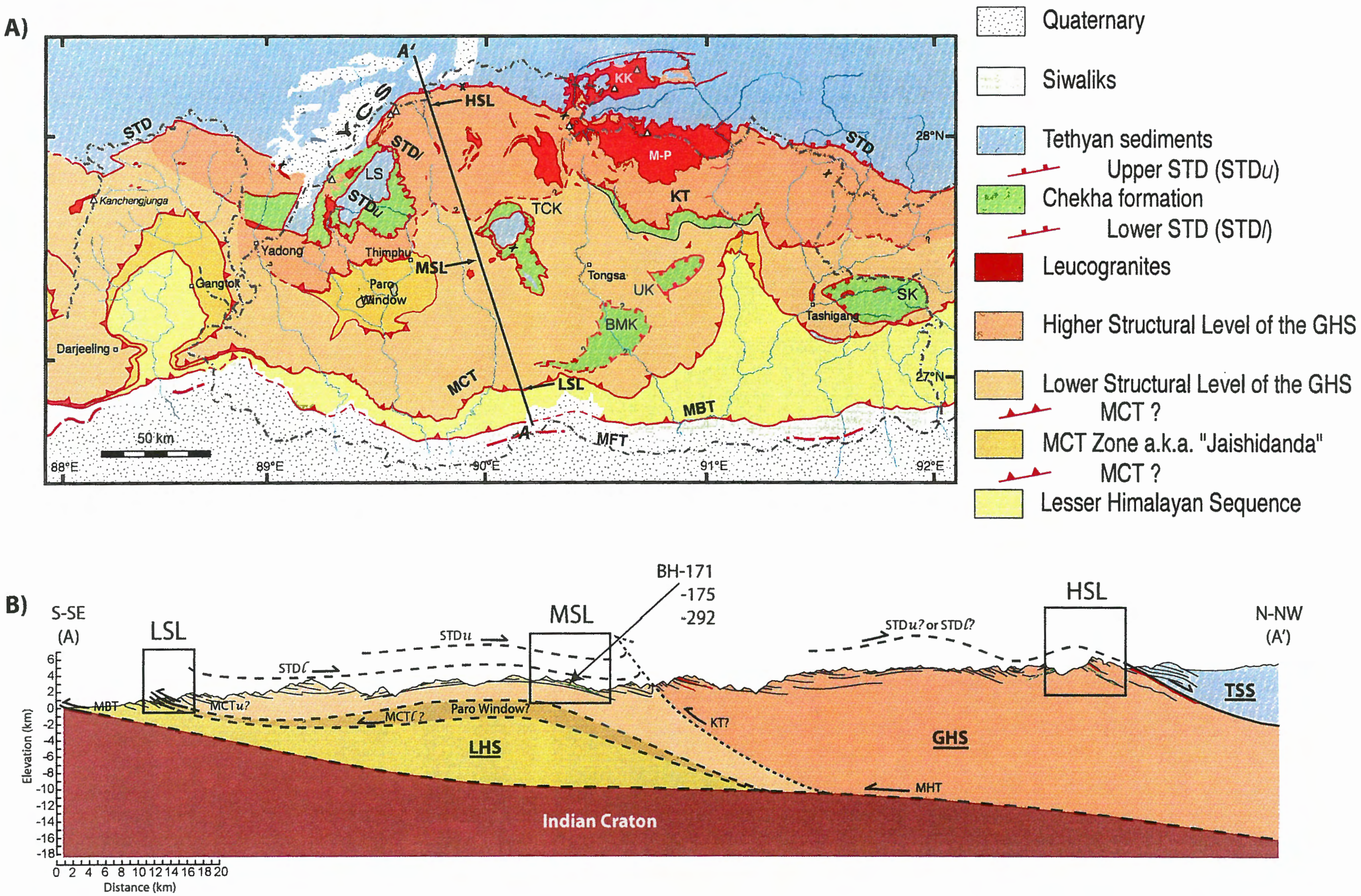
A)
A'
HSL
STD
YCS
STDl
LS
STDu
KK
M-P
28°N
STD
Kanchengjunga
TCK
KT
Yadong
Thimphu
MSL
Gangtok
Paro Window
Tongsa
UK
SK
Tashigang
BMK
Darjeeling
MCT
LSL
27°N
MBT
50 km
A
MFT
88°E
89°E
90°E
91°E
92°E
Quaternary
Siwaliks
Tethyan sediments
Upper STD (STDu)
Chekha formation
Lower STD (STDl)
Leucogranites
Higher Structural Level of the GHS
Lower Structural Level of the GHS
MCT ?
MCT Zone a.k.a. "Jaishidanda"
MCT ?
Lesser Himalayan Sequence
B)
S-SE
(A)
LSL
MSL
BH-171
-175
-292
HSL
N-NW
(A')
STDu
STDl
STDu? or STDl?
MBT
MCTu?
MCTl?
Paro Window?
KT?
TSS
LHS
GHS
MHT
Indian Craton
Elevation (km)
6
4
2
0
-2
-4
-6
-8
-10
-12
-14
-16
-18
0 2 4 6 8 10 12 14 16 18 20
Distance (km)

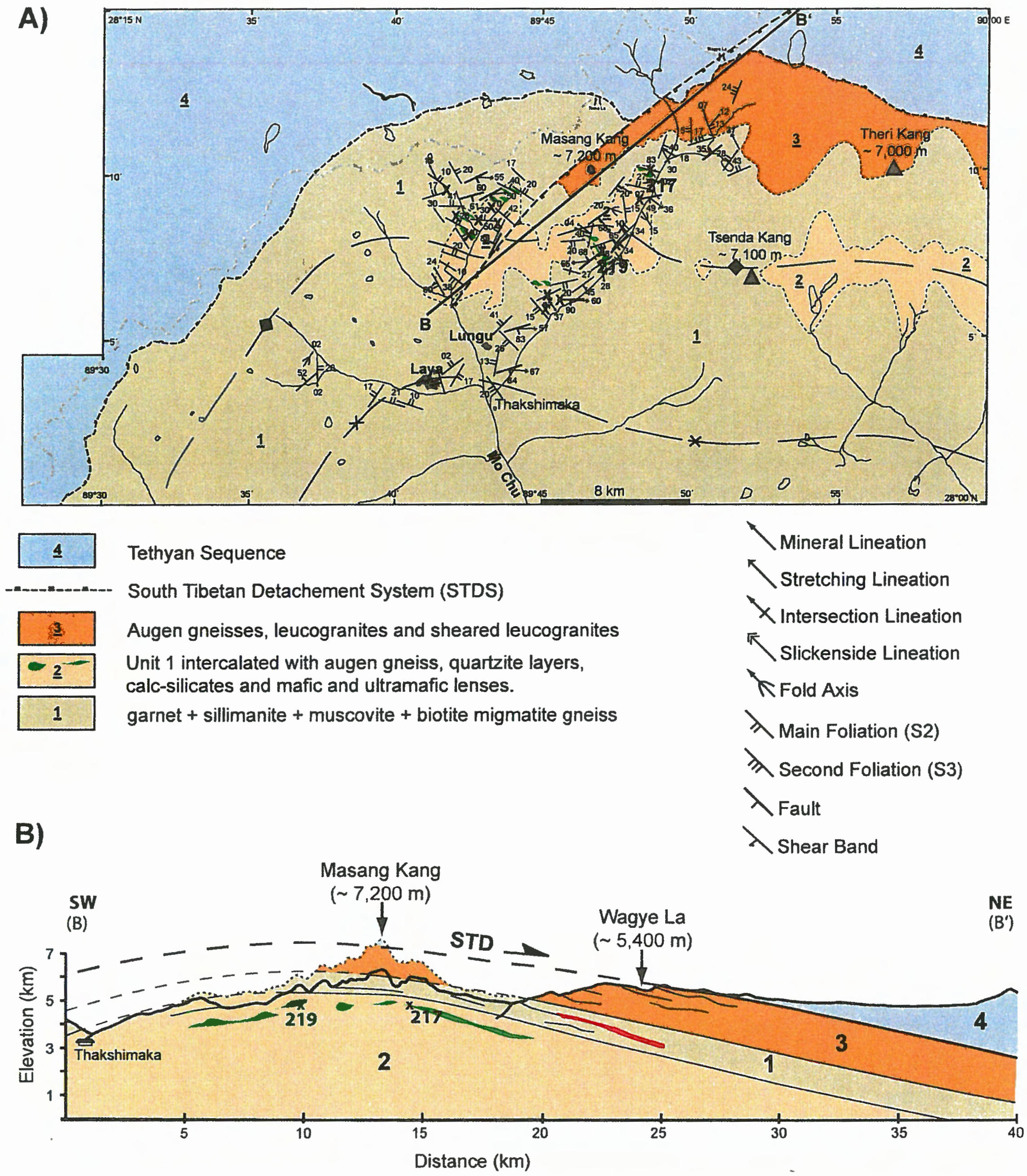

Figure 2.2: Study area map and cross-section. **A)** Geological map of northwestern Bhutan on which locations of metasedimentary and metabasic samples from the HSL have been marked. Information was compiled from Gansser, (1983), Burchfiel et al. (1992), Wu et al. (1998), and this study. The heavy, grey, dash-dot line marks the Bhutanese border. B-B', marks the position of the cross-section in Figure 3.2b. Xs mark the locations from which metabasic boulders were collected. Labelled locations (i.e. 217 and 219) mark outcrops. **B)** Geological cross-section through Masang Kang and into southern Tibet. ***Solid, heavy line:*** the topographic profile based on SRTM data; ***dashed, heavy-line:*** topographic profile to the true elevation; ***green layers and boudins:*** position of metabasic rocks; ***red:*** late Miocene leucogranites.

Indian basement material is not confined to the Lesser Himalayan Sequence (LHS), and that the north Indian margin was affected by magmatic activity during that time.

2.2 U-Pb GEOCHRONOLOGY: ZIRCONS

Zircon fractions were separated from two of the garnet + pyroxene bearing amphibolite samples (BH-217 and -219; Figure 2.2) using standard heavy liquid and Frantz magnetic separation techniques. Individual zircons were handpicked, mounted, polished and coated with gold prior to analysis. Individual spot analyses were made with the Cameca IMS 1270 in the Secondary Ion Mass Spectrometry Laboratory at the Centre de Recherches Pétrographiques et Géochimiques in Vandœuvre lès Nancy (CRPG-Nancy), France following the technique of Deloule et al. (2002).

Cathodoluminescence (CL) images of euhedral zircon grains highlight the presence of two types of zoned zircons, those with dark cores and others with luminescent cores. In sample BH-217, poorly luminescent cores correspond to inclusion rich, ‘spongy’ parts of the grains in backscattered electron images (Figure 2.3), which we can interpret either as the remnants of igneous zircons that grew in the mafic melt; as the remnant of a detrital zircon; or as the remnants of an earlier metamorphic event. Individual rim and core analyses illustrate the presence of three groups of ages (Table 2.1). The dark, spongy cores preserve discordant Proterozoic ages, while grains lacking the spongy texture but with a dark core preserve discordant Paleozoic ages. Luminescent rims show no unique chemical or morphological features in backscattered images, and preserve mostly concordant Miocene ages. In sample BH-219, darker cores correspond to inclusion rich, ‘spongy’, relict cores. Only one grain was found to preserve a discordant Proterozoic age while three others preserved discordant Paleozoic ages. Rims in both samples consistently yield concordant Miocene ages.

In both samples, $^{206}Pb/^{238}U$ and $^{207}Pb/^{235}U$ ages exceeding ~ 500 Ma are commonly discordant while younger ages are consistently concordant (Table 2.1). For sample BH-217, plotting the $^{206}Pb/^{238}U$ and $^{207}Pb/^{235}U$ data corresponding to Proterozoic and Paleozoic (i.e. core) ages on a concordia diagram illustrates that the data fall along a discordia line with an upper intercept of 1822 ± 11 Ma and a lower intercept of 404 ± 21 Ma (MSWD = 0.093; Figure 2.3a). In BH-219, core and rim data fall along a discordia line with an upper intercept of 1742 ± 39 Ma and a lower intercept of 12.3 ± 4.6 Ma

Table 2.1: U-Pb isotopic data for analyzed zircons

							Atomic Ratios						Apparent Ages (Ma)					
Analysis		**U ppm**	**Pb ppm**	**^{206}Pb/^{204}Pb**	**^{206c}Pb/^{206}Pb (%)**	**Th/U**	**^{206}Pb/^{238}U**	**± (1σ)**	**^{207}Pb/^{235}U**	**± (1σ)**	**^{207}Pb/^{206}Pb**	**± (1σ)**	**^{206}Pb/^{238}U**	**± (2σ)**	**^{207}Pb/^{235}U**	**± (2σ)**	**^{207}Pb/^{206}Pb**	**± (2σ)**
bh217-15a@8	rim	1016	256.1	34976	0.05	1.813	0.29341	0.00433	4.44052	0.065876	0.11004	0.000156	1658.6	21.5	1719.9	12.2	1795.5	2.8
bh217-16b@11	core	918	188.5	111892	4.87	1.75	0.23898	0.006119	3.50978	0.091089	0.10653	0.000445	1381.4	31.8	1529.4	20.3	1740.6	7.8
bh217-1a@15	core	974	148.6	141638	0.01	1.108	0.1776	0.006373	2.44356	0.089058	0.09979	0.000631	1053.8	34.8	1255.5	25.9	1620.2	11.8
bh217-10a@33	core	3614	509.5	13926	0.11	1.067	0.16409	0.002387	1.9928	0.029359	0.08899	0.00018	979.5	13.2	1113.1	9.9	1384.2	4.5
bh217-11b@36	core	1067	69.5	3339	0.47	0.688	0.07579	0.001264	0.89151	0.019622	0.08941	0.001069	470.9	7.6	647.2	10.5	1322.8	27.6
bh217-12b@40	core	1281	91.1	5588	0.28	0.284	0.0828	0.001646	0.80098	0.017179	0.07263	0.000244	512.8	9.8	597.4	9.6	933	16.5
bh217-13a@51	core	1250	53.4	1033	1.81	1.479	0.04971	0.001059	0.4443	0.020416	0.07859	0.001207	313	6.5	373	14.3	—	—
bh217-9a@30	core	131	0.285	6634	0.24	0.051	0.00253	0.000078	0.01834	0.00319	0.05477	0.001705	16.3	0.5	18.4	3.2	—	—
bh217-11a@35	rim	230	0.53	-5114	0	0.008	0.00268	0.000067	0.01884	0.001736	0.04803	0.001325	17.3	0.4	19	1.7	—	—
bh217-12a@39	rim	289	0.723	1512	1.04	0.007	0.00291	0.000065	0.01518	0.001977	0.04751	0.001247	18.7	0.4	15.3	2	—	—
bh217-16a@10	rim	275	0.556	1833	0.86	0.007	0.00235	0.000066	0.01415	0.002476	0.05155	0.001117	15.1	0.4	14.3	2.5	—	—
bh217-2a@18	rim	1138	2.4	787.9	2	0.019	0.00247	0.000076	0.01417	0.00136	0.06021	0.001538	15.9	0.5	14.3	1.4	—	—
bh217-6b@24	rim	6484	16.7	23512	0.07	0.069	0.00299	0.000046	0.01936	0.000568	0.04749	0.000466	19.3	0.3	19.5	0.6	—	—
bh217-7a@26	rim	2832	7.9	15584	0.1	0.039	0.00324	0.000051	0.02149	0.000679	0.04899	0.000559	20.9	0.3	21.6	0.7	—	—
bh217-8b@29	rim	295	0.68	2228	0.71	0.008	0.00268	0.000065	0.01589	0.001611	0.04955	0.001278	17.2	0.4	16	1.6	—	—
bh217-9b@31	rim	1907	4.9	17083	0.09	0.022	0.00298	0.000053	0.01887	0.00134	0.04676	0.00089	19.2	0.3	19	1.3	—	—
bh217-14a@53		7181	9	-5079.3	0	0.052	0.00147	0.000024	0.01034	0.000444	0.04822	0.000588	9	0.2	10	0.4	—	—
bh219-6a@63	core	1133	177.7	365477	0	0.312	0.18258	0.004097	2.65258	0.062021	0.1053	0.000691	1081	22.3	1315	17.1	1721	12
bh219-9a@71	core	307	21.2	61504	0	0.418	0.08035	0.001211	1.19097	0.018988	0.10761	0.000545	498	7.2	796	8.8	1757	9.5
bh219-7a@66	core	743	24	14772	0	0.103	0.03755	0.001356	0.52338	0.019257	0.10192	0.000653	238	8.4	427	12.8	1644	12.9
bh219-8a@68	core	275	8.4	210291	0	0.216	0.03561	0.002212	0.51252	0.032316	0.10435	0.001062	226	13.8	420	21.5	1704	19.7
bh219-1b@57	rim	638	1.7	4090	0	0.006	0.00312	0.000065	0.03365	0.003936	0.0815	0.005739	20	0.4	34	3.9	—	—
bh219-7b@67	rim	340	0.549	326	0.06	0.004	0.00188	0.000052	0.01666	0.002839	0.10792	0.003575	12	0.3	17	2.8	—	—
bh219-8b@69	rim	168	0.309	4395	0	0.003	0.00215	0.000045	0.0135	0.001661	0.04889	0.00132	14	0.3	14	1.7	—	—
bh219-9b@72	rim	277	0.467	-4700	0	0.005	0.00196	0.000033	0.01379	0.001601	0.04785	0.00114	13	0.2	14	1.6	—	—

Figure 2.3: U-Pb concordia diagrams for metabasites. a) Concordia diagram for garnet + pyroxene bearing amphibolite, sample BH-217. Cathodoluminescence (CL) and backscatter (BS) images are of one representative zircon in which a spongy dark core can be seen. b) Concordia diagram for garnet + pyroxene bearing amphibolite, sample BH-219. Cathodoluminescence (CL) and backscatter (BS) images are of one representative zircon in which a spongy dark core can be seen.

A)

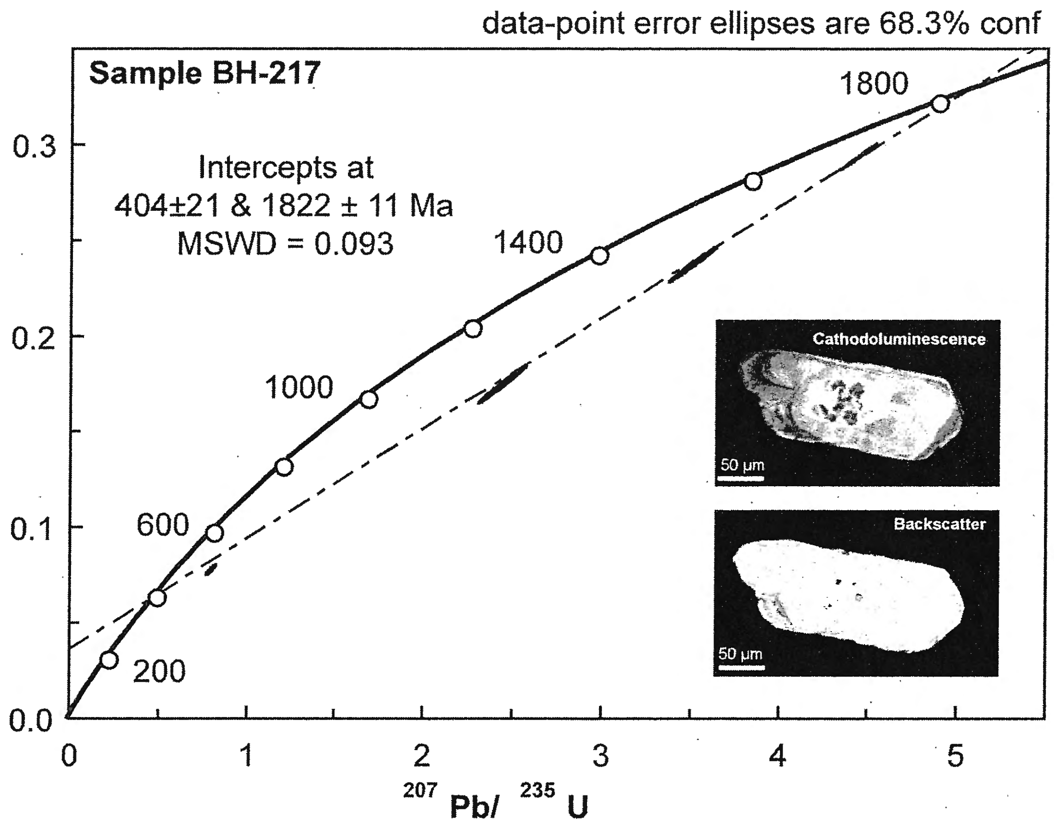
data-point error ellipses are 68.3% conf
Sample BH-217
Intercepts at
404±21 & 1822 ± 11 Ma
MSWD = 0.093
1800
1400
1000
600
200
0.3
0.2
0.1
0.0
0
1
2
3
4
5
207 Pb/ 235 U
Cathodoluminescence
50 µm
Backscatter
50 µm

B)

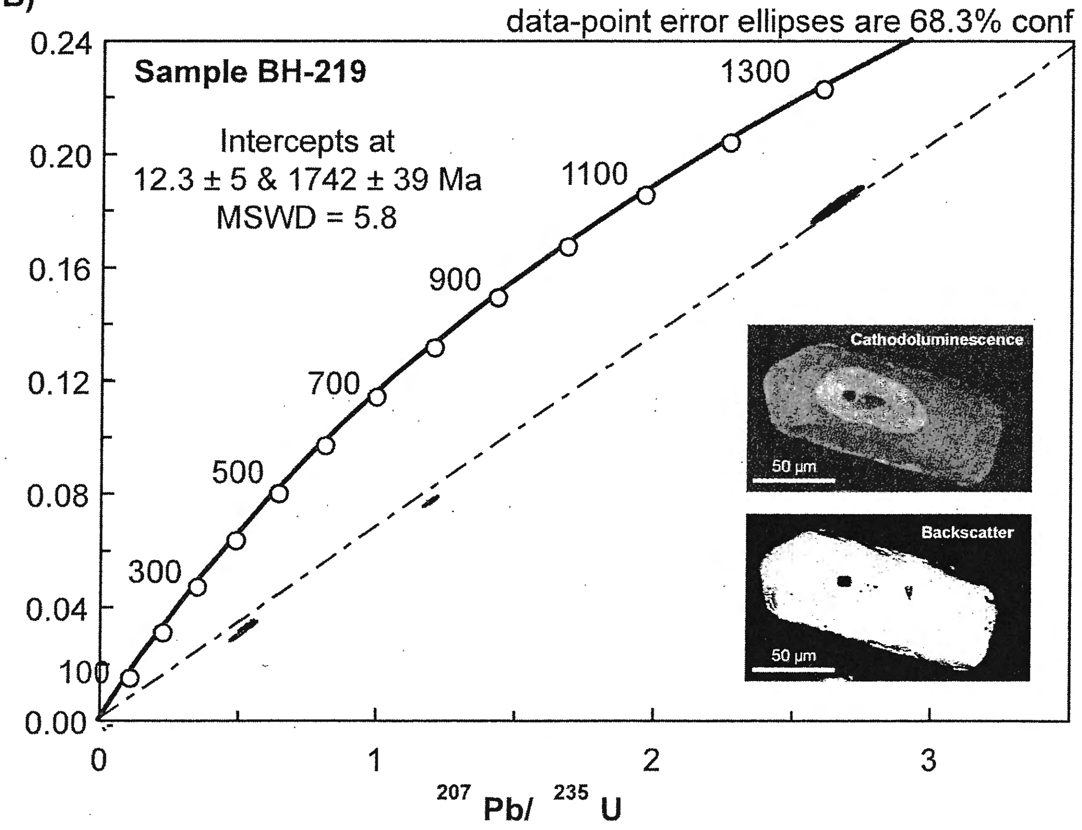
data-point error ellipses are 68.3% conf
Sample BH-219
Intercepts at
12.3 ± 5 & 1742 ± 39 Ma
MSWD = 5.8
1300
1100
900
700
500
300
100
0.24
0.20
0.16
0.12
0.08
0.04
0.00
0
1
2
3
207 Pb/ 235 U
Cathodoluminescence
50 µm
Backscatter
50 µm

(MSWD = 5.8; Figure 2.3b). The concordant Miocene rim ages in BH-217, and the lower Miocene intercept age calculated for BH-219 are interpreted to represent high temperature metamorphism associated with the Himalayan orogeny and will be discussed further in chapter 3. The preservation of Paleozoic ages in both samples, and the lower intercept age of 404 ± 21 Ma calculated for BH-217 may be representative of a pre-Himalayan thermal event for which evidence has been found in both the LHS and GHS elsewhere in the Himalaya (Le Fort et al. 1986; Catlos et al. 2002; Gehrels et al. 2003). However, for the purposes of this provenance study, the Paleozoic thermal event will not be discussed further.

As noted by previous authors (e.g. Martin et al. 2005), the discordance between $^{206}Pb/^{238}U$ and $^{207}Pb/^{235}U$ ages greater than 500 Ma may be the result of lead loss during new zircon growth related to Himalayan orogenesis. For this reason $^{207}Pb/^{206}Pb$ ages are considered more reliable for analyses greater than 500 Ma. Upper intercept ages for both samples bracket the range of corresponding $^{207}Pb/^{206}Pb$ ages, though the value calculated for BH-217 appears a little high while the age calculated from BH-219 is within error of the $^{207}Pb/^{206}Pb$ ages. Thus, the upper intercept of 1742 ± 39 Ma, which corresponds well with the recalculated $^{207}Pb/^{206}Pb$ ages, is representative of the core age of the metabasites and ultramafic rocks. Since the data in both samples define a disconcordia line suggests cores that were analyzed must have had a common origin, implying that the zircons are not likely to be detrital. Deciphering whether or not they are of magmatic or metamorphic orogen is slightly more problematic. However, assuming the metabasites are magmatic as opposed to sedimentary in origin, evidence for which is presented below, the preservation of magmatic zircons albeit rather limited could be expected. Also, that zircon cores are characterized by Th/U ratios in excess of 0.1, while metamorphic rims are characterized by values less than 0.04, is a good indication that cores are magmatic relicts and that the upper intercept of 1742 ± 39 Ma represents the crystallization age of the metabasites.

2.3 WHOLE-ROCK Nd ISOTOPES

Whole-rock Sm-Nd analysis were conducted on three rocks (Table 2.2). Depending on the concentration of Sm and Nd in each rock, 40 - 60 milligrams of sample were dissolved, digested, separated and analyzed by Micromass MC-ICPMS in the

Table 2.2: Major, trace, REE and Nd isotopic data for the Masang Kang suite.

	Group I		Group II			Group III												Group IV
	BH-220	BH-274	BH-175A	BH-254	BH-256	BH-203	BH-217A	BH-219	BH-245	BH-246	BH-249	BH-252	BH-253	BH-255	BH-257	BH-266	BH-292	BH-268
Major Oxides (wt%)																		
SiO_2	42.71	43.05	48.52	47.71	49.56	49.76	51.66	48.64	52.69	48.77	49.82	49.55	51.03	49.39	53.87	51.29	51.78	39.30
TiO_2	0.03	0.03	1.69	1.44	0.95	1.05	1.89	0.57	0.81	0.67	2.90	1.11	1.06	1.76	0.75	0.88	1.31	2.99
Al_2O_3	1.53	1.47	15.06	15.32	13.40	14.81	13.14	14.38	11.71	16.55	12.22	15.53	16.40	13.59	14.23	15.00	13.77	16.75
Fe_2O_3	8.93	8.83	13.11	10.22	12.26	13.00	16.88	11.89	12.85	6.34	20.50	13.38	12.22	14.71	11.58	12.15	13.45	18.74
MnO	0.13	0.13	0.21	0.20	0.20	0.18	0.26	0.18	0.19	0.10	0.25	0.26	0.18	0.23	0.19	0.21	0.14	0.26
MgO	40.53	41.36	6.60	9.41	8.34	7.59	4.53	10.52	7.76	9.11	4.04	5.87	5.09	6.27	5.73	6.08	7.62	8.13
CaO	1.84	1.74	11.28	11.24	11.07	10.43	7.47	10.38	9.42	12.48	6.67	7.10	8.58	11.09	9.08	9.12	8.57	9.67
Na_2O	0.17	0.14	0.93	0.98	2.17	0.81	1.66	1.61	1.29	2.39	1.15	2.91	3.06	1.14	1.90	2.84	1.58	0.99
K_2O	0.02	0.03	0.63	1.50	0.79	0.50	1.93	0.23	0.92	0.57	1.45	1.80	1.28	0.38	0.94	1.14	0.42	1.30
P_2O_5	0.01	0.01	0.14	0.13	0.09	0.10	0.26	0.05	0.88	0.08	0.25	0.14	0.12	0.17	0.08	0.11	0.13	0.68
LOI	2.88	1.80	0.60	1.21	0.38	0.31	0.19	0.14	0.92	1.64	0.20	1.41	0.00	0.39	0.39	0.29	0.00	0.30
TOTAL	98.78	98.59	98.77	99.36	99.21	98.54	99.88	98.59	99.45	98.71	99.46	99.05	99.01	99.12	98.74	99.10	98.77	99.11
Mg #	89.99	90.27	49.92	64.58	57.40	53.62	34.70	63.67	54.46	74.00	28.07	46.49	45.20	45.77	49.49	49.77	52.89	46.21
Trace elements (ppm)																		
V	28	30	296	215	213	223	318	148	264	141	525	227	278	304	190	202	269	418
Cr	1529	2813	190	399	232	170	44	337	46	942	26	99	52	109	50	81	66	97
Ni	2408	2244	48	136	120	96	35	202	54	107	16	52	49	48	45	49	33	96
Co	112	108	51	48	52	58	63	63	53	33	69	60	53	54	52	51	55	74
Cu	—	—	63	—	13	191	67	61	113	105	227	75	61	21	23	10	50	263
Zn	52	53	91	103	89	69	139	70	177	51	175	207	84	112	92	105	65	171
Ga	—	—	19.00	15.00	14.00	16.00	18.00	14.00	26.00	14.00	18.00	21.00	20.00	17.00	19.00	19.00	16.00	20.00
Rb	0.34	8.00	5.38	103.00	23.14	22.93	109.05	5.35	35.22	42.62	51.00	84.00	45.63	10.00	47.55	45.00	10.00	68.37
Sr	14.00	6.00	132.00	106.00	68.00	55.00	50.00	39.00	125.00	429.00	101.00	173.00	237.00	107.00	103.00	81.00	88.00	48.00
Ba	46.00	82.00	79.00	177.00	96.00	45.00	262.00	0.00	—	70.00	369.00	367.00	317.00	30.00	232.00	352.00	97.00	116.00
Y	0.89	4.00	32.37	31.66	21.78	21.23	51.60	14.12	28.23	15.44	35.00	23.00	23.01	29.00	19.87	20.00	27.00	45.18
Zr	1.23	—	115.00	91.00	53.00	87.00	202.00	51.00	85.00	81.00	219.00	111.00	108.00	104.00	68.00	86.00	79.00	222.00
Nb	0.09	1.00	7.10	4.10	5.10	6.10	19.10	5.10	7.10	4.10	14.10	7.00	6.10	8.00	7.10	6.00	6.00	34.90
Pb	4.00	7.00	3.00	—	—	26.00	12.00	6.00	6.00	12.00	6.00	12.00	3.00	—	—	—	12.00	6.00
Th	—	—	1.60	0.46	0.48	1.66	6.15	1.66	24.19	1.44	7.00	2.00	2.23	0.48	1.35	3.00	—	15.67
U	0.06	2.00	0.44	0.47	0.89	3.08	3.38	1.05	4.39	0.53	—	—	0.38	1.00	1.03	2.00	2.00	5.18
P	48.00	43.64	624.03	571.66	375.29	449.47	1147.68	231.28	3862	349.11	1104	593.48	501.84	733.12	366.56	475.66	567.30	2971.76
Ta	—	—	0.38	0.21	0.28	0.44	1.80	0.27	0.67	0.22	—	—	0.38	—	0.44	—	—	3.72
Hf	0.04	—	3.60	2.75	1.30	2.10	4.93	1.27	1.90	2.10	—	—	2.63	—	1.70	—	—	5.40
Rare earth elements (ppm)																		
La	0.06	5.00	7.15	5.17	3.93	9.29	28.70	4.93	50.00	6.91	24.00	10.00	14.43	13.00	10.60	13.00	11.00	50.76
Ce	0.16	—	17.94	15.32	10.25	20.11	64.56	11.19	40.81	15.59	—	—	30.79	—	24.02	—	—	104.56
Pr	0.02	—	2.89	2.40	1.57	2.65	8.76	1.55	—	2.11	—	—	3.97	—	3.18	—	—	13.69
Nd	0.10	—	13.94	12.49	7.84	11.68	35.84	6.91	64.00	9.36	21.00	14.00	16.62	17.00	13.18	14.00	11.00	55.48
Sm	0.06	—	4.48	4.21	2.39	3.17	8.69	1.87	28.78	2.58	—	—	3.71	—	3.06	—	—	12.56
Eu	0.03	—	1.60	1.50	0.91	1.09	2.36	0.67	0.00	1.00	—	—	1.28	—	1.10	—	—	3.30
Gd	0.07	—	5.53	5.22	3.24	3.49	9.53	2.30	18.37	2.98	—	—	3.94	—	3.46	—	—	11.45
Tb	0.02	—	0.94	0.92	0.60	0.63	1.63	0.42	1.80	0.50	—	—	0.68	—	0.59	—	—	1.70
Dy	0.12	—	5.90	5.51	3.90	3.83	9.60	2.53	6.51	2.87	—	—	3.99	—	3.65	—	—	9.23
Ho	0.04	—	1.27	1.18	0.84	0.89	2.02	0.55	1.05	0.60	—	—	0.87	—	0.76	—	—	1.74
Er	0.11	—	3.59	3.36	2.46	2.50	5.65	1.70	2.69	1.58	—	—	2.40	—	2.18	—	—	4.55
Tm	0.03	—	0.52	0.49	0.38	0.39	0.85	0.26	0.38	0.22	—	—	0.37	—	0.32	—	—	0.65
Yb	0.14	—	3.38	3.10	2.37	2.36	5.08	1.54	2.41	1.34	—	—	2.24	—	2.07	—	—	4.05
Lu	0.03	—	0.50	0.47	0.35	0.39	0.79	0.25	0.38	0.20	—	—	0.37	—	0.34	—	—	0.63
$^{147}Sm/^{144}Nd_{m}$	—	—	—	—	—	—	0.141523	0.158144	—	—	—	—	—	—	—	—	0.172029	—
$^{143}Nd/^{144}Nd_{m}$	—	—	—	—	—	—	0.511836	0.512625	—	—	—	—	—	—	—	—	0.512521	—
Error (2σ)	—	—	—	—	—	—	0.000005	0.000012	—	—	—	—	—	—	—	—	0.000007	—
εNd (0)	—	—	—	—	—	—	-15.64	-0.26	—	—	—	—	—	—	—	—	-2.29	—
εNd (500)	—	—	—	—	—	—	-12.14	2.20	—	—	—	—	—	—	—	—	-0.72	—
εNd (1742)	—	—	—	—	—	—	-3.33	8.40	—	—	—	—	—	—	—	—	3.24	
T_{DM} (Ma)	—	—	—	—	—	—	2759	1439	—	—	—	—	—	—	—	—	2291	—

CRPG-Nancy, France following the technique outlined by (Luais et al. 1997). Repeated analysis of the JNdi-1 standard during the analytical session yielded $^{143}Nd/^{144}Nd$ values of 0.512117 ± 32 (2σ, n=7) which is within error of the reference value of 0.512115 ± 7 (2σ; Tanaka et al. 2000). Due to the fact that several isotopic studies report Nd data relative to present day chondritic values, $\varepsilon_{Nd(0)}$ (e.g. Robinson et al. 2001; Martin et al. 2005), while others report data relative to 500 Ma – the last pre-Himalayan metamorphic event experienced by both units (e.g. Richards et al. 2005), we present both values in addition to the initial value in Table 2.2.

For the three metabasic rocks from the Masang Kang suite, present day epsilon values ($\varepsilon_{Nd(0)}$) range between -16 and -0.3 while $\varepsilon_{Nd(500)}$ values range between -12 and +2. In either case, calculated values for the three metabasic rocks fall well within the range presented in studies of the GHS throughout the western Himalaya. The low initial values (i.e. -12) suggest that recycled continental crust may have played an important role in the source of the metabasites (Miller et al. 2001). Nd depleted mantle model ages (T_{DM}) are also presented in Table 2.2 and were calculated following the procedure of De Paolo (1988). The variability of the calculated model ages is interpreted to be the result of a mixed-source of Archean crust and mantle protoliths, thus the T_{DM} ages presented in Table 2.2 cannot be representative of the fusion age. Rather, we consider the upper intercept of the U-Pb concordia for BH-219 to be the true igneous crystallization age.

2.4 MAJOR & TRACE ELEMENT GEOCHEMISTRY

The rocks of the Masang Kang suite have been metamorphosed at relatively high temperatures and moderate pressures (Chakungal et al. 2002). At such high temperature conditions some elements might be mobile, however, assuming that some elements are not significantly affected by thermal and/or deformational events, the chemical composition of intensely metamorphosed igneous rocks may be used to constrain the tectonic setting of their emplacement (e.g. de Sigoyer et al. 1997; Slagstad et al. 2004). In the case of the Masang Kang suite of rocks, consistency of variation trends and compositional similarity with modern igneous rocks suggests that many of the major elements such as Si, Al, Fe, Mg and Ti in addition to the relatively immobile high-field-strength-elements (Zr, Hf, Y, Nb), rare earth elements (REE) and the transition elements (Cr, Ni, and V), retained their original distribution.

For major and trace element analyses, samples were analysed with a Philips PW2400 X-ray Spectrometer at the Regional Geochemical Centre in the Department of Earth Sciences at Saint Mary's University in Halifax, Nova Scotia, Canada. Major elements and V, Cr, Ba, Ni, Zn, Ga, Sr, Zr and Nb measurements were made on glass disks. All other trace element (i.e. Co, Cu, Rb, Pb, P, Ta, Hf) analyses were made on pressed pellets. Rare earth elements (REEs), high field strength elements (HFSE), and Y, U, Ta, Hf and Th were analysed by inductively coupled plasma-mass spectrometry (ICP-MS) at the Geoscience Laboratories in the Ministry of Northern Development and Mines at Sudbury, Ontario, Canada. Details of the analytical procedures, uncertainties and precision of the ICP-MS and XRF techniques are discussed by Ayer and Davis (1997) and Dostal et al. (1986)

The Masang Kang suite differ chemically from para-amphibolites and plot in the field of orthoamphibolites of basaltic affinity (i.e. Leake 1964; Van de Kemp 1964). Based on the major element and REE concentrations, rocks of the suite can be divided into four geochemically different groups, which are discussed in detail below.

Group I

Group I comprises rocks that have the lowest SiO_2 (avg 43 wt. %) and highest MgO (avg. 41 wt%) contents (Table 2.2). High MgO contents correspond with low TiO_2 (avg. 0.03%), Al_2O_3 (avg. 1.5%), and CaO (avg. 1.8%) contents. The whole rock composition is therefore, a reflection of the high olivine and orthopyroxene content in these rocks and confirms the observations under optical microscope. The proportions of K_2O, Na_2O and P_2O_5 are also very low (avg 0.02%, 0.16% and 0.1% respectively). Rocks of this group are further characterized by the highest Cr and Ni concentrations, which can be correlated with high magnesium numbers (Mg# = Mg/(Mg+Fe)), confirming the cumulate nature of this group of samples. Chondrite normalized REE patterns (Figure 2.4) reveals that Group I rocks are characterized by the greatest depletion of the light ((Ce/Sm)N = 0.67 and (Ce/Yb)N = 0.32), middle and heavy REEs [(Gd/Er)N = 0.51 and (Gd/Yb)N = 0.43].

Groups II and III

SiO_2 contents averaging 49 wt % define Group II with individual analyses displaying some overlap with samples of Group III, which are characterized by a higher

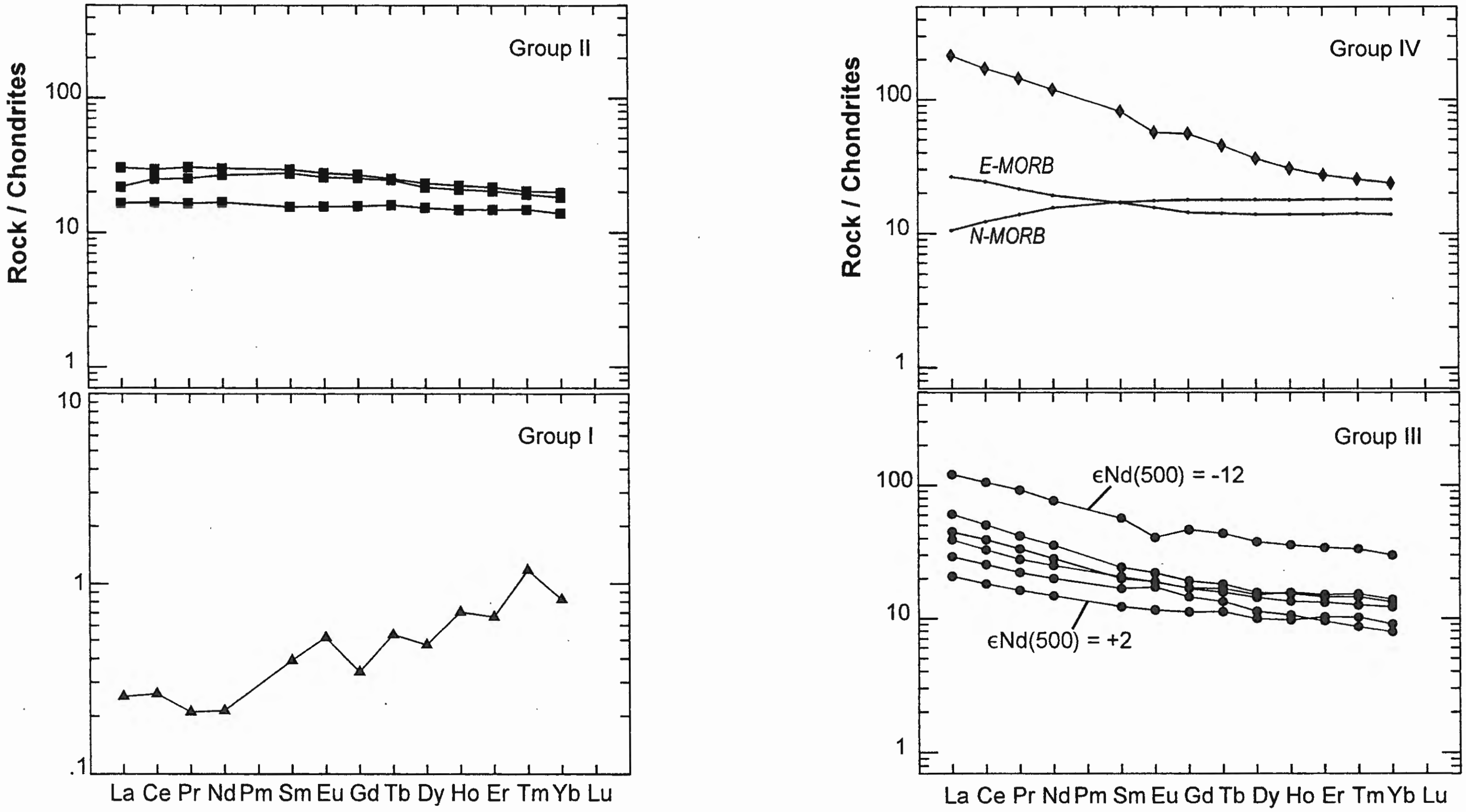

Figure 2.4: Chondrite normalized REE element plots. Normalization values are those from Sun & McDonough (1989). Note that the vertical scale of the plot for Group I differs from the other three plots. **Legend:** ***triangles,*** Group I ultramafics; ***squares,*** Group II MORB like tholeiites; ***circles,*** Group III gabbroic tholeiites; ***diamonds,*** Group IV alkali basalts.

SiO_2 average (avg. 51 wt %). The difference between the two groups becomes obvious from the chondrite normalized REE patterns that characterize each (Figure 2.4). Group II contains the lowest absolute abundance of REEs producing a flat pattern [avg. (Ce/Sm)N = 1.0 and (Ce/Yb)N = 1.3] that parallels the MORB pattern (Sun and McDonough 1989), while patterns for Group III display an enrichment in the LREEs [avg (Ce/Sm)N = 1.0 and (Ce/Yb)N = 2.0] and parallel the enriched MORB pattern (EMORB; Sun and McDonough 1989). The most enriched sample of Group III also displays a negative Eu anomaly implying plagioclase fractionation. Thus, based on the REE patterns Group II metabasites are more primitive than Group III. The higher concentration of Cr in Group II (average 274 ppm) confirms this interpretation (Wilkinson and Maitra 1987; Abu-Hamatteh 2005).

A negative correlation between SiO_2 and MgO implies fractional crystallization processes played an important role in the genesis of both groups. Magnesium numbers and MgO contents (Table 2.2) are not only significantly lower than those characterizing Group I, but also are lower than primitive basaltic melts suggesting these samples experienced magmatic differentiation. Relative to Group III, however, Group II is characterized by higher Mg#'s and MgO contents once again confirming the more primitive nature of Group II relative to Group III. CaO/Al_2O_3 ratios show a positive relationship with increasing Mg# which is indicative of the crystallization of clinopyroxene. Both groups have average CaO/Al_2O_3 ratios that are less than that of Group I, though the average ratio for Group II is higher (0.8) than Group III (0.6) implying that Group II rocks were generated at a shallower crustal depth then rocks forming Group III, perhaps in the spinel stability field.

Group IV

The sole sample that comprises Group IV contains 39 wt. % SiO_2, relatively high FeO and MgO concentrations (Table 2.2), that resemble alkali basalts. It is difficult to establish whether fractional crystallization processes played a role in the genesis of this rock as the lack of additional samples prohibits the correlation between SiO_2 and MgO. MgO and Mg# values are however lower than primitive mantle values suggesting that this group also experienced magmatic differentiation. The lowest Mg# and CaO/Al_2O_3 ratios are also associated with this sample implying it is the most evolved of the four

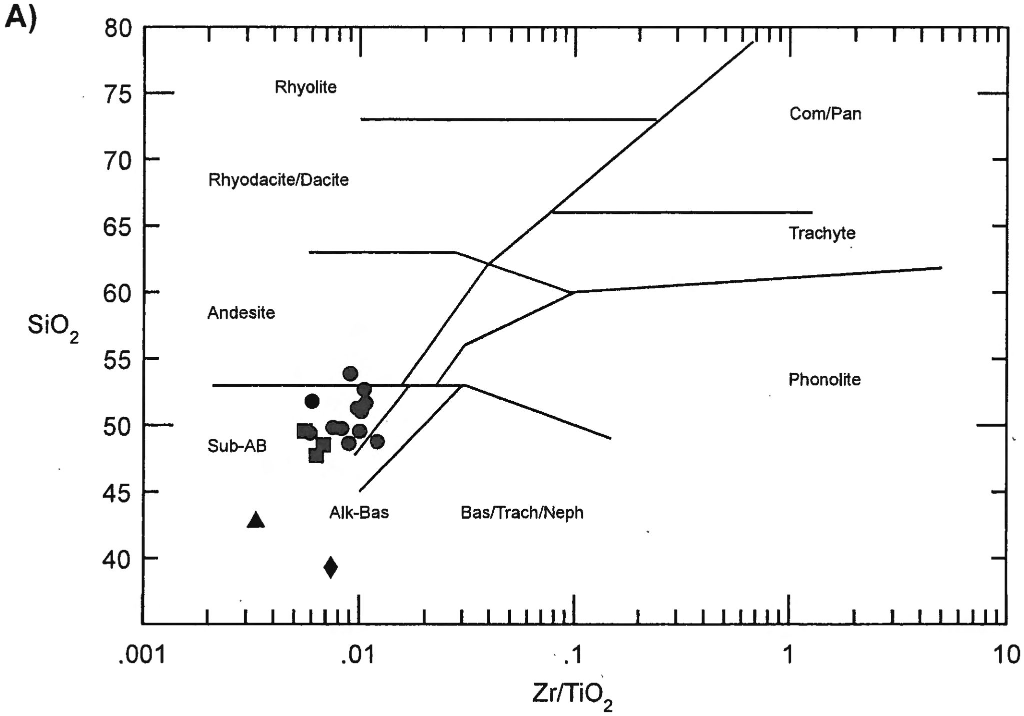

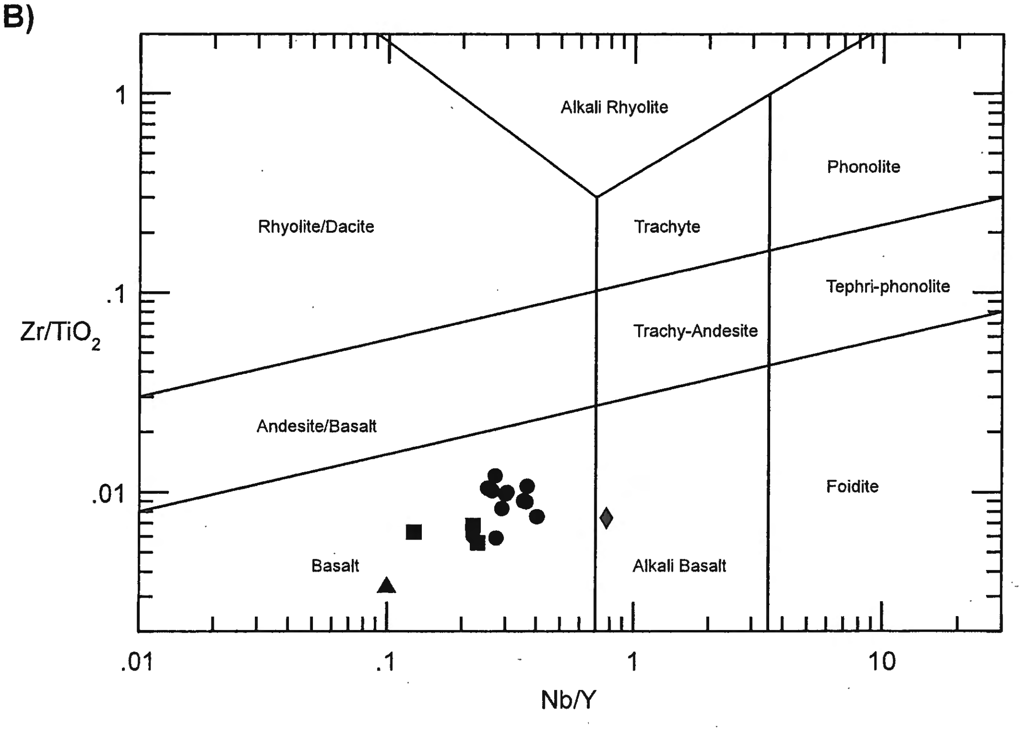

Figure 2.5: Discrimination diagrams. **A)** Zr/TiO2 vs SiO2 discrimination diagram of Winchester and Floyd (1977). **B)** Nb/Y vs. Zr/Ti discrimination diagram of Winchester and Floyd (1977), modified by Pearce (1996), which classifies samples using immobile elements. Legend: triangles, Group I ultramafics; squares, Group II MORB like tholeiites; circles, Group III gabbroic tholeiites; diamonds, Group IV alkali basalts.

geochemical groups, and that it may have been generated at greater depths than the Group III tholeiites. This interpretation is supported by the chondrite normalized REE pattern (Figure 2.4) which is characterized by a fractionated middle to heavy REE pattern [(Ce/Sm)N = 2.1 and (Ce/Yb)N = 7.2], suggesting this sample was generated in the presence of garnet which retains heavy REEs. The presence of a negative Eu anomaly also implies the fractionation of plagioclase.

2.5 IGNEOUS & TECTONIC ENVIRONMENTS

The Zr/TiO_2 vs. SiO_2 and Nb/Y vs. Zr/Ti diagrams of Winchester and Floyd (1977) illustrates and confirms that the rocks of Groups II and III are subalkaline basalts with the one exception (Group IV) plotting in the alkali basalt field (Figure 2.5). Low Nb/Y ratios (0.13 – 0.37) for Groups II and III are also typical of subalkaline magmatic series as they commonly exhibit Nb/Y ratios less than 1 (Winchester and Floyd 1977). All samples display a typical tholeiitic trend of increasing TiO_2 and V with increasing FeO/MgO ratios (Figure 2.6), which is confirmed with the AFM diagram of Irvine and Baragar (1971; Figure 2.6).

Group I: Cumulates

The primitive mantle normalized multi-element pattern for Group I (Figure 2.7), confirms that the cumulate rocks of the Masang Kang suite are strongly depleted in all elements relative to the primitive mantle. The low absolute abundance of the these elements is indicative of the absence of an interstitial melt which would have been enriched in some or all of the incompatible elements, a signature that would be observed in the multi-element pattern. For these reasons we suggest that Group I represents cumulates of a magma source from which the incompatible trace and LREEs were removed by varying degrees of partial melting.

Groups II & III: Tholeiitic Basalts

Group II and III tholeiites are characterized by high Ti/V (>20; Shervais 1982) and Zr/Y (>3; Pearce and Norry 1979), and a negative correlation between Cr and Ti - trends that are characteristic of intraplate basalts (Figure 2.8A-C). Furthermore, overlapping of the MORB field with the volcanic arc and within-plate fields on the Zr/Y diagram of Pearce and Norry (1979) indicates that the chemical distinction between the different tectonic environments is not clear cut. On the Zr/Y diagram and the trivariate

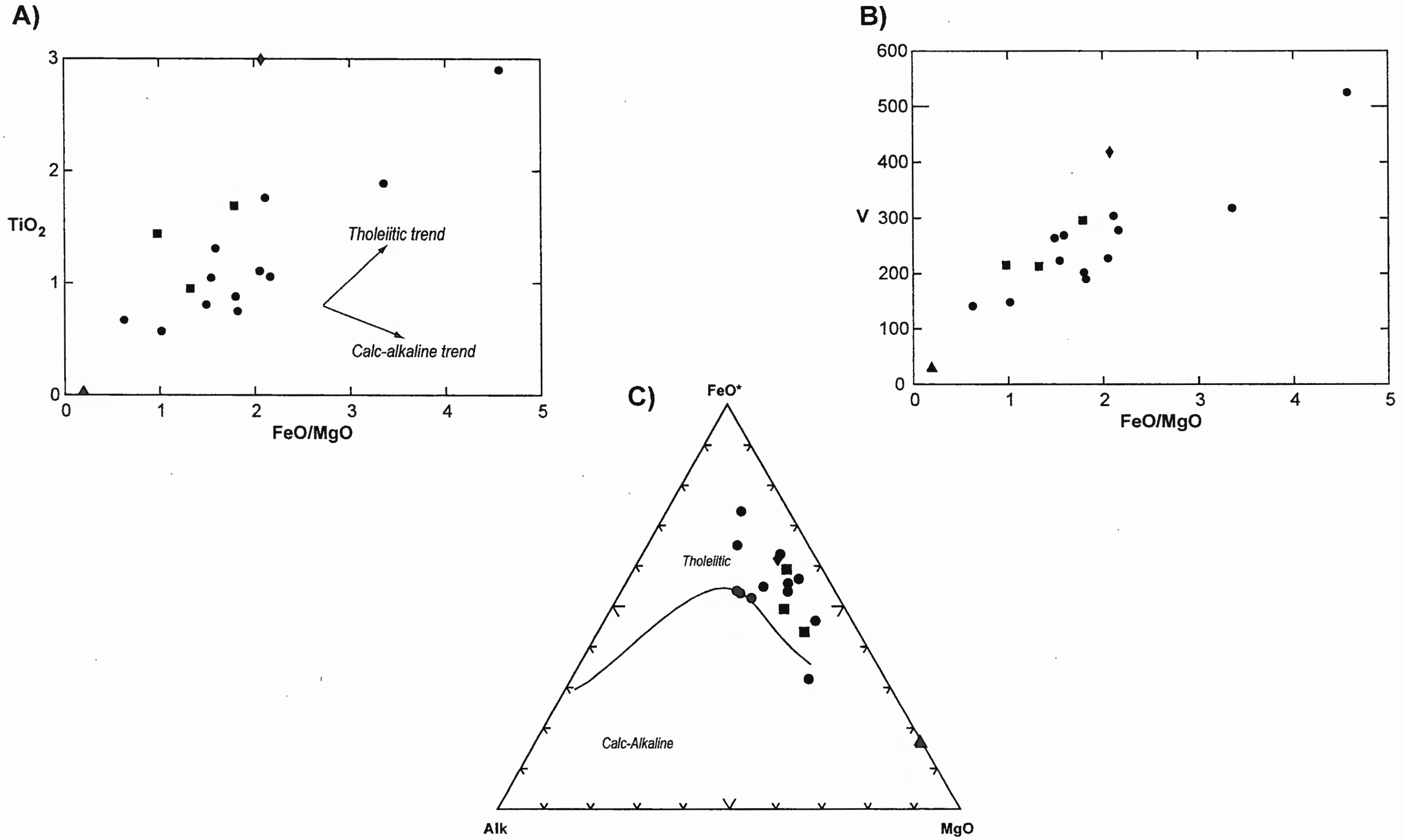

Figure 2.6: Tholeiite trends. **A)** FeO*/MgO vs. TiO2 diagram which illustrates that samples are rich in iron where iron enrichent is positively correlated with an enrichment in titanium, suggesting samples are tholeiitic basalts. **B)** FeO*/MgO vs. V diagram confirming the tholeiitic nature of Groups II and III. **C)** Trivariate plot of Irvine and Baragar (1971). **Legend:** ***triangles,*** Group I ultramafics; ***squares,*** Group II MORB like tholeiites; ***circles,*** Group III gabbroic tholeiites; ***diamonds,*** Group IV alkali basalts; ***FeO*,*** total iron.

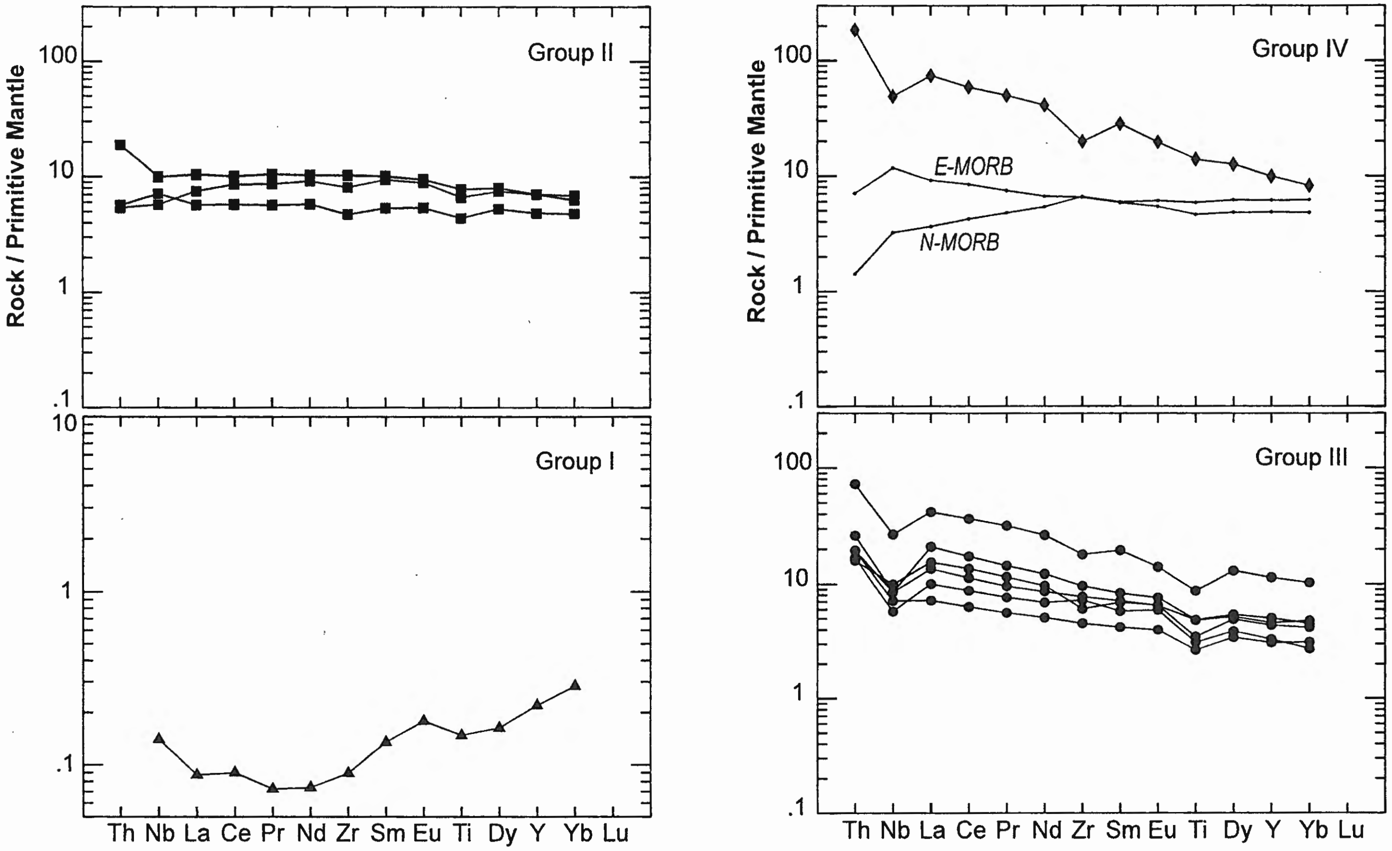

Figure 2.7: Primitive mantle multielement plots. Multielement plots normalized to primitive mantle values obtained from Sun & McDonough (1989). Note that the verticle scale of the plot for Group I differs from the other three plots. **Legend:** ***triangles,*** Group I ultramafics; ***squares,*** Group II MORB like tholeiites; ***circles,*** Group III gabbroic tholeiites; ***diamonds,*** Group IV alkali basalts.

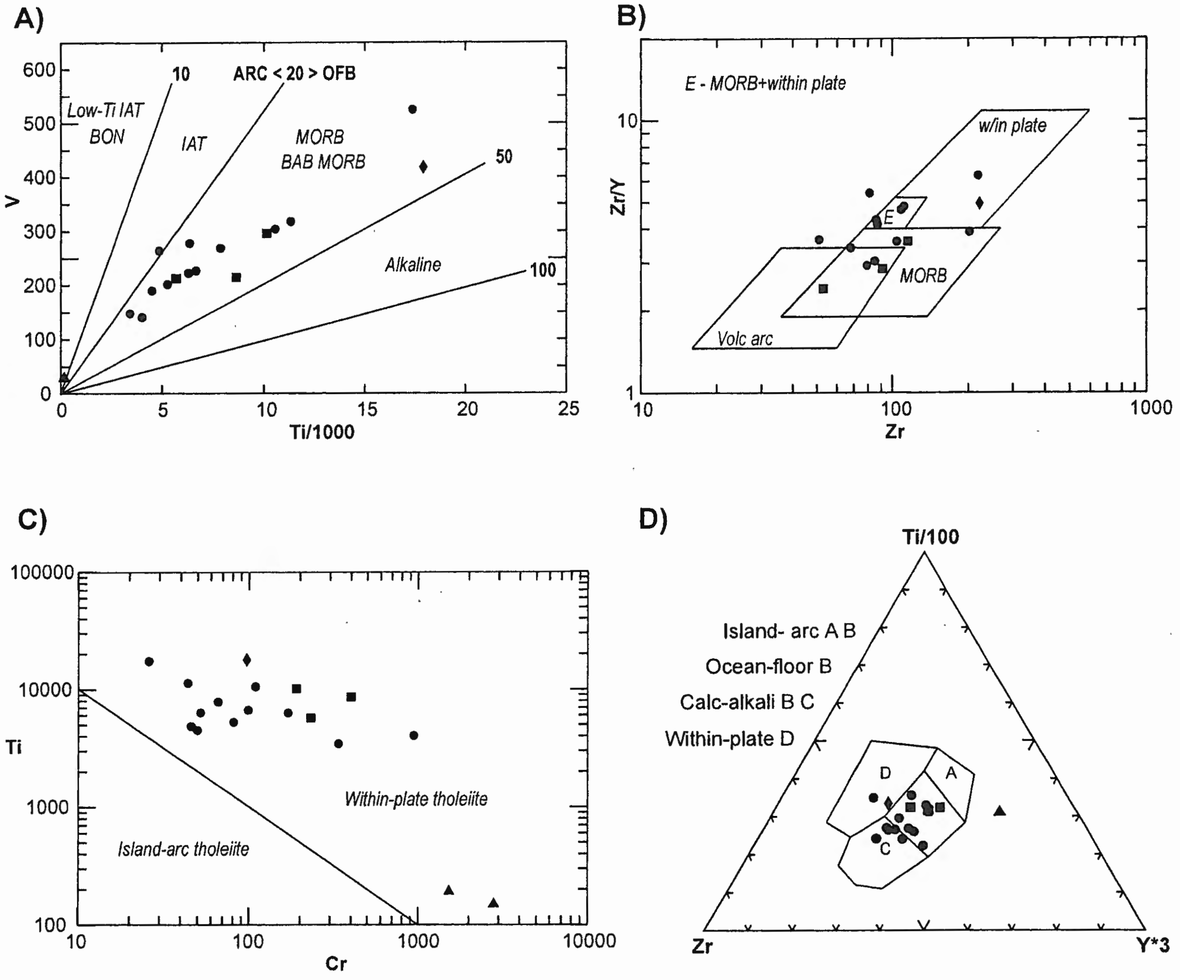

Figure 2.8: Tectonic environment classifications diagrams: **A)** Ti vs. V of Shervais (1982); **B)** Zr vs. Y plot of Pearce and Norry (1979); **C)** Cr vs. Ti plot after Beccaluva et al., (1979); **D)** Trivariate immobile element discrimination diagram of Pearce and Cann (Pearce and Cann 1973). **Legend:** ***triangles,*** Group I ultramafics; ***squares,*** Group II MORB like tholeiites; ***circles,*** Group III gabbroic tholeiites; ***diamonds,*** Group IV alkali basalts.

plot of Pearce and Cann (1973), Group II tholeiites consistently plot within the MORB field, lending support to the MORB-like signature observed in the REE patterns for this group (Figure 2.4). Group III samples are not confined to a single field but instead plot in all fields implying the transitional nature of this group between MORB, E-MORB and within-plate affinity.

To further correlate the magma type of Group II and III tholeiites, primitive mantle normalized multi-element patterns were used (Figure 2.7). Patterns for all of the samples are roughly parallel. Group II tholeiites exhibit progressive enrichment of the most incompatible, large ion lithophile elements (LILE) on the left side of the diagram. The pattern for the high field strength elements (HFSE), from Ce to Yb lies roughly parallel to, though higher than the N-MORB tholeiitic pattern (Pearce 1983). Patterns characterizing Group III tholeiites are similar to Group II in that they also exhibit an overall progressive enrichment of the LILE, though they are more enriched in all (LILE and HFSE) elements with respect to N-MORB which is typical of within-plate basalts of continental and/or oceanic affinity (Thompson et al. 1983). In either case, the primitive mantle normalized patterns illustrate that both groups were generated from a source that was enriched in all of the elements relative to the primitive mantle.

Samples of both groups exhibit negative Nb, Zr and Ti anomalies, which is characteristic of tholeiitic basalts emplaced in a volcanic arc setting above a subduction zone or within-plate basalts of continental and/or oceanic affinity (Pearce 1983). Despite the presence of the negative anomalies however, all samples particularly those of Group III, are relatively enriched in Nb, Zr and Ti with respect to N-MORB. Low εNd(500) values ranging between -12 and +2 imply that the sub-lithospheric mantle source for these tholeiites was enriched either via subduction related processes, or the assimilation of continental lithospheric components (Pearce 1983; Thompson et al. 1983).

Group IV: Alkaline Basalts

A comparison of the Group IV alkali basalt with tholeiites of the other two groups illustrates that Group IV has even higher Ti/V and Zr/Y ratios, which is characteristic of intraplate basalts (Figures 2.8A and B). In the diagram of Pearce and Norry (1979) and the immobile element trivariate plot of Pearce and Cann (1973), the intraplate nature of the alkali basalt is supported by the fact that the sample consistently plots in the within-plate field.

With respect to the primitive mantle normalized multi-element plot and compared to the other geochemical groups of the Masang Kang suite (Figure 2.7), the alkali basalt of Group IV shows the greatest enrichment in all of the elements and has a pattern that parallels that of the Group III tholeiites. Marked negative Nb and Zr anomalies, and a slight negative Ti anomaly also characterizes the pattern. However, despite the negative anomalies this sample is relatively enriched in Nb, Zr and Ti with respect to the primitive mantle and N-MORB thereby implying that the source was not only affected by a subduction component, but was also enriched in these elements relative to a primitive mantle source. Thus, as discussed by Pearce (1983) the magma source could have been an enriched portion of the convecting upper mantle, or more probably an enriched sublithospheric mantle source.

2.6 DISCUSSION WITH RESPECT TO TRACE ELEMENT GEOCHEMISTRY

The preservation of Paleoproterozoic cores in zircons from two different samples suggests that rocks of the Masang Kang suite are of similar age. Geochemically the data follow common trends in different variation diagrams suggesting that the nature of their source must also have been similar.

The fractionation of Ti-bearing phases during the evolution of a magma source can be correlated with a drastic decrease in the Ti/Zr ratio of the evolving melt, as well as decreases in relative Cr and Ni contents (Watters and Pearce 1987; Abu-Hamatteh 2005). In the case of the Masang Kang suite, we observe a positive correlation between TiO_2 and Zr (Figure 2.9). In addition, rocks with low TiO_2 tend to have relatively high Cr and Ni concentrations implying that Ti-bearing minerals were not fractionating phases in the evolution of the Masang Kang suite. Instead, the trend between TiO2 and Zr suggests that olivine and clinopyroxene were the crystallizing phases in all samples for which negative Eu anomalies are not observed in the REE patterns (i.e. Groups I, II and the majority of Group III; Figure 2.4). The presence of negative Eu anomalies in the REE patterns of Group IV and sample 217 of Group III implies a combination of olivine, plagioclase and clinopyroxene as fractionating phases in their evolution (Abu-Hamatteh 2005).

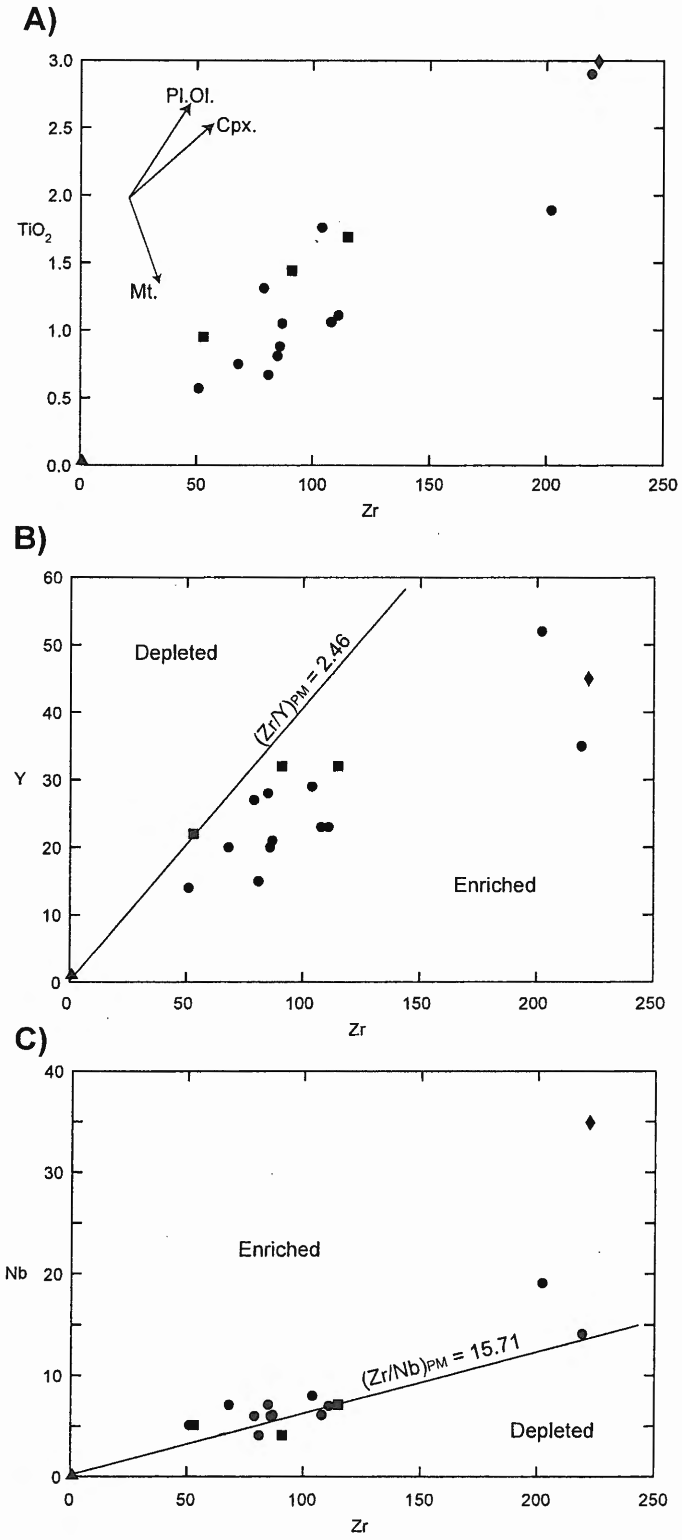

Figure 2.9: Trace element plots: **A)** Zr vs. TiO2; **B)** Zr vs. Y; **C)** Zr vs. Nb diagrams after Abu-Hamatteh (2005) illustrating the enriched nature of the magma source from which the Masang Kang suite of rocks were derived.

For most of the samples, multi-element patterns illustrate an overall enrichment in all of the incompatible elements with respect to primitive mantle abundances (Figure 2.7). With the exception of Group I ultramafic rocks, (Ce/Sm)N ratios are higher than N-MORB [(Ce/Sm)N = 0.71] and lower than ocean island basalts [OIBs; (Ce/Sm)N = 2], indicating the transitional geochemical nature of the Masang Kang suite between these two end-members (Holm 1985; Abu-Hamatteh 2005). Thus, the enrichment of LREEs and incompatible elements may be accounted for by one, or a combination of the following three scenarios: i) enrichment due to crustal contamination via the subduction of Archean sediments, ii) assimilation-fractional crystallization of the melt in the magma chamber or during its ascent through the lithosphere, assuming an initially depleted source, or iii) the enrichment of the LREEs due to partial melting of an initially enriched source at varying depths in the garnet and spinel stability fields respectively.

Enrichment due solely to crustal contamination can be ruled out based on the high TiO_2 and FeO_T contents in these samples (Table 2.2), as most rocks with a significant crustal component generally have lower concentrations then what is observed in the Masang Kang suite (Carlson et al. 1981; Abu-Hamatteh 2005). Furthermore, all continental crust is characterized by the presence of a negative Nb anomaly, similar to the sublithospheric mantle immediately above a subduction zone (Ahmad and Tarney 1991). Nb/La and Nb/Ce ratios in the Masang Kang tholeiites average 0.49 and 0.21 respectively, which is lower than both the primitive mantle (Sun and McDonough 1989), and the average crust (Taylor and McLennan 1985). Such low Nb/La and Nb/Ce values in the Masang Kang tholeiites imply that the observed elemental signature was inherited from a source that was contaminated by a crustal component with a larger than average negative Nb anomaly (i.e. Archean crust; Taylor and McLennan 1985). In addition, Archean crust is also characterized by rather significant positive Eu and Sr anomalies (Taylor and McLennan 1985). Thus, considering the lack of positive Eu and Sr anomalies in the Masang Kang tholeiites it is unlikely that contamination by the Archean crust alone could have produced the multi-elemental pattern observed in this study. The initial enrichment of the source for the Masang Kang suite is also indicated by the relationships between Zr-TiO_2, Zr-Nb and Zr-Y (Figure 2.9). Samples in this study are characterized by ratios that exceed primitive mantle values, implying the source was initially enriched in elements that are relatively less incompatible compared to the LREEs.

Nb/La and Nb/Ce values for Groups II-IV are remarkably similar to values obtained from Mesoproterozoic mafic dykes in the LHS of the Garhwal Himalaya to the west (Ahmad and Tarney 1991), which are very similar to those of average subduction-related basalts presented by Holm (1985). A plot of Nd vs. Ce (Figure 2.10) can be used to test whether the magma source was initially enriched by contamination (i.e. by an earlier subduction event or influx of the enriched convecting upper mantle) or by assimilation during magma ascent. In the event that a source with chondritic Ce/Nd ratios experienced low degrees of melting, the melt will be enriched in the LREEs and plot along a line through the Nd – Ce data that intersects along the Nd axis, not the origin (Horan et al. 1987). However, the Masang Kang tholeiites, like the Garhwal volcanics and dykes, plot along a line that intersects the origin with a steeper slope then that of chondrite suggesting that the source of the Masang Kang tholeiites was enriched in the LREEs prior to melting. The fractionation trends observed in the REE patterns for the different groups might, therefore be attributed to varying degrees of crystal fractionation or partial melting at varying depths.

If the observed LREE enrichment evolved solely as function of fractionation processes, the FeO_T/MgO ratios of the samples would be expected to show a systematic change with progressive crystal fractionation. The FeO_T/MgO ratios of the samples however, show a large degree of overlap implying that the tholeiites of Groups II and III, and the alkaline basalt of Group IV were derived by variable degrees of partial melting of the an enriched source at varying depths. The Group IV alkaline basalt might represent an initial, low degree partial melt into which the LREEs would be most compatible. Group III tholeiites might represent a moderate degree of partial melting, and Group II a relatively higher degree of partial melt that would be least abundant in the LREEs as a consequence of removal in earlier melt phases (i.e. Groups IV and III). Group I therefore, might be representative of the magma chamber residue following the removal of all melt.

A La/Yb vs. Th/Ta plot clearly illustrates that La/Yb ratios vary greatly with the degree of melting such that basalts with high ratios (i.e. > 7) reflect small degrees of

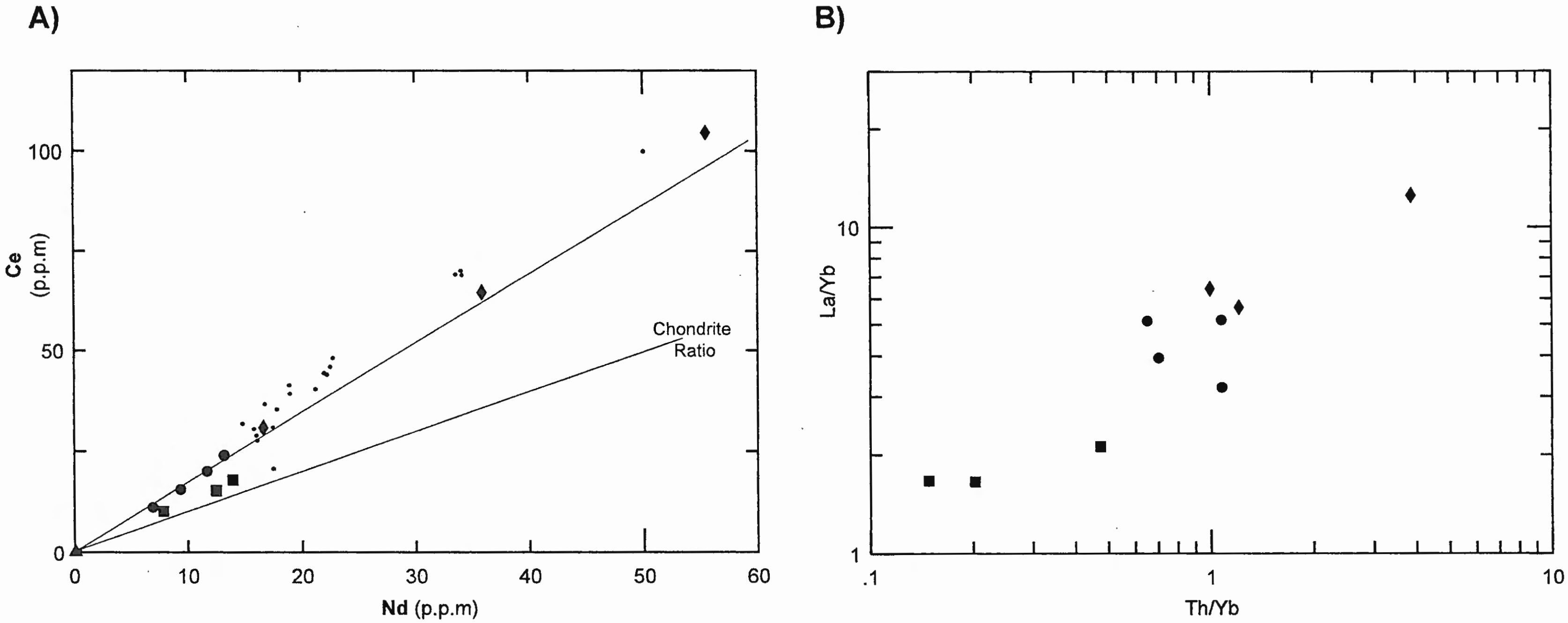

Figure 2.10: A) Nd vs. Ce plot taken from Ahmad & Tarney (1991) illustrating the enriched nature of the initial source of the Masang Kang suite. **B)** La/Yb versus Th/Yb plot after Condie (1990) illustrating the presence of a positive trend which is suggestive of the relationship between each of the groups constituting the Masang Kang suite by varying degrees of partial melting of a single source. **Legend:** ***triangles,*** ultramafic Cumulates; ***squares,*** Group III tholeiites; ***circles,*** Group II tholeiites; ***diamonds,*** Group I tholeiites; ***dots,*** data for the Garhwal volcanics and related dykes taken from Ahmad & Tarney (1991).

melting when garnet is left in the restite (Figure 2.10b; Condie 1994). In the Masang Kang suite, the alkali basalts of Group IV have the highest La/Yb ratios, while intermediate values characterize Group III tholeiites, followed by Group II tholeiites and finally Group I cumulates with the lowest ratios. Therefore, the alkali basalt of Group IV may have been produced at great depths by a low degree of melting of an initially enriched mantle source in the garnet stability field ((Gd/Yb)N = 1.2 – 2.3), hence the relatively low abundance of the heavy REEs. Average Nb/La and Nb/Ce values of 0.55 and 0.26 respectively for Group IV are similar to values for the lower crust (Taylor and McLennan 1985), lending support for a relatively deep crustal magma source. Flat REE patterns and Nb/La and Nb/Ce values of 0.60 and 0.23 for Group II tholeiites are only a little lower than average bulk crustal values (Taylor and McLennan 1985), suggesting they were derived by a high degree of melting at shallow crustal depth, in the spinel stability field ((Gd/Yb)N = 1.1 – 1.4). Group III tholeiites were most likely to have been produced by moderate degrees of melting at moderate depth ((Gd/Yb)N = 1.2 – 1.9). The most enriched Group III sample (BH-217), which may consequently be representative of the earliest partial melt of the Group III tholeiites, is characterized by a whole rock εNd(500) value of -12. Sample BH-219, the least enriched and most primitive Group III tholeiite is characterized by a whole rock εNd(500) value of +2, which confirms the primitive signature observed in the REE pattern.

Chondrite and mantle normalized multi-element plots for the Mesoproterozoic Garhwal volcanics and dykes in the western Himalaya (Ahmad and Tarney 1991and references therein), and the Paleoproterozoic basal Aravalli volcanics in Rajasthan (Ahmad and Tarney 1994 and references therein) show marked similarities with patterns for Groups II-IV of the Masang Kang suite (Figure 2.11). Similarities between the data sets include the presence of significant negative Nb and Ti anomalies and an overall enrichment of the LREE and LILE incompatible elements. The largest discrepancy is the marked negative Zr anomaly in samples from this study. Considering the spatial and temporal distance between the Garhwal, Aravalli and Masang Kang suites, it is difficult to attribute the geochemical similarity between groups solely to crustal contamination because of the chemical variability of crustal components in both space and time. It would seem, therefore, that the similar geochemical signatures observed at all three

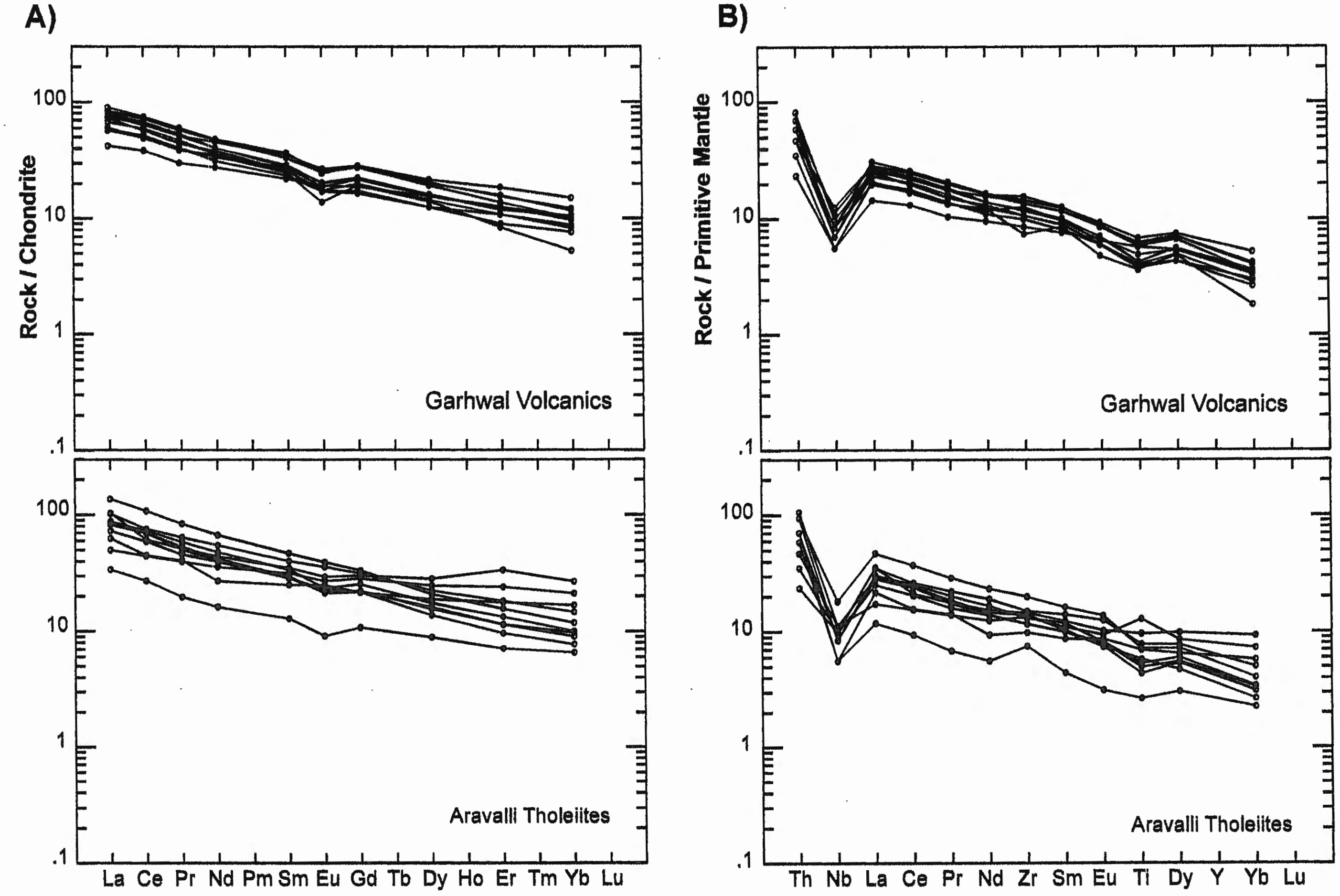

Figure 2.11: Multi element comparison. **A)** Chondrite normalized REE patterns for the Garhwal and Aravalli volcanics. **B)** Primitive mantle normalized multielement patterns for the Garhwal and Aravalli volcanics. Data from Ahmad & Tarney (1991) and Ahmad & Tarney (1994), normalization values are taken from Sun & McDonough (1989).

sample locales were inherited from the mantle source, which was further modified by partial melting and fractional crystallization.

For the metabasites in the western Himalaya, Ahmad & Tarney (1991; 1994) suggested the development of the within-plate pattern was not a random feature but instead might have been controlled by the crystallization of one or more mineral phases during the evolution of the subcontinental lithospheric mantle, and that the achievement of chemical homogeneity by crustal contamination and assimilation would be extremely difficult over such vast distances and over prolonged periods of geological time. As a result Ahmad & Tarney (1991) invoked the need for the subduction of a source similar in composition to the post-Archean terrestrial shale to produce the observed REE and trace element patterns in the Garhwal and Aravalli volcanics. Kesson and Ringwood (1989) proposed the mobilization of hydrous fluids within subduction zones to depths in excess of 150 km, where they could scavenge the lithospheric mantle for LILE and LREEs and stabilize them at higher levels in phlogopite. An alternate explanation is that in the late Archean – early Proterozoic period, during which time the temperature of the lithosphere may have been higher than at present, the oceanic lithosphere did not subduct completely but merely underplated the progressively developing continental lithosphere (Ahmad and Tarney 1991). Such mafic material would be particularly prone to melting during subsequent thermal events, giving rise to LREE and LIL element enriched melts and melts that would carry a subduction related signature.

2.7 CONCLUSIONS

In northwestern Bhutan, the close association of metabasic and ultramafic rocks with rocks representative of a continental margin, and their chemical affinity with oceanic volcanic arc magmas suggests the Masang Kang suite was emplaced into a passively extending margin, which may have lead to complete rifting and separation of the proto Indian margin from cratonic fragments that now comprise Eurasia. The chemical similarity between the rocks of this study and the Garhwal and Aravalli volcanics, which show marked chemical similarities with Phanerozoic continental flood basalts and Proterozoic dyke swarms (Sheraton and Black 1981; Weaver and Tarney 1981; Mantovani et al. 1985; Myers et al. 1987; Hawkesworth et al. 1988), lead us to suggest that the rocks of the Masang Kang suite were produced during a major Paleo-

Mesoproterozoic thermal event that caused the mobilization and enrichment of the sub-continental lithosphere beneath the proto Indian margin. The geochemical arc-like signature of these metabasic rocks may have been produced during an earlier episode of oceanic underplating from which the fluid needed to mobilize and enrich the overlying sublithospheric mantle may have been produced.

Finally, the preservation of Paleoproterozoic crystallization ages in zircons from metabasic rocks of the Masang Kang suite refutes the observation that the GHS is lacking in igneous ages > 800 Ma. In fact, the occurrence of Paleoproterozoic igneous rocks within the GHS of Bhutan suggests that though sparse, evidence for early Proterozoic basement material is present within the GHS. Furthermore, despite the apparent heterogeneity of ages and lithologies in small areas across the Himalaya, the preservation of distinct age clusters (i.e. 12-25 Ma, ~ 400-600 Ma and > 1000 Ma) across the length of the orogen in both the LHS and GHS implies that the tectonic setting along the extensive Paleoproterozoic proto-Indian margin was similar long before the onset of the Himalayan orogeny.

CHAPTER III: P-T-T HISTORIES OF THE MSL AND HSL

3.1 INTRODUCTION

It is well established that across the length of the Himalaya, metamorphic grade within the Greater Himalayan Sequence (GHS) increases from amphibolite facies at low structural levels immediately above the MCT to granulite facies at higher structural levels immediately below the STD. Locally, the preservation of kyanite inclusions in garnet, and pseudomorphing of kyanite by sillimanite in metasedimentary rocks, has served as evidence for the existence of an earlier relatively high pressure (HP) mineral assemblage that probably developed as GHS protolith material was buried during the earlier stages of Himalayan deformation (D_1) and metamorphism (M_1). Studies have illustrated that in Bhutan the HP (i.e. > 8.5 kbar; Swapp and Hollister 1991) assemblage has been almost completely overprinted by a later high-temperature (HT) assemblage (e.g. Ganser 1983; Brunel and Kienast 1986; Hodges et al. 1988; Swapp and Hollister 1991; Davidson et al. 1997). Development of the HT assemblage and the pervasive foliation that is present in the metasediments throughout the GHS has been attributed to a second stage of deformation (D_2) and metamorphism (M_2), when GHS material was exhumed between the MCT and STD from mid-crustal levels at relatively high temperatures. Overprinting of the HT assemblage by a MP-LT assemblage, development of large east-west trending open folds and more localized, brittle ductile shear zones are attributed to the third and final stage of Himalayan deformation (D_3) and metamorphism (M_3), which is associated with continued exhumation of GHS material beneath the South Tibetan Fault System (STFS) and along the MBT and MFT.

In the Bhutan Himalaya, demarcation of the metamorphic isograds within the GHS is based primarily on assemblages observed in the metasedimentary rocks (Gansser 1983). In this study, the absence of muscovite coupled with the presence of sillimanite and K-feldspar in metasediments at the highest structural level is consistent with the characteristic granulite facies assemblage described by Gansser (1983) and Swapp and Hollister (1991), while muscovite coupled with sillimanite pseudomorphing kyanite characterises the upper amphibolite facies assemblage at the mid-structural level. The intensely metamorphosed tholeiitic rocks, which are the primary focus of this chapter, were collected within a granulite facies domain in the highest structural level (HSL) of

Figure 3.1: Geological map and cross-section of Bhutan. **a)** Geological map of Bhutan modified from Grujic et al. (2002). A-A' marks the trend of the cross-section presented in Figure 3.1b. The relative positions of the mid- (MSL), higher- (HSL) and lower structural (LSL) levels are indicated along A-A'. **Legend:** ***MFT***, Main Frontal Thrust; ***MBT***, Main Boundary Thrust; ***MCTl,*** lower Main Central Thrust; ***MCTu***, upper Main Central Thrust; ***KT***, Kakhtang Thrust; ***STDl***, lower South Tibetan Detachment; ***STDu***, upper South Tibetan Detachment. **b)** Geological cross-section through the GHS of western Bhutan illustrating the nature of the boundaries between units, and the relative locations of the three structural levels that are discussed in this study. Information was compiled from Gansser, (1983), Burchfiel et al. (1992), Wu et al. (1998), and this study. The position of the MHT has been extrapolated from INDEPTH results (Hauck et al. 1998).

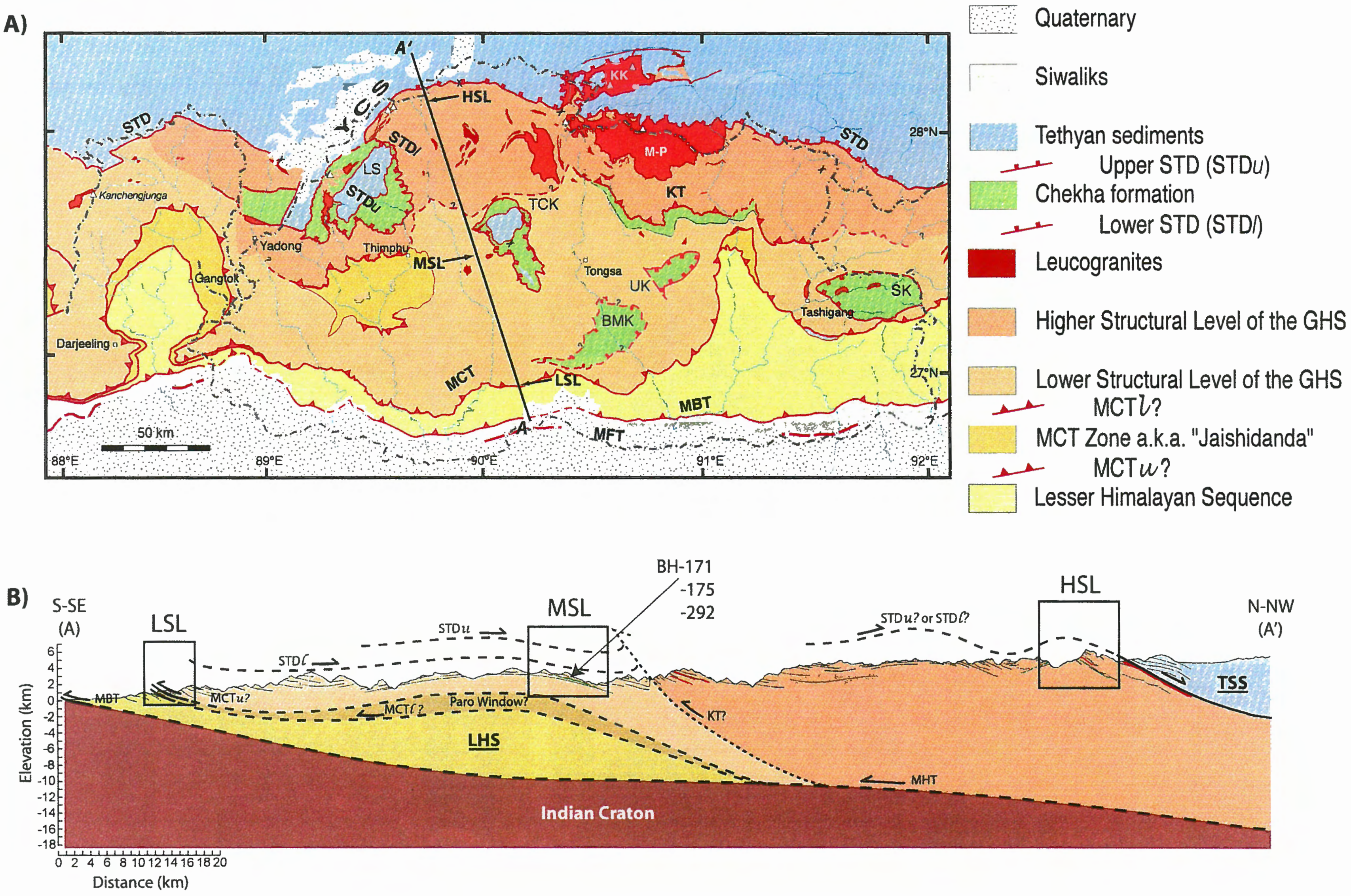
A)
A'
A
HSL
MSL
LSL
STD
STD*l*
STD*u*
YCS
LS
KK
M-P
KT
TCK
UK
BMK
SK
MCT
MBT
MFT
Kanchengjunga
Yadong
Thimphu
Gangtok
Darjeeling
Tongsa
Tashigang
28°N
27°N
88°E
89°E
90°E
91°E
92°E
50 km
Quaternary
Siwaliks
Tethyan sediments
Upper STD (STD*u*)
Chekha formation
Lower STD (STD*l*)
Leucogranites
Higher Structural Level of the GHS
Lower Structural Level of the GHS
MCT*l*?
MCT Zone a.k.a. "Jaishidanda"
MCT*u*?
Lesser Himalayan Sequence
B)
S-SE
(A)
N-NW
(A')
LSL
MSL
HSL
BH-171
-175
-292
STD*u*
STD*l*
STD*u*? or STD*l*?
MBT
MCT*u*?
MCT*l*?
Paro Window?
KT?
TSS
LHS
MHT
Indian Craton
Elevation (km)
6
4
2
0
-2
-4
-6
-8
-10
-12
-14
-16
-18
0 2 4 6 8 10 12 14 16 18 20
Distance (km)

the GHS, and from upper amphibolite facies rocks in the mid-structural level (MSL; Figure 3.1). At both levels, the metabasites are present as discontinuous layers and boudins that are encompassed by sillimanite ± muscovite metasediments. Boudins are variable in size ranging from one to several metres in diameter, while the layers that were encountered range from a few centimetres up to a meter in thickness. Granulite facies metabasites are pyroxene-bearing garnet-amphibolites, while those sampled from the upper amphibolite facies are pyroxene absent garnet-amphibolites. With the exception of the meta-ultramafic rocks in the area, primary igneous textures and minerals are not preserved. Locally, at the outcrop scale, a weakly developed foliation can be observed in the fine-grained boudins in which the foliation is discordant to the main planar fabric in the surrounding migmatites and may likely be related to an earlier phase of deformation. A lack of sufficient structural field data makes it difficult to assess whether or not it developed during D_1.

3.2 HIGHER STRUCTURAL LEVEL (HSL)

As discussed in Chapter 1, metabasites from the highest structural levels of the GHS are hosted by intensely foliated and migmatitized metasediments, and form discontinuous layers and boudins in an ~ 2 km thick zone in the core of an antiform (Figure 3.2). The following is a description of the mineral assemblages and micro-textures observed in the metabasites and encompassing metasediments. For sample locations refer to Figure 3.2. Data presented for the metasediments are a summary of the work carried out by David Moynihan during a summer work term in 2004, while all other data was produced by the author. Detailed micro-structural analyses were restricted to the metasedimentary rocks from the highest structural level since metabasites sampled in this study are coarse grained and lack appropriate features. Micro-structural analyses for metasediments at the mid-structural level are not available due to the lack of samples from this level.

3.2.1 MICRO-TEXTURES

Metasedimentary rocks are compositionally banded with alternating biotite-sillimanite-rich melanocratic and quartz-feldspar-rich leucocratic layers (Figure 3.3), which defines the main, penetrative foliation that is interpreted to correlate with the regional north-dipping S_2 foliation. Where garnet porphyroclasts are present, ribbons of

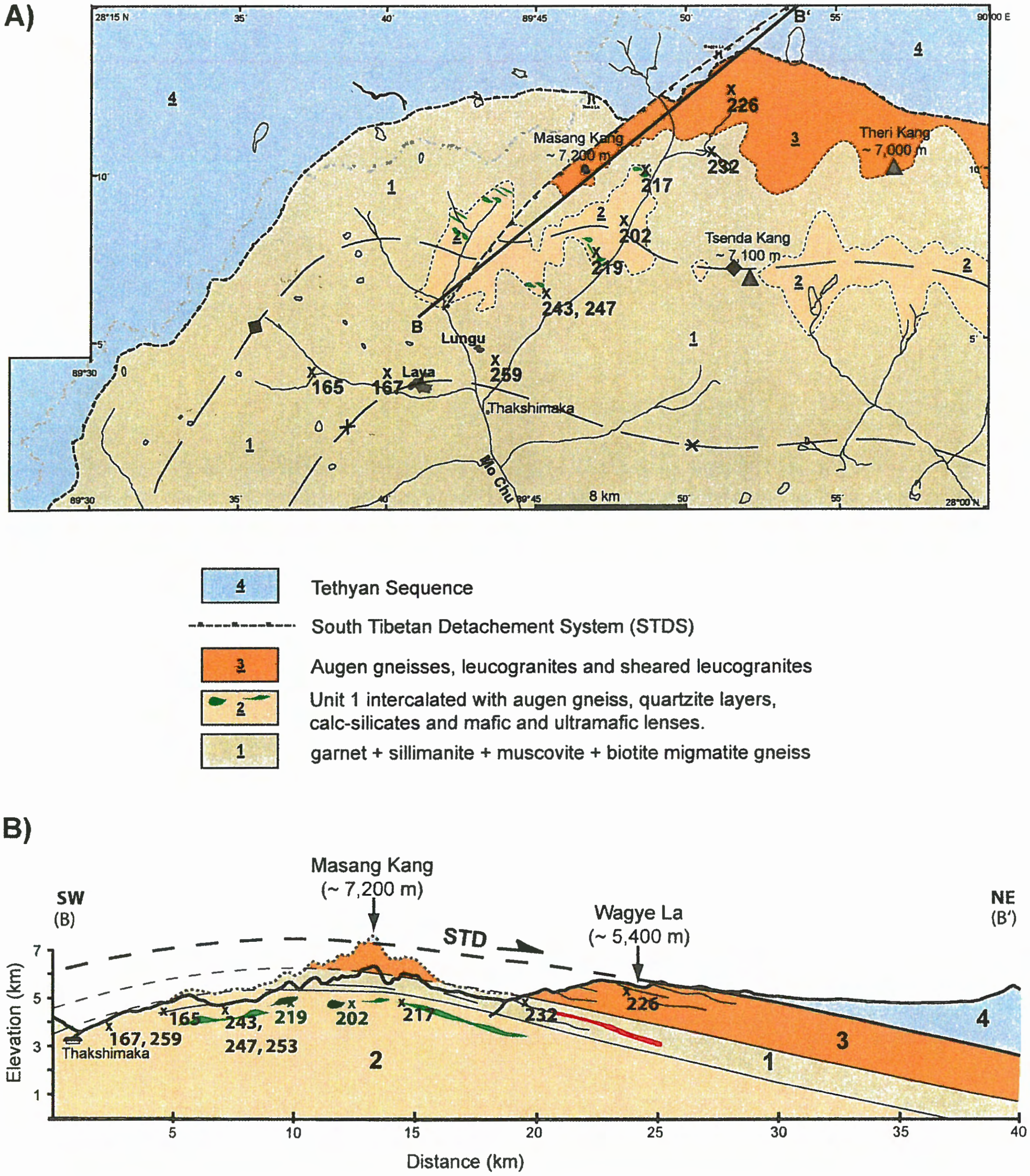

Figure 3.2: Map and cross-section through NW Bhutan. **A)** Geological map of northwestern Bhutan on which locations of metasedimentary and metabasic samples from the HSL have been marked. Information was compiled from Gansser, (1983), Burchfiel et al. (1992), Wu et al. (1998), and this study. The heavy, grey, dash-dot line marks the Bhutanese border. B-B', marks the position of the cross-section in Figure 3.2b. **B)** Geological cross-section through Masang Kang and into southern Tibet. ***Solid, heavy line:*** the topographic profile based on SRTM data; ***dashed, heavy-line:*** topographic profile to the true elevation; ***green layers and boudins:*** position of metabasic rocks; ***red:*** late Miocene leucogranites.

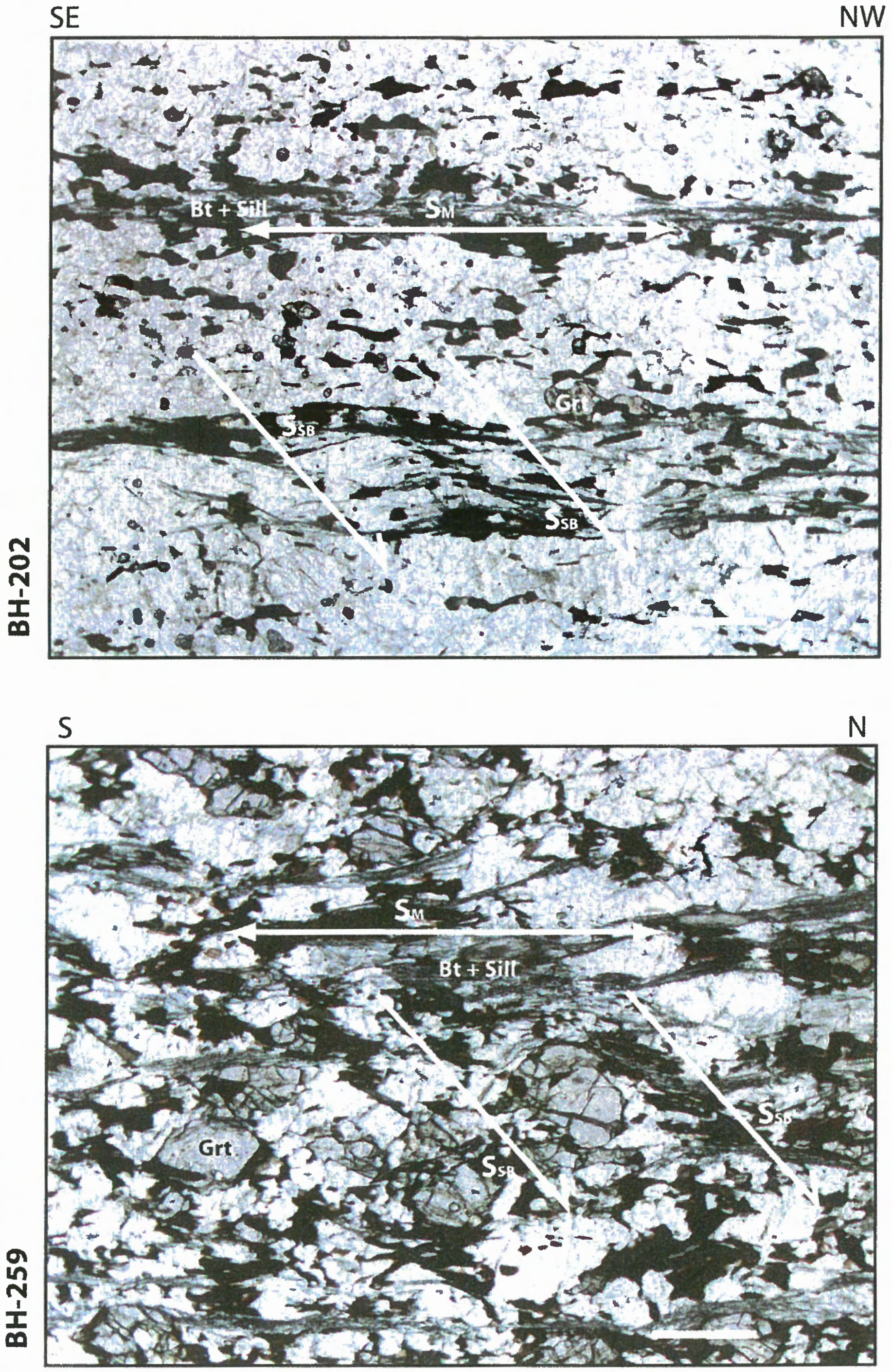

Figure 3.3: Photomicrographs of two representative metasedimentary samples from the higher structural level highlighting the microstructures observed in thin-section. For sample locations refer to figure 3.1b. Photographs were taken at 1.6x magnification such that the total field of view is ~ 7.5 mm. The length of the scale bar in the bottom right corner of each photo marks 1 mm. **Legend:** S_M, main foliation defined by biotite + sillimanite intergrowths; S_{SB}, shear bands that crosscut the main foliation.

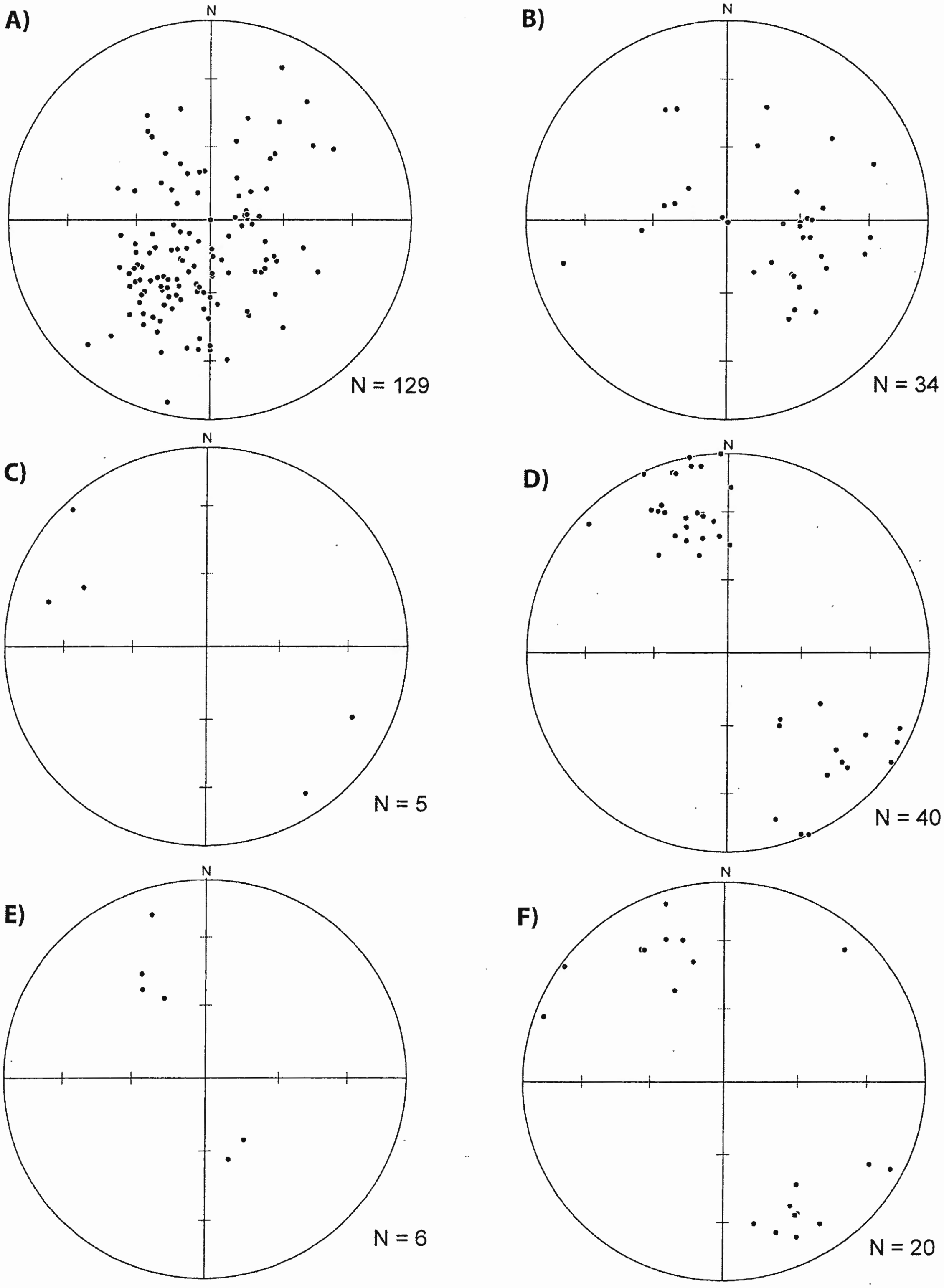

Figure 3.4: Equal area projections of structural data from the higher structural level (HSL) of the GHS in northwestern Bhutan. **A)** poles to the main foliation (S_2); **b)** stretching lineation measured on foliation planes; **c)** fold axes; **d)** poles to fault planes; **e)** poles to shear bands; **f)** stretching lineations measured on fault planes and within shear bands. Tick mark spacing on stereonet is 30 degrees.

the S_2 biotite-sillimanite intergrowths wrap them (Figure 3.3). Many of the garnet porphyroclasts are partially replaced by biotite and sillimanite suggesting garnet growth occurred prior to the development of the main foliation, perhaps during an early, prograde stage of metamorphism (M_1). Earlier garnet growth implies that its breakdown and development of the minerals defining the main foliation was contemporaneous with the second, regional stage of deformation and metamorphism (D_2), and leucogranite intrusion.

Cross-cutting the S_2 foliation are small, moderately developed C – type shear bands. The biotite and sillimanite clots, which define the main foliation, are bent into them. Most samples contain only one set of shear bands with top-to-the north-northwest sense of displacement. Locally, conjugate C – type shear bands are observed, one set with top-to-the north-northwest and the other with top-to-the southeast kinematics - both consistent with field observations of shear bands associated with the STD (Figure 3.4). Based on the cross-cutting relationship with the main foliation, shear bands must have formed late- to post-M_2, most likely early- to syn-M_3.

3.2.2 MINERAL ASSEMBLAGES & CHEMISTRY: METABASITES

The following is a summary of the petrographical analysis carried out on the metabasites. A summary of the mineralogy and mineral reaction textures is given in Tables 3.1 and 3.2.

Metabasites immediately below the STD have the mineral assemblage garnet + clinopyroxene + plagioclase + orthopyroxene + amphibole + quartz + biotite ± anthophyllite-gedrite ± K-feldspar. Accessory minerals include rutile, zircon, titanite, apatite, ilmenite, and epidote (Table 3.1; Figure 3.5). Garnets are embayed and relatively small ($\leq\sim$ 2mm) with core compositions of $Alm_{44-57}Py_{13-32}Grs_{24-29}Sps_{0.9-1.5}$ and rims $Alm_{46-59}Py_{13-32}Grs_{21-25}Sps_{1.5-3}$. Zoning profiles are flat with increases in Fe, Mn, and concomitant decreases in Mg and Ca at the rims (Figure 3.6 and Appendix D), suggesting that metabasites, like the surrounding metasediments, were subjected to temperatures above 800 °C for at least 2 Myr to permit for the homogenization of garnets (Tracy 1982; O'Brien 1997; O'Brien 1999; Pattison 2003). A decrease in Mg along grain margins can be attributed to cation exchange between garnet and the matrix during decompression and cooling (Spear 1993; O'Brien 1997), while a decrease in Ca along garnet rims is likely to

Table 3.1: Major silicate phases in metapelites and metabasites from the highest structural levels of the GHS, northeastern Bhutan.

	Pl	Kfs	Bt	Grt	Ky	Sil	Crd	Amp	Opx	Cpx	Oamp	Acc
Metapelites												
BH-165	X	X	X	X	–	X	X	–	–	–	–	Sp
BH-167	X	X	X	X	–	X	–	–	–	–	–	Sp
BH-243	X	–	X	X	–	t	X	–	X	–	X	trace Tour, Herc
BH-247	X	–	X	X	t	t	–	–	X	–	–	Tour, Ru, Ilm
Metabasites												
BH-173	X	–	–	X	–	–	–	X	X	–	X	Ru, Mag, Ilm, Ap
BH-175A	X	–	–	X	–	–	–	X	–	–	–	Zr, Ti, Ap, Ilm
BH-217A	X	X	X	X	–	–	–	X	X	X	X	Zr, Ti, Ap, Ilm, Mag
BH-219	X	–	X	X	–	–	–	X	X	X	X	Sp, Zr, Ilm
BH-292	X	X	X	X	–	–	–	X	–	–	X	Zr, Ti, Ru, Mag, Ilm, Ap

Table 3.2: Metamorphic reactions in metapelites and meta-tholeiites from northeastern Bhutan.

Mineral Reaction	Texture (w/ reference to micrographs)	Garnet Composition (w/ reference to X-ray maps)
Metapelites		
3.1) Ms + Qtz ± Pl → Ky + Ksp + fluid	– Ky included in Grt (BH-247)	– Grt rims have high Fe, Mn and low Mg relative to cores. Ca concentrations relatively uniform, though some grains display higher Ca concentrations in core relative to rims. – large garnets (i.e. > 3 mm) preserve bell shaped, growth Mn profiles through inclusion rich cores.
3.2) Bt + Ky + Qtz ± Pl → Grt + Kfs + Liq	– Ky only observed as inclusions in Grt (BH-247)	
3.3) Grt + Kfs + fluid → Bt + Pl	– Grt partially replaced by Bt and Sil (BH-165)	
3.4) Bt + Grt + Qtz ± Pl → Opx + Sil + Liq ± Kfs	– Orthopyroxene associated with melanocratic layers – Grt partially replaced by Crd	
3.5) Bt + Grt + Qtz ± Pl → Crd + Opx + Liq ± Kfs		
3.6) Bt + Qtz ± Pl → Opx + Liq ± Grt ± Crd ± Kfs		
3.7) Bt +Sil + Qtz ± Pl → Grt + Crd + Liq ± Kfs		
3.8) Grt + Kfs + Liq → Bt + Sil	– Grt resorbed and partially replaced by Bt and Sil	
3.9) Grt + Sil + Bt → Crd + Sp + Kfs (BH-165, 167, 243)	– Crd overgrowing and partially replacing Sil – Crd replacing Grt and Bt – Sp + Qz symplectite around Grt – Incl of Sill in Grt	
Metabasites		
3.10) Amp + Pl +Qtz → Grt + Cpx + Liq ± Opx	– Grt and Cpx never juxtaposed.	– slight decrease in Fe, Ca and Fe/(Fe+Mg) along outter rim with corresponding increase in Mg and Mn, followed by an increase in Fe, Ca and Fe/(Fe+Mg) and corresponding decrease in Mg and Mn. (BH-173) – slight increase in Fe, Mn and Fe/(Fe+Mg) along rims with corresponding decrease in Mg and Ca. (BH-217, 219, 292)
3.11) Grt + Cpx + Liq → Opx + Pl	– coronas of symplectic Opx + Pl around anhedral Grt (BH-217, 219) or completely replacing Grt (BH-219) – inclusions of Cpx in Opx (BH-219)	
3.12) Cpx + Opx +Pl + Liq → Amp + Qtz	– inclusions of Amp in matrix Cpx and Grt (BH-219) – inclusions of Opx and Cpx in Amp. (BH-217, 219) – coronas of Amp around Opx and Cpx intergrowths. (BH-217, 219)	

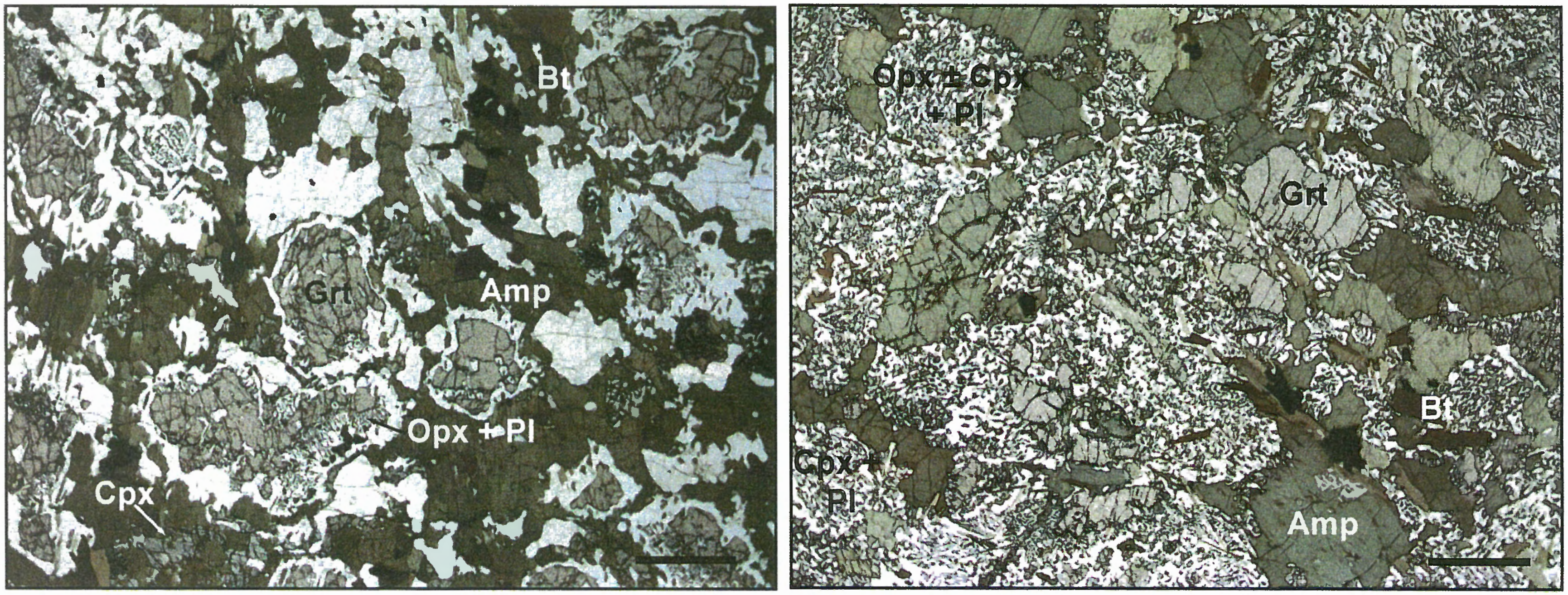

BH-217 **BH-219**

Figure 3.5: Photomicrographs of metabasites from the HSL. Micrographs were taken at 1.6x magnification such that the total field of view is ~ 7.5 mm. The length of the scale bar in the bottom right corner of each micrograph marks 1 mm. ***Grt,*** garnet; ***Amp,*** amphibole; ***Cpx,*** clinopyroxene; ***Opx,*** orthopyroxene; ***Bt,*** biotite; ***Pl,*** plagioclase.

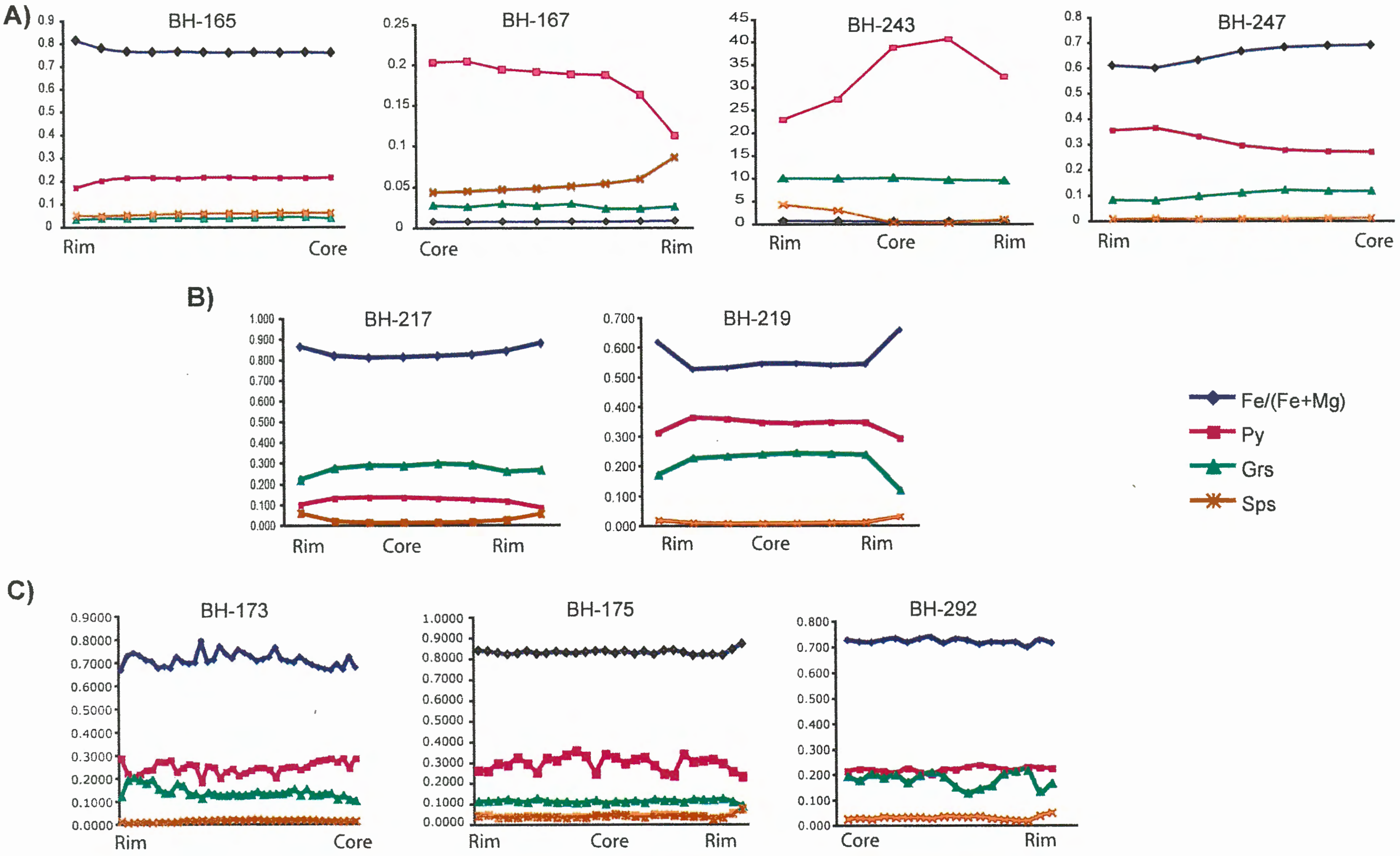

Figure 3.6: Zoning profiles through garnets in a) metasediments from the HSL; b) metabasites from the HSL, and c) metabasites from the MSL. ***Py,*** pyrope; ***Grs,*** grossular; ***Sps,*** spessartine.

be the consequence of net-transfer reactions during the breakdown of garnet to plagioclase and orthopyroxene upon decompression.

Garnets contain randomly oriented inclusions of clinopyroxene, plagioclase, quartz, ilmenite, magnetite, zircon, titanite, epidote and apatite. Plagioclase inclusions in BH-219 and -217 are calcium-rich (An_{87} and An_{69} respectively). Clinopyroxene appearing as inclusions in garnet (e.g. BH-217) are compositionally similar to those in the matrix, suggesting that they may be windows into the matrix. Garnet and clinopyroxene probably grew synchronously according to the reaction (Pattison 2003):

$$\text{Amp} + \text{Pl} + \text{Qtz} \rightarrow \text{Grt} + \text{Cpx} + \text{Liq}\ (\pm\ \text{Opx})\ \mathbf{(3.1)}$$

which is characteristic of high-pressure granulite facies metamorphism (Yardley 1989) at temperatures above ca. 775°C (Figure 3.7; Spear 1993; Pattison 2003). Depending on the bulk composition and pressures, orthopyroxene may develop in addition to or instead of clinopyroxene.

Typically, garnets are separated from the matrix by a corona of anorthitic plagioclase (An_{87} in BH-219; An_{57} in BH-217) and symplectic orthopyroxene, and/or amphibole. The matrix in both samples comprises 'spongy' clinopyroxene that is also mantled by orthopyroxene and plagioclase intergrowths. Therefore, the breakdown of garnet and clinopyroxene may have occurred by the reverse form of reaction (3.1) in addition to the steep, high-temperature, moderate pressure (i.e. < 10 kbar) reaction with the form (Neogi et al. 1998):

$$\text{Grt} + \text{Cpx} + \text{Liq} \rightarrow \text{Opx} + \text{Pl}\ \mathbf{(3.2)}$$

as orthopyroxene is unstable at pressures > 10 kbar (Spear 1993; Pattison et al. 2003). Hence, the breakdown of garnet and clinopyroxene was the result of a decrease in pressure but not necessarily a decrease in temperature. Matrix clinopyroxene is both Ca and Mg rich with Al concentrations varying from 0.44 where Cpx is intergrown with orthopyroxene, to 0.05 away from the intergrowths. Cpx is never observed juxtaposed with garnets. Orthopyroxene in mantles on matrix clinopyroxene is characterized by low Al concentrations (0.06), while grains in plagioclase - orthopyroxene coronas on garnet are slightly more Al-rich (Appendix C). Breakdown of clinopyroxene and orthopyroxene to amphibole probably occurred upon progressive decompression and cooling by the reaction (Spear 1993; Pattison 2003):

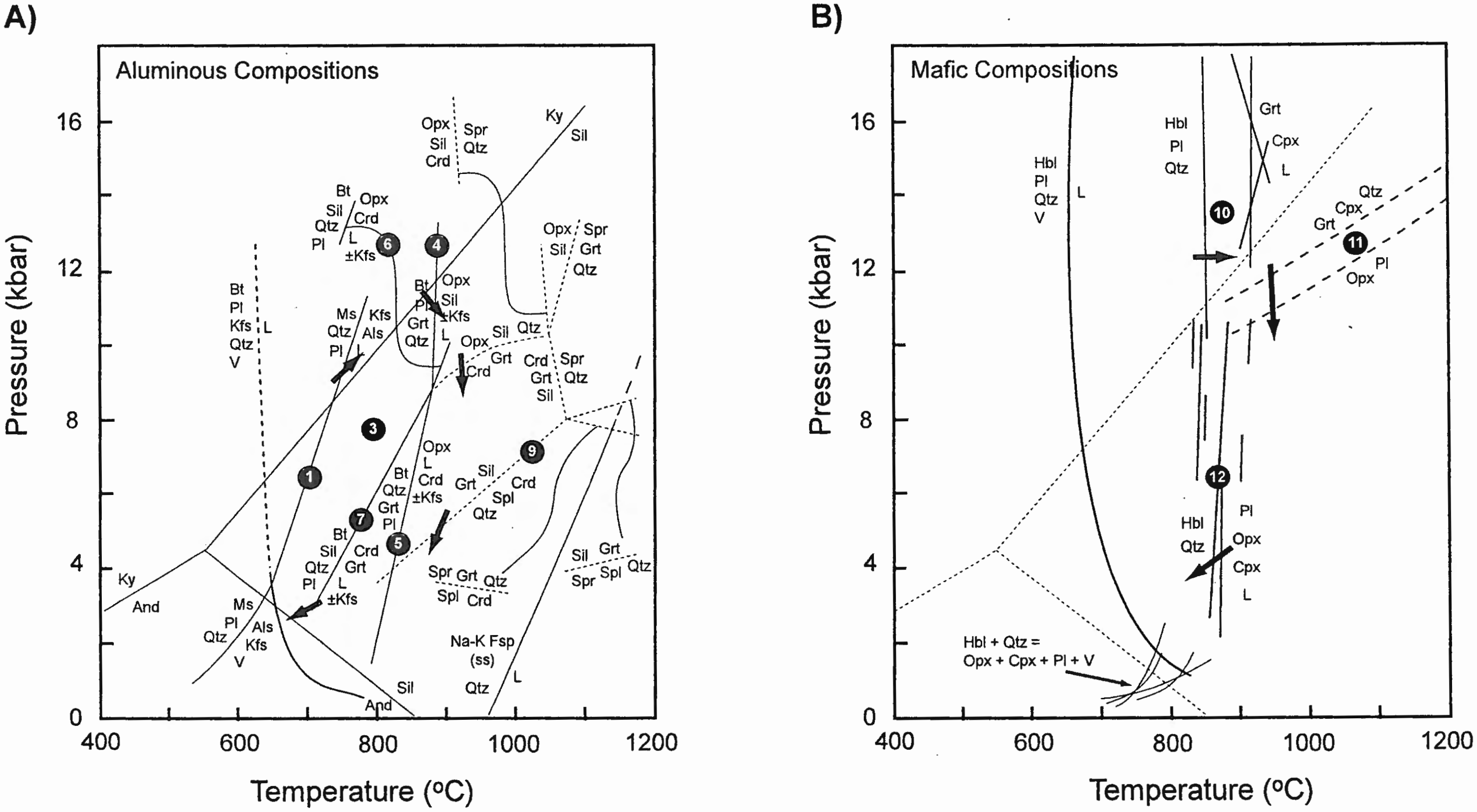

Figure 3.7: Petrogenetic grids highlighting the thermodynamic and experimentally determined positions of reactions that limit the stability of granulite facies mineral assemblages in **a)** aluminous and **b)** mafic rock compositions. Graphs have been modified from Pattison et al. (2003), and references therein. The position of the Al_2SiO_5 triple point is after Pattison (1992), while the position of the muscovite melting curve is after the reference Pëto (1976) given in Pattison (2003). Numbered reactions correspond to those discussed in the text. Heavy arrows illustrate the direction in which samples at the highest structural levels of the GHS in Bhutan might have progressed through P-T space, and the reaction boundaries they must have crossed based on the mineral assemblages and textures observed in thin-sections.

Cpx + Opx + Pl + Liq ± Grt→ Amp + Qtz **(3.3)**

Amphibole in coronas on matrix clinopyroxene is slightly less Al-rich (Appendix C). Secondary amphiboles that replace orthopyroxene are anthophyllite to ferro-anthophyllite with FeO and MgO up to 22% each. Replacement of orthopyroxene and pargasitic amphibole by anthophyllite is associated with a decrease in temperature.

Chemically, matrix plagioclase in BH-217 is not distinct from that in garnet coronas (An_{57-69}). However, matrix plagioclase in BH-219 is strongly zoned with highly calcic rims (An_{87}) and significantly less calcic cores (An_{54}). This suggests that chemistry of matrix plagioclase rims and those in garnet coronas developed as a result of the net transfer of Ca from garnet to plagioclase during decompression.

3.2.3 P-T ESTIMATES: METABASITES

The highest pressure estimate of 13.5 ± 1.33 kbar (BH-219; Figure 3.8) was calculated using orthoamphibole inclusions with garnet core compositions (Appendix C), implying that reaction 3.1 took place at relatively high pressures. The associated temperature for the core assemblage was calculated at 508 ± 60 °C, lower than is suggested by reaction 10 in Figure 3.7. Garnet in this sample is not in textural equilibrium with the matrix, thus the temperature estimate calculated for this sample is a minimum at best. Omitting garnet from the calculation, the breakdown of matrix clinopyroxene and orthopyroxene to amphibole and plagioclase shifts estimates towards higher temperatures of 680 ± 44 °C at 9.2 ± 1.5 kbar. Using garnet rims and the matrix assemblage in the same sample yields estimates for the breakdown of garnet and clinopyroxene to produce amphibole, plagioclase and biotite at 582 ± 50 °C and 9.3 ± 1.1 kbar. The replacement of orthopyroxene by anthopyllite appears to have taken place at similar temperatures (613 ± 35 °C) but significantly lower pressures (4.7 ± 1.3 kbar) implying near – isothermal decompression (Figure 3.8).

Clinopyroxene, plagioclase, K-feldspar and biotite inclusions in combination with garnet core compositions (BH-217) produced average estimates of 9.8 ± 1 kbar and 820 ± 51 °C (Figure 3.8). However, garnet core compositions in combination with the matrix assemblage minus matrix orthopyroxene yielded slightly higher estimates of 10.8 kbar, 722 ± 39 °C, suggesting that the peak garnet-clinopyroxene assemblage may have developed at slightly higher pressures and lower temperatures than estimates based on

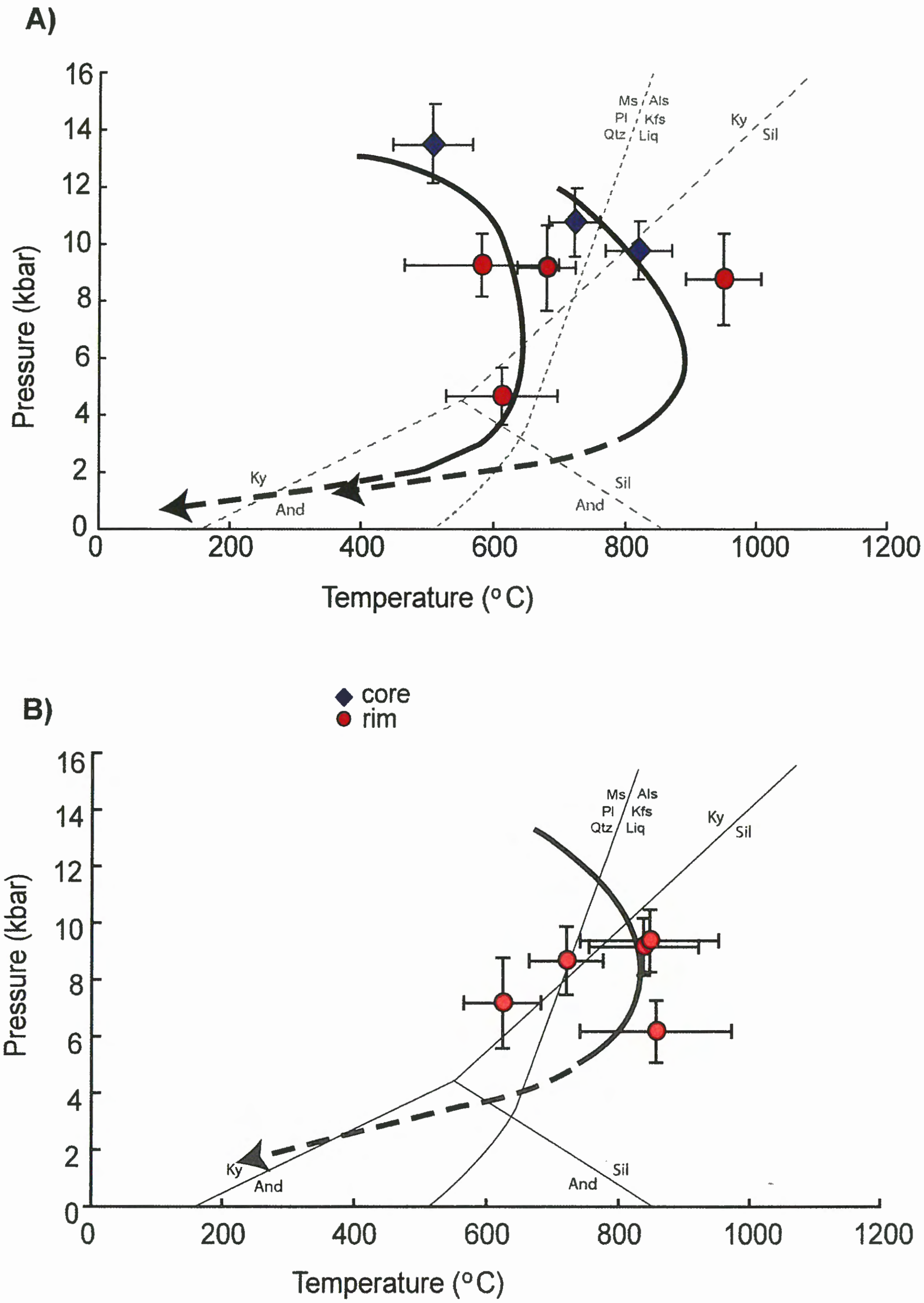

Figure 3.8: P-T data for the HSL. a) P-T data for metabasitic rocks from the HSL b) P-T data for metasedimentary rocks from the HSL. The position of the Al_2SiO_5 triple point isafter Pattison (1992), while the position of the muscovite melting curve is after the reference Pëto (1976) given in Pattison (2003).

core and inclusion compositions would suggest. Breakdown of garnet and matrix clinopyroxene to orthopyroxene and plagioclase is estimated at 8.8 ± 1 kbar, 950 ± 69 °C suggesting heating during early decompression.

3.2.4 MINERAL ASSEMBLAGES & CHEMISTRY: METASEDIMENTS

The following is a summary of the petrographical analysis carried out on the metasediments by David Moynihan during a summer work term in 2004. A summary of the mineralogy and mineral reaction textures is given in Tables 3.1 and 3.2.

Metasediments are compositionally banded with alternating leucocratic (cordierite + plagioclase + quartz ± K-feldspar ± spinel) and melanocratic (biotite + sillimanite ± spinel ± orthopyroxene ± orthoamphibole) layers. The most commonly observed assemblage is garnet + biotite + plagioclase + sillimanite ± K-feldspar ± kyanite; depending on the bulk chemistry orthopyroxene + orthoamphibole may also be present (Figure 3.9). Accessory minerals include tourmaline, hercynite, rutile, ilmenite, magnetite and titanite.

In samples with orthopyroxene, garnets are large (i.e. ≥ 3 mm) and have marked zoning profiles with outward increases in Pyr, and concomitant decreases in Alm and Grs. Close to the rim there is a Grs plateau (7-8%) followed by a sharp drop at the rim (Figure 3.6; Appendix D). Sps proportions are low in garnet core regions, decrease outwards, and then increase dramatically at the rim. The small-scale reversal/plateau in Grs is interpreted as a growth-zoning feature, and is supported by its euhedral form and truncation along irregular, resorbed crystal boundaries. The outward increase in Pyr and decrease in Sps is also interpreted to reflect prograde growth zoning. Based on diffusion coefficients calculated at 850°C, it should take less than ~ 2 Myr for Fe-Mg exchange to penetrate 3 mm into a garnet grain (Chakraborty and Ganguly 1992; O'Brien 1997). This implies that in the event a small garnet (i.e. < 3 mm) is subjected to temperatures above 800°C, the Fe-Mg growth profile will be completely overprinted and homogenized in less than 2 Myr. The local preservation of garnet growth zoning in metasediments of the HSL may, therefore, be a consequence of their large grain size (> 3 mm), or a short residence time at high temperatures. A marked decrease in Pyr and increase in Sps at the rims reflects garnet consumption and back-diffusion during retrograde net-transfer reactions (e.g. Kohn and Spear 2000).

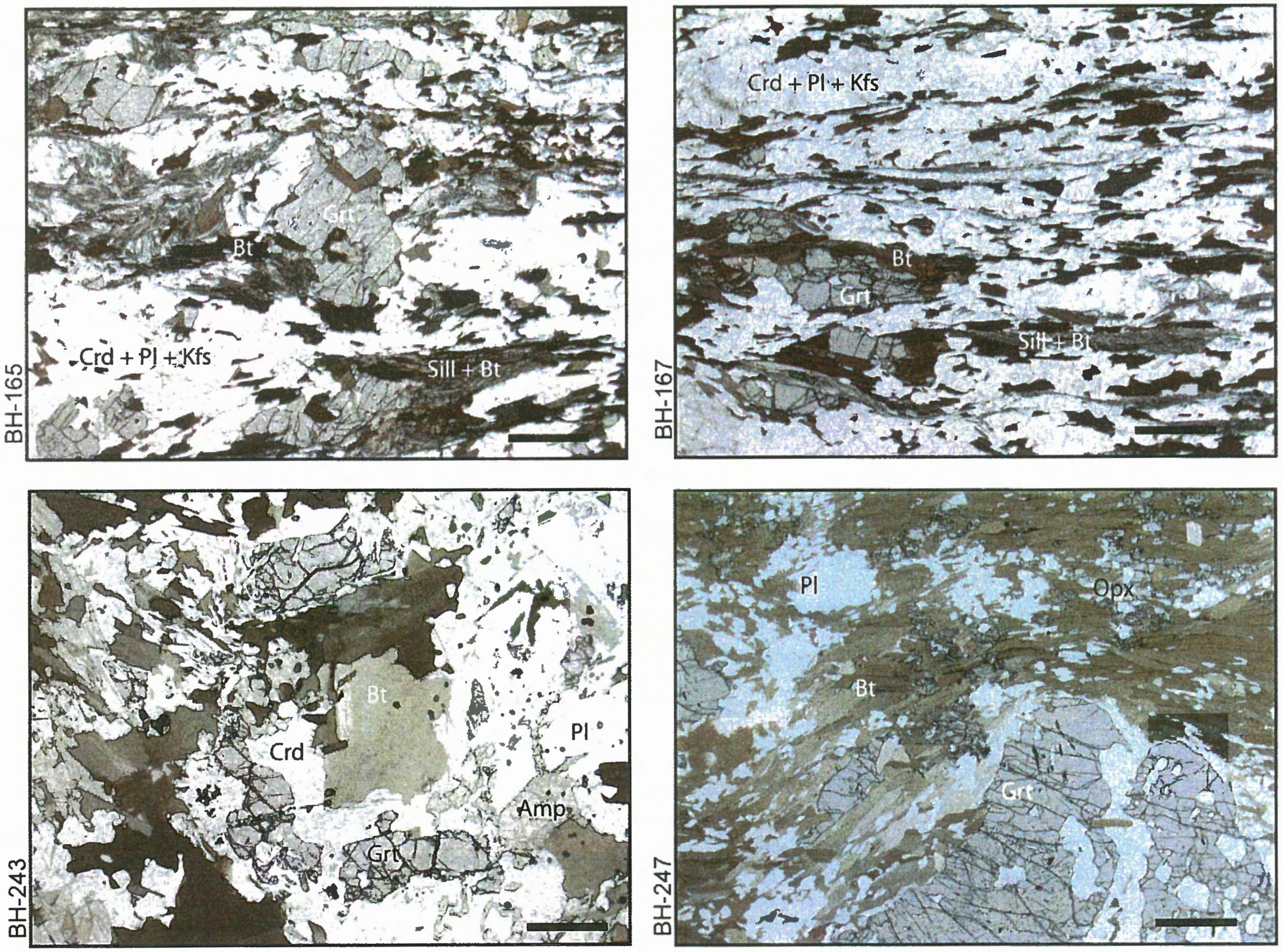

Figure 3.9: Photomicrographs of metasediments from the HSL. Micrographs were taken at 1.6x magnification such that the total field of view is ~ 7.5 mm. The length of the scale bar in the bottom right corner of each photomicrograph marks 1 mm. ***Grt,*** garnet; ***Amp,*** amphibole; ***Opx,*** orthopyroxene; ***Bt,*** biotite; ***Pl,*** plagioclase; ***Kfs,*** potassium feldspar; ***Pl,*** plagioclase; ***Crd,*** cordierite.

The absence of muscovite in the high and mid-structural levels, the pervasive presence of leucogranites and the presence of kyanite inclusions in garnet (BH-247) suggests that kyanite was part of an earlier peak pressure assemblage and may have formed during muscovite-dehydration melting according to a reaction of the form (Figure 3.7):

$$\mathrm{Ms} + \mathrm{Qtz} \pm \mathrm{Pl} \rightarrow \mathrm{Ky} + \mathrm{Kfs} + \mathrm{Liq} \quad \mathbf{(3.4)}$$

That kyanite is only found as inclusions in garnet implies that garnet grew during or after production of kyanite, possibly as a result of a continuous reaction such as:

$$\mathrm{Bt} + \mathrm{Ky} + \mathrm{Qtz} \pm \mathrm{Pl} \rightarrow \mathrm{Grt} + \mathrm{Kfs} + \mathrm{Liq} \quad \mathbf{(3.5)}$$

which may partially account for the absence of kyanite in the matrix. Where present, plagioclase inclusions in garnet are calcic (An_{80}). Where orthopyroxene is present in the matrix, garnets have been overgrown and replaced by biotite and plagioclase, by the reaction (O'Brien 1999):

$$\mathrm{Grt} + \mathrm{Kfs} + \mathrm{Liq} \rightarrow \mathrm{Bt} + \mathrm{Pl} \quad \mathbf{(3.6)}$$

In these samples, matrix plagioclase grains are markedly zoned with cores that are depleted in Ca (An_{50}) relative to the rims (An_{80}). Grains with moderately calcic cores (An_{50}) are restricted to areas where biotite and plagioclase have completely replaced garnet, however, plagioclase adjacent to garnet is commonly more calcic. The observed zoning pattern is interpreted to reflect growth of increasingly calcic plagioclase during progressive garnet breakdown, which releases Grs (garnet–aluminosilicate–plagioclase–quartz (GASP) reaction). Biotite is chemically homogeneous with Ti ranging between 0.28 – 0.34 and Mg numbers ranging between 0.7 – 1.7 (Appendix C).

Locally, orthopyroxene is found in the melanocratic layers, where it is typically adorned with reaction rims dominated by orthoamphibole and magnetite (Bh-243, 247). The presence of orthopyroxene in metapelitic rocks implies granulite-facies metamorphism. It typically develops during the dehydration of biotite by reactions with the general form (Figure 3.7; Yardley and Valley 1997; Spear et al. 1999):

Bt + Grt + Qtz ± Pl → Opx + Sil + Liq ± Kfs **(3.7)**
or
Bt + Grt + Qtz ± Pl → Crd + Opx + Liq ± Kfs **(3.8)**
or
Bt +Qtz ±Pl → Opx + Liq ± Grt ± Crd ± Kfs **(3.9)**

These reactions have steep positive slopes in P-T space and indicate temperatures of 800 -900 °C in the pressure interval 1-15 kbar (Spear 1993; Pattison et al. 2003). At pressures less than 9 kbar, cordierite develops downgrade of orthopyroxene by the reaction (Figure 3.7; Spear et al. 1999):

Bt +Sil + Qtz ± Pl → Grt + Crd + Liq ± Kfs **(3.10)**

Thus, the presence of orthopyroxene suggests that the peak P-T conditions in the HSL were above 800 °C and 9 kbar. Orthopyroxene rules out very high pressures (i.e. > 11 kbar; O'Brien and Rötzler 2003), thus the preservation of kyanite inclusions in one sample also containing matrix orthopyroxene (BH-247) implies that peak pressure conditions preceded the growth of orthopyroxene. Co-existence of orthopyroxene with sillimanite in the matrix indicates that high-temperature metamorphism took place at moderately high pressures between 6 – 10 kbar (Spear 1993), following peak pressure conditions.

In samples lacking orthopyroxene, garnets are small (≤ 2 mm) and are not zoned except at the rims, which have higher Alm and Sps, and lower Pyr than the remainder of the grain (Figure 3.6). The absence of marked zoning in combination with a decrease in Mg and increase in Mn concentrations at the rims, suggests garnets were internally homogenized, with zoning at the rims resulting from late diffusive exchange between garnet and the matrix minerals. Many of the garnet grains are strongly resorbed and partially replaced by biotite and sillimanite, probably reflecting interaction with melt according to the reaction:

Grt + Kfs + Liq = Bt + Sil **(3.11)**

Matrix biotite grains are chemically homogeneous and characterized by Mg numbers ranging between 0.42 - 0.46, while biotite inclusions are distinguished from matrix grains by slightly higher Mg numbers. Matrix plagioclase is homogeneous and relatively sodic (An_{27-30}). Biotite masses in the matrix of these samples are overgrown by sillimanite ±

chlorite, which together define the main, pervasive planar fabric (S_2) observed in all thin sections. Garnet with matrix biotite, sillimanite, plagioclase ± K-feldspar is interpreted to represent the peak temperature assemblage in the orthopyroxene-absent rocks.

In both rock types, cordierite + quartz + plagioclase + K-feldspar coronas, or less commonly, symplectic intergrowths of quartz + spinel + cordierite separate garnet grains from the surrounding biotite + sillimanite ± orthopyroxene matrix which defines the pervasive fabric. There is strong textural evidence for the replacement of garnet, biotite, sillimanite and orthopyroxene by cordierite. Spinel is locally observed in spinel-quartz symplectites rimming garnet, suggesting cordierite and spinel were produced by the reaction with the form (Figure 3.7; O'Brien 1999):

$$\mathrm{Grt + Bt + Sil \rightarrow Crd + Spl + Qtz} \quad \textbf{(3.12)}$$

According to the grid of Spear et al. (1999), this reaction has a steep negative slope and requires the breakdown of garnet, biotite and sillimanite on cooling and/or decompression (associated with M_3?) at relatively high temperatures (i.e. ≥ 700 °C; Hollister 1982; Neogi et al. 1998). The retrogression of biotite to sillimanite followed by chlorite, and orthopyroxene to cordierite and orthoamphibole in these samples suggests the influx of fluids, or fluid expulsion of fluid from crystallizing melt in the sillimanite stability field.

3.2.5 P-T ESTIMATES: METASEDIMENTS

Average P-T estimates for metasediments and metabasites were calculated with the mineral data presented in Appendix C using Thermocalc v. 3.25, a thermobarometric program which uses the internally consistent thermodynamic database of Holland and Powell (1998). P-T calculations made using garnet rim compositions with kyanite and matrix compositions of biotite, sillimanite and plagioclase yields an estimate of 721 ± 56°C and 8.7 ± 1.2 kbar (BH-247). Calculations made on garnet rim and matrix assemblages in BH-243 indicate that the breakdown of garnet to biotite, sillimanite and orthopyroxene occurred at temperatures > 800°C and pressures of ~ 9 kbar (Table 3.3). A lower pressure estimate of 6 kbar was obtained from BH-165, using compositions of the post-peak assemblage that developed during decompression. This pressure, which lies within the sillimanite stability field, is consistent with the mineralogy and it is likely the P-T estimates represent the retrograde, post peak-temperature portion of the metamorphic history rather than the peak P or T. As is illustrated in the garnet profiles,

Table 3.3: Summary of P-T data calculated from metasediments and metabasites from the MSL and HSL of the GHS, northwestern Bhutan.

			Temperature	±	Pressure	±	Comments
	Metabasites						
	BH-173	core	690	48	7.5	1.4	lrg g core-incl assem
	BH-173	rim	709	78	7.9	1.8	lrg g rim- mtx assem
MSL	BH-173	rim	609	61	5.7	1.4	sml g rim-mtx
	BH-175	rim	744	78	7.5	1.4	rim-mtx assembl
	BH-292	core	666	49	7.2	1.2	core-incl assembl
	BH-292	rim	764	57	8.6	1.3	rim-mtx assembl
	Metabasites						
	BH-217	core	722	39	10.8	1.2	core+mtx less opx
	BH-217	core	820	51	9.8	1	core-incl assembl
	BH-217	rim	950	69	8.8	1.2	rim-mtx assembl
	BH-219	core	508	60	13.5	1.33	core-incl assem
	BH-219	matrix	680	44	9.2	1.5	mtx less g rim
	BH-219	rim	582	50	9.3	1.1	rim-mtx less opx
HSL	BH-219	rim	613	35	4.7	1.33	mtx less cpx
	Metasediments						
	BH-165	rim	858	116	6.2	1.1	
	BH-243	rim	839	84	9.2	1	grt rim - mtx ass
	BH-243	rim	625	58	7.2	1.6	grt rim -mtx ass less crd
	BH-243	rim	848	106	9.4	1.1	grt rim -mtx ass less oamp
	BH-247	rim	721	56	8.7	1.2	grt rim-mtx ass + ky

rocks in the HSL were subject to high temperatures long enough to allow for post-peak diffusion to homogenize garnet zoning profiles, suggesting the P-T estimates presented here may be minimum estimates for peak metamorphism in the HSL. The large error values associated with the temperature estimates for these rocks may also be a consequence of the post-peak diffusion between minerals, meaning mineral assemblages no longer retain peak temperature equilibrium compositions.

3.3 MID-STRUCTURAL LEVEL (MSL)

At what appears in map view to be the mid-structural levels of the GHS (Figure 3.1), three metabasites were sampled from what appeared to be discontinuous layers that were encompassed by sillimanite + muscovite metasediments. The following is a detailed description of these samples, which is presented in a similar format to the description given for samples collected from the higher-structural level.

3.3.1 MINERAL ASSEMBLAGES & CHEMISTRY: METABASITES

Garnet amphibolites collected from the mid-structural levels of the GHS have the mineral assemblage garnet + amphibole + plagioclase + quartz + biotite ± K-feldspar (Figure 3.10) with accessory rutile, titanite, apatite, ilmenite, magnetite and zircon. A summary of the mineralogy is given in Table 3.1 and a summary of mineral reaction textures can be found in Table 3.2. In two of the three samples, garnet grains are large (> 2 cm), subhedral, and have texturally distinct cores and rims suggesting garnet growth occurred during two distinct phases. Inclusion-rich cores are compositionally similar to inclusion-free rims ($Alm_{57-61}Py_{22-25}Grs_{13-18}Sps_{0.7-2.8}$). Except for chemical irregularities proximal to inclusions, garnet profiles are relatively flat (Figure 3.6; Appendix D). A bell curve distinguishes the spessartine profile for the inclusion-rich core of BH-173, suggesting temperatures at the MSL of the GHS may not have been high enough (i.e. > 700°C), or that rocks were not subjected to high temperatures long enough, to homogenize large garnets completely. Chemical homogenization in small garnets (i.e. < 1 mm) of BH-173 is apparent, with increases in Fe, Mg and Mn at the rims probably resulting from late diffusive exchange between garnet and matrix minerals.

Cores of the large garnets commonly contain randomly oriented inclusions and varying proportions of plagioclase, anthophyllite-gedrite, tschermakitic amphibole, quartz, ilmenite ± rutile, titanite and a trace amount of orthopyroxene. Inclusions of

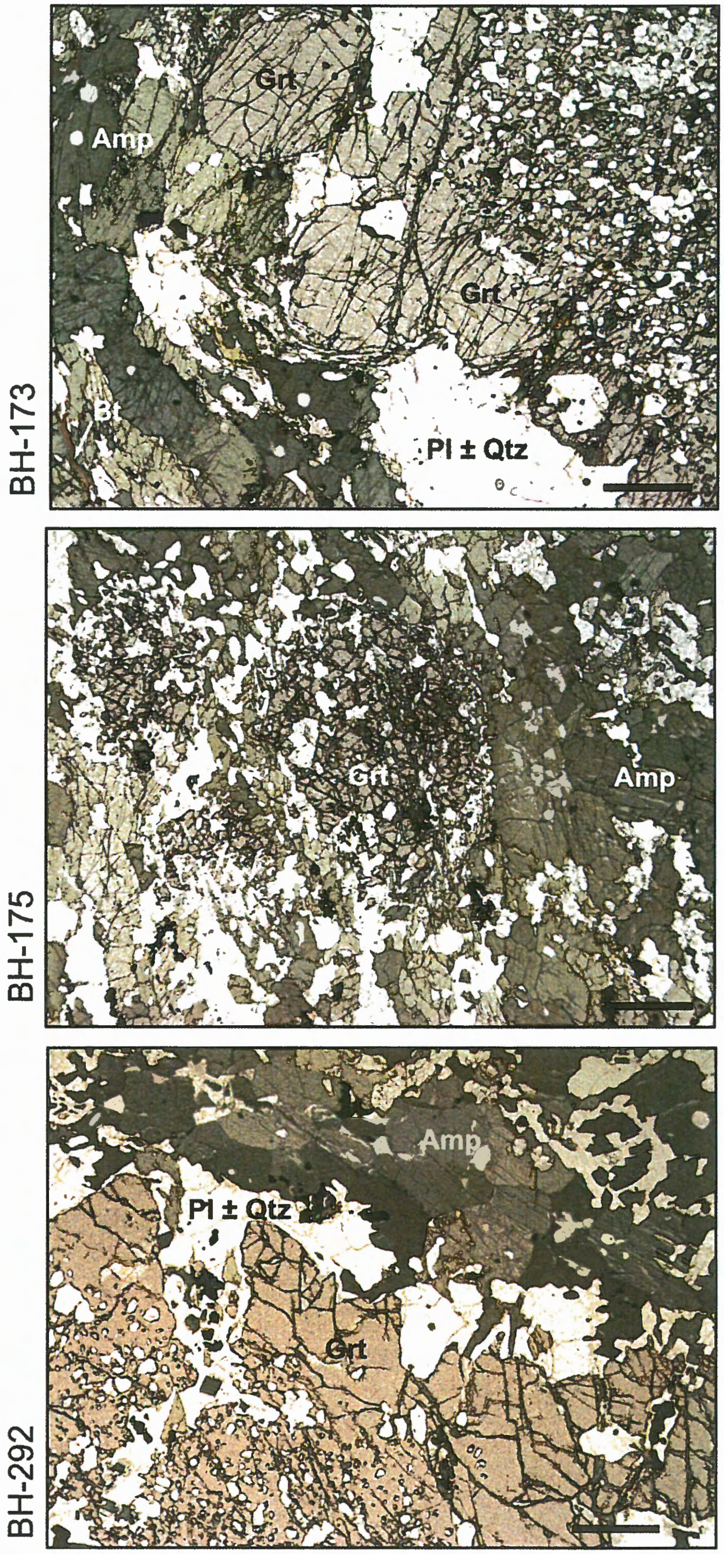

Figure 3.10: Photomicrographs of metabasites from the MSL. Micrographs were taken at 1.6x magnification such that the total field of view is ~ 7.5 mm. The length of the scale bar in the bottom right corner of each micrograph marks 1 mm. ***Grt,*** garnet; ***Amp,*** amphibole; ***Bt,*** biotite; ***Pl,*** plagioclase.

tschermakitic amphibole are commonly more enriched in Al (~ 2.5) relative to tschermakitic amphiboles in the matrix (~ 1.8). In sample BH-292, plagioclase inclusions are anorthitic (An_{82}) and lack chemical zoning, while those in BH-173 are zoned with distinct cores (An_{52}) and rims (An_{75}). Orthoamphibole + tschermakitic amphibole + plagioclase are interpreted to represent the relict assemblage from which the garnet + orthopyroxene + plagioclase assemblage formed (reaction 6 above), as temperatures increased. In sample BH-173, coronas of quartz + plagioclase ± antiperthite separate garnet poikiloblasts from the matrix. Highly calcic plagioclase (An_{81-89}) in the corona suggests net transfer of Ca from garnet to plagioclase during decompression. This is not the case in BH-292, where plagioclase in coronas is less anorthitic (An_{53}) than inclusions in garnet. The matrix in all three samples comprises tschermakitic amphibole intergrown with biotite, ilmenite, quartz and plagioclase which probably grew at the expense of garnet, orthopyroxene and plagioclase as temperatures dropped (reversed form of reaction 10). The retrogression of amphibole and biotite to orthoamphibole followed by chlorite suggests a decrease in temperature.

3.3.2 P-T ESTIMATES

Average pressure - temperature (P-T) estimates were made with the mineral data presented in Appendix C. Estimates made on core compositions of large garnets in combination with plagioclase and amphibole inclusions yield P-T estimates with relatively large errors, probably the consequence of chemical disequilibrium. Core assemblages yielded temperatures of 666 ± 49 °C and pressures of 7.2 ± 1.2 kbar (BH-292), and 690 ± 48°C, 7.5 ± 1.4 kbar (BH-173; Table 3.3; Figure 3.11). Large garnet rim compositions in combination with matrix amphibole and plagioclase yield estimates of 764 ± 57 °C, 8.6 ± 1.3 kbar and 744 ± 78 °C, 7.5 ± 1.4 kbar for samples BH-292 and -175 respectively (Table 3.3; Figure 3.11), and are probably representative of conditions along the decompression and cooling segment of the P-T path.

3.4 GEOCHRONOLOGY

In an attempt to understand the timing of high-temperature metamorphism in the metabasites, U-Pb analyses were conducted on zircon separates. To estimate the timing of low temperature metamorphism on decompression, $^{40}Ar/^{39}Ar$ analyses were conducted

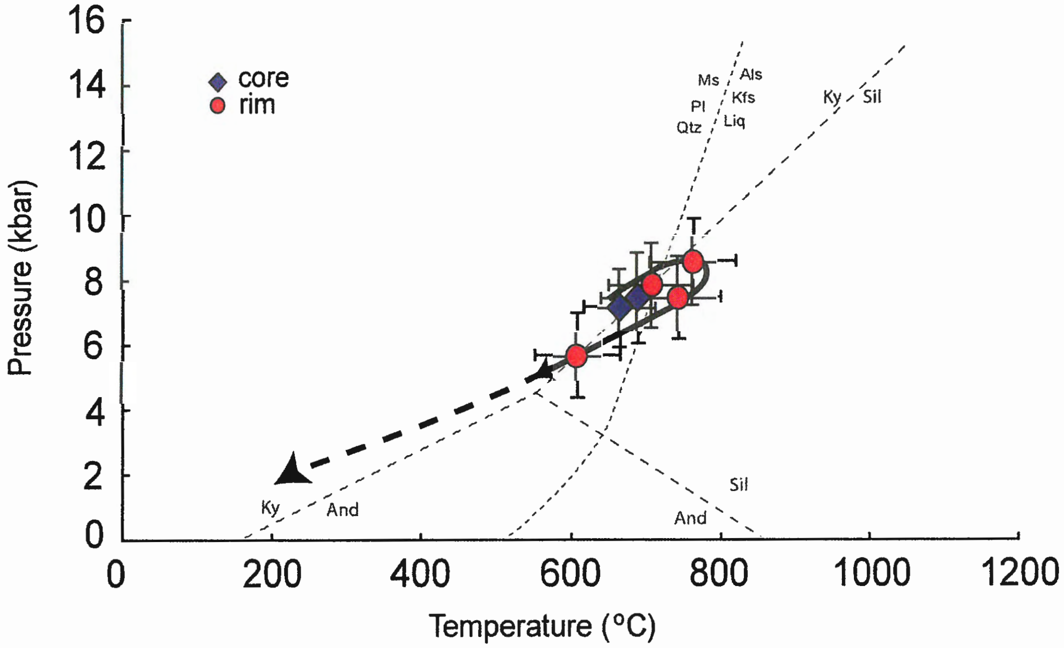

Figure 3.11: P-T data for the MSL. P-T estimates and associated errors calculated for three meta-basic samples from the MSL. The position of the Al_2SiO_5 triple point is after Pattison (1992), while the position of the muscovite melting curve is after the reference Pëto (1976) given in Pattison (2003).

on amphiboles and biotite separated from the metabasites. Where possible, $^{40}Ar/^{39}Ar$ data for biotite from metasediments were also yielded for comparison purposes.

3.4.1 SIMS U-Pb GEOCHRONOLOGY: ZIRCONS

Zircon fractions were separated from two metabasic samples of the HSL suite (BH-217, 219), and one sample from the MSL suite (BH-292) using standard heavy liquid and Frantz magnetic separation techniques. Individual zircons were handpicked, mounted, polished and coated with gold prior to analysis. Individual spot analyses were made with the Cameca IMS 1270 in the Secondary Ion Mass Spectrometry Laboratory at the Centre de Recherches Pétrographiques et Géochimiques in Vandœuvre lès Nancy (CRPG-Nancy), France following the technique of Deloule et al. (2002).

Though generally rare to find in mafic rocks, detailed petrographic analysis and X-ray mapping of the three metabasites in this study indicate that euhedral zircons are associated with matrix amphibole and less commonly as inclusions in garnets. Zircon inclusions in garnet are small (≤ 100 μm), while matrix grains are variable in size (~ 2 mm ~ ≤ 100 μm). The majority of zircons analysed for this study were approximately 100 μm in length. Cathodoluminescene (CL) images show zircons with dark cores and others with luminescent cores (Figure 3.12). In two of the samples (BH-217, 219) CL imaged dark cores correspond to inclusion-rich, 'spongy' sections in BSE images, which are interpreted as remnant igneous zircons. Luminescent cores, on the other hand, show no unique chemical or morphological features. Zircon rims in all samples are characterized by a lack of systematic zoning patterns, but rather preserve diffuse and irregular zoning.

Analytical data are presented in Table 3.4 where $^{206}Pb/^{238}U$, $^{207}Pb/^{235}U$ and $^{207}Pb/^{206}Pb$ ages are reported with their 2σ uncertainties. A histogram of individual rim and core analyses (Figure 3.13) illustrates the preservation of three age populations in the zircons. Relict igneous cores commonly preserve Proterozoic ages (~ 1000 ~ 1700 Ma; Chapter 2), while grains with dark CL cores that lack the relict igneous texture tend to preserve Paleozoic ages (~ 800 ~ 300 Ma). Grains preserving Proterozoic cores may have been inherited from the host rocks during magmatic emplacement or may represent the timing of magmatic crystallization of the metabasic suite of rocks (refer to Chapter 2) and are not discussed further here. Paleozoic ages preserved in the cores of a select few

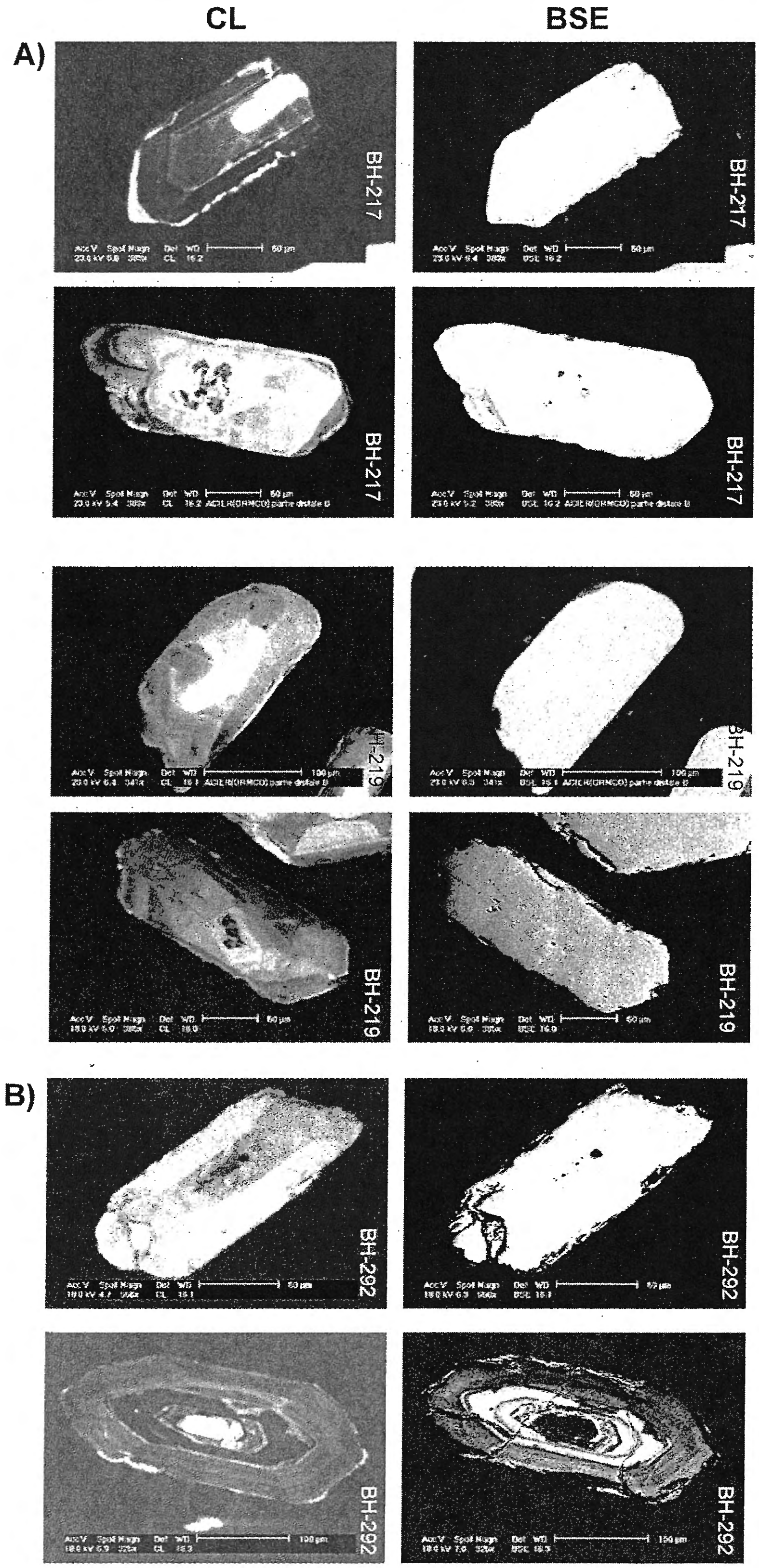

Figure 3.12: Cathodoluminescence (CL) and backscatter(BSE) images of zircons from a) BH-217 and -219 in the HSL, and b) BH-292 from the MSL.

Table 3.4: U-Pb isotopic data for analyzed zircons

							Atomic Ratios						Apparent Ages (Ma)					
Analysis		U ppm	Pb ppm	^{206}Pb/^{204}Pb	^{206c}Pb/^{206}Pb (%)	Th/U	^{206}Pb/^{238}U	± (1σ)	^{207}Pb/^{235}U	± (1σ)	^{207}Pb/^{206}Pb	± (1σ)	^{206}Pb/^{238}U	± (2σ)	^{207}Pb/^{235}U	± (2σ)	^{207}Pb/^{206}Pb	± (2σ)
bh217-15a@8	rim	1016	256.1	34976	0.05	1.813	0.29341	0.00433	4.44052	0.065876	0.11004	0.000156	1658.6	21.5	1719.9	12.2	1795.5	2.8
bh217-16b@11	core	918	188.5	111892	4.87	1.75	0.23898	0.006119	3.50978	0.091089	0.10653	0.000445	1381.4	31.8	1529.4	20.3	1740.6	7.8
bh217-1a@15	core	974	148.6	141638	0.01	1.108	0.1776	0.006373	2.44356	0.089058	0.09979	0.000631	1053.8	34.8	1255.5	25.9	1620.2	11.8
bh217-10a@33	core	3614	509.5	13926	0.11	1.067	0.16409	0.002387	1.9928	0.029359	0.08899	0.00018	979.5	13.2	1113.1	9.9	1384.2	4.5
bh217-11b@36	core	1067	69.5	3339	0.47	0.688	0.07579	0.001264	0.89151	0.019622	0.08941	0.001069	470.9	7.6	647.2	10.5	1322.8	27.6
bh217-12b@40	core	1281	91.1	5588	0.28	0.284	0.0828	0.001646	0.80098	0.017179	0.07263	0.000244	512.8	9.8	597.4	9.6	933	16.5
bh217-13a@51	core	1250	53.4	1033	1.81	1.479	0.04971	0.001059	0.4443	0.020416	0.07859	0.001207	313	6.5	373	14.3	—	—
bh217-9a@30	core	131	0.285	6634	0.24	0.051	0.00253	0.000078	0.01834	0.00319	0.05477	0.001705	16.3	0.5	18.4	3.2	—	—
bh217-11a@35	rim	230	0.53	-5114	0	0.008	0.00268	0.000067	0.01884	0.001736	0.04803	0.001325	17.3	0.4	19	1.7	—	—
bh217-12a@39	rim	289	0.723	1512	1.04	0.007	0.00291	0.000065	0.01518	0.001977	0.04751	0.001247	18.7	0.4	15.3	2	—	—
bh217-16a@10	rim	275	0.556	1833	0.86	0.007	0.00235	0.000066	0.01415	0.002476	0.05155	0.001117	15.1	0.4	14.3	2.5	—	—
bh217-2a@18	rim	1138	2.4	787.9	2	0.019	0.00247	0.000076	0.01417	0.00136	0.06021	0.001538	15.9	0.5	14.3	1.4	—	—
bh217-6b@24	rim	6484	16.7	23512	0.07	0.069	0.00299	0.000046	0.01936	0.000568	0.04749	0.000466	19.3	0.3	19.5	0.6	—	—
bh217-7a@26	rim	2832	7.9	15584	0.1	0.039	0.00324	0.000051	0.02149	0.000679	0.04899	0.000559	20.9	0.3	21.6	0.7	—	—
bh217-8b@29	rim	295	0.68	2228	0.71	0.008	0.00268	0.000065	0.01589	0.001611	0.04955	0.001278	17.2	0.4	16	1.6	—	—
bh217-9b@31	rim	1907	4.9	17083	0.09	0.022	0.00298	0.000053	0.01887	0.00134	0.04676	0.00089	19.2	0.3	19	1.3	—	—
bh217-14a@53		7181	9	-5079.3	0	0.052	0.00147	0.000024	0.01034	0.000444	0.04822	0.000588	9	0.2	10	0.4	—	—
bh219-6a@63	core	1133	177.7	365477	0	0.312	0.18258	0.004097	2.65258	0.062021	0.1053	0.000691	1081	22.3	1315	17.1	1721	12
bh219-9a@71	core	307	21.2	61504	0	0.418	0.08035	0.001211	1.19097	0.018988	0.10761	0.000545	498	7.2	796	8.8	1757	9.5
bh219-7a@66	core	743	24	14772	0	0.103	0.03755	0.001356	0.52338	0.019257	0.10192	0.000653	238	8.4	427	12.8	1644	12.9
bh219-8a@68	core	275	8.4	210291	0	0.216	0.03561	0.002212	0.51252	0.032316	0.10435	0.001062	226	13.8	420	21.5	1704	19.7
bh219-1b@57	rim	638	1.7	4090	0	0.006	0.00312	0.000065	0.03365	0.003936	0.0815	0.005739	20	0.4	34	3.9	—	—
bh219-7b@67	rim	340	0.549	326	0.06	0.004	0.00188	0.000052	0.01666	0.002839	0.10792	0.003575	12	0.3	17	2.8	—	—
bh219-8b@69	rim	168	0.309	4395	0	0.003	0.00215	0.000045	0.0135	0.001661	0.04889	0.00132	14	0.3	14	1.7	—	—
bh219-9b@72	rim	277	0.467	-4700	0	0.005	0.00196	0.000033	0.01379	0.001601	0.04785	0.00114	13	0.2	14	1.6	—	—
bh292-10a@85	core	25	2.3	113973	0	1.405	0.10779	0.00319	1.04314	0.036056	0.07024	0.00059	660	18.5	725	17.8	—	—
bh292-11a@87	core	10.4	0.789	44.7	0.42	0.751	0.08855	0.00876	0.43269	0.355665	0.36518	0.011398	547	51.7	365	225.2	—	—
bh292-9b@78	rim	1164	46.2	4150	0	0.214	0.04621	0.001156	0.32106	0.008512	0.05383	0.000136	291	7.1	283	6.5	—	—
bh292-6b@81	rim	9854	75.5	326	0.06	0.066	0.00892	0.000517	0.0504	0.005564	0.08592	0.002503	57	3.3	50	5.4	—	—
bh292-6a@80	core	681	2.1	15944	0	0.028	0.00363	0.000069	0.02399	0.000778	0.04873	0.000395	23	0.4	24	0.8	—	—
bh292-13a@4	rim	8827	17.3	4108	0.38	0.039	0.00229	0.000035	0.0148	0.000518	0.05044	0.000803	14.7	0.2	14.9	0.5	—	—
bh292-13b@5	core	5989	20.1	15166	0.1	0.076	0.00391	0.00006	0.02564	0.000565	0.04852	0.00049	25.1	0.4	25.7	0.6	—	—
bh292-13c@7	rim	17205	49.6	13328	0.12	0.06	0.00335	0.000054	0.02111	0.000497	0.0467	0.000354	21.6	0.3	21.2	0.5	—	—

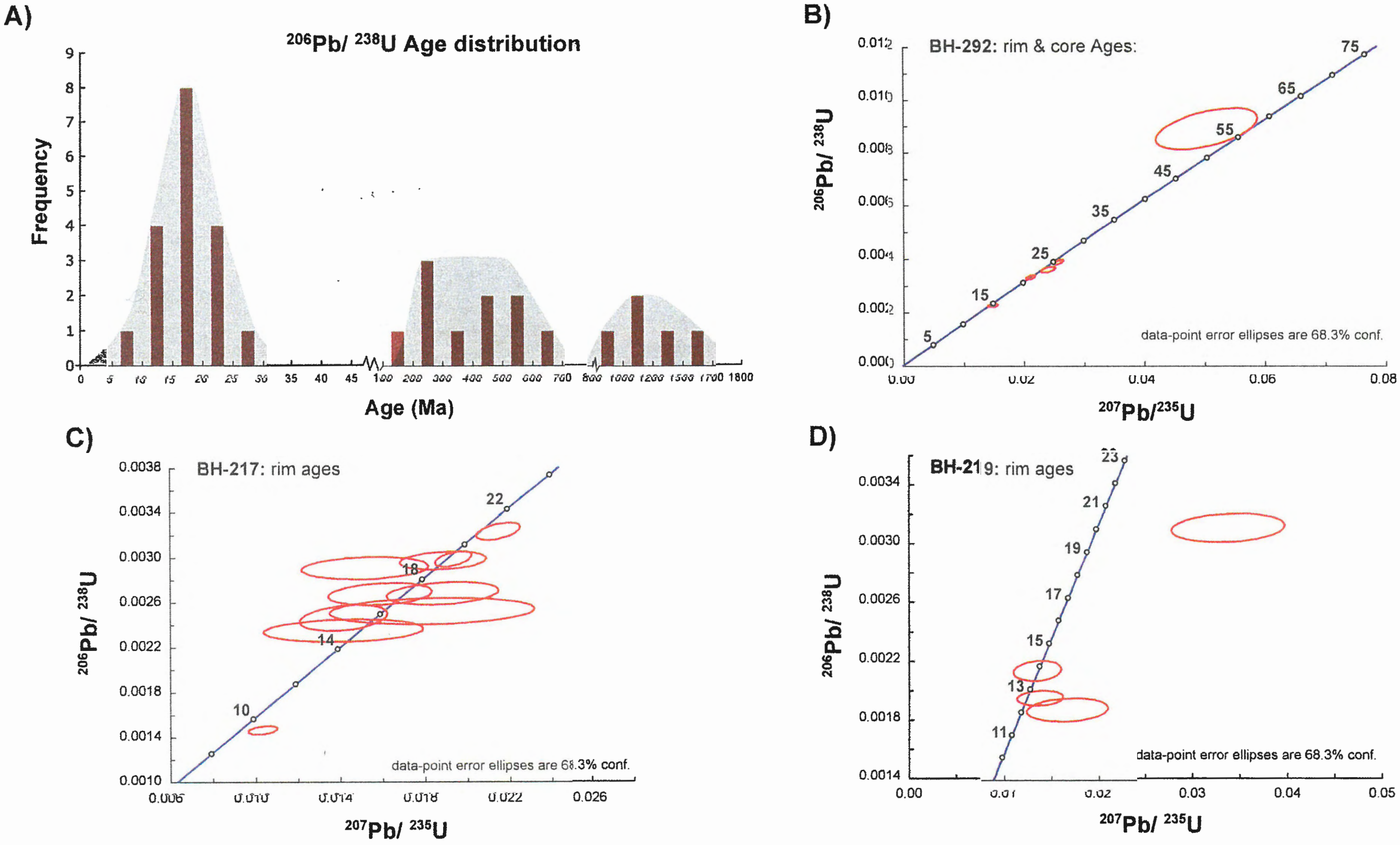

Figure 3.13: U-Pb zircon ages. a) Age distribution of zircon core and rim ages from three samples in the high- and mid-structural levels of the GHS. b) Concordia diagram for zircons from garnet amphibolite sample BH-292 from the MSL. c) Concordia diagram for zircons from pyroxene bearing garnet amphibolite sample BH-217 from the HSL. d) Concordia diagram for zircons from pyroxene-bearing garnet-amphibolite sample BH-219 also from the HSL.

grains may also represent magmatic crystallization of the metabasic suite or might be attributed to Pb- loss from initial igneous grains. The preservation of Paleozoic igneous and metamoprhic ages in zircons from the LHS, GHS and TSS elsewhere in the orogen (Miller et al. 2001; e.g. Gehrels et al. 2003; Myrow et al. 2003; Martin et al. 2005; Richards et al. 2006), suggests that the proto-Indian margin was affected by a regional tectonic event that either modified the chemistry of pre-existing zircons, or induced the growth of Paleozoic igneous and/or metamorphic zircons. Rims in all samples consistently preserve concordant Miocene ages (~ 25 to ~ 14 Ma; Table 3.4). Relatively low Th/U ratios (i.e. < 0.03; Table 3.4) in zircon rims suggest that they developed in the presence of anatectic melts formed by a low degree of partial melting (Williams et al. 1996) or at sub-solidus conditions (≤ 600 °C; Rubatto and Gebauer 2000).

3.4.2 ^{40}Ar/ ^{39}Ar GEOCHRONOLOGY

Samples for ^{40}Ar/^{39}Ar in this study were selected based on the presence of the K-bearing minerals hornblende, biotite, and muscovite. Final selection was based on the appearance of the K-bearing phases in thin section. Where possible, grains selected for analysis lacked alteration, and were not intergrown with any other phases that might contaminate the analysis. Mineral fractions were extracted using conventional magnetic and heavy liquid separation techniques followed by hand-picking. Separated mineral concentrates were wrapped in foil, then stacked in the irradiation canister along with aliquots of the flux monitor and the hornblende standard, MMhb-1 (Samson and Alexander 1987). Samples were irradiated in the McMaster University reactor. Isotopic analyses at Dalhousie University were made with a VG3600 mass spectrometer coupled to a double-vacuum tantalum resistance furnace. Unless specified otherwise, plateau ages were defined using the criteria outlined by Fleck et al (1977). Age data (Appendix E) are reported with their 2σ uncertainties and includes the uncertainty in the J parameter (Mitchell 1968), but not in the assumed age of the flux monitor (Merrihue and Turner 1966). For a more detailed, thorough discussion of the technical aspects that were followed here, refer to McDougall and Harrison (1988).

Amphibole and biotite ages and corresponding ^{37}Ar/^{39}Ar spectra for amphibole only, are presented in Figures 3.14 and 3.16. The ^{37}Ar/^{39}Ar spectrum plots permit the correlation of ^{37}Ar (Ca-derived) to ^{39}Ar (K-derived) ratios from the isotopic analyses with Ca/K ratios calculated from microprobe analyses (Appendix C).

Results: Higher Structural Level

Amphiboles from samples BH-217, -219 and -253 yielded moderately U-shaped argon spectra, with maximum ages recorded at low temperature steps in all three samples (Figure 3.14), implying the presence of excess argon. For BH-217, eleven increments contributing 95% of the total gas released define a mean age of 21.6 ± 0.3 Ma, and a minimum spectrum age at 16 ± 1 Ma. Isotope correlation analysis suggests an age of 17 ± 2 Ma and an initial ^{40}Ar/^{36}Ar value of ~ 650, substantially higher than the atmospheric value of 295.5 which further supports the presence of excess argon. Measured ^{37}Ar/^{39}Ar values correspond to the lower limit of values calculated from microprobe data. Biotite from the same sample yielded a slightly discordant spectrum, and a plateau age of 13.6 ± 0.7 Ma defined by seven increments over which 86% of the total gas was released (Figure 3.14).

For BH-219, not only is the amphibole spectrum U-shaped, but it is also highly discordant with several steps recording anomalously old ages (Figure 3.14). For this reason a mean age was not calculated. Measured ^{37}Ar/^{39}Ar values are lower then those calculated from microprobe data. Biotite from this sample also yielded a moderately U-shaped spectrum with maximum ages recorded in the low and high temperature steps (Figure 3.14). Three steps contributing over 94% of the total gas released define an anomalously old age of 55 ± 2 Ma.

The amphibole spectrum for BH-253 is slightly U-shaped (Figure 3.14), with maximum ages recorded in the low temperature steps and minimum ages recorded at higher temperatures. For the most part, measured ^{37}Ar/^{39}Ar values overlap with calculated values. A plateau age of 14.7 ± 0.8 Ma was calculated over four steps contributing 63% of the total gas released. Biotite from the same sample yielded a spectrum that is slightly discordant (Figure 3.14); ten steps contributing 80% of the total gas define a plateau age of 13.6 ± 0.4 Ma. As is discussed in section 3.2.4, amphiboles in the HSL metabasites formed by the hydration of clinopyroxene. The generation of U-shaped spectra for amphiboles from the three metabasites is therefore not unusual as fluid

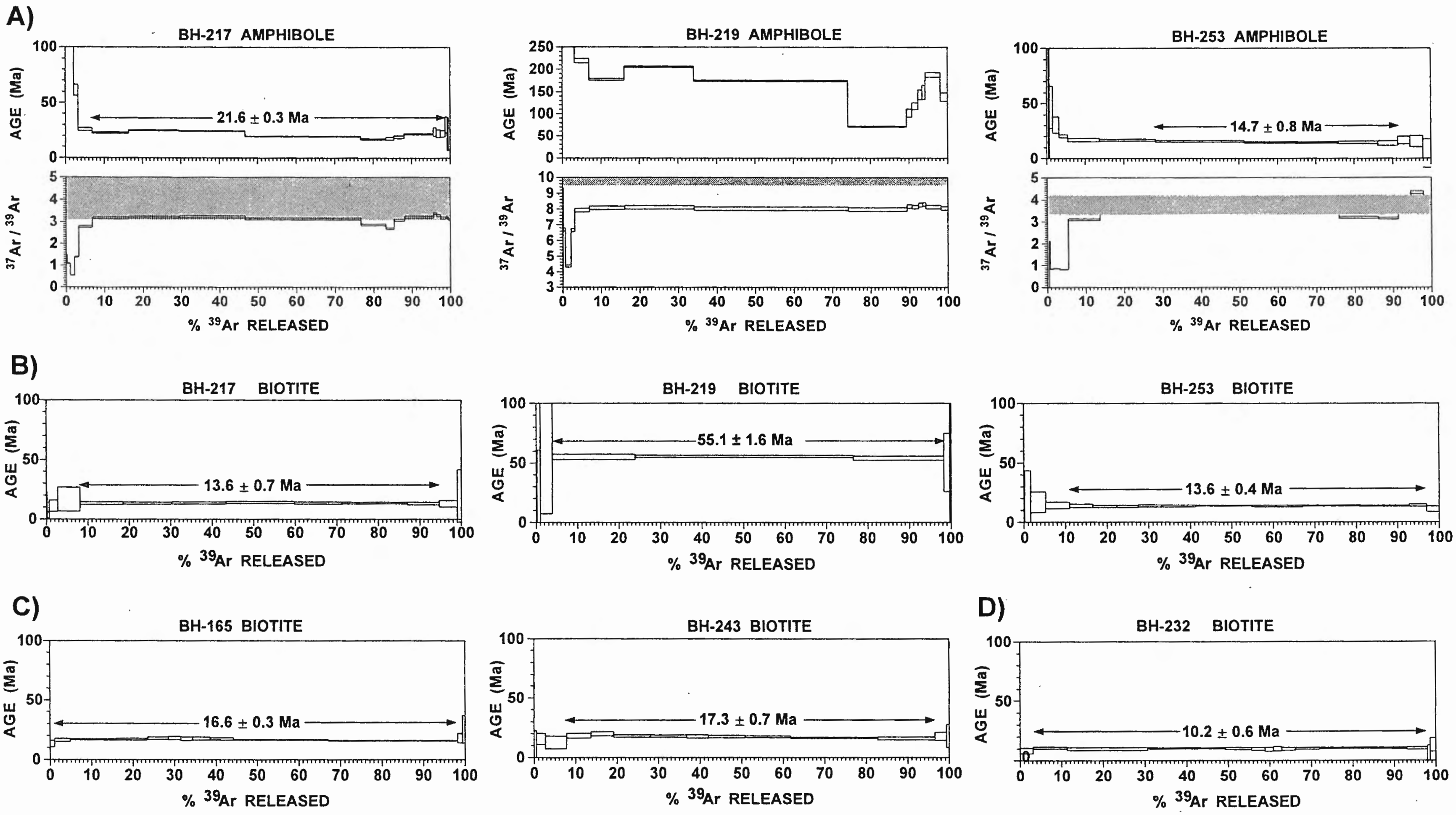

Figure 3.14: Argon data for the HSL. **A)** ^{40}Ar/^{39}Ar amphibole age spectra and corresponding ^{37}Ar/^{39}Ar spectra for metabasites from the higher structural levels. Shaded areas in the ^{37}Ar/^{39}Ar spectra indicate the range of Ca/K ratios calculated from microprobe data. **B)** Corresponding ^{40}Ar/^{39}Ar biotite age spectra for metabasites in Figure 3.12A. **C)** ^{40}Ar/^{39}Ar biotite age spectra for meta-sediments also in the high structural levels of the GHS. **D)** ^{40}Ar/^{39}Ar biotite age spectra for a leucogranite immediately below the STD.

associated with the hydration of clinopyroxene was a likely source of excess argon in these rocks.

For comparison purposes, biotites from two metasedimentary samples (BH-165 and -243) situated at approximately the same structural levels to the metabasites (Figure 3.2) were analyzed. Ten steps contributing 97% of the total gas released define a plateau with an age of 16.6 ± 0.3 Ma for BH-165. In the case of BH-243, 88% of the total gas released over seven steps defines a plateau with an age of 17 ± 0.9 Ma (Figure 3.14).

Structurally up-section, biotite from a Miocene leucogranite situated immediately below the STD (BH-232) yielded a spectrum in which twelve steps contributing 94% of the gas released define a mean age of 10.2 ± 0.6 Ma. The age calculated for this sample is the youngest biotite age obtained in this study.

A comparison of argon ages from metabasites with those from the metasedimentary rocks (Figure 3.15) reveals significant discrepancies among biotite and amphibole ages. Combined with the evidence for excess argon in the structure of the amphibole spectra, the lack of age correlations between samples further substantiates the evidence for excess argon in the highest structural levels of the GHS. Thus, with the exception of BH-232, the mean amphibole and biotite ages yielded from rocks at the highest structural level of the GHS probably represent maximum ages. The youngest age yielded from BH-232 is likely related to cooling of the late stage leucogranite.

Mid-Structural Level

Amphibole from sample BH-292 is characterized by a moderately U-shaped argon spectrum, with maximum ages recorded at low temperatures. The minimum spectrum age is ~ 14 Ma, but is not well defined. Measured $^{37}Ar/^{39}Ar$ values, however, are significantly lower then the values calculated from microprobe data, suggesting contamination by a high-K phase such as biotite (Figure 3.16). Biotite from the same sample yielded a concordant spectrum (Figure 3.16), in which eight increments contributing 90% of the total gas released defines a mean age of 12.6 ± 0.5 Ma.

A moderately discordant spectrum characterizes amphibole from sample BH-175. Seven steps over which 85% of the total gas was released define plateau with a mean age of 16.1 ± 0.7 Ma. Measured $^{37}Ar/^{39}Ar$ values correspond to the lower limit of values calculated from microprobe data. Biotite from the same sample yielded a highly

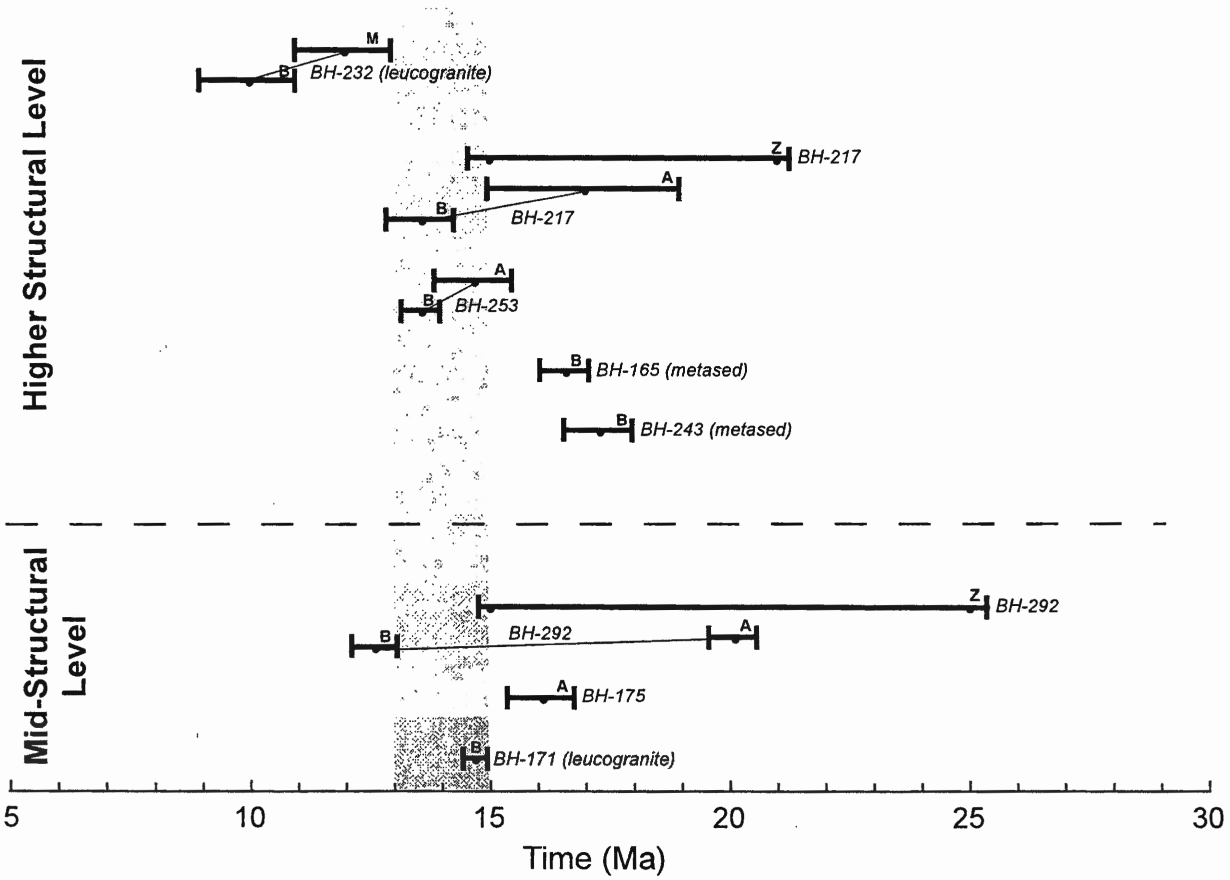

Figure 3.15: Age data comparison. A comparison of all the available age data for the higher- and mid-structural levels of the GHS in north-western Bhutan. Data points that are labelled with only the sample number are results from metabasites. In all other cases, the lithologies of the samples are indicated. **Legend:** ***Z,*** zircon; ***M,*** monazite; ***A,*** amphibole; ***B,*** biotite; ***grey bar,*** highlights the time span over which samples at both structural levels cooled through amphibole (500 ± 50 °C) and biotite (300 ± 50 °C) closure temperatures respectively.

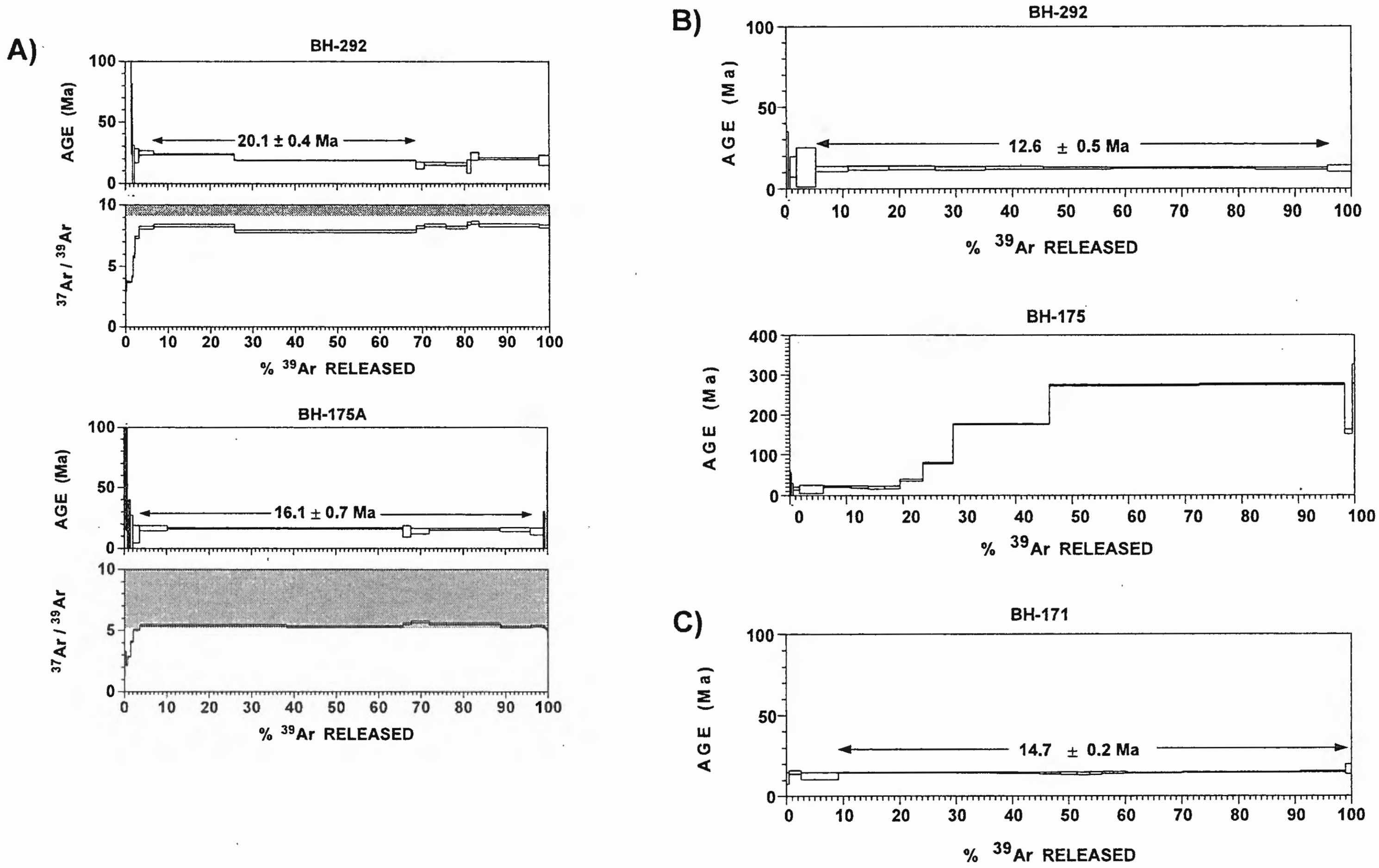

Figure 3.16: Argon data for the MSL. **A)** ^{40}Ar/^{39}Ar amphibole age spectra and corresponding ^{37}Ar/^{39}Ar spectra for metabasites from the apparent mid-structural levels. Shaded areas in the ^{37}Ar/^{39}Ar spectra indicate the range of Ca/K ratios calculated from microprobe data. **B)** Corresponding ^{40}Ar/^{39}Ar biotite age spectra for metabasites in Figure 3.14A. **C)** ^{40}Ar/^{39}Ar biotite age spectra for a leucogranite intruding into the surrounding metasediments.

discordant spectrum, therefore a mean age was not calculated. Biotite from a leucogranite (BH-171) that is interpreted to be Miocene in age yielded a concordant spectrum (Figure 3.16). A mean age of 14.7 ± 0.2 Ma was calculated over 11 steps contributing 89% of the total gas released.

The structure of the amphibole spectra combined with the discrepancy between amphibole and biotite ages for the samples implies the incorporation of excess argon in these samples. Thus, it is apparent that excess argon was not confined to the highest structural levels of the GHS, but rather extends down to at least the mid structural levels and that the ages presented for the mid-structural level may represent maximum ages.

3.5 DISCUSSION: P-T-t-d PATHS

3.5.1 HIGHER STRUCTURAL LEVEL

A summary of the P-T data presented in the earlier sections is given in Table 3.3. P-T estimates calculated from garnet core and inclusion compositions (plagioclase + orthoamphibole) in BH-219 coupled with the presence of kyanite included in a garnet of one metasedimentary sample implies that the peak garnet – clinopyroxene – plagioclase assemblage may have developed during burial and prograde metamorphism to ~ 13 kbar and 500°C. Estimates made on the peak pressure assemblage (garnet + clinopyroxene + plagioclase) in BH-217 suggest the assemblage persisted to a minimum of ~ 11 kbar and temperatures in excess of ~ 700°C. Breakdown of the peak pressure assemblage to orthopyroxene and plagioclase is estimated at ~ 9 kbar and ~ 950°C, and probably coincided with the development of the main planar fabric (S_2) that is observed in the metasediments. Flat zoning profiles through garnets indicate chemical homogenization of all garnets at this structural level. P-T estimates on garnet rim and matrix compositions suggest that breakdown of the peak assemblage to amphibole and plagioclase occurred between ~ 600 – 700°C at pressures of ~ 9 kbar. Replacement of orthopyroxene by orthoamphibole appears to have taken place at similar temperatures, but at pressures of 5-6 kbar. Figure 3.17 shows that the high temperature portion of the P-T path that best fits the data is a broad loop implying that rocks in the HSL decompressed at high temperatures prior to cooling. The near-isothermal decompression segment of the path for HSL samples supports what is evident from homogenized zoning

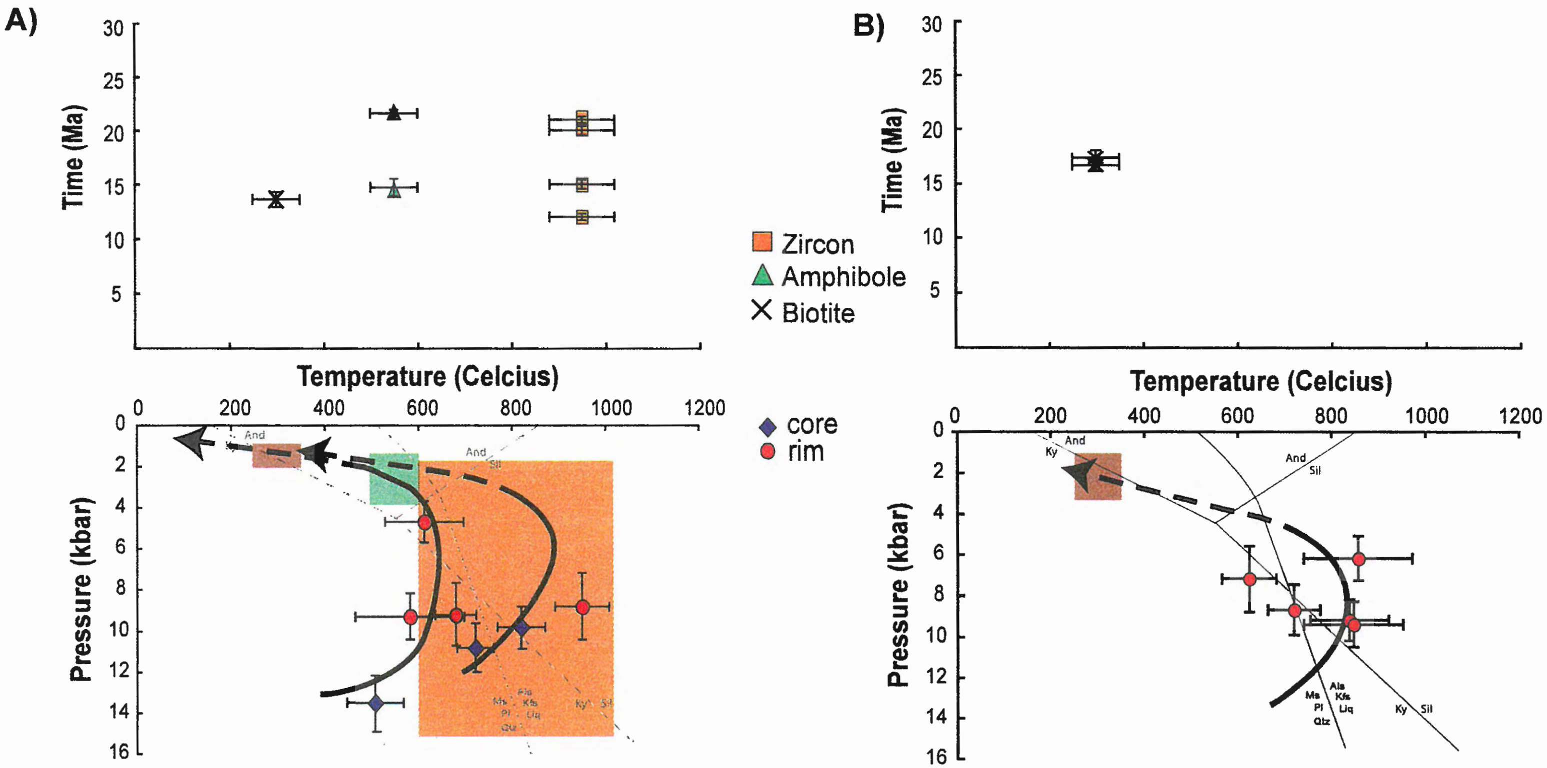

Figure 3.17: P-T-t data for the HSL. a) T-t and P-T data for metabasitic rocks from the HSL. Time data are a compilation of ages obtained on minerals separated from BH-217 and -219. b) T-t and P-T data for metasedimentary rocks from the HSL. Time data are a compilation of ages obtained on minerals separated from BH-165 and -243. The position of the Al_2SiO_5 triple point is after Pattison (1992), while the position of the muscovite melting curve is after the reference Pëto (1976) given in Pattison (2003).

profiles through garnet - that rocks in the HSL were subjected to elevated temperatures (> 800°C) for at least 1 Myr prior to cooling and exhumation.

A comparison of these P-T data with data from the surrounding metasedimentary rocks reveals similar P-T paths (Figure 3.17). The local preservation of kyanite inclusions in a garnet of one metasedimentary sample (BH-247) is evidence that host rocks were subjected to peak-P conditions in the kyanite stability field, consistent with a high-P estimate of ~ 13 kbar from BH-217, prior to the peak-T event. Thus, the development of kyanite probably coincided with an early phase of high-P metamorphism, the evidence for which has almost been completely overprinted in the HSL. P-T calculations indicate that the peak biotite + sillimanite ± orthopyroxene assemblage developed in the sillimanite stability field at $P \geq 9$ kbar and $T \geq 800$°C, consistent with peak-T estimates calculated from metabasites. That biotite and sillimanite define the pervasive micro-fabric also implies that peak-T metamorphism was contemporaneous with the development of S_2 (Figure 3.18). In the HSL therefore, the regional D_2 coincided with peak-T conditions and development of the regional S_2 fabric. The breakdown of garnet, biotite and sillimanite to cordierite and spinel is estimated to have taken place at ~ 800°C and 5-6 kbar, during near-isothermal decompression. Cordierite overgrows the biotite and sillimanite that define both the S_2 fabric and S_3 shear bands, implying the breakdown of the peak-T assemblage in the HSL was contemporaneous with isothermal decompression and exhumation of the GHS beneath the STD, which is interpreted to coincide with D_3 (Figure 3.18).

Concordant rim ages suggest metamorphic zircon growth in the HSL spanned ~ 8 million years (21~14 Ma). ^{40}Ar/^{39}Ar data from the same and an additional two samples overlap with the lower limit of the U-Pb data. The most reliable amphibole ages span 17 – 15 Ma while biotite for the same two samples yields an age of ~14 Ma implying that rocks in the HSL cooled through the closure temperature for amphibole and biotite, nominally 500 ± 50°C by ~ 15 Ma and 300 ± 50°C, by ~ 17-14 Ma. Biotite in two samples from the surrounding metasediments yielded an age of ~ 17 Ma, four million years older than ages yielded from the metabasites (Figure 3.15). The discrepancy between biotite ages for samples at the same structural level supports the inference for excess argon. Therefore, either argon amphibole and biotite ages are far too old to be

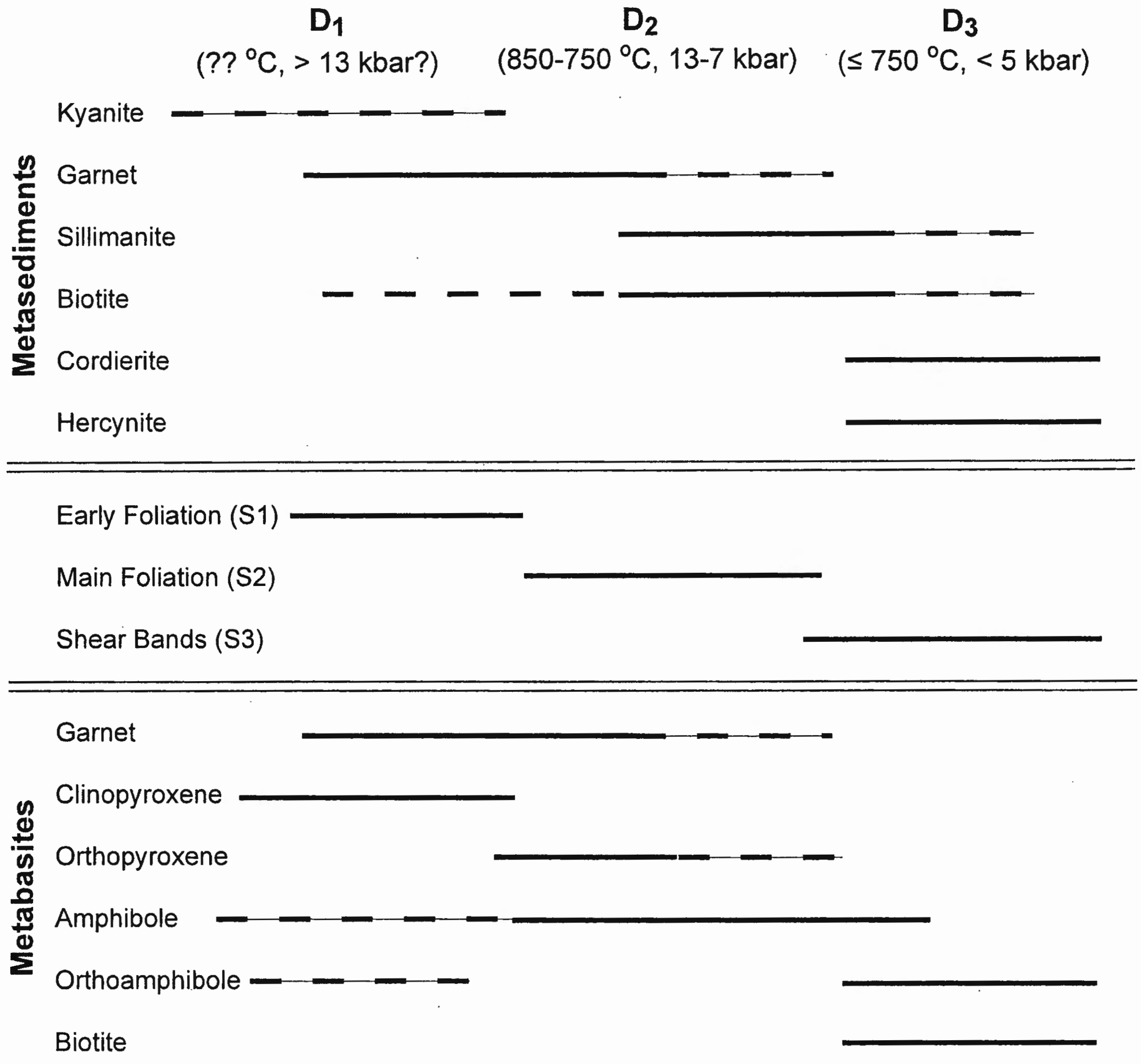

Figure 3.18: Mineral growth and deformation. Summary diagram relating mineral growth in metasedimentary and metabasic rocks from the HSL of the GHS in Bhutan to stages of deformation. The range of P-T condistions presented for each stage of deformation and metamorphism are the range of estimates calcaulated in this study.

meaningful, or the lower limit of each age range represents the upper time limit on cooling through 500°C and 300°C respectively. Heaman and Parrish (1991) noted that zircon growth occurs at temperatures in excess of 800°C and can persist to temperatures as low as 500°C. Since most of the zircons in these samples are commonly associated with matrix amphibole, the overlap of U-Pb ages with amphibole argon ages may imply that zircon growth persisted from temperatures above ~ 800 °C (calculated from the retrograde assemblage) down to 500 ± 50°C, with the maximum zircon age of 21 Ma (BH-217) representing the lower limit to which high-temperatures in the HSL persisted.

Taking into account the errors in both data sets, a comparison of the thermochronological data with P-T estimates indicates that by 21 Ma, rocks in the HSL were on the HT decompression segment of their P-T paths (Figure 3.17). By 15 Ma the same rocks cooled through 500°C approximately 6-12 km below the surface. By ~ 14 Ma, with continued exhumation, rocks should have cooled through 300°C at depths between 3-6 km.

Structurally up-section, an argon age of ~ 10 Ma was obtained for biotite from a leucogranite situated immediately below the STD (BH-232). This is the youngest argon age obtained in this study. A monazite from the same leucogranite has been dated at 12 Ma (Wu et al. 1998) implying that the leucogranite was emplaced ~ 2 Myr after the rocks it intruded cooled through 300°C. Thus, emplacement and cooling of this leucogranite through biotite closure temperatures was delayed and occurred when surrounding rocks of the GHS were at temperatures < 300°C and relatively shallow depths.

3.5.2 MID-STRUCTURAL LEVEL

The presence of large garnets with inclusion-rich cores and relatively inclusion-free rims implies that garnet growth in MSL rocks occurred in two stages. The Sps zoning profile for a large garnet from one sample reveals the preservation of growth zoning, implying that rocks at this structural level were not subjected to high temperatures (i.e. > 700°C) for more than ~2 Myr to permit homogenization of garnets. An alternate explanation is that this particular garnet was too large to be homogenized given the time it spent at high-T. P-T estimates calculated with garnet core and inclusion compositions suggest that garnet cores developed at the expense of plagioclase and orthoamphibole at ~ 650°C and pressures of ~ 7 kbar. Calculations made with garnet rim and matrix mineral compositions reveal that garnet growth continued to T ≥ 750°C and P ~ 8.5 kbar. In the same samples, small garnet crystals are characterized by flat profiles which suggest that temperatures were > 750°C long enough to homogenize small (i.e. < 1 mm) garnets. P-T estimates calculated using matrix and small garnet rim compositions reveal that the breakdown of garnet to amphibole and plagioclase took place at a minimum of 650°C at ~ 6 kbar. The P-T path through these estimates (Figure 3.19) illustrates that rocks in the MSL followed a tight, hairpin path, reaching peak-T contemporaneously with peak-P and remaining at elevated temperatures for a relatively short period of time before reaching the surface.

U-Pb analysis of metamorphic zircons extracted from one metabasic sample (BH-292) yielded concordant core (~ 25 Ma) and rim (21~14 Ma) ages suggesting zircon growth, as in the HSL, spanned ~ 8 My. ^{40}Ar/^{39}Ar data from the same and two additional samples overlap with the lower limits of the U-Pb data. Amphibole ages calculated for two samples span 20 Ma ~ 16 Ma, while biotite for one of the samples yields an age of ~13 Ma implying that rocks in the MSL cooled through 500 ± 50°C by ~ 20 Ma and 300 ± 50°C by ~ 13 Ma. Biotite from a leucogranite at the same structural level yielded an age of ~ 15 Ma, two million years older than the biotite age from the metabasite which presumably should have cooled through 300°C earlier than or contemporaneously with the leucogranite. The overlap of U-Pb ages with amphibole argon ages again implies that zircon growth persisted from temperatures in excess of ~ 750 °C (estimate calculated from the mineral assemblage) to ~ 500 ± 50°C, with the maximum U-Pb age of 21 Ma representing the lower limit to which high-temperatures in the MSL persisted.

Taking into account the errors from both isotopic data sets, a comparison of the thermochronological data with P-T estimates indicates that by 21 Ma, rocks in the MSL were on the decompression and cooling segment of the P-T path, at depths between 12-21 km (Figure 3.19). By ~ 13 Ma rocks had cooled through 300°C at depths of 3-9 km. The overlap of U-Pb with argon amphibole ages implies that zircons grew during burial and continued to develop on decompression and cooling to depths of ~ 12 km, and that the D_2 phase of deformation and metamorphism was over by 21 Ma in the MSL.

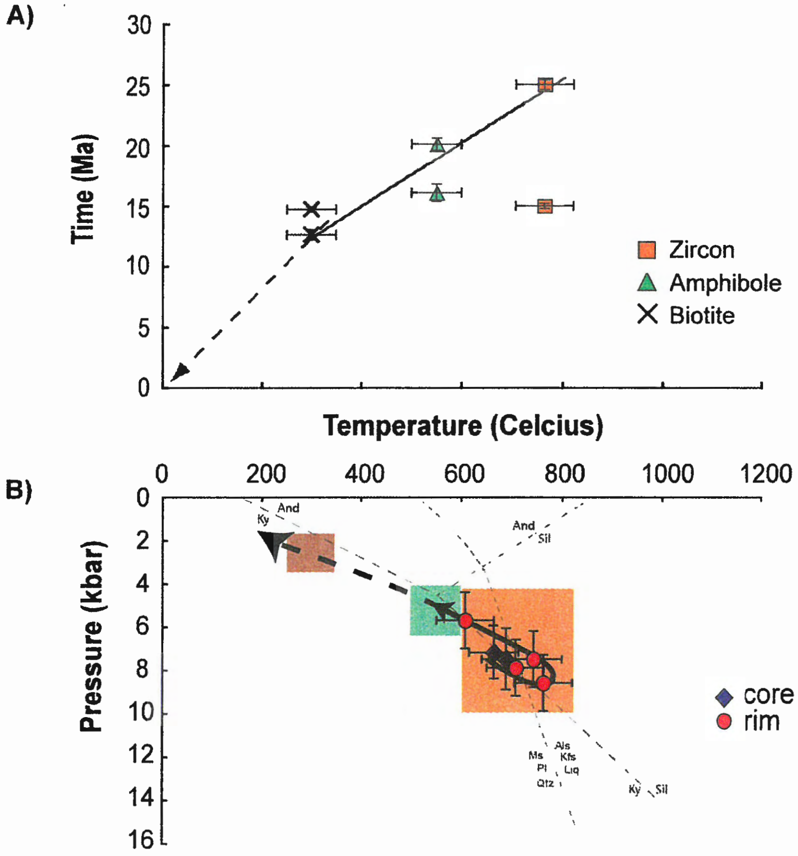

Figure 3.19: P-T-t data for the MSL. a) T-t for two metabasitic rocks and one leucogranite from the MSL. Time data are a compilation of ages obtained on minerals separated from BH-292, -175 and -171. b) P-T estimates and associated errors calculated for three meta-basic samples from the MSL. The position of the Al_2SiO_5 triple point is after Pattison (1992), while the position of the muscovite melting curve is after the reference Pëto (1976) given in Pattison (2003).

3.6 CONCLUSIONS

Rocks from the HSL were subjected to pressures of ~ 13 kbar, followed by decompression at high-T for a protracted period of time such that the P-T loops are characterized by HT segments that extend over a broad range of pressures. P-T paths for metabasites from the MSL, on the other hand, indicate that rocks at this structural level followed a tight, hairpin path, reaching pressures of ~ 10 kbar (~ 30 km) and remaining at elevated temperatures for a relatively short period of time. Based on the upper limit of zircon rim ages, rocks at both structural levels were on the decompression and cooling segments of their paths by ca. 21 Ma. Assuming the lower limit of each set of argon data represents the upper limit for cooling through the closure temperature for each mineral, then rocks at both structural levels cooled to 500°C at ca. 15-16 Ma, and rapidly through 300°C by 13-14 Ma. In the event that the argon data has been interpreted correctly, the overlap of zircon ages with argon ages suggests that zircon growth extended to temperatures as low as amphibole closure temperatures.

Microtextural analysis of metasediments from the HSL reveals that the high-T assemblage defines the regional fabric (S_2), suggesting it developed during D_2, prior to 21 Ma. C-type shear bands (S_3) that cross-cut S_2 and have developed parallel to the trend of the STD, appear to have been contemporaneous with the breakdown of the peak temperature assemblage upon decompression. This suggests that S_3 developed with decompression and cooling associated with exhumation of the GHS beneath the STD. Based on upper limit of the U-Pb data from zircon rims/overgrowths, exhumation of the GHS must have been well on its way by 21 Ma. Retrogression of the peak assemblage, and development of the S_3 fabric must have occurred during exhumation, between ~ 21 Ma and 13 Ma.

In north-western Bhutan, metabasites and metasedimentary rocks at the highest structural levels of the GHS have been subjected to high temperatures for protracted periods of time, so that all information pertaining to their early, prograde peak-pressure history has been overprinted. Within the GHS the probability of preserving information regarding the prograde, peak-pressure segments of P-T loops is greatest in rocks of lower metamorphic grade (i.e. the base of the GHS?) and thus lower structural position where rocks were either not subjected to such high temperatures, or were not subjected to protracted temperatures for periods of time long enough to permit complete overprinting of the prograde assemblage.

CHAPTER IV: P-T HISTORY OF THE LSL

4.1 INTRODUCTION

Since before the pioneer mapping days of Gansser (1964), it has been established that highly sheared deep crustal rocks of the GHS have been thrust southward over less deformed and low-grade metasedimentary rocks of the LHS along the Main Central Thrust (MCT). Early Himalayan geologists also noted, however, that not everywhere in the Himalaya is the MCT clearly defined (Gansser 1964), but rather, is a broad zone of distributed top-to-the-south shear across which metamorphic grade increases from the LHS into the GHS as a result of pervasive ductile shearing (Bhattacharyya and Das 1983; Burg and Chen 1984; Jain and Manickavasagam 1993; Grujic et al. 1996; Grasemann et al. 1999; Grasemann and Vannay 1999; Vannay et al. 1999; Stephenson et al. 2000). Since this zone of high finite strain and condensed isograds extends from the upper structural levels of the LHS into the lower structural levels of the GHS, the zone is commonly referred to as the MCT Zone (MCTZ; Grujic et al. 1996; Davidson et al. 1997). The MCT, on the other hand, is defined as the protolith boundary between gneissic rocks of the GHS and lower grade metasediments of the LHS (Davidson et al. 1997), which may or may not be incorporated within the MCT zone.

In eastern Bhutan, like areas to the west (e.g. Zanskar; Stephenson et al. 2001), detailed mapping of the MCT reveals that the protolith boundary is not confined to a single plane, but appears to be an intercalation of gneisses and schists, with the trace of the MCT drawn at the lowest (or southernmost) occurrence of orthogneiss (Gansser 1983; Davidson et al. 1997). In Bhutan, the trace of the MCT separates a package of Lesser Himalayan quartzites (Daling-Shumar Formation?) and garnet mica schists and orthogneisses of the Jaishidanda Formation from biotite rich schists and orthogneisses of the GHS (Figure 4.1; Bhargava 1995; Daniel et al. 2003). In eastern Bhutan, the trace of the MCT has also been inferred to coincide with and parallel the kyanite-in isograd in the GHS (Gansser, 1983; Daniel et al. 2003). However, to the west in Sikkim, the MCT cross-cuts the kyanite-in isograd implying the boundary between the GHS and LHS does not always parallel the isograds. The study of the Jaishidanda Formation here will serve to resolve whether or not it correlates with the MCT zone as defined elsewhere in the

Figure 4.1: Geological map and cross-section for Bhutan. **a)** Geological map of Bhutan modified from Grujic et al. (2002). A-A' marks the trend of the cross-section presented in Figure 4.1b. The relative positions of the mid- (MSL), higher- (HSL) and lower structural (LSL) levels are indicated along A-A'. **Legend:** ***MFT***, Main Frontal Thrust; ***MBT***, Main Boundary Thrust; ***MCTl,*** lower Main Central Thrust; ***MCTu***, upper Main Central Thrust; ***KT***, Kakhtang Thrust; ***STDl***, lower South Tibetan Detachment; ***STDu***, upper South Tibetan Detachment. **b)** Geological cross-section through the GHS of western Bhutan illustrating the nature of the boundaries between units, and the relative locations of the three structural levels that are discussed in this study. Information was compiled from Gansser, (1983), Burchfiel et al. (1992), Wu et al. (1998), and this study. The position of the MHT has been extrapolated from INDEPTH results (Hauck et al. 1998).

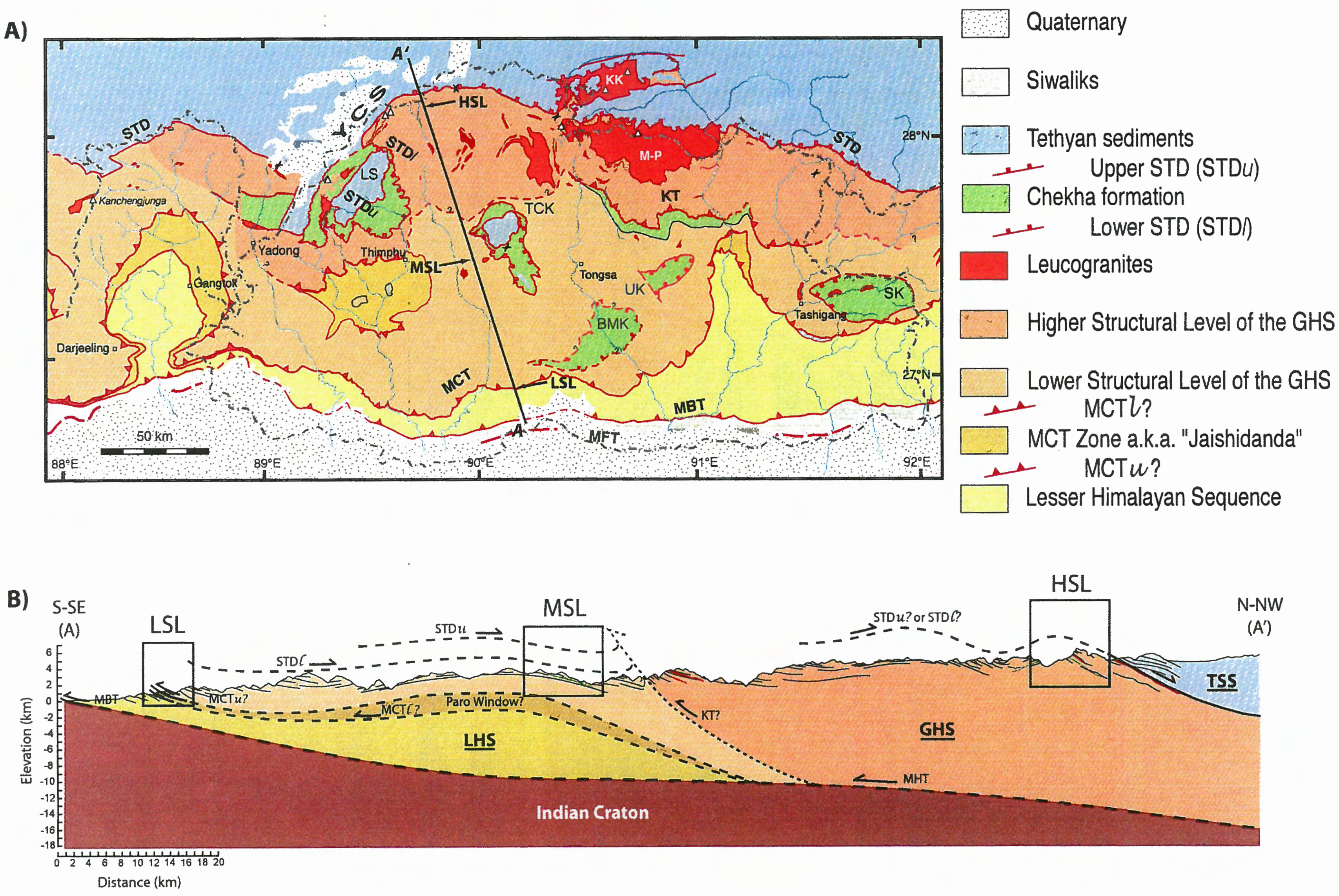
A)
A'
A
HSL
MSL
LSL
STD
STDl
STDu
LS
YCS
KK
M-P
KT
TCK
UK
BMK
SK
MCT
MBT
MFT
Kanchengjunga
Yadong
Thimphu
Gangtok
Darjeeling
Tongsa
Tashigang
28°N
27°N
88°E
89°E
90°E
91°E
92°E
50 km
Quaternary
Siwaliks
Tethyan sediments
Upper STD (STDu)
Chekha formation
Lower STD (STDl)
Leucogranites
Higher Structural Level of the GHS
Lower Structural Level of the GHS
MCTl?
MCT Zone a.k.a. "Jaishidanda"
MCTu?
Lesser Himalayan Sequence
B)
S-SE
(A)
N-NW
(A')
LSL
MSL
HSL
STDu
STDl
STDu? or STDl?
MBT
MCTu?
MCTl?
Paro Window?
KT?
MHT
LHS
GHS
TSS
Indian Craton
Elevation (km)
6
4
2
0
-2
-4
-6
-8
-10
-12
-14
-16
-18
0
2
4
6
8
10
12
14
16
18
20
Distance (km)

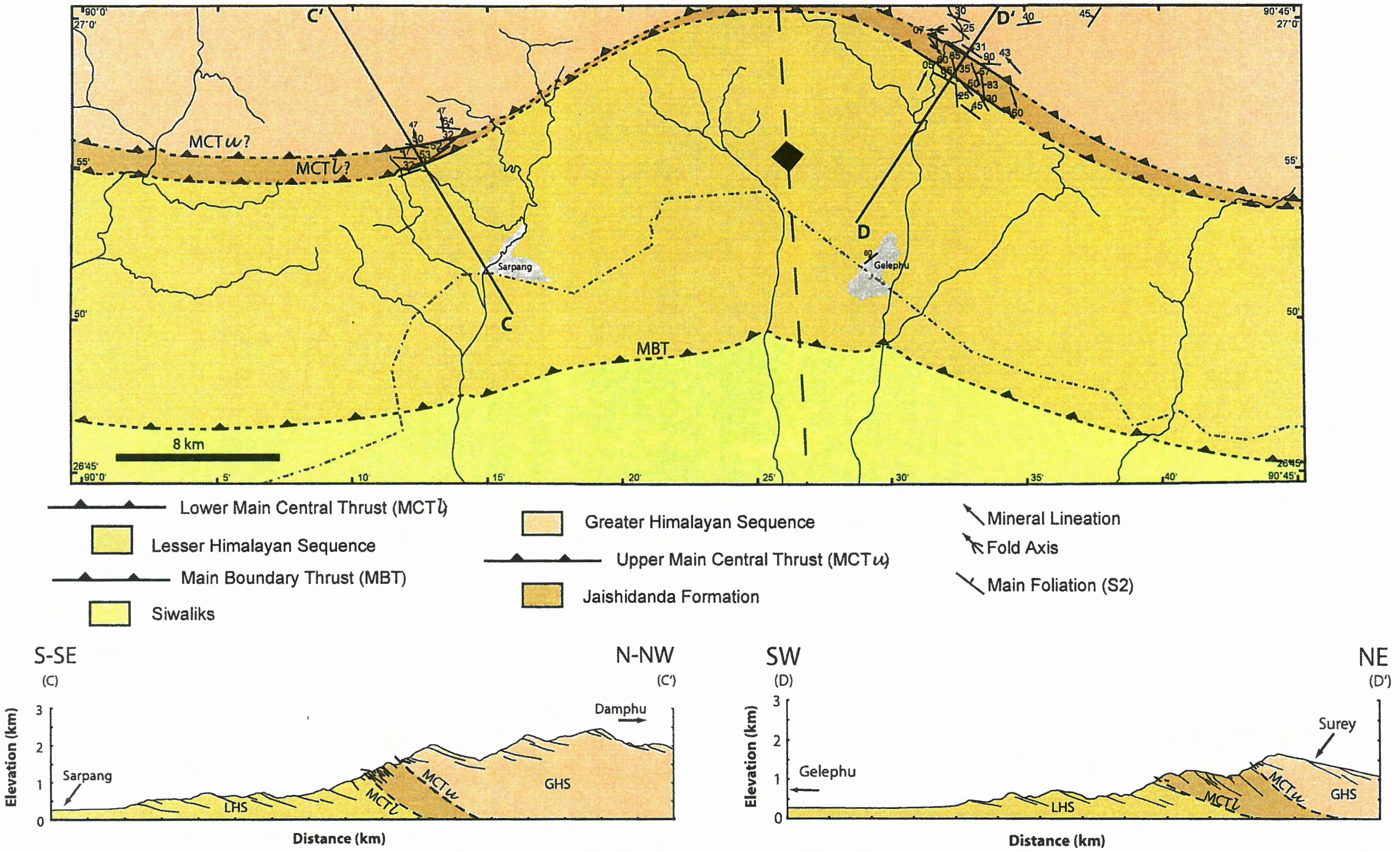

Figure 4.2: Geological map of southern Bhutan. Information was compiled from Gansser (1983), Bhargava (1995), and this study. The heavy, grey, dash-dot line is the Bhutanese border. Line C-C' indicates the position of the Sarpang-Damphu transect and line D-D' indicates the position of the Gelephu-Surey transect, which are both presented here.

Himalaya, and if so, whether or not it also incorporates the boundary (i.e the MCT) between the LHS and GHS.

Due to time constraints, sampling of the Jaishidanda Formation was carried out in southern Bhutan, along the Gelephu—Surey and Sarpang—Damphu sections previously studied by the Indian Geological Survey (Bhargava 1995), where the unit is thickest (~ 400 m; Figure 4.2). The base of the formation is marked by the Shumar quartzites, which characterize the highest structural levels of the LHS while the top of the formation is marked by a garnet – two-mica granite gneiss. The Jaishidanda Formation comprises intercalated and mylonitized garnet-mica schists, micaceous quartzites, rare carbonate bands, orthogneisses, augen gneisses and leucogranites (Figure 4.3).

Along the Sarpang – Damphu section (Figure 4.2) the main, penetrative foliation observed in the LHS, Jaishidanda Formation and GHS is parallel, dipping to the north – northwest. Further east, along the Surey-Jigmecholing section the same foliation dips to the northeast (Figure 4.4), implying the presence of an antiform between the two transects and that the main foliation has been deformed. Stretching lineations measured within the foliation planes along both transects trend to the north – northwest (Figure 4.4c). The penetrative foliation observed at the lower structural level (LSL) of the GHS is interpreted to correspond to the regional S_2 fabric that is also observed in the MSL and HSL.

4.2 MICRO-TEXTURES

Metasediments are compositionally banded with alternating garnet + muscovite + biotite and quartz + feldspar layers (Figure 4.5), which define the main, penetrative foliation that corresponds to the regional north-dipping S_2 foliation. Where garnet porphyroclasts are present, ribbons of muscovite-biotite intergrowths wrap them (Figure 4.5). A number of samples contain garnets with inclusion trails that are at a high angle to the main foliation and truncated by it (Figure 4.5). The relationship between inclusion trails and the encompassing foliation, with the observation that many garnets are partially replaced by biotite suggests garnet growth occurred prior to M_2 probably during an earlier prograde phase (M_1). This implies that garnet breakdown and development of the minerals defining S_2 was contemporaneous with the regional D_2 deformation.

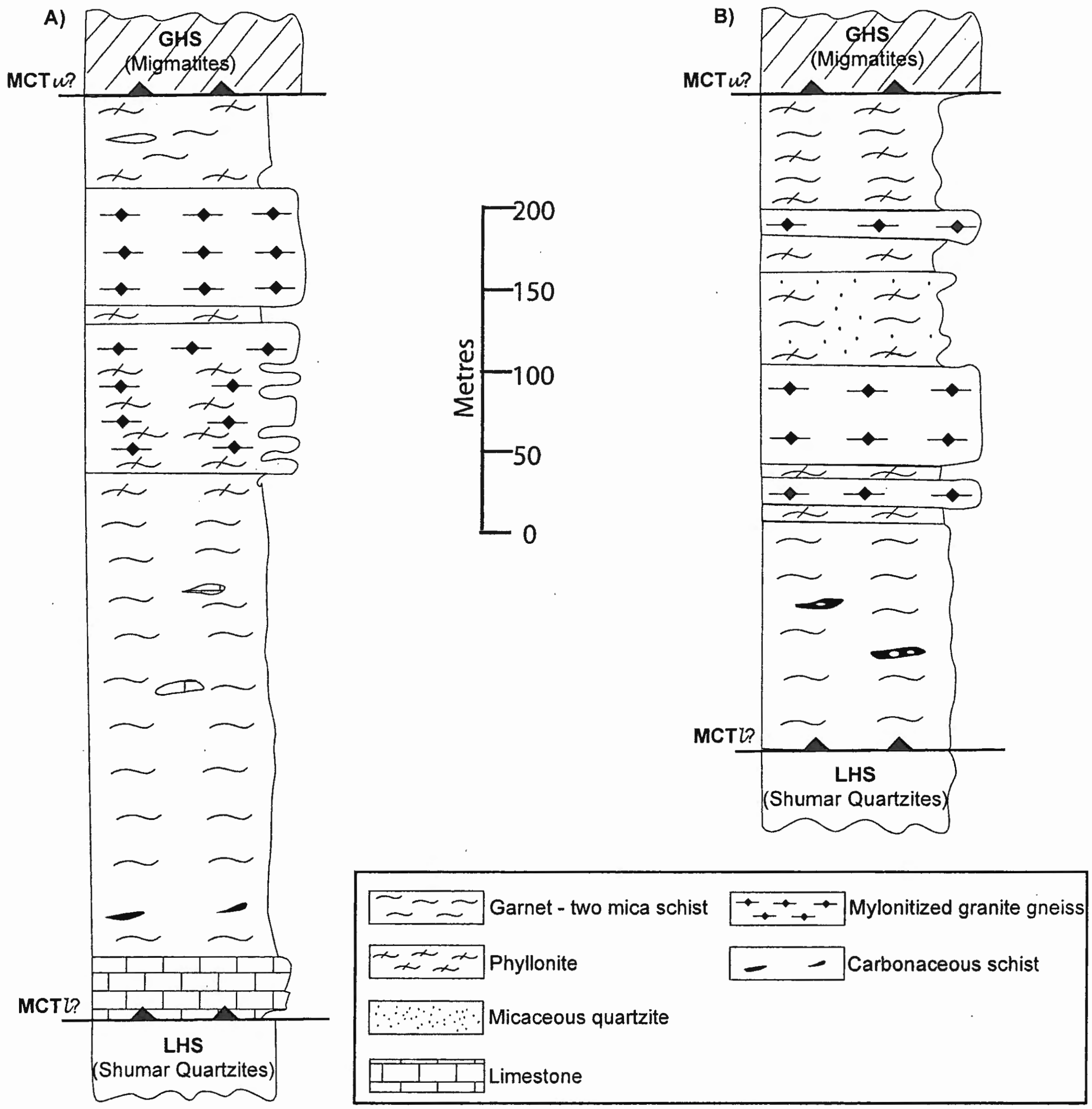

Figure 4.3: Lithological cross-sections of the Jaishidanda Formation. Lithological cross-sections of Dasgupta (1995) through the Jaishidanda Formation along the a) Sarpang-Damphu and b) Gelephu-Surey transects. Note the intercalation of phyllonites and garnet-mica schists with mylonitized granite gneisses.

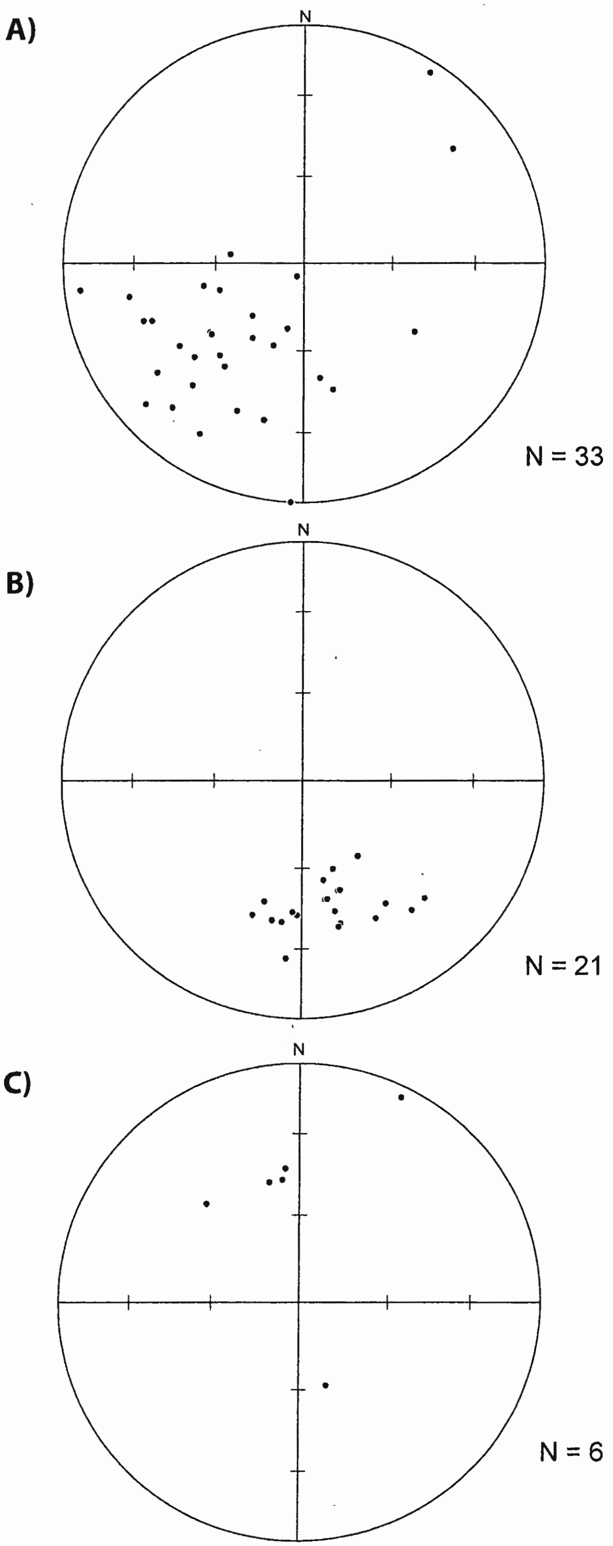

Figure 4.4: Equal area projections of structural data from the Jaishidanda Formation in southern Bhutan. A) Poles to the main foliation measured along the Surey-Jigmecholing section; b) Poles to the main foliation measured along the Sarpang - Damphu section; c) stretching lineations measured where possible in both sections.

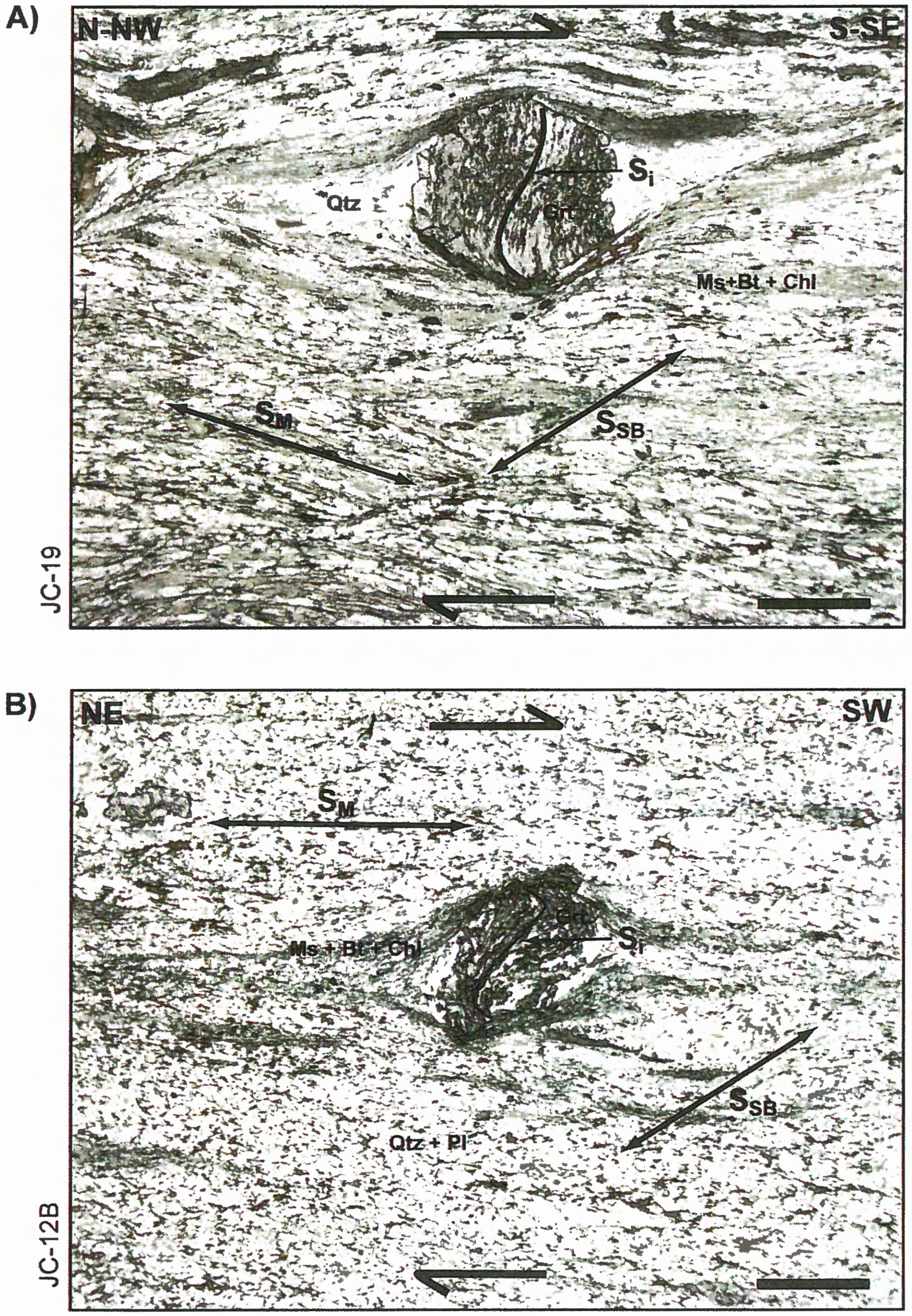

Figure 4.5: Microstructures in the Jaishidanda Formation. Photomicrographs highlighting the microstructures observed in a) a garnet mica schist from the Sarpang - Damphu transect, b) a garnet mica schist from the Gelephu - Surey transect. Photographs were taken at 1.6x magnification such that the total field of view is ~ 7.5 mm. The length of the scale bar in the bottom right corner of each photomicrograph marks 1 mm. **Legend:** S_i, internal foliation defined by inclusion trails in garnet; S_M, main external foliation defined by muscovite and biotite intergrowths; S_{SB}, shear bands that cross-cut the main foliation.

Superimposed onto the S_2 foliation are small, moderately developed C′-type shear bands defined by biotite grains which have been bent into the shear bands and appear to be breaking down to muscovite and chlorite. Most samples contain only one set of shear bands with top-to-the south – southeast sense of displacement (Figure 4.5). Based on the continuous relationship with the main foliation, development of shear bands must have occurred syn - late M_2, and most likely syn-M_3.

4.3 MINERAL ASSEMBLAGE & CHEMISTRY

Metasediments, ortho- and augen gneisses comprising the Jaishidanda Formation have the assemblage garnet + biotite + muscovite + quartz + plagioclase ± K-feldspar with accessory ilmenite ± magnetite ± rutile + tourmaline + epidote + zircon + apatite (Table 4.1). The same mineral assemblage characterizes rocks in the lowest structural levels of the GHS (JC-2A, 17, 24). In most samples, porphyroblasts of garnet are wrapped by, or encased in, biotite-muscovite intergrowths that define the main foliation (Figure 4.6). Garnet, biotite and muscovite in all but two samples have been overgrown by retrograde chlorite. The absence of staurolite, kyanite and/or sillimanite at this level could reflect either bulk composition (i.e. rocks at the base of the GHS are low in Al, Mg and Fe relative to those at higher structural levels) or the P-T conditions to which these rocks were subjected. Compositional profiles of garnet reveal that some garnets preserve growth zoning, while others are characterized by relatively flat profiles. In the following discussion samples have been subdivided into two groups – those in which growth zoning patterns are preserved in garnets, and those in which garnet zoning profiles are flat. For samples associated with each group, refer to Figure 4.6.

4.3.1 GARNETS - GROWTH ZONING PROFILES

Ten of the 15 samples contain garnet with growth zoning. Alm, Pyr, Grs and Sps profiles are continuous and smooth from core to rim with high Fe/(Fe+Mg) values in cores (0.95 – 0.86) and lower values near rims (0.92 – 0.81; Appendix A). Sps profiles are bell shaped (Figures 4.7, 4.8) with high-Sps cores ($X_{Sps} = 0.24 - .07$) and low-Sps rims ($X_{Sps} = 0.16 - 0.003$), a pattern that is indicative of manganese depletion during garnet growth with increasing temperature (Hollister 1966; Spear et al. 1991). Superimposed on the normal growth patterns, garnets in JC-2A, -9A and -10 show evidence for diffusional re-equilibration of Mn with increased proportions at the

Table 4.1: Major silicate phases and associated εNd values for rocks from the lowest structural levels of the GHS, Jaishidanda Formation, southern Bhutan.

	Rock type	Pl	Kfs	Grt	Bt	Ms	Chl	Acc	Zoning in Grt	εNd(0)	εNd(500)	T_{DM} (Ma)
JC-2A	Grt-Bt gneiss	X	t	X	X	t	X	Opx, Rt, Ilm, Ep, Ap, Zr	growth w/ 'wings'	–	–	–
JC-3	Grt-Bt-Mu gneiss	X	–	X	X	X	X	Tour, Rt, M, Ilm, Ep, Ap, Zr	growth	-18	-12	2105
JC-4	Grt-Bt-Mu gneiss	X	–	X	X	X	X	Rt, Ilm, Ep, Ap, Zr	growth	-18	-13	2197
JC-6	Grt-Bt-Mu augen gneiss	X	X	X	X	X	X	Ep, Ap,Ttn	growth	-13	-8	2101
JC-7	Grt-Bt-Mu schist	X	–	X	X	X	X	Rt, Ilm, M, Ep, Ap, Zr, Tour	growth	-13	-7	1734
JC-9A	Grt-Bt-Mu gneiss	X	t	X	X	t	X	Ep, Ap,Ttn	growth w/ 'wings'	-12	-7	1745
JC-10	Mylonitized Grt-Bt-Mu granite	X	X	X	X	X	–	Ep, Ap	growth w/ 'wings'	-12	-7	1755
JC-12B	Grt-Bt-Mu schist	X	–	X	X	X	X	Ap, Ilm, Tour	growth	–	–	–
JC-13	Grt-Bt-Mu schist	X	–	X	X	X	X	Ap, Ilm, Tour	growth	-17	-12	2205
JC-17	Grt-Bt-Mu schist	X	t	X	X	X	–	Ilm, Tour, Zr	flat	–	–	–
JC-18	Grt-Bt-Mu schist	X	–	X	X	X	X	Ru, Ilm, Tour, Zr	flat	-12	-6	1703
JC-19	Grt-Bt-Mu schist	–	–	X	X	X	X	Ilm, Tour, Zr	growth	-15	-10	1985
JC-22	orthogneiss	X	–	X	X	X	X	Rt, Ep, Ap, Zr	flat	-17	-12	2273
JC-23	Mylonitited Grt-Bt-Mu augen gneiss	–	–	X	X	X	X	Ilm	flat	–	–	–
JC-24	Grt-Bt-Mu augen gneiss	X	X	X	X	X	X	Ilm, Ep, Ttn, Ap	flat	–	–	–

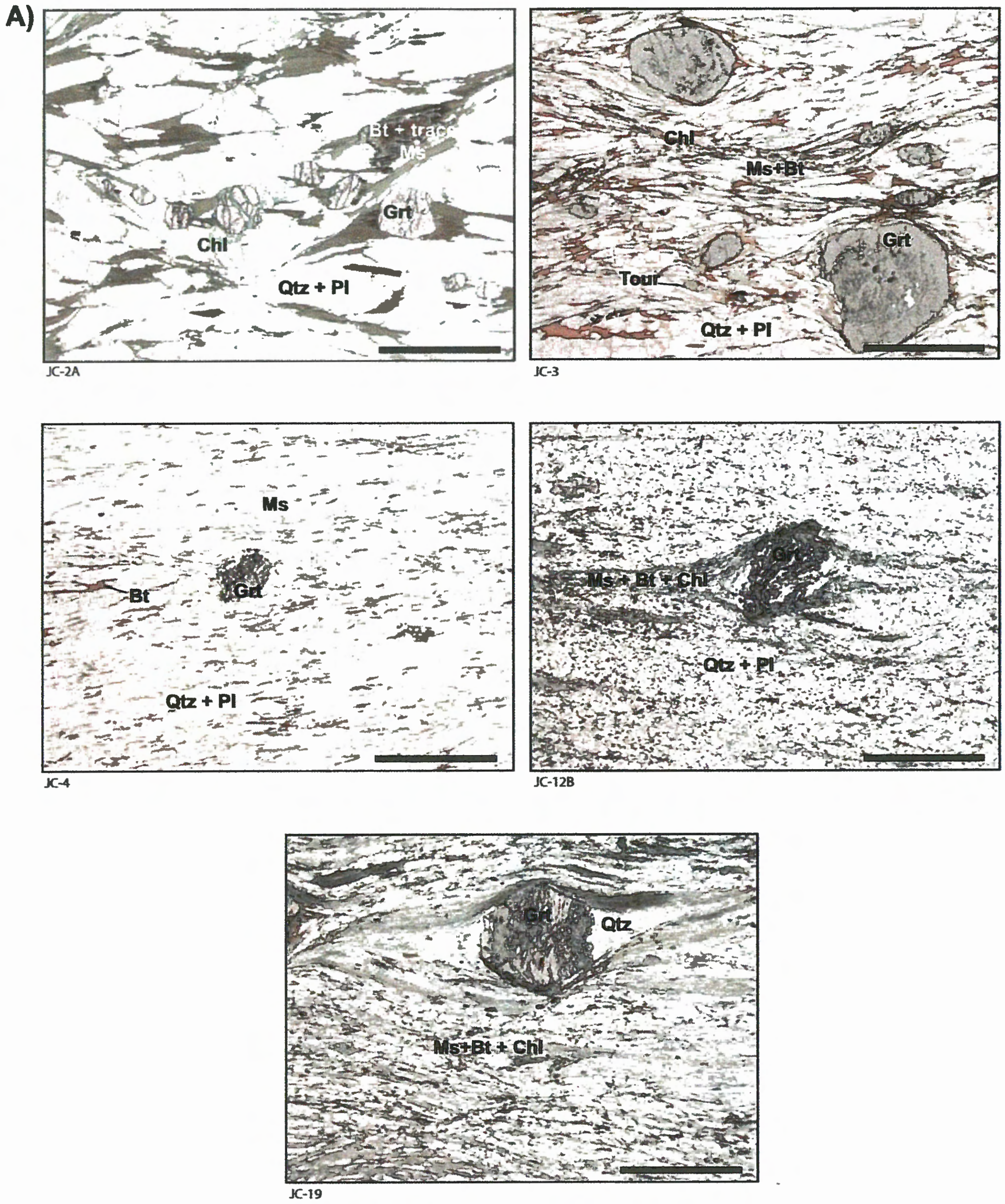

Figure 4.6: Photomicrographs of prograde garnets of the Jaishidanda: samples from the lower structural level of the GHS, Jaishidanda Formation, with prograde garnets. Micrographs were taken at 1.6x magnification such that the total field of view is ~ 7.5 mm. The length of the scale bar in the bottom right corner of each photomicrograph marks 1mm. **Legend:** ***Grt,*** garnet; ***Bt,*** biotite; ***Ms,*** muscovite; ***Pl,*** plagioclase; ***Kfs,*** potassium feldspar.

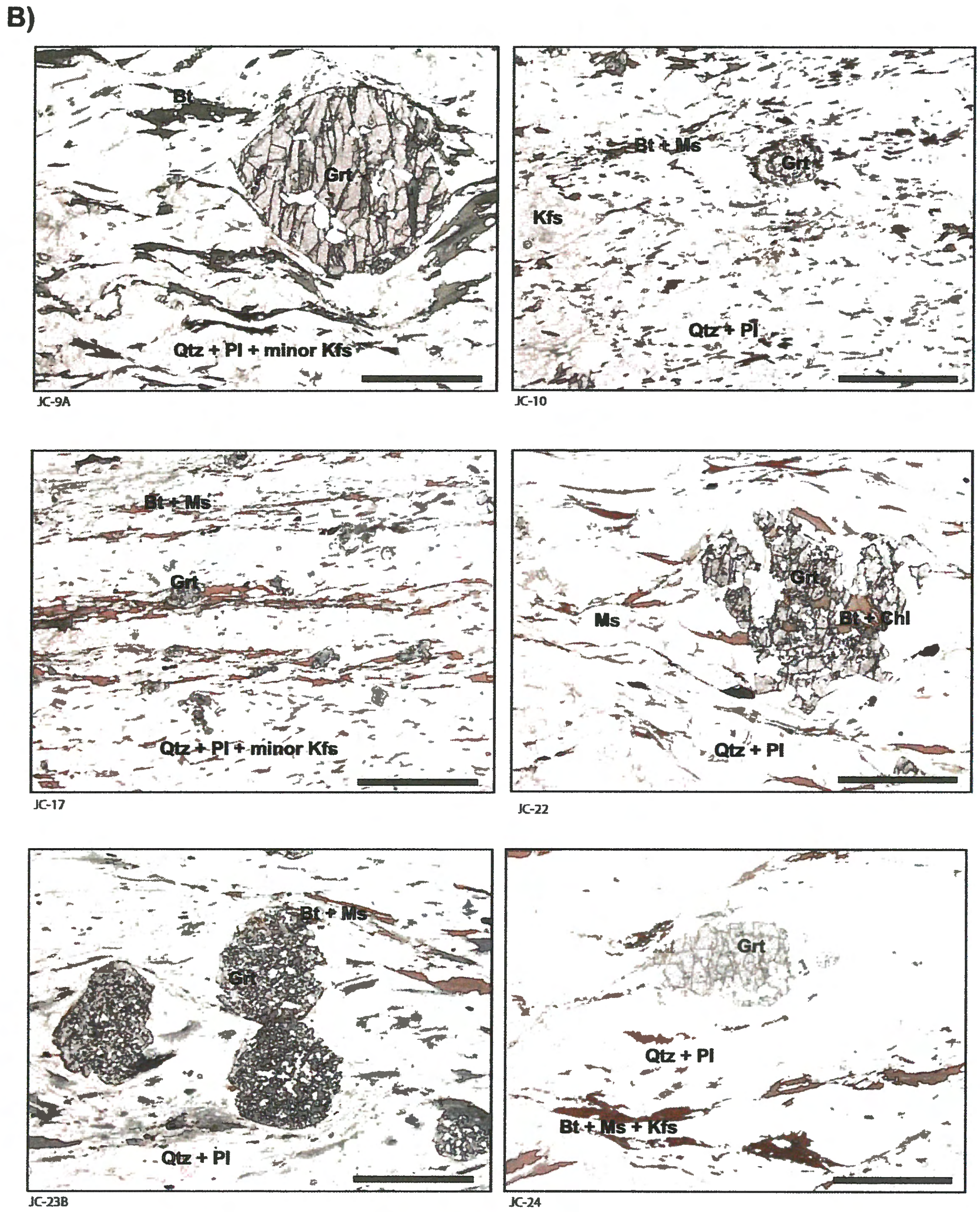

Figure 4.6i: Photomicrographs of unzoned garnets of the Jaishidanda: samples from the lower structural level of the GHS, Jaishidanda Formation, with homogeneous garnets. Micrographs were taken at 1.6x magnification such that the total field of view is ~ 7.5 mm. The length of the scale bar in the bottom right corner of each photo-micrograph marks 1mm. **Legend:** ***Grt,*** garnet; ***Bt,*** biotite; ***Ms,*** muscovite; ***Pl,*** plagioclase; ***Kfs,*** potassium feldspar.

outermost rims ($X_{Sps} = 0.14 - 0.13$). Excluding JC-3, -6 and -10 (Figure 4.8), Grs profiles are also 'normal' decreasing from the cores (X_{Grs} 0.23 – 0.12) to the rims ($X_{Grs} = 0.11 - 0.01$).

Considering the presence of leucogranites at this structural level, garnets probably formed from the breakdown of chlorite following the reaction with the form (Spear 1993):

$$\text{Qtz} + \text{Ms} + \text{Chl} \rightarrow \text{Grt} + \text{Bt} + \text{Liq} \quad \textbf{(4.1)}$$

Considering the Grs contents, and the abundance of accessory epidote, it is apparent that the bulk composition of the rocks along both transects is Ca- and Mn-rich, and Al-poor. Since the development of chlorite is restricted to Mg-rich compositions, the absence of primary chlorite in these rocks may be accounted for by the relative abundance of Mn and Ca, which may have decreased the temperature to which garnet + chlorite is stable (Spear 1993). An increased concentration of Mn and Ca, and expanded stability field for garnet might have led to the complete consumption of chlorite early on, at relatively low temperatures following reaction 4.1.

In JC-6, garnets have relatively low-Grs cores ($X_{Grs} = 0.39$) followed by high-Grs overgrowths ($X_{Grs} = 0.45$) that drop slightly ($X_{Grs} = 0.43$) at the rim. This pattern suggests increasing, then decreasing, pressure during prograde growth. Garnets in JC-3 and -10 are characterized by oscillatory Grs zoning. Garnet cores in JC-3 and particularly JC-10 are relatively enriched in Grs ($X_{Grs} = 0.43$), followed by a decrease ($X_{Grs} = 0.38$), subsequent high-Grs overgrowth ($X_{Grs} = 0.40$), and a marked decrease towards the rims ($X_{Grs} = 0.28$).

Truncation of Mn and Ca zoning, the presence of deep embayments, and replacement by chlorite in virtually all samples suggests considerable dissolution of garnets following reactions with the form (Spear 1993):

$$\text{Grt} + \text{Bt} + \text{Liq} \rightarrow \text{Qtz} + \text{Ms} + \text{Chl} \quad \textbf{(4.2)}$$

and/or

$$\text{Ms} + \text{Bt} + \text{Qtz} + \text{Liq} \rightarrow \text{Chl} + \text{Kfs} \quad \textbf{(4.3)}$$

Garnet porphyroblasts are commonly subhedral and 7 to ≤ 1 mm in size. Irrespective of structural level, garnet cores in a number of samples preserve spiral — sigmoidal inclusion trails that have been overgrown by inclusion free rims (BH-3, 12B, 19; Figure

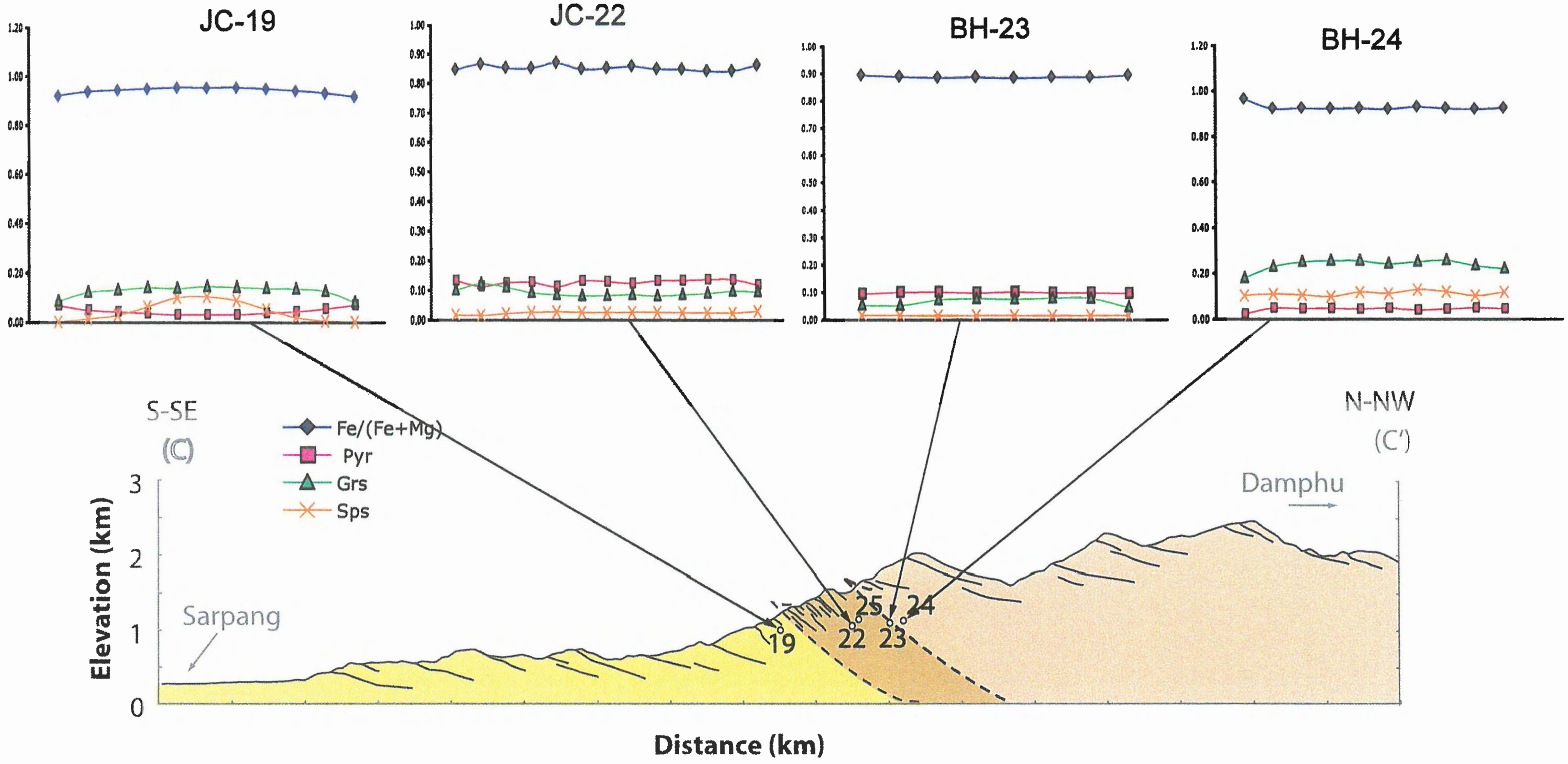

Figure 4.7: Garnet profiles along the Sarpang - Damphu transect. Location of samples along the Sarpang – Damphu transect, and zoning profiles through their associated garnets. Pyr, pyrope - magnesium end-member; Grs, grossular – calcium end-member; Sps, spessartine – manganese endmember.

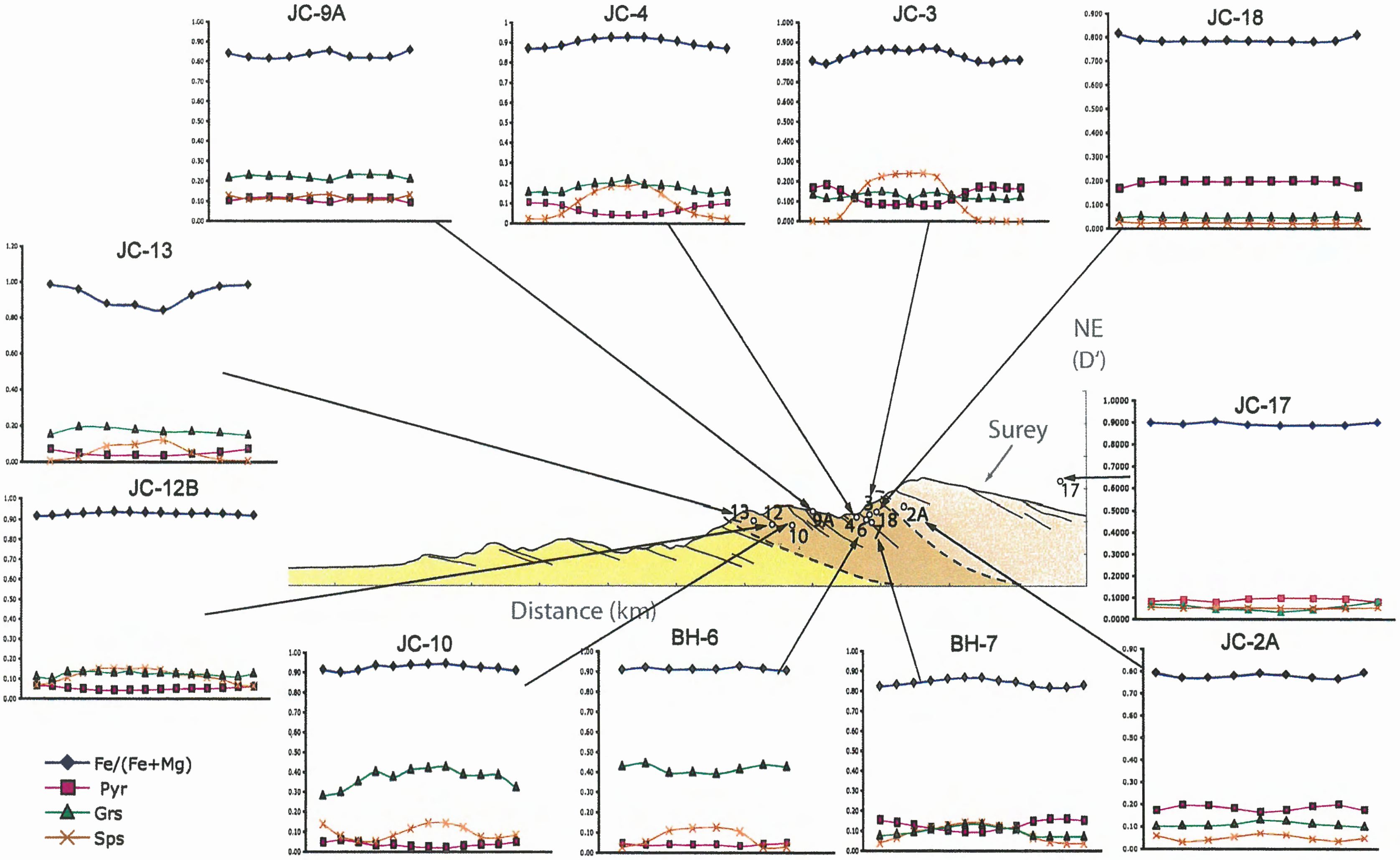

Figure 4.8: Garnet profiles along the Gelephu - Surey transect. Location of samples along the Gelephu – Surey transect, and zoning profiles through their associated garnets. Pyr, pyrope - magnesium end-member; Grs, grossular – calcium end-member; Sps, spessartine – manganese endmember.

4.6), suggesting growth in two stages. Curved and spiral inclusion trails in garnet cores are truncated, and at a high angle to the main foliation in the matrix. Most garnets also have quartz and/or mica pressure shadows (Figure 4.6), and the matrix foliation (S_2) wraps around them, implying pre- and syn-deformational growth. Mineral inclusions in garnets are some combination of quartz ± plagioclase ± rutile ± ilmenite ± zircon ± epidote ± apatite ± tourmaline ± muscovite ± biotite. Plagioclase inclusions and matrix grains in all samples are sodic ($X_{An} = 14 - 28\%$), displaying minor variation between plagioclase core and rim compositions. Matrix biotite and muscovite also lack marked compositional variations. Biotites do have slightly higher Fe/(Fe+Mg) values to within a few microns of garnet contacts, which may reflect Fe-Mg cation exchange between the two, or the net transfer reaction with the form:

$$\text{Grt} + \text{Ms} \rightarrow \text{Bt} + \text{Pl} \quad \mathbf{(4.4)}$$

4.3.2 GARNETS - HOMOGENOUS ZONING PROFILES

In addition to the samples described above, five others collected from the higher structural levels of the unit contain subhedral to anhedral garnets (3- ≤ 1 mm) that preserve flat, homogeneous zoning profiles (Figure 4.6). Fe/(Fe+Mg) ratios range from ca. 0.81- 0.93 between samples, with slight increases at the rims particularly where garnet does not abut biotite. Similarly, Pyr, Grs and Sps are flat with Sps increasing and Grs decreasing at the rims (Figures 4.7, 4.8), implying diffusional re-equilibration between garnet rims and matrix minerals with decompression. The absence of growth zoning in these garnets suggests high-T (i.e. > 750 °C) diffusional homogenization, which could have eradicated the original growth zoning with an increase in the proportion of Alm, Sps, and Pyr at the rims reflecting retrogression. An alternate explanation is that garnet growth was slow and occurred at temperatures < 750 °C over an extended period of time permitting equilibration of garnet with matrix minerals (Hollister 1966; 1969). The presence of deep embayments, and replacement by biotite and chlorite, suggests considerable dissolution of garnets following reactions 4.2 and 4.3 above.

Garnet cores are characterized by straight or sigmoidal inclusion trails and thin, inclusion free rims. Inclusion trails are at a high angle to the main matrix foliation (S_2), which also wraps around grains. Garnets also have quartz pressure shadows (Figure 4.6), implying inter- to syn-tectonic garnet growth. As noted above, inclusions are some combination of quartz ± plagioclase ± rutile ± ilmenite ± zircon ± epidote ± apatite ± tourmaline ± muscovite ± biotite. Plagioclase inclusions and matrix grains in all samples are sodic (X_{An} = 6 –19%), displaying minor zoning. Matrix biotite and muscovite are compositionally homogeneous.

4.4 P-T ESTIMATES

Average P-T estimates for garnet mica schists and orthogneisses of the Jaishidanda Formation were calculated with the mineral data presented in Appendix A using Thermocalc v. 3.25, the internally consistent thermodynamic database of Holland and Powell (1998). In two samples with garnets that preserve growth zoning, P-T estimates made on garnet core and biotite + muscovite + plagioclase + epidote garnet inclusion compositions yielded P-T estimates of ~ 8.5 ± 1 kbar and 535 - 575 °C (Table 4.2; Figure 4.9). The matrix assemblage combined with garnet rims yielded estimates of 616 ~ 647 °C and 9-11 kbar (Table 4.2; Figure 4.9). These results suggest that garnet growth might have taken place at constant pressure and increasing temperature conditions (Figure 4.9). The preservation of growth zoning with low T estimates yielded from the core and higher T estimates restricted to the rims implies that garnets were not subjected to T > 700 °C for extended periods prior to cooling and decompression (Figure 4.9).

For samples with homogeneous garnets, garnet core and biotite + muscovite + plagioclase + epidote inclusion compositions in one sample (JC-24) yielded a P-T estimate of 710 ± 35 °C at ~ 14 ± 1.6 kbar. This is considered a minimum temperature because based on diffusion coefficients calculated at 850°C (Chakraborty and Ganguly 1992), it should take less than 1 Myr for Fe-Mg exchange to penetrate a garnet that is 3 mm in diameter at T = 850°C (O'Brien 1997). Considering many garnets in the Jaishidanda Formation are less than 3 mm in size, they could have been homogenized had they been subjected to temperatures in excess of ~ 750 °C for at least 2-3 Myr or, as illustrated by Hollister 1966 and 1969, could reflect growth over an extended period of time at temperatures below 750 °C which would facilitate chemical equilibration of the garnets with the matrix material. P-T estimates from matrix and garnet rim compositions suggest samples with homogeneous zoning profiles cooled on decompression to 643 ± 23 °C at 8 ± 1 kbar prior to chloritization. Due to the absence of index minerals (i.e.

Table 4.2: Summary of P-T data calculated for samples from the lower structural levels of the GHS, Jaishidanda Formation, southern Bhutan.

			Temperature	±	Pressure	±	comments
Prograde Garnets	JC-3	rim	631	30	11.1	1.2	rim+mtx less chl
	JC-3	rim	587	18	9.4	1	rim+mtx w/ chl
	JC-4	core	535	30	7	2	core+incls
	JC-4	rim	647	28	10.3	1.1	rim+mtx less chl
	JC-4	rim	576	20	7.9	1	rim+mtx w/ chl
	JC-6	core	619	42	10	1.5	core+mtx less chl
	JC-6	rim	681	67	12.3	2.5	rim+mtx less chl
	JC-6	rim	634	44	10.7	1.7	rim+mtx w/ chl
	JC-7	core	490	40	9	1	core+incls; T estimate only
	JC-7	rim	590	14	7.2	1.7	rim+mtx w/ chl; T estimate only
	JC-12B	core	590	36	8.2	1.4	core+mtx less chl
	JC-12B	core	549	17	7.7	1.1	core+mtx w/ chl
	JC-12B	rim	616	28	9	1	rim+mtx less chl
	JC-12B	rim	564	17	7	1	rim+mtx w/ chl
	JC-13	core	575	18	8.5	1	core+incls
	JC-13	rim	622	29	8.6	1.2	rim+mtx less chl
	JC-13	rim	578	17	7	1	rim+mtx w/ chl
	JC-19	rim	749	168	10.4	2.3	rim+mtx less chl
	JC-19	rim	552	17	8.3	2.3	rim+mtx w/ chl
Homogeneous Garnets	JC-2A	rim	660	30	10	1	rim+mtx less chl; prerim yields very similar estimate with greater errors
	JC-9A	prerim	666	39	10.8	1.3	prerim+mtx less chl; rim comp yields similar estimate
	JC-9A	rim	564	27	7.6	1.1	rim+mtx w/ chl
	JC-10	rim	695	41	12	1.6	rim+mtx less chl; prerim yields very similar estimate
	JC-10	rim	537	38	6	2	rim+mtx w/ chl
	JC-17	rim	654	30	8	1.2	rim+mtx (no chl in sample)
	JC-18	rim	643	23	8.4	1.2	rim+mtx less chl
	JC-18	rim	600	15	7	1	rim+mtx w/ chl
	JC-22	rim	664	29	11	1	rim+mtx less chl
	JC-22	rim	588	23	8.2	1.4	rim+mtx w/ chl
	JC-24	core	710	35	14	1.6	core+incls

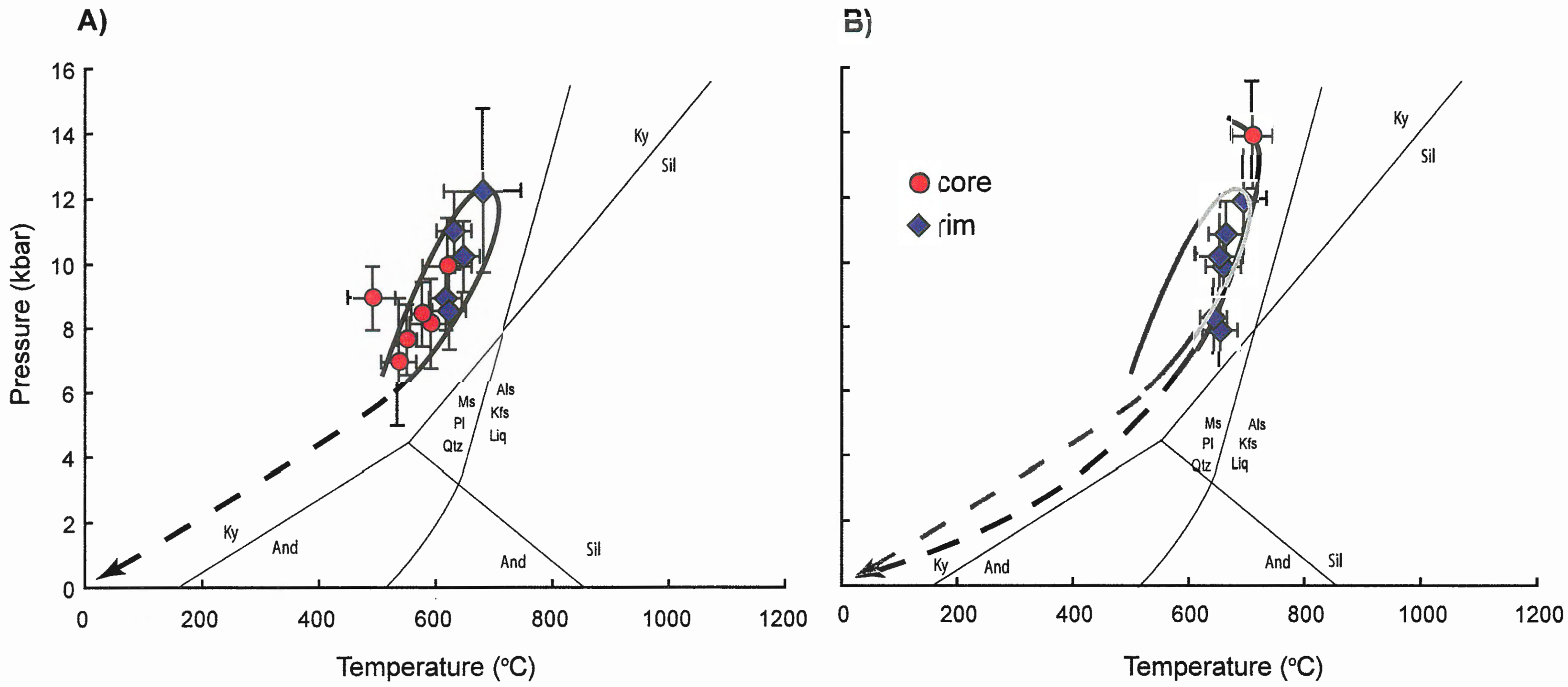

Figure 4.9: P-T estimates for the Jaishidanda Formation. a) Pressure – temperature (P-T) data and the estimated P-T path calculated for prograde garnet rim and core compositions in combination with matrix and inclusion assemblages. b) P-T data and the estimated P-T path calculated for homogeneous garnet rim combinations in combination with the matrix assemblage. The grey curve is the path calculated for prograde garnets presented in figure 4.9a that has been superimposed onto the graph for comparison purposes. The position of the Al_2SiO_5 triple point is after Pattison (1992), while the position of the muscovite melting curve is after the reference Pëto (1976) given in Pattison (2003).

staurolite, sillimanite and/or kyanite) as inclusions in the cores of these garnets, the exact nature of the P-T path cannot be determined here.

4.5 PROVENANCE: ε_{Nd} RESULTS

Whole rock Nd isotopic data obtained for samples from the Surey and Saprang transects are presented in Table 4.3 and Figure 4.10. As explained in Chapter 2, several isotopic studies of the LHS and GHS report Nd data relative to present day chondritic values, $\varepsilon_{Nd(0)}$ (e.g. Ahmad et al. 2000; Robinson et al. 2001; Martin et al. 2005). Other studies have reported data relative to 500 Ma (Ahmad et al. 2000; Richards et al. 2005; Richards et al. 2006), which corresponds to a tectono-thermal metamorphic event for which there is evidence throughout the GHS and LHS further to the west. Thus, for comparison purposes Nd model ages and both $\varepsilon_{Nd(0)}$ and $\varepsilon_{Nd(500)}$ values for the LSL are presented in Table 4.3.

With the exception of two samples from the Surey-Jigmecholing section (JC-9C and -14B), Nd model ages calculated for samples from both transects range between 1.7 – 2.4 Ga with corresponding $\varepsilon_{Nd(500)}$ values ranging from -6.4 to -15.7. Sample 9C yielded an Archean Nd model age of 2.9 Ga but an unusually high $\varepsilon_{Nd(500)}$ value of -9.0, sample 14B on the other hand yielded an anomalous model age of -5.6 Ga. The anomalous values for both JC-9C and -14B are attributed perhaps to post formation mixing particularly since there is evidence for late stage leucogranite intrusion in the area.

4.6 DISCUSSION

A recent study in Bhutan (Richards et al. 2006) showed that rocks of the LHS are isotopically distinct from rocks of the GHS, implying the material in each unit was derived from different sources at different times. In their study, quartzites from the LHS yielded Nd model ages ranging between 2.5 – 2.6 Ga and $\varepsilon_{Nd(500)}$ values between -20 and -26 (Figure 4.11). A rhyolite and quartzites from the GHS yielded Nd model ages ranging between 1.7 – 2.1 Ga with $\varepsilon_{Nd(500)}$ values between -7 and -13 (Figure 4.11). In this study, neodymium data for the Jaishidanda Formation are consistent with the findings of Richards et al. (2006) for rocks of GHS affinity, implying that the mica schists and orthogneisses along the Surey and Sarpang sections of the Jaishidanda Formation are all of GHS affinity (Figure 4.11). The implications of the isotopic data are

Table 4.3: Nd isotopic data for the lowest structural levels of the GHS, Jaishidanda Formation, southern Bhutan.

	Sample	Rock Type	Sm (ppm)	Nd (ppm)	2σ error	^{147}Sm/^{144}Nd	^{143}Nd/^{144}Nd	εNd(0)	εNd(500)	T_{DM} (Ma)
Surey - Jimecholing	**JC - 2B**	Grt-Bt-Mu gneiss	6.06	31.66	0.10	0.115384	0.511846	-15.5	-10.3	2015
	JC - 3	Grt-Bt-Mu gneiss	7.03	37.81	0.24	0.112036	0.511741	-17.5	-12.1	2105
	JC - 4	Grt-Bt-Mu gneiss	3.79	19.69	0.19	0.115986	0.511736	-17.6	-12.5	2197
	JC - 5	Augen gneiss	6.50	35.11	0.16	0.111624	0.511558	-21.1	-15.7	2367
	JC - 6	Grt-Bt-Mu augen gneiss	7.60	35.10	0.11	0.130581	0.511999	-12.5	-8.2	2101
	JC - 7	Grt-Bt-Mu schist	4.10	21.96	0.10	0.112503	0.511996	-12.5	-7.2	1734
	JC - 9A	Grt-Bt-Mu gneiss	4.14	21.40	0.09	0.116583	0.512035	-11.8	-6.6	1745
	JC - 9C	orthogneiss	3.97	15.20	0.22	0.157245	0.512050	-11.5	-9.0	2945
	JC - 10	Mylonitized Grt-Bt-Mu granite	5.90	30.37	0.16	0.117030	0.512034	-11.8	-6.7	1755
	JC - 11	Mylonitized Qtz-mica schist	4.72	23.45	0.05	0.121178	0.511890	-14.6	-9.8	2069
	JC - 12A	Phyllite (Mu schist)	6.30	33.82	0.35	0.112231	0.511737	-17.6	-12.2	2115
	JC - 12B	Grt-Bt-Mu schist	–	–	–	–	–	–	–	–
	JC - 13	Grt-Bt-Mu schist	6.29	32.12	0.55	0.118107	0.511762	-17.1	-12.1	2205
	JC - 14B	Mylonitized Grt-Bt-Mu schist	8.01	20.37	0.05	0.236962	0.512328	-6.1	-8.6	-5594
	JC - 15	Grt-Bt-Mu schist	6.39	33.36	0.15	0.115372	0.512008	-12.3	-7.1	1766
	JC - 16	orthogneiss	–	13.45	0.04	–	0.512183	–	–	–
	JC - 18	Grt-Bt-Mu schist	7.11	37.41	0.04	0.114478	0.512039	-11.7	-6.4	1703
Sarpang-Damphu	**JC - 19**	Grt-Bt-Mu schist	8.58	44.54	0.48	0.116132	0.511875	-14.9	-9.7	1985
	JC - 20	Grt-Bt-Mu psammite	2.99	15.51	0.07	0.116205	0.511981	-12.8	-7.7	1822
	JC - 22	orthogneiss	7.42	36.51	0.45	0.122408	0.511782	-16.7	-12.0	2274

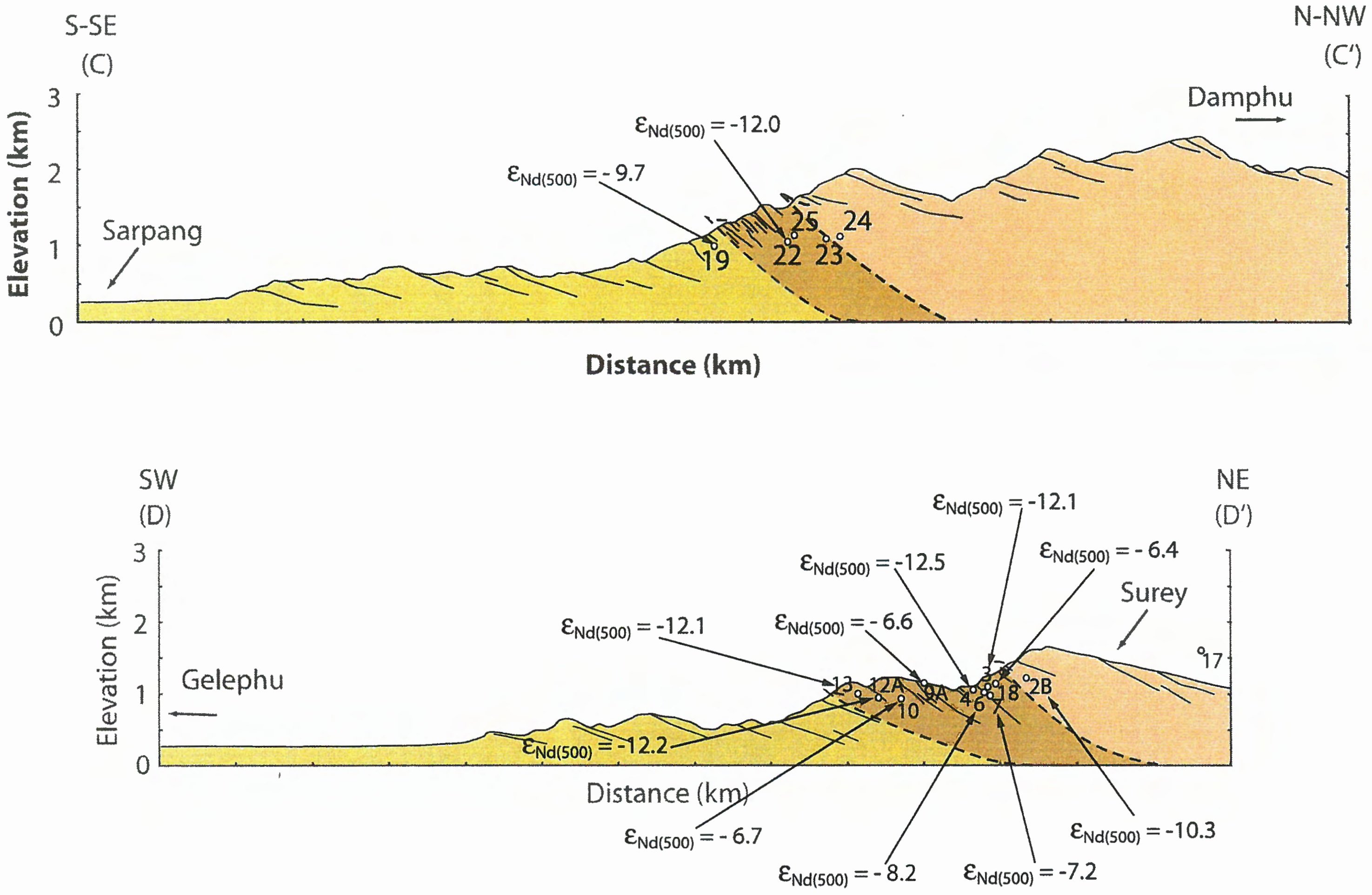

Figure 4.10: $\varepsilon_{Nd(500)}$ values in the Jaishidanda Formation. Location of samples along the Sarpang - Damphu and Gelephu – Surey transects, and $\varepsilon_{Nd(500)}$ values associated with the samples for which isotopic data is available.

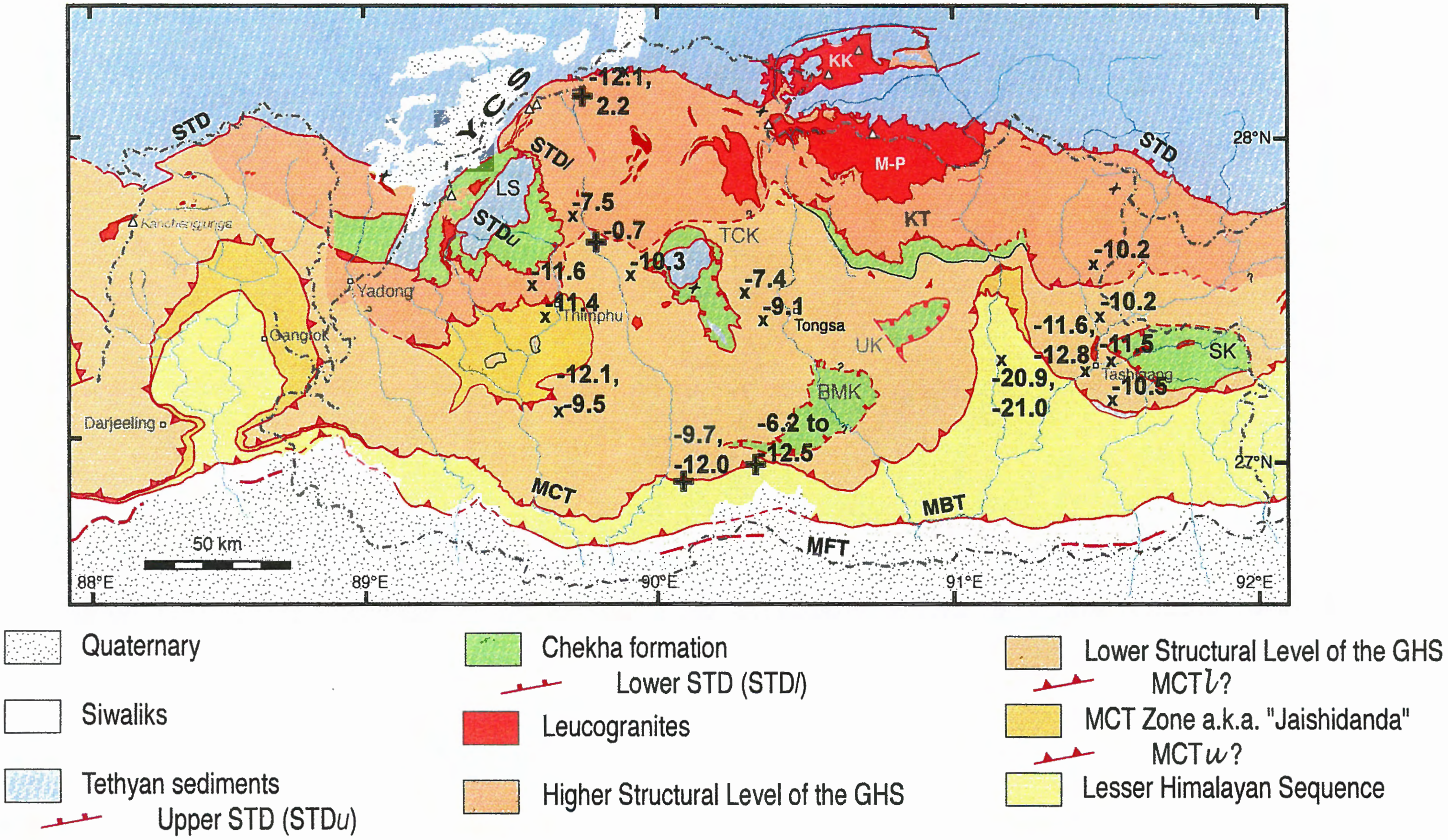

Figure 4.11: Distribution of $\varepsilon_{Nd(500)}$ in Bhutan. Regional map of Bhutan illustrating the sample locations and associated $\varepsilon_{Nd(500)}$ values. X's mark the location of samples analyzed and presented by Richards et al. (2006) as compared with values from this study. ✚'s mark the location of samples analyzed in this study.

that the zone of high strain, which is likely related to the MCT zone, is here confined to the base of the GHS and does not incorporate material from the highest structural levels of the LHS. There does not appear to be a correlation between samples that preserve growth zoned versus homogeneous garnets and their associated Nd model ages and/or ε_{Nd} values.

The presence of rocks in which garnets preserve growth zoning and their apparent intercalation and juxtaposition with rocks that preserve flat garnet profiles implies that an important metamorphic boundary exists within the Jaishidanda Formation and within the mylonite zone. Largely due to the absence of indicator minerals, it is difficult to constrain for both sample types, the nature of the prograde P-T path. However, preservation of growth zoning in samples yielding peak T approaching ~ 700 °C implies they were not subjected to peak temperature conditions for an extended period of time. In contrast, the preservation of homogeneous garnets in other samples suggests they were subjected to peak temperatures for a longer period than samples with growth zoned garnets. Samples were subjected to high T for periods long enough to either chemically homogenize previously zoned garnets or, as proposed by Hollister 1966 and 1969, to permit garnet growth such that garnets are in constant chemical equilibrium with the surrounding matrix minerals thereby preserving homogeneous growth profiles. Based on the P-T estimates, these samples do not appear to have exceeded $T > \sim 710$ °C, however this must be a minimum estimate because homogenization of the growth zoning could be expected to yield T estimates that are lower than true peak T conditions.

As discussed in the introductory chapter, throughout the GHS there is evidence for two stages of deformation and metamorphism, while locally there is textural evidence for three. The first stage (D_1) has been associated with under-plating of Indian continental material to high- and ultra-high pressure eclogite conditions beneath the Eurasian continent and Transhimalayan Zone (Pognante and Spencer 1991; Guillot et al. 1995). Associated with the second stage (D_2, ca. 23 - 16 Ma) is the continued development of south-directed thrusts and isoclinal folds throughout the GHS and TSS, as the GHS was experiencing partial melting followed by exhumation to the surface from midcrustal depths. The pervasive east-west trending foliation (S_2) observed throughout the GHS defines the axial plane of the isoclinal folds. Most prominent of the D_2

structures are the east-west striking, north-dipping MBT, MCT, and STD. Finally, deformation of the D_2 structures and the development of broad east-west trending open folds and shear bands (S_3) that cross cut the pervasive S_2 foliation occurred during the most recent, Neohimalayan phase of deformation (D_3) which is associated with continued exhumation and decompression of the GHS.

Microtextural analysis of metasediments from the Jaishidanda Formation reveals that the peak-T assemblage defines the regional fabric (S_2), suggesting it developed during D_2. In garnets of both types, the preservation of sigmoidal inclusion trails (S_1) that are discordant to the external foliation and the partial replacement of garnets by S_2 biotites suggest garnet growth commenced prior to and perhaps during the early stages of the main D_2 event (Figure 4.12). Inclusion free rims likely grew during a brief period of continued heating, perhaps during the initial stages of D_2. The intergrowth of biotite with muscovite, which defines the main foliation and C′-type shear bands (S_3) that cross-cut S_2, appears to have been contemporaneous with decompression at relatively high temperatures. This suggests that the breakdown of biotite to muscovite and the development of S_3 shear bands occurred with decompression associated with exhumation of the GHS between the STD and MCT zone. Truncation of zoning in many of the garnets also implies considerable dissolution upon decompression. Though sufficient field structural data is not available, intercalation of rocks that have experienced different metamorphic histories within the Jaishidanda Formation may have resulted from folding into a series of large-scale, tightly spaced isoclinal folds that might have been associated with the initial stages of channel exhumation. Development of the broad, open, north – south trending antiform, and breakdown of the micas to chlorite is probably associated with continued decompression and cooling.

In the context of the question, "How should the MCT be defined?", as discussed at the beginning of this chapter, the MCT has been defined as the boundary between the LHS and GHS. Davidson et al (1997) defined it as a protolith boundary between low-grade rocks of the LHS and high-grade rocks of the GHS, which may be found within a zone of intense/condensed top-to-the-south shearing (the MCT zone). This study reveals that the MCT zone in south-western Bhutan does in-fact incorporate a protolith boundary, however it is a boundary between low- and high-grade rocks that are *all* of GHS affinity.

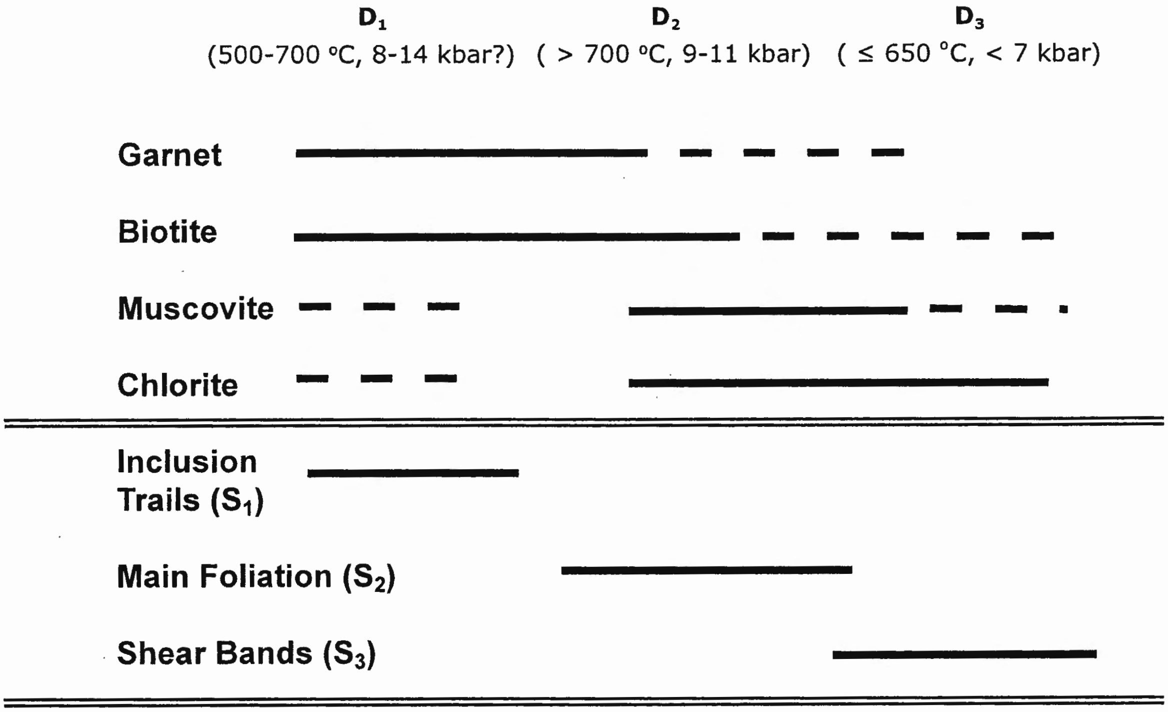

Figure 4.12: Mineral growth and deformation. Summary diagram relating mineral growth in the Jaishidanda Formation to stages of deformation. The range of P-T conditions presented for each stage of deformation and metamorphism are the range of estimates calculated in this study.

This implies that the MCT as defined by Davidson et al (1997) does not hold true along the transects presented here. In south-western Bhutan the trace of the MCT (i.e. the boundary between the LHS and GHS), should be drawn structurally below the MCT zone between the garnet-mica schists of the GHS and phyllites and quartzites of the LHS.

4.7 CONCLUSIONS

The Jaishidanda Formation in southwestern Bhutan marks a mylonite zone in which there has been intense top-to-the-south shearing. As a result it appears in outcrop as a unit of intercalated metasediments, augen- and orthogneisses that have been folded into a series of large-scale isoclinal folds between quartzites of the LHS and gneisses of the GHS.

Micro-textural analysis reveals garnet growth occurred prior to and perhaps during the earliest stages of D_2. Peak-T assemblages in the rocks define the regional S_2 foliation that developed during D_2, which is associated with mid-crustal heating leading to development of a mid-crustal channel followed by decompression at moderately high temperatures as the channel is extruded. Further breakdown of the peak assemblage is associated with continued decompression and cooling as the channel is exhumed to the surface, which is facilitated by surface erosion.

Nd Isotopic data implies that the rocks within the formation are of GHS affinity. P-T estimates suggest rocks were subjected to a minimum T of ~ 700 °C however, preservation of garnets with homogeneous and growth zoning suggests that the Jaishidanda Formation includes GHS rocks that were subjected to $T > \sim 700$ °C for protracted periods and GHS rocks that were not. The implications for this are that the Jaishidanda Formation, which is probably not a distinct unit but may rather be correlated with the MCT zone elsewhere in the Himalaya, is a zone of intense top-to-the-south shearing that has developed at the base of the GHS along a pre-existing metamorphic discontinuity within the GHS and does not correlate with a protolith boundary between the LHS and GHS as defined. Along the transect presented here, the boundary between the LHS and GHS lies structurally below the Jaishidanda Formation.

CHAPTER V: DISCUSSION

5.1 INTRODUCTION

The purpose of this study was to investigate the provenance, structure, and metamorphic history of the GHS in Bhutan with the aim of understanding the tectonic evolution of this relatively poorly known part of the Himalaya. In so doing, a secondary aim of the project was to test the applicability of the channel flow-extrusion hypothesis and its variants to this segment of the orogen. Specific objectives included: i) determining the age and protolith of metabasites within the GHS using geochemical and isotopic data (Chapter 2); ii) to determine P-T-t paths from different structural levels of the GHS using new and compiled structural and metamorphic data (Chapter 3); iii) to use geochemical and metamorphic data to determine whether or not the lowest structural levels of the GHS, called the Jaishidanda Formation in Bhutan, corresponds to the MCT zone, and if so, where within the unit the boundary between the LHS and GHS (the MCT) lies (Chapter 4). The purpose of this chapter is to synthesize the various datasets in order to evaluate the channel flow-extrusion as a valid hypothesis for the GHS in Bhutan.

The presence of pervasively sheared, migmatitic and high-grade rocks of the GHS between the MCT and STD, and the realization that movement along the two structures was contemporaneous has led geologists to view the GHS as an extruding channel of mid-crustal material that has flowed southward from beneath the Tibetan Plateau where the crust is thick, into relatively thinner crust (Hubbard and Harrison 1989; Searle and Rex 1989). The model that best illustrates this concept is the thermo-mechanical channel flow-extrusion models (HT1 and HT111) of Beaumont et al. (2001; 2004), which predicts the development of a low-viscosity channel in a thickened crust by partial melting of material derived from the Indian margin, that has been underthrust to mid-crustal levels at $T \geq 700$ °C (Figure 5.1). The low-viscosity material, which is bounded on two sides by more competent crust, deforms by induced shear and gravity driven flow as a consequence of topographically induced pressure gradients above the channel. With surface erosion, outward flow of the subsurface channel is directed upwards towards the eroding front, leading to ductile extrusion of the low-viscosity material. The rate at

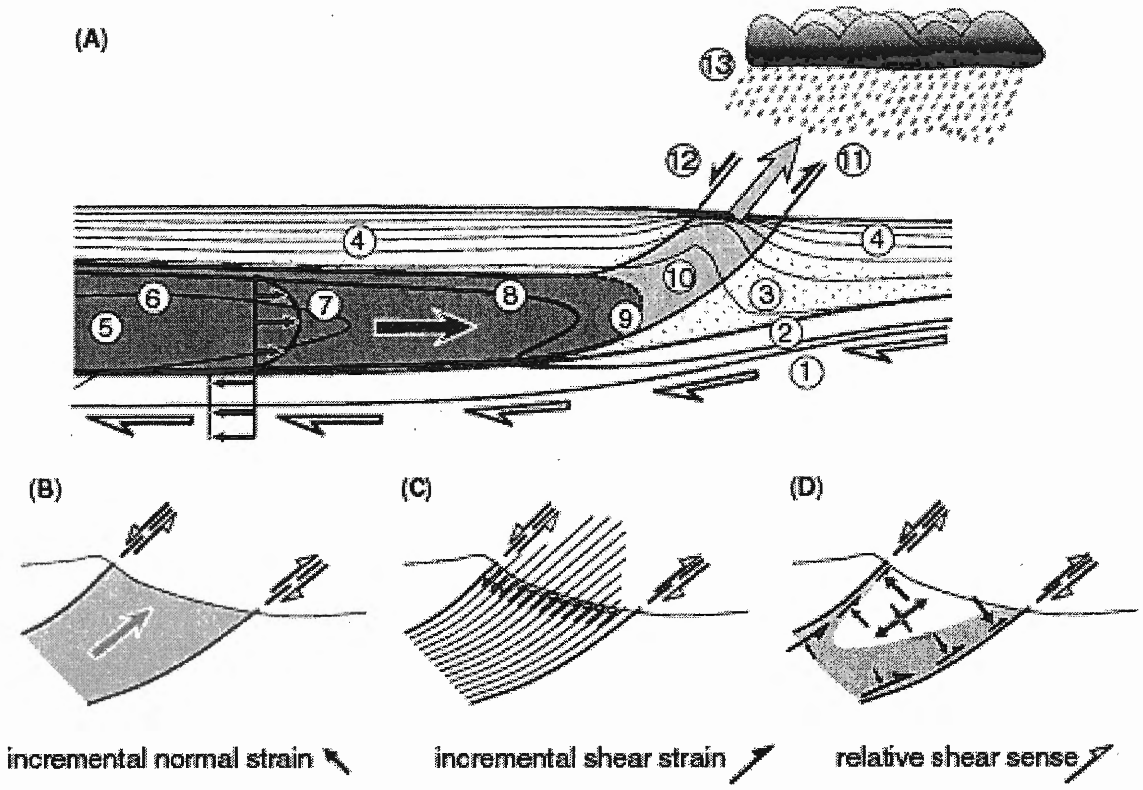

Figure 5.1: Relationship betwen channel flow and extrusion of a palaeo-channel.
A) A schematic diagram taken directly from Godin et al. (2006) illustrating the kinematic relationship between channel flow and extrusion of a palaeo-channel. **Legend:** ***1***, Lithospheric mantle; ***2***, lower crust; ***3,*** mid-crust; ***4,*** upper crust; ***5,*** weak crustal channel; ***6,*** isotherms (taken from Beaumont et al. 2004), ***7,*** schematic velocity profile during return channel flow; ***8,*** 750 °C isotherm structurally below which partial melt starts; ***9,*** rheological tip of the channel: at lower temperatures (for a given channel width and pressure gradient) Couette flow will dominate and all the material will be underthrust; ***10,*** extruding crustal block (palaeo-channel): if the rheological tip is at steady state, material points may move through this tip and pass from the weak crustal channel into the extruding block; ***11,*** lower shear zone of the extruding crustal block (thrust-sense kinematics); ***12,*** upper shear zone of the extruding crustal block (normal-sense kinematics); ***13,*** focused surface denudation which is controlled by surface slope and by orographic precipitation at the topographic front. (B)–(D) Potential endmembers for strain distribution in an extruding crustal block(after Grujic et al. 1996; Grasemann et al. 1999). (B) Rigid block with high concentration of strain along the boundaries (Hodges et al. 1996). (C) Ductile block deforming by pervasive simple shear. (D) Ductile block deforming by general shear with a pure shear component increasing towards the bottom of the wedge, as well as with time following a 'decelerating strain path' (Grasemann et al. 1999; Vannay & Grasemann 2001).

which material is extruded/exhumed is proportional to the rate of channel flow and the rate of erosion.

The model also predicts that extrusion of the low-viscosity channel occurs between two bounding shear zones that have opposite shear sense - the roof accommodating either normal or thrust sense displacement depending on the relative velocities of the channel and overlying crust, while displacement on the sole shear zone is always thrust sense (Figure 5.1). If the channel is exhumed as a rigid body, deformation could be expected to be confined to the boundaries (Figure 5.1B; Hodges et al. 1996). However, field evidence for top-to-the south shear sense kinematics is pervasive throughout the GHS, implying the extrusion of the GHS as a ductile body (Figure 5.1C & D). Surface exposures of the channel margins reveal that they are zones of intense strain. Whether these zones of high strain are features of late-stage exhumation rather than deformational features that developed within the channel at depth remains poorly constrained.

Detailed descriptions of the model parameters can be found in Beaumont et al. (2001; 2004) and Jamieson et al. (2004). A comparison of the two models of Beaumont et al. (2001; 2004) and the conceptual model of Hollister and Grujic (2006) is presented in Table 5.1. For the most part, model HT111 is similar to HT1 except that a thin weak layer has been embedded into the upper crust, which has a significant effect on its evolution. In both models, which are run for 54 million years, the onset of channel flow occurs at ca. 30 Ma and exhumation begins at ~ 15 Ma. Initially, the head or rheological tip of the channel is symmetrical, but with detachment and outward flow of the overlying crust becomes asymmetrical. In model HT1, domes (equivalent to the northern gneiss domes in southern Tibet) do not develop between the suture and erosion front because the overlying "Tethyan" crust remains relatively thick and strong (Figure 5.2a). HT111, on the other hand, behaves differently from HT1 after 24 Ma. In the second model, detachment and outward flow is facilitated in the upper crust above the channel due to the presence of the weak layer. As a result of the enhanced southward flow, the orogenic front in HT111 propagates further to the south relative to HT1 leading to the enhanced advection of the isotherms, which form a lobe in the mid- and upper crust. As cold and strong Indian cratonic material continues to move northward, the hot channel is forced to

Table 5.1: Comparison of thermo-mechanical models HT1, HT111, and the conceptual model of Hollister and Grujic (2006).

Model HT1	Model HT111	Pulsed Flow
** For detailed description of model parameters, refer to Beaumont et al. (2004) and Jamieson et al. (2004)	** For detailed description of model parameters, refer to Jamieson et al. (2006)	** For detailed description of model parameters, refer to Hollister and Grujic (2006)
1) Advancing subduction model with a three-layered crust and focused denudation.	1) Advancing subduction model very similar to HT1. Difference is presence of an additional weak layer in the upper crust.	1) Concept based on the basic HT1 model of Beaumont et al. (2004). Inconsistencies between model predictions and field data rationalized by considering pulsed channel flow rather than the single, temporaly and spatially continuous episode of channel flow of model.
2) Channel flow initiates at c. 30 Ma. North of suture, upper crust thickens significantly leading to necking and detachment of mid-crust from strong lower Asian crust.	2) Channel flow initiates at c. 30 Ma. Because of weak layer, upper crust north of suture does not thicken significantly. Asian mid- and lower crust remain strongly coupled and are transported southward over thin (< 20 km) attenuated zone of "Indian" crust.	2) Initial pulse of channel flow between 22-16 Ma, bringing presently exposed GHS into juxtaposition with the LHS at depth between 18-16 Ma.
3) Onset of channel extrusion at ca. 15 Ma.	3) Weak layer in upper crust facilitates detachment and outward flow of upper crust above the channel, permitting propagation of orogen further southward than in model HT1. As a result, region between suture and orogenic front is wider, and advection of isotherms is enhanced forming a lobe that extends into mid- and upper crust.	3) Second pulse of channel flow between 16-13 Ma, leading to rapid exhumation of GHS AND portion of LHS under the MCT zone to depth of 15 km, above closure T for micas.
4) Extruded channel initially symmetrical but with detachment and weakening of upper crust becomes asymmetrical. Crust above channel remains coherent, therefore domes do not develop between suture and erosional front.	4) Underthrusting of cool and relatively stronger mid-crust forces hot channel over the cooler mid-crustal ramp, further destabilizing upper crust and forming a dome that is underlain by channel material. Doming is continuous process with flow and extrusion of channel (i.e. no pulsing).	4) Third pulse of channel flow between 12-10 Ma, leading to doming of North Himalayan Gneiss domes and extrusion of upper portion of GHS in Bhutan between out of sequence Kakhtang Thrust and STD.
5) Region between erosional front and suture underlain by "Indian" material, as is "Asian" upper and mid-crust ≥ 200 km north of suture.	5) Region between erosional front and suture underlain by "Asian" and thin bit of "Indian material. Upper two-thirds of crust north of suture comprises "Asian" material.	5) Leucogranites at the MCT first to solidify because quenched by cooler rocks of the footwall. Presence of andalusite in leucogranite just below the STD suggests fluid-present melting and solidification at fairly low- P.
7) Region between suture and orogenic front occupied by "Indian" derived material. Offset on MCT > 600 km. "GHS" derived from distal "Indian" mid- and upper crust originiating < 1000 km south of suture.	7) Region between suture and orogenic front occupied by "Indian" derived material. Offset on MCT > 400 km. "GHS" derived from distal "Indian" mid- and upper crust originiating < 1000 km south of suture.	6) Hanging wall of STD south of Kakhtang Thrust comprises low grade rocks of Chekha Formation. Encasement of GHS in low-grade Jaishidandha and Chekha Formations consistent with GHS being at ~ 15 km at final stage of extrusion.
8) P-T-t paths for lower "GHS" pass through medium-P muscovite dehydration melting field between 30-15 Ma.	8) P-T-t paths for lower "GHS" pass through medium-P muscovite dehydration melting field between 30-15 Ma.	
9) P-T-t paths for upper "GHS" pass through fluid-present melting field some passing through as early as 40 Ma.	9) P-T-t paths for upper "GHS" pass through fluid-present melting field some passing through as early as 40 Ma.	
10) P-T-t paths for "GHS" never passes through andalusite + melt field, therefore cannot account for low-P andalusite bearing leucogranites.	10) Doming and extrusion leads to isothermal decompression. P-T-t paths stay in melting field to medium - shallow P, crossing andalusite + melt field at ca. 12 Ma.	

A) Model HT1: Simple Channel Flow with focused erosion.

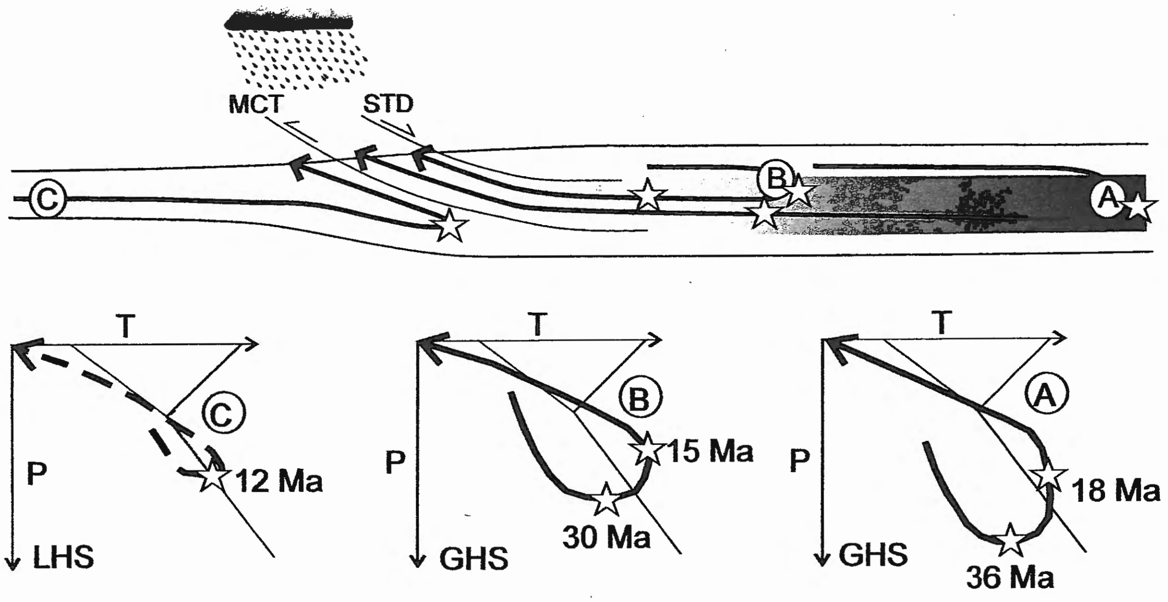

B) Model HT111: Channel Flow and extruded dome.

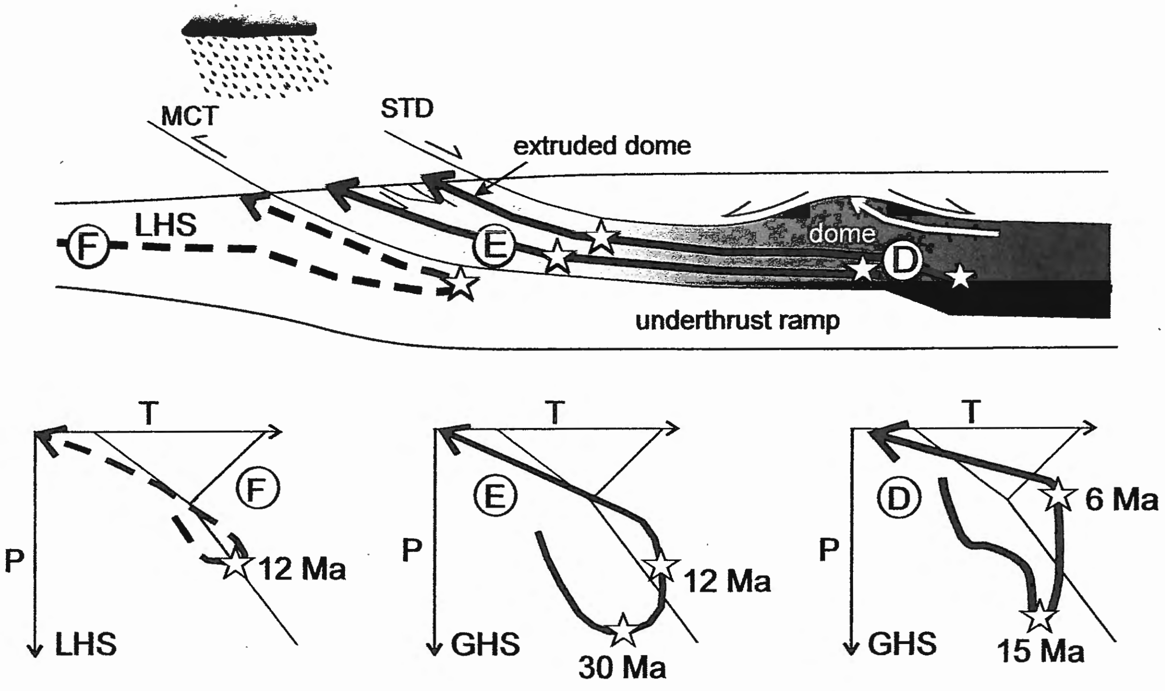

Figure 5.2: Schematic diagrams of thermomechanical models a) HT1 of Beaumont et al. (2001, 2004) and Jamieson et al. (2004), and particle paths associated with particles in the model "LHS" and "GHS"; b) HT111 of Beaumont et al. (2006) and Jamieson et al. (2006) and particle paths associated with the model "LHS" and "GHS". This second model is that on which the conceptual model of Hollister and Grujic (2006) is based.

flow up and over the cool incoming mid-crustal ramp further destabilizing and forming a gap in the upper crust giving rise to a dome of low-viscosity material (Figure 5.2b). With extrusion of this dome, initially formed structures may evolve into flattened nappes. Continued convergence eventually leads to the exhumation of a second dome. The third, conceptual model of Hollister and Grujic (2006) is largely based on models HT1 and HT111. The major difference between them is that flow and subsequent exhumation of the channel and later domes is a continuous process in models HT1 and HT111, while Hollister and Grujic (2006) interpret the process to occur in pulses that are largely controlled by variations in surface erosion and/or convergence rates.

Tracking particle paths in the "GHS" of models HT1 and HT111 reveals that they follow relatively broad loops through P-T space in roughly three stages (Figure 5.2; Jamieson et al. 2004). All particles are characterized by an initial stage of burial and heating with relatively steep prograde P-T paths into the kyanite field. Depending where within the channel particles are entrained, prograde metamorphism is followed by a stage of near isobaric heating (i.e. particles that become entrained in the low-viscosity channel) and then experience near isothermal decompression at high-T. The third and final stage, which is associated with cooling and decompression along a moderately sloped retrograde path, is common to all particles (Figure 5.2). In contrast, tracking particle paths in the "LHS" of model HT1 reveals that they follow tight hairpin loops. All particles are characterized by an initial stage of burial and heating into the kyanite field where peak-P conditions are reached at approximately the same time as peak-T, reflecting brief residence times in the orogen (Figure 5.2). Heating during exhumation is experienced only by "LHS" particles that are buried earlier and deeper relative to shallower particles, thereby reflecting longer residence times in the orogen.

5.2 PROVENANCE OF METABASIC ROCKS

Major and trace element geochemistry suggests metabasic rocks collected from the GHS immediately below the STD (the higher structural level), and further south ("mid"-structural level) are tholeiitic in nature. With respect to major and high-field strength elements, metabasites are characterized by slight negative Nb, Zr and Ti anomalies, which are commonly associated with melts derived from a source situated above a subduction zone. In addition, all metabasites are enriched in the REEs and high field strength elements relative to primitive mantle and NMORB, implying an enriched sub-lithospheric mantle source for these rocks either via subduction-related processes or by the assimilation of continental lithospheric components. The close association of the metabasites with the large volume of metasedimentary paragneisses that were originally deposited on the Indian continental margin suggests the metabasites likely intruded into the basement and overlying cover rocks of the Indian plate as dykes and sills. Zircons in these rocks preserve Paleo - Mesoproterozoic cores that are interpreted to represent the timing of magmatism.

The results of this study correspond with observations made further to the west, in the Garhwal and Zanskar Himalaya (Ahmad and Tarney 1991; Miller et al. 2000). In the west, preservation of Paleo-Mesoproterozoic within-plate basalts in the LHS that are chemically similar to the metabasites studied here, implies a major thermal event caused the mobilization and enrichment of the sub-continental lithosphere beneath much of the northern continental margin of India, and that magmatic activity was prevalent along the margin between the Paleo-Mesoproterozoic when India would have formed part of northern Gondwanaland (Figure 5.3; Brookfield 1993). Paleo-reconstructions of the Indian margin from the Precambrian through to the present indicate four main periods of rifting affected the passive margin of northern Gondwanaland. The earliest of these magmatic phases occurred during the Neoproterozoic and was followed by a period of early Ordovician deformation prior to the development of the stable shelf (Brookfield, 1993). The results of Ahmad and Tarney (1991), Miller et al. (2000) and this study would suggest an even earlier period of rifting along the northern Gondwanaland margin, during the Paleo- Mesoproterozoic.

Extensive provenance studies carried out on detrital zircons from the LHS and GHS in the western and central Himalaya (e.g. Parrish and Hodges 1996; Hodges 2000; DeCelles et al. 2000; Argles et al. 2003; Gehrels et al. 2003; DeCelles et al. 2004; Martin et al. 2005) suggest that all crustal material between the Indus-Tsangpo suture and orogenic front comprises deformed and metamorphosed north Indian continental margin material (Myrow et al. 2003). The isotopic signature of the LHS (U-Pb 1600 – 2600 Ma; $T_{DM} > 2.0$ Ga; $\varepsilon_{Nd} < -20$) indicates it is a Paleo- to Mesoproterozoic sequence, and that it is isotopically distinct from the GHS which is believed to represent a Neoproterozoic to

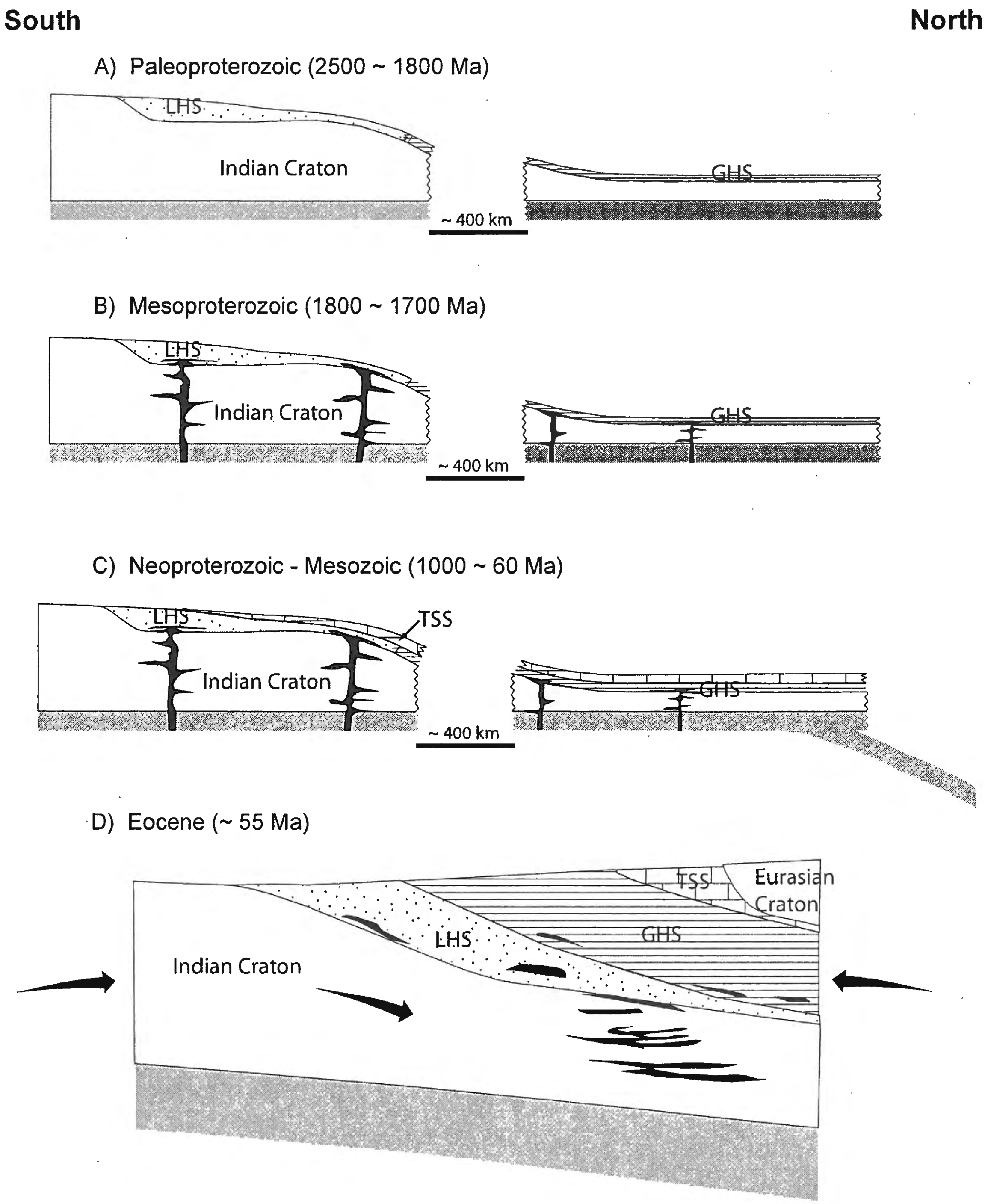

A) Paleoproterozoic (2500 ~ 1800 Ma)

B) Mesoproterozoic (1800 ~ 1700 Ma)

C) Neoproterozoic - Mesozoic (1000 ~ 60 Ma)

D) Eocene (~ 55 Ma)

Figure 5.3: A schematic cartoon illustrating the evolution of the north Indian margin from the Paleoproterozoic to the Eocene, prior to the development and extrusion of the mid-crustal channel. A) The north Indian margin in the Paleoproterozoic; B) Based on U-Pb data from this study and the Garwhal Himalaya, the margin was affected by a period of magmatism that affected the LHS and GHS. C) The margin was affected by a period of deformation and metmamorphism during the Cambro-Orodovician, followed by three more periods of magmatism prior to the subduction of the proto-Tethys Ocean. D) The initial stages of continent-continent collision in the Himalayan orogen.

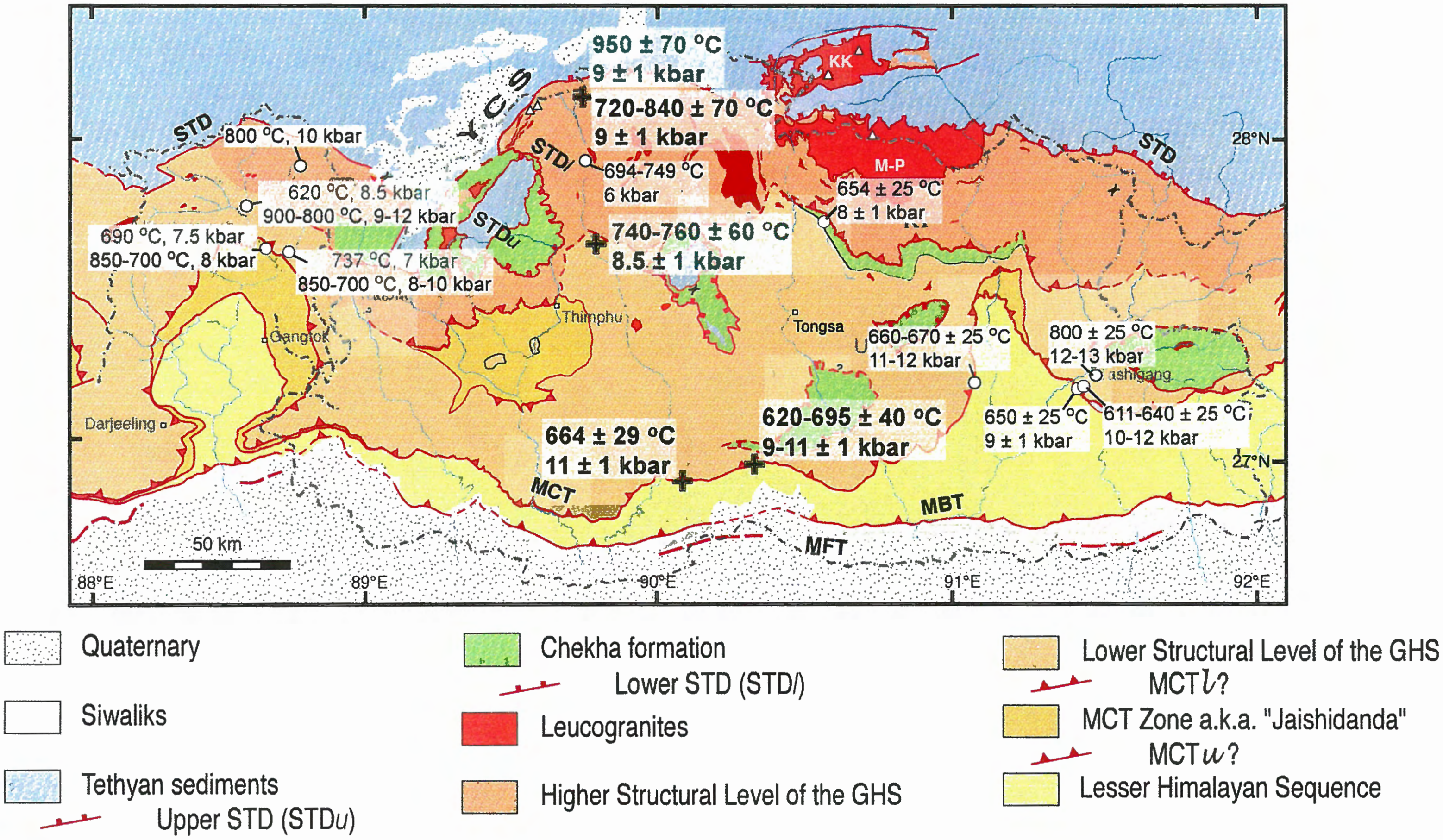

Figure 5.4: Regional distribution of P-T data. Regional map of Bhutan illustrating the spatial variation of sample locations and the associated P-T estimates that have been presented in Chapters 3 and 4 (✚) and in previous studies (○). Values presented in green are estimates made on metabasic rocks, values presented in black are for metasedimentary rocks. P-T estimates that were not calculated in this study have been compiled from Davidson et al. (1997), Neogi et al. (1998), Ganguly et al. (2000), Daniel et al. (2003) and Ritchie (2004).

early Paleozoic succession (U-Pb 500 – 1000 Ma; $T_{DM} < 2.0$ Ga; $\varepsilon_{Nd} > -20$). Studies of magmatic zircons in igneous units also suggest the rocks of the LHS were affected by magmatic activity during the Paleo- and Mesoproterozoic (2.0 - 1.8 Ga; DeCelles et al. 2004). Similar studies have suggested that magmatic activity during the Neoproterozoic (~ 823 Ma; Singh et al. 2002 and references therein) and upper Cambrian – Ordovician (490 – 470 Ma; DeCelles et al. 2004 and references therein) was restricted to rocks of the GHS. The U-Pb and Sm-Nd results of this study, though admittedly limited, suggest that locally within the GHS evidence for Mesoproterozoic magmatic activity does exist and that Paleo-Mesoproterozoic magmatism was not confined solely to the LHS.

With respect to the thermo-mechanical model results of Beaumont et al (2001; 2004), models HT1 and HT111 predict that the region between the suture and orogenic front is occupied by Indian material (Jamieson et al. 2006), supporting the observations made across the orogen. In both experiments, the LHS is derived from the mid- and upper paleo-Indian crust that was deposited > 1400 km south of the suture - proximal to the continental margin (Figure 5.3), while the GHS is derived from mid- and upper Indian crust deposited ≤ 1000 km south of the suture – further offshore than LHS detritus. Depending on the model, this implies ≥ 600 km (HT1) to ≥ 400 km (HT111) of offset along the MCT (Jamieson et al. 2004; 2006).

5.3 TECTONIC AND METAMORPHIC EVOLUTION OF THE GHS

The P-T estimates calculated for metabasic and metasedimentary rocks in Chapters 3 and 4 have been compiled and summarized in Figure 5.4. A spatial comparison of the data with data from previous studies conducted in Sikkim and Bhutan reveals that i) peak-T estimates are greatest (> 800 °C) in the highest structural levels of the GHS, proximal to the STD, and decrease (650-700 °C) down-section to the MCT zone, ii) pressures associated with peak-T estimates are moderate proximal to the STD (~ 9 kbar) and increase down-section towards the MCT zone (11-12 kbar), and iii) the data are comparable with the estimates calculated in previous studies for Bhutan (i.e. Davidson et al. 1997; Daniel et al. 2003; Ritchie 2004) and Sikkim (Neogi et al. 1998; Ganguly et al. 2000). A spatial comparison of the curves drawn through the estimates reveals that the shape of the P-T paths followed by rocks also varies with structural level,

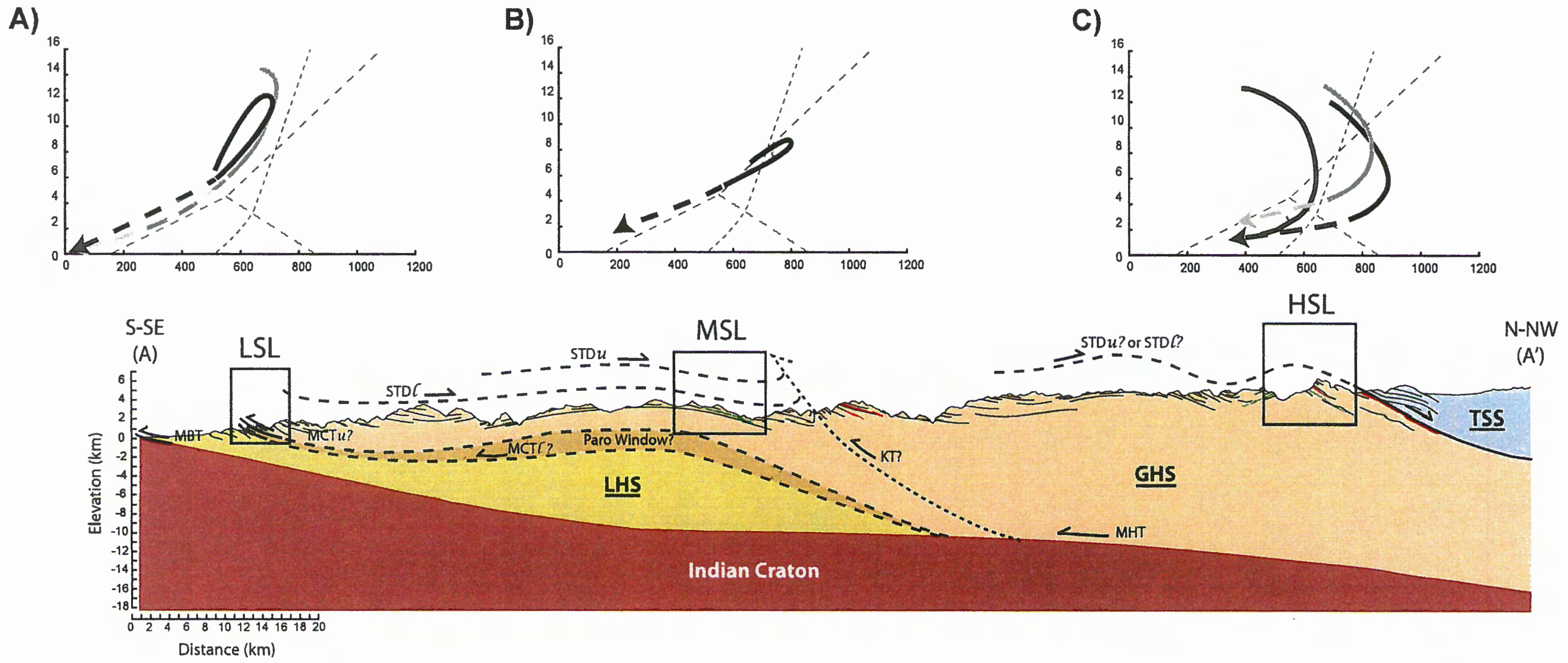

Figure 5.5: Shape of P-T paths across the GHS in western Bhutan in the context of the cross-section presented in Figure 4.1. A) Estimated P-T path for metasediments from the Jaishidanda Formation with growth zoned garnets (black curve) and homogeneous garnets (grey curve). B) The P-T path for metabasites from the "mid"-structural level of the GHS. C) P-T curve for metasediments (grey curve) and metabasites (black curves) from the highest structural position along the transect, just below the STD. The position of the Al_2SiO_5 triple point is after Pattison (1992), while the position of the muscovite melting curve is after the reference Pëto (1976) given in Pattison (2003).

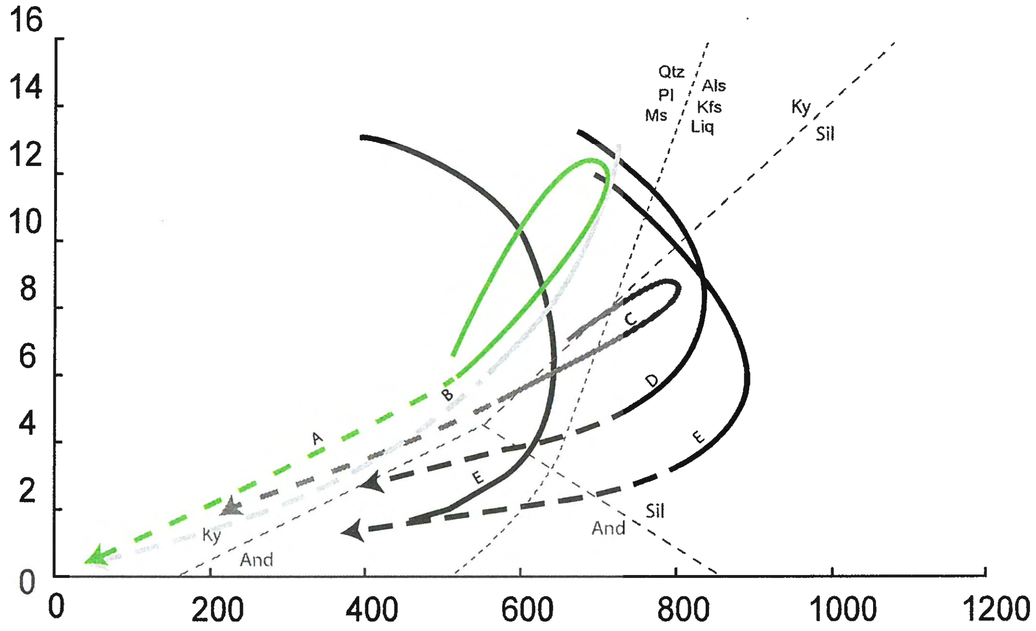

Figure 5.6: A comparison of P-T paths across the GHS in western Bhutan. A) Estimated P-T path for metasediments from the Jaishidanda Formation with growth zoned garnets. B) P-T path for metasediments from the Jaishidanda Formation with homogeneous garnets. C) The P-T path for metabasites from the apparent mid-structural level of the GHS. D) P-T curve for metasediments from the highest structural position along the transect. E) Curves for the metabasites from the highest structural postion along the transect, just below the STD. The position of the Al_2SiO_5 triple point is after Pattison (1992), while the position of the muscovite melting curve is after the reference Pëto (1976) given in Pattison (2003).

hairpin loops characterizing rocks that were not subjected to peak-T for protracted periods versus broad and open loops characterizing those that were (Figure 5.5 and 5.6).

Comparing the P-T paths (Figure 5.5) to the predicted particle paths in model HT1 (Figure 5.2a; Jamieson et al. 2004), there are marked similarities. The estimated P-T paths for rocks with homogeneous garnets in the lowest structural levels, and all rocks in the highest structural levels are similar in appearance to the predicted path for particle A, which starts in the model GHS, ~ 400 km north of the orogenic front (Figure 5.2a). With continued orogenesis, the particle is buried and subject to increasing temperatures along a relatively steep prograde path into the kyanite stability field. The particle then becomes entrained within the model channel where, as it is carried towards the orogenic front, it undergoes continued heating at near isobaric conditions until it reaches maximum temperatures of > 800 °C. With the onset of extrusion, and as a consequence of the lobate form of isotherms, the rock is exhumed briefly at near isothermal conditions. Despite the compatibility between the shape of the predicted and actual particle paths, the model predicts that the particle will be exhumed to a position above but proximal to the MCT (i.e. the base of the channel). This corresponds well with the curve for relatively high-grade rocks at the lowest structural levels (i.e. samples with homogenous garnets), but not with the curve for rocks at the highest structural levels just below the STD.

For rocks from the "mid"-structural level, the actual P-T loop closely resembles the path followed by particle B in model HT1 (Figure 5.2a). The particle is characterized by a hairpin P-T loop because it does not have a long residence time within the channel, perhaps because its initial position was closer to the orogenic front and at shallower levels within the crust relative to A. The model however, predicts that the particle will be exhumed below but proximal to the STD (i.e. the top of the channel). As described in chapter 3, metabasites were collected in what appeared to be the 'middle' of the channel. The implications of this are that either the model predictions are incorrect, or that rocks that appear to be in 'the middle' are actually situated at the top of an early channel over which a second channel or dome has been exhumed (Figure 5.2b). In either case, model HT1 predictions are not compatible with the data for rocks from the highest and "mid"-structural level of the GHS in western Bhutan, thus an alternate model must be used to explain the data, the most plausible being HT111.

As discussed above, the major difference between model HT111 and HT1 is that a weak layer has been embedded into the crust above the channel thereby facilitating enhanced southward flow of the low-viscosity material (Beaumont et al. 2004). Particles in the first channel follow paths very similar to those presented for model HT1 (Figure 5.2b particle E). As cold and strong Indian cratonic material continues to move northward, the hot channel at depth flows up and over the cool incoming mid-crustal ramp, further destabilizing and forming a gap in the upper crust giving rise to a dome of low-viscosity material (Figure 5.2b). The particle path for this dome corresponds with P-T path D in Figure 5.2b, which broadly corresponds with the path associated with the rocks at the highest structural level in that it is characterized by a relatively long segment that is associated with decompression at high-T. As a result of the exhumation of a dome over a pre-existing channel, the surficial extent of the high-grade material would appear to be significantly broader than in the case of only one channel. Also, rocks at the 'mid'-structural level of the unit (actually the top of an earlier channel) could be expected to preserve P-T paths (particle E, Figure 5.2b; Jamieson et al. 2006) that are similar in appearance to the path predicted for particle A, which was extruded at the top of the channel in model HT1. Material in the second channel/dome remains at high-T during exhumation of the first channel, and during the initial stages of its exhumation. In this second channel, rocks are predicted to follow paths that are characterized by longer segments associated with high-T decompression (i.e. Figure 5.2b, particle D). Model HT111 predicts that the time gap between the exhumation of the two units is <10 million years, thus extrusion of the two is a continuous process. Whether or not this process of doming is a continuous process, or occurs in pulses with significant time gaps (i.e. > 20 Myrs?) between extrusion of the individual channel bodies depends on any variations in surface erosion and/or convergence rates (Hollister and Grujic, 2006).

5.3.1 DETAILED COMPARISON OF THE DATA WITH MODEL HT111

Following the onset of continent-continent collision between the Indian and Eurasian margins at ~ 55 Ma (Rowley 1996; Searle et al. 1997) a period of large scale thrusting and isoclinal folding has been associated with crustal thickening and underthrusting of the Indian continental crust (Figure 5.7a; Stephenson et al. 2000 and references therein). Though deformation and metamorphism were not confined to a

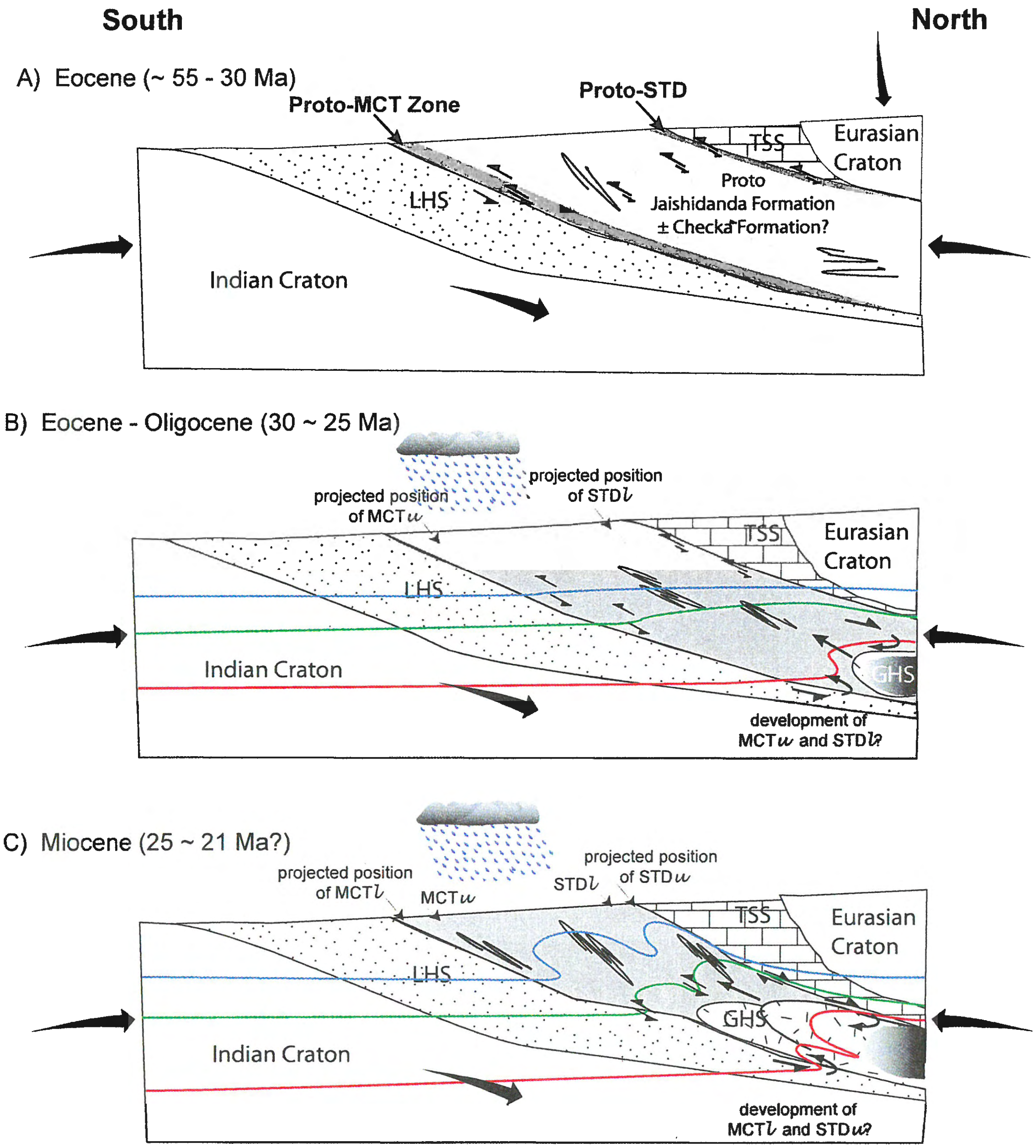

Figure 5.7: Schematic diagram illustrating the evolution of the GHS in Bhutan. Ideas presented in the diagram are based on the concepts of Beaumont et al. (2001, 2004) and Jamieson et al. (2004, 2006). Coloured lines drawn through the crust represent isotherms, red being deeper and hotter relative to the blue isotherm which is shallower and therefore cooler. A) The early stages of crustal thickening, prior to the development of a mid-crustal, low viscosity channel. B) Radiogenic heating of over thickened mid-crustal material leads to the development of a low-viscosity channel that is driven to flow as a consequence of topographically induced pressure gradient. C) Incoming mid-crustal ramp forces its way under the earlier channeland leads to development and migration of a low-viscosity dome overtop the first.

particular zone, indirect evidence for this stage of orogenesis is largely restricted to the Transhimalayan zone and TSS of the Tso Morari and Zanskar regions, where high- and ultrahigh-pressure eclogite facies metamorphism of the TSS and possible GHS affinity are exposed and have not been overprinted by subsequent metamorphism (Pognante and Spencer 1991; Guillot et al. 1995; de Sigoyer et al. 1997). Barrovian metamorphism associated with this period of crustal thickening gave rise to the regional development of garnet, staurolite, kyanite and sillimanite as pelitic and semipelitic rocks of the GHS were underthrust to 9-10 kbar between ~ 44 – 25 Ma (Bhattacharyya and Das 1983; Stephenson 1997; Vance and Harris 1999; Foster et al. 2000).

In Bhutan, metabasites and metasediments immediately below the STD have, for the most part, been erased of all mineralogical information pertaining to the prograde segment of their metamorphic evolution. However, the localized preservation of kyanite inclusions in garnet of metasedimentary rocks (Swapp and Hollister 1991; Davidson et al. 1997; this study), and the coexistence of garnet and clinopyroxene in metabasites suggests rocks at the highest structural level were subject to peak pressures of 10-13 kbar at temperatures of 500 ~ 750 °C (Figure 5.5, 5.6), which is in agreement with estimates calculated for metabasic rocks at similar structural levels in the Sikkim Himalaya (Figure 5.4; Neogi et al. 1998). Following peak-P, the breakdown of garnet and clinopyroxene to orthopyroxene in metabasites illustrates that rocks experienced continued heating associated with decompression to ~ 9 kbar and > 800 °C (Figure 5.5, 5.6; Neogi et al. 1998; this study). This is also reflected in the P-T evolution of the encompassing metasediments in which garnet breakdown was associated with development of fibrolitic sillimanite (Ganguly et al. 2000; this study) and/or the pseudomorphing of kyanite by fibrolite (Swapp and Hollister 1991; Davidson et al. 1997; Stephenson et al. 2000). The implications of this are that peak-T conditions in the highest structural levels of the GHS across the orogen were not attained concomitantly with peak-P, but after a period of decompression followed by a protracted period of near isobaric heating (Swapp and Hollister 1991), an observation that is also reflected in the predicted paths (Figure 5.2). The penetrative planar fabric observed throughout the GHS (S_2) is defined by biotite and sillimanite that developed as a consequence of the breakdown of garnet. Thus, ductile deformation in the GHS was probably contemporaneous with the persistence of peak-T conditions.

Further down section, in the apparent mid-structural levels of the GHS in Bhutan, metasedimentary rocks are of garnet-sillimanite grade and contain muscovite. Metabasites lack clinopyroxene and contain large (> 2 cm) garnets that weakly preserve growth zoning. Garnet cores in these metabasites developed during prograde metamorphism at 600 – 700°C and 7 - 8 kbar (Figure 5.5). P-T estimates made on large garnet rims in metabasites indicate continued garnet growth from 700 – 800 °C at near isobaric conditions (8 - 9 kbar; Figure 5.5). Once peak conditions were reached, the hairpin P-T loop illustrates that metabasites at this level were not at high temperatures for very long before the onset of decompression and cooling.

In the lower structural levels, rocks in the Jaishidanda Formation contain garnets with sigmoidal inclusion trails characterizing their cores, and thin inclusion-free rims. Based on the shape of the P-T loop that characterizes these samples, inclusion-free rims appear to have developed during a brief period of increasing temperature at near isobaric conditions followed by garnet and biotite breakdown to muscovite and chlorite during isothermal decompression between ~ 650 - 700 °C. Homogenization of these garnets suggests that they may have remained at high temperatures for 2-3 Myr. Growth zoned garnets, however, are associated with hairpin paths suggesting they were rapidly exhumed following peak-T metamorphism.

As discussed in chapter 1, several heat sources that may account for high-T metamorphism of the GHS have been proposed (Le Fort 1975; Hodges and Silverberg 1988; Molnar and England 1990). In this study, however, the model of Beaumont et al. (2001; 2004), which relies on a radiogenic heat source in a tectonically thickened crust, is preferred. In their model, tectonic thickening of the crust gives rise to a large volume of low-viscosity radiogenic material at mid-crustal levels where temperatures are > 750 °C (Figure 5.7b). Due to the variation in crustal thickness between the Tibetan Plateau to the north and orogenic foreland to the south, the resulting pressure gradient in the upper crust forces the low-viscosity material to flow laterally, which may account for a period of near isobaric heating that is observed in this study and the GHS of the Sikkim and Zanskar Himalaya (Neogi et al. 1998; Stephenson et al. 2000). As the model progresses, surface denudation on the pro-side of the orogen facilitates rapid exhumation of the mid-crustal channel towards the erosional front. Migration of the hot channel material beneath the relatively cold upper crust leads to enhanced advection of the isotherms, which forms a thermal lobe in the mid- and upper crust (Figure 5.7c). With erosion at the surface, the extruding channel material undergoes a period of relatively rapid isothermal decompression at high temperatures particularly during the initial stages of extrusion (Figure 5.7c).

Evidence for out-of-sequence thrusting in western Bhutan?

In eastern Bhutan, at mid-structural levels sillimanite grade gneisses and leucogranites are thrust over lower, staurolite grade rocks along the out-of-sequence Kakthang Thrust (KT; Swapp and Hollister 1991; Grujic et al. 1996; Davidson et al. 1997). The local preservation of an inverted metamorphic gradient in the mid-structural levels of the GHS along the KT implies that the GHS must have cooled relatively rapidly such that advective heat from hanging wall rocks did not overprint the underlying 'cool' footwall rocks, or that movement along the thrust occurred after hanging wall rocks had cooled to temperatures low enough not to affect the footwall. An alternate explanation is that in the type locality for the KT, where staurolite-grade rocks are preserved below sillimanite grade rocks, leucogranites are not common thus excess heat was not available to facilitate heating of the footwall rocks (Davidson et al. 1997).

In this study, which is to the west, along strike from the type locality, leucogranites are associated with GHS rocks both above and below the projected KT. Rocks on either side of the thrust are also of sillimanite grade with migmatites in the footwall containing minor muscovite. The P-T path for metabasites in the footwall appears similar in shape to the path associated with particle E, which is predicted to appear at the top of the first exhumed channel in model HT111 (Jamieson et al. 2006). Davidson et al. (1997) have accounted for the lack of variation in metamorphic grade by suggesting that leucogranite intrusion provided additional heat to the surrounding rocks to facilitate high-T sillimanite growth, heat that was not available to rocks in the Kakthang type locality. Assuming this is a reasonable explanation, the implication for the preservation of high-grade rocks both above and below the projected out-of-sequence thrust is that in western Bhutan, the temperature gradient between rocks at lower versus higher structural levels was not significant. However, preservation of P-T paths that might represent the upper margin of a channel in the midst of this material can only be reconciled by invoking exhumation of an equally hot low-viscosity dome over a pre-existing hot body (e.g. model HT111 of Beaumont et al. 2004; Figure 5.2b). If in western Bhutan the GHS comprises two channels or domes, rocks at the top of the earlier channel should in outcrop be situated in the mid-structural levels of what would appear as a single orogenic channel. Identification of the boundary between the two units in outcrop could be expected to be difficult because both units contain the same index minerals (Jamieson et al. 2004). Rocks in the lower, earlier channel should have experienced peak metamorphic conditions and some degree of cooling, during exhumation between the MCT and a 'lower' STD, prior to rocks in the overriding channel. Rocks within the younger dome might also be expected to have remained at high temperatures for protracted periods relative to rocks at the structural top of the earlier channel, following a P-T path that might resemble those associated with the highest structural level rocks of this study (Figure 5.5, 5.6; Jamieson et al. 2006). The absence of a marked metamorphic break between the two units in outcrop implies that, unlike in the type locality, footwall rocks did not have much time to decompress and cool prior to exhumation of the overriding dome. Therefore, the transition between channel extrusion and doming must have been a continuous process as predicted by model HT111, and did not occur in pulses as is suggested by Hollister and Grujic (2006).

Concordant U-Pb ages from zircon core and rims at the mid-structural level range from ca. 25–15 Ma, while ages from zircon rims at the higher structural level range from ca. 21 – 14 Ma (Figure 5.8). Since zircon growth can persist to temperatures below 800 °C (Heaman and Parrish 1991) the upper limits of each range is taken to represent the lower limit to which peak temperatures persisted at the two structural levels. Due to the lack of sufficient data these conclusions are admittedly speculative, however, it appears that rocks at mid-structural levels were at peak-T conditions ~ 4 Myr earlier than rocks at higher structural levels. Unfortunately, U-Pb data are not currently available for the rocks from the lowest structural levels, however it is assumed that they would yield ages that are older than those obtained at mid-structural levels because the base of the earlier

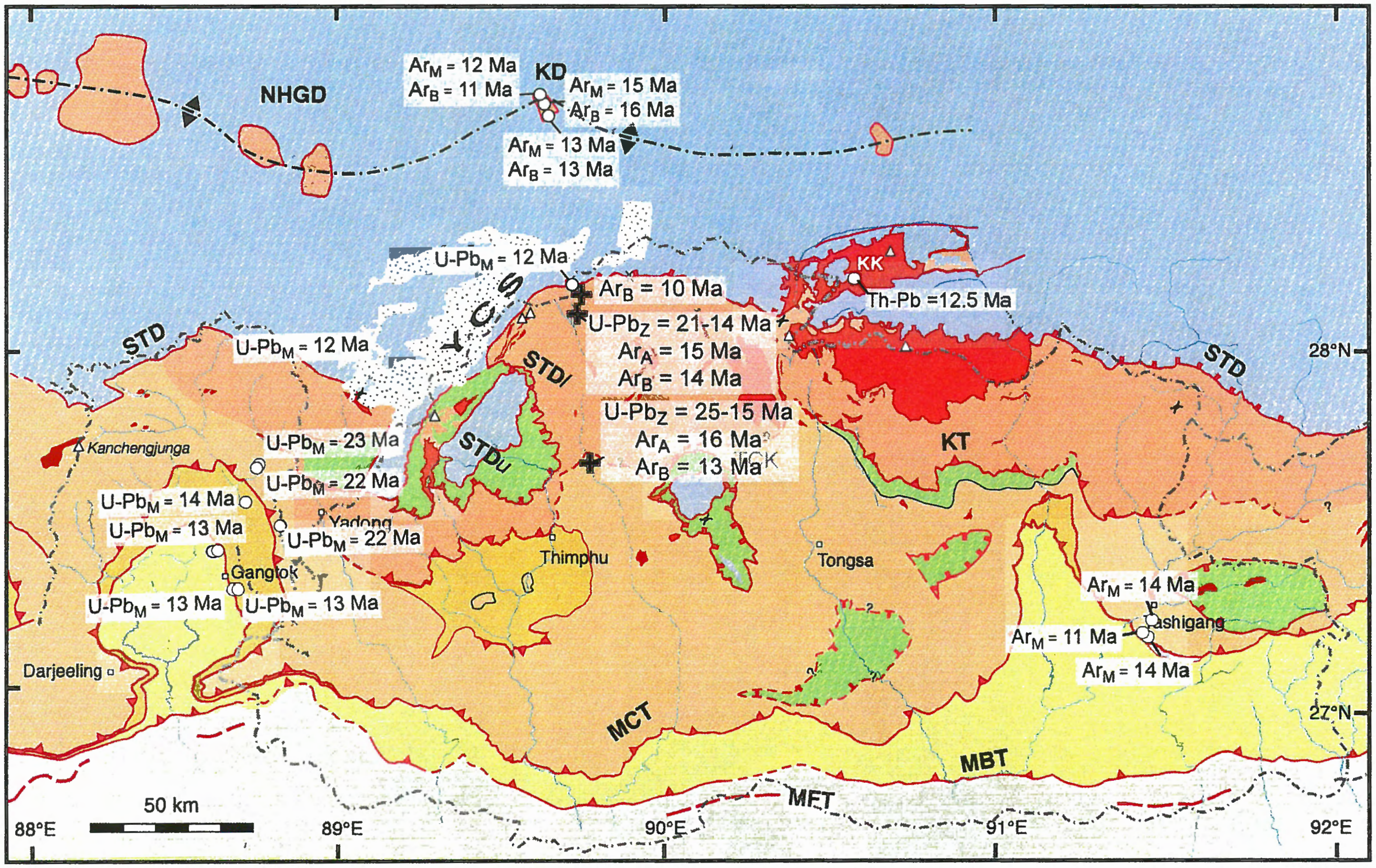

Figure 5.8: Regional distribution of geochronological data. Regional map of Bhutan and southern Tibet illustrating the spatial variation of U-Pb monazite (U-Pb$_M$) and zircon (U-Pb$_Z$) ages, and argon amphibole (Ar$_A$), muscovite (Ar$_M$) and biotite (Ar$_b$) cooling ages. **Legend:** ***NHGD,*** northern gneiss domes; ***KD,*** Kangmar dome; ✚, sample location and associated U-Pb and argon ages obtained in this study; ○, sample location and associated U-Pb and argon ages from previous studies (Neogi et al., 1998; Wu et al., 1998; Lee et al., 2000; Stüwe and Foster, 2001; Catlos et al., 2004). The legend for units corresponds with the legend presented in Figure 5.4.

channel would have experienced peak metamorphic conditions earlier than rocks at the top.

Throughout the Himalaya, it is recognized that movement along the margins of the GHS is not confined to a single plane but has been diffused over multiple fault strands that operated under different mechanical conditions (brittle versus ductile) at different times. Godin et al. (2006) refers to the various strands as the lower MCT (MCT*l*), upper MCT (MCT*u*), lower STD (STD*l*) and upper STD (STD*u*). A compilation of the data available across the orogen reveals that the MCT*u* and STD*l* were active between 25-14 Ma and 24-12 Ma respectively (Figure 5.7; Godin et al. 2006 and references therein), suggesting the earliest movement along the structures was contemporaneous with peak-T metamorphism. The implication for this is that displacement along the structures was initiated at mid-crustal depths under ductile conditions. Following high-T metamorphism between 25-21 Ma, rocks in the lower and higher channels experienced decompression and cooling, which is consistent with the interpretations of Swapp and Hollister (1991). In the highest and mid- structural levels this is associated with the breakdown of the peak-T mineral assemblage in metasediments to cordierite beginning at ~ 700 °C, and orthoamphibole in metabasites at ~ 600 °C and 5 kbar. The latest stages of retrogression are marked by chlorite overgrowth at all structural levels and in all lithologies.

Concomitant with retrogression throughout the GHS was the development of shear bands. At the highest structural levels the kinematics of the shear bands in metasedimentary rocks is top-to-the north-northwest, correlating with north-directed normal faulting along the STD (Burg and Chen 1984; Burchfiel and Royden 1985; Burchfiel et al. 1992; Grujic et al. 2002). At the lowest structural levels, the kinematics throughout the Jaishidanda Formation is top-to-the south-southeast, which is consistent with top-to-the south directed thrusting throughout the MCT zone (Brunel 1986; Burchfiel et al. 1992; Jain and Manickavasagam 1993; Grasemann et al. 1999). Development of shear bands at the upper margin of the GHS upon decompression suggests that normal movement along the upper STD (upper boundary of channel/dome 2?) was contemporaneous with decompression and thrusting in the MCT zone as the GHS was extruded southward over the LHS. Normal slip along STD*u* in the Himalaya to the west has been dated between 19~12 Ma (zircon and monazite; Hodges et al. 1998;

Murphy and Harrison 1999; Catlos et al. 2004), and movement along the MCT*l* between 15-0.7 Ma (Searle and Godin 2003; Catlos et al. 2004). Thus, following peak-T metamorphism, movement along the margins of the low-viscosity channel continued with its exhumation into the upper crust, deformation penetrating from the original strands (MCT*u*, STD*l*) outward to the MCT*l* and STD*u* strands (Godin et al. 2006; Hollister and Grujic 2006).

With respect to the timing of cooling to lower temperatures in Bhutan, argon amphibole and biotite ages have proven to be problematic owing to the presence of excess argon. However, the lower limits of argon ages have been interpreted to represent the maximum limit at which rocks cooled through the closure temperatures for amphibole (500 ± 50 °C) and biotite (300 ± 50 °C) respectively. Thus, rocks in the mid-structural levels would have cooled through 500 ± 50°C by ~ 16 Ma, while those higher up cooled by 15 Ma, ~ 1 Myr later (Figure 5.8). In the context of model HT111, delayed cooling of the extruded dome in the higher structural levels of the GHS would be expected, though should exhumation have been a continuous process the delay might not be significant or detectable at all. If however, exhumation was pulsed, as suggested by the model of Hollister and Grujic (2006), a significant (i.e > 10 Myr) delay should be recorded in the amphibole ages. Biotite ages are a bit more complicated in that they suggest mid-structural levels cooled through 300 ± 50 °C by ~ 13 Ma, while those higher up cooled by ~ 14 Ma. The apparently delayed cooling through biotite closure at mid-structural levels might be due to incipient heating in upper parts of an early channel as the younger, relatively hot dome was extruded over top of it.

To the north of the study area, the Kangmar Dome – a crystalline complex that occurs within the TSS, yields biotite cooling ages of 11 -16 Ma (Lee et al. 2000), suggesting that to the north of the STD, doming and cooling of the core complex must have been contemporaneous with exhumation of the main two channels/domes in Bhutan. Immediately below the STD a foliated leucogranite dated at 12 Ma (U-Pb of monazite; Wu et al. 1998) yielded a biotite argon age of 10 Ma. Intrusion and cooling of this granite was contemporaneous with intrusion of a leucogranite in central Bhutan, which has been dated at 13 Ma (Th-Pb; Edwards and Harrison 1997) and cooled through biotite and muscovite closure temperatures by 11 Ma (Maluski et al. 1988). The overlap of granite crystallization and cooling ages in the GHS suggests decompression and cooling of the GHS in Bhutan, and doming in Southern Tibet occurred pre- to syn-leucogranite intrusion at ~ 12 Ma (Stüwe and Foster 2001).

Unfortunately, argon ages are not currently available for the rocks of the lowest structural level. However, muscovite ages along strike in eastern Bhutan yielded cooling ages of 11 Ma in the immediate hanging wall of the MCT and 14 Ma ~ 400 m structurally up-section (Figure 5.8; Stüwe and Foster 2001). Increase in cooling ages towards the center of the channel implies that the central portions of the channel cooled through muscovite closure temperatures (350 ± 50 °C) earlier than rocks at its margins, perhaps because the central portions of the channel were exhumed more rapidly relative to the base. With the exception of a muscovite cooling age of 12 Ma in the Everest region (Hubbard and Harrison 1989), argon muscovite ages in the Sutlej Valley, central and eastern Nepal range between 4 - 9 Ma (Maluski et al. 1988; Copeland et al. 1991; Vannay et al. 2004; Theide et al. 2005), at least 2 Myr after rocks cooled through 350 ± 50 °C in the east. In the Annapurna region and Pakistan muscovites have yielded ages of 14-15 Ma (Vannay and Hodges 1996), 30 Ma, and 40 Ma (Zeitler 1985). Cooling within the hanging wall of the MCT appears, therefore, to have been earlier in the far east and west relative to the central portions of the orogen implying that exhumation of the GHS was earlier in the east and west segments of the orogen, proximal to the syntaxes (Stüwe and Foster 2001).

5.3.2 WHAT AND WHERE IS THE MCT?

Along the entire length of the Himalaya, the boundary between the GHS and underlying LHS has been described as a high strain zone of variable thickness, commonly coincident with a zone of inverted metamorphism, placing high-grade rocks of the GHS over lower-grade rocks of the LHS (Arita 1983; Searle et al. 1992; Davidson et al. 1997; Stephenson et al. 2000). Since south-directed thrusting is distributed over a broad zone of protomylonites with both LHS and GHS affinities (Brunel 1986; Grujic et al. 2002), the zone is most commonly known as the MCT zone (Grujic et al. 1996). Locating the exact position of the boundary between the LHS and GHS within or outside this zone has been a source of confusion with some workers placing it at the kyanite-in isograd (Le Fort et al. 1986; Pêcher 1989) while others place it within the zone of intense shearing, below the last appearance of migmatite (Mohan et al. 1989; Searle et al. 1992; Metcalfe 1993; Stephenson et al. 2001).

In Bhutan, the boundary between the GHS and LHS is marked by the Jaishidanda Formation, which comprises a group of mylonitized garnet-mica schists, micaceous quartzites, rare carbonate bands, leucogranites, ortho- and augen gneisses. Although staurolite, kyanite and/or sillimanite have not been observed along the transects studied here, garnet zoning profiles and P-T estimates reveal that the metamorphic grade across this zone is inverted with peak-T increasing with increasing structural position. All of these observations suggest the Jaishidanda Formation is likely the eastern equivalent to the MCT zone of the western and central Himalaya. Nd isotopic data reveal, however, that rocks within the formation are of GHS affinity, implying all the rocks of the Jaishidanda Formation constitute the lowest structural levels of the GHS. Assuming the Nd data are robust and that correlation of the Jaishidanda Formation with the MCT zone is also correct, the implications of the isotopic data are that the MCT zone in Bhutan corresponds with a zone of intense shear at the base of the GHS, structurally above the boundary with the LHS.

P-T paths across the unit appear to be consistent with P-T loops predicted by model HT111 for particles that are of "LHS" and "GHS" affinity (Figure 5.2; Jamieson et al. 2004). Jaishidanda samples with homogeneous garnets are associated with P-T loops similar to that predicted for particle A, which is buried and subjected to increasing temperatures along a steep prograde path into the kyanite stability field and extruded immediately above the MCT. In contrast, the P-T loop associated with samples preserving growth zoned garnets resembles the path generated for particles C and F (Figure 5.2), which is underthrust to moderate depths (~ 9-11 kbar) but not subjected to high-T for very long before being exhumed to the surface at the base of the channel, in a zone of intense south directed shearing that develops between out-flowing channel material and incoming, newly accreted material.

The preservation of GHS material that was buried to depths of 11 kbar but exhumed rapidly so as to preserve the growth zoning in garnets implies that not everywhere in the orogen has all GHS material been underthrust and incorporated into the mid-crustal, low-viscosity zone that was extruded to form the metamorphic core of the Himalaya. Preservation of the lower-grade GHS rocks in a zone of intense shearing at the base of the migmatites suggests that channel material (partially melted GHS) was exhumed to the base of GHS material that had been under-thrust but not deep enough to have experienced partial melting (Figure 5.7). The implication for this is that in south-western Bhutan the MCT zone does not incoporate the protolith boundary between the LHS and GHS, as it is defined elsewhere in the orogen. Instead, the MCT zone is a zone of intense top-to-the-south shear, as suggested by Searle et al. (2006), that has developed across a metamorphic discontinuity between GHS rocks that were subjected to high-T metamorphism for a protracted period of time and GHS rocks that were not. The boundary between the GHS and LHS (i.e. the MCT) is observed below this zone.

5.4 RELEVANCE OF DATA TO THE CHANNEL FLOW-EXTRUSION MODEL

Geochemical and isotopic data suggest that metabasites found at the highest and apparent mid-structural levels of the GHS in western Bhutan are continental tholeiites that intruded the northern margin of Gondwanaland, which included India, during a period of Paleo - Mesoproterozoic magmatism. Thus, the idea that the metamorphic core of the Himalaya represents partially melted material that originally formed the north Indian margin still holds true.

With respect to the metamorphic and structural evolution of the metamorphic core, thermomechanical model HT1 of Beaumont et al. (2001 and 2004) provides a basic approximation for the development and exhumation of the GHS, though the results of this study reveal inconsistencies between model predictions and real data. P-T paths yielded for particles in the model "GHS" resemble P-T paths associated with actual rocks, however the model predicts their exhumation to positions that are opposite to where they have been found in reality. Doming of low-viscosity material over a pre-existing low-viscosity body along an out-of-sequence thrust could potentially account for the observed results, and seems to be best illustrated by model HT111. The current comparison is, however, based on very rudimentary P-T paths that have been predicted for only three particles in the model. Without a more detailed comparison of the spatial variation of predicted P-T-t paths with the available real data, it is difficult to adequately assess the validity of the model as an analogue for the GHS in Bhutan. The conceptual model of Hollister and Grujic (2006) cannot be considered as a viable analogue due to the absence in the real data for a significant time delay between exhumation of the main channel and subsequent dome to invoke pulsed channel flow.

In regards to the MCT zone, P-T paths associated with the laterally equivalent rocks in south-western Bhutan are markedly similar to paths predicted for "LHS" and "GHS" particles on either side of the model MCT in HT111. The discrepancy is that the model MCT develops along a metamorphic discontinuity that corresponds with a protolith boundary that demarcates the boundary between the GHS (out-flowing channel material) and LHS (incoming, newly accreted material). Nd data presented in this study have revealed that both high- and lower-grade rocks in the MCT zone are of GHS affinity. The implications for this are that development of the MCT zone as defined elsewhere in the orogen, is not valid in south-western Bhutan as the real data illustrates that the zone does not correspond with the boundary between the two units. For the purposes of identification in the field, the MCT zone should be correlated with a zone of protomylonites in which top-to-the-south kinematics is prevalent, and has developed over a metamorphic discontinuity between rocks that have been subjected to high-T metamorphism for prolonged periods (i.e. migmatites) versus rocks that have not (i.e. garnet mica schists). Where within the crust the zone develops will undoubtedly be dictated by lithology (i.e. more likely to develop in less competent pelitic rocks versus competent psammitic rocks), which may or may not correlate with a protolith boundary between the LHS and GHS.

5.5 CONCLUSIONS

To summarize, the broad conclusions of the GHS in western Bhutan include:

i) The local preservation of within-plate basalts in the GHS serves as evidence for magmatic activity, perhaps during a period of rifting for which evidence has been found elsewhere in the orogen, along the northern margin of Gondwanaland during the Paleo- to Mesoproterozoic.

ii) Peak-T estimates increase with increasing structural position across the unit, from the MCT zone to the STD. Corresponding pressure estimates decrease. The spatial variation of the associated P-T paths across the GHS reveals that the broad exposure of high-grade material may be accounted for by the exhumation of two channels or domes.

iii) Peak-T conditions in the two channels persisted until 25-21 Ma. Amphibole and argon ages suggest both channels cooled through 500° and 350 °C by 15 Ma and 13 Ma respectively, which was contemporaneous with doming in southern Tibet and the early phases of leucogranite intrusion.

iv) The Jaishidanda Formation corresponds with a zone of intense top-to-the-south shearing that could be equivalent to the MCT zone. It has developed over a metamorphic discontinuity between GHS rocks that have been subjected to high-T for protracted periods versus GHS rocks that have not. Since the boundary between the GHS and LHS is observed below this zone, the MCT zone in south-western Bhutan does not correspond with the MCT zone as defined elsewhere in the orogen (i.e. as the high-strain protolith boundary between the LHS and GHS).

5.6 SUGGESTIONS FOR FUTURE WORK

1) Based on Nd isotopic signatures and the distribution of detrital U-Pb ages, it is generally agreed that the LHS was derived from a predominantly Archean – Paleoproterozoic source, probably the Indian continental margin, while the GHS mainly comprises Neoproterozoic – Paleozoic material. The geographic location of the source for the GHS however, remains poorly constrained. A detailed study directed at correlating the detritus in the GHS with a source may be of interest in understanding the paleo-tectonic distribution of continents and/or microcontinents throughout the region during the late Proterozoic – Paleozoic.
2) A comparison between P-T-t paths associated with real rocks and paths predicted by model HT111 is necessary to assess the validity of the model as an analogue for the exhumation of the GHS in Bhutan. Also, a much more detailed geochronological study across the structure is necessary to adequately assess whether exhumation of the low-viscosity material is a continuous process, or depending on the rate of convergence and denudation, is pulsed as suggested by Hollister and Grujic (2006).
3) U-Pb and argon analyses of rocks within the MCT zone (Jaishidanda Formation) would resolve the timing of metamorphism and subsequent cooling in the lowest structural levels of the GHS, and be of benefit in understanding whether

development of the metamorphic discontinuity is the consequence of Himalayan orogenesis or some earlier event.

4) The Chekha Formation is a thick package of rocks observed between the crystalline rocks of the GHS and the relatively unmetamorphosed rocks of the TSS. Metamorphic grade within the formation is right-way-up decreasing from staurolite grade at its base to biotite at the top. Might the Chekha Formation correlate with rocks that preserve growth zoning in the Jaishidanda Formation? Could the Chekha Formation represent GHS rocks that were not thrust to mid-crustal levels and incorporated into the channel, but were instead the 'roof' rocks beneath which the channel and subsequent domes have been extruded? Detailed metamorphic, isotopic and geochronological studies of the Chekha Formation might provide answers to these questions. An understanding of where in the tectonic evolution of the Bhutan Himalaya the Chekha Formation fits may assist in correlating the lower and upper STDs, which may ultimately provide constraints on the timing of movement along them.

REFERENCES

Abu-Hamatteh ZSH (2005) Geochemistry and petrogenesis of mafic magmatic rocks of the Jharol Belt, India: geodynamic implication. Journal of Asian Earth Sciences 25:557-581

Ahmad T, Harris N, Bickle M, Chapman H, Bunbury J, Prince C (2000) Isotopic constraints on the structural relationships between the Lesser Himalayan Series and the High Himalayan Crystalline Series, Garhwal Himalaya. GSA Bulletin 112(3):467-477

Ahmad T, Tarney J (1991) Geochemistry and petrogenesis of Garhwal volcanics: implications for evolution of the north Indian lithosphere. Precambrian Research 50:69-88

Ahmad T, Tarney J (1994) Geochemistry and petrogenesis of late Archean Aravalli volcanics, basement enclaves and granitoids, Rajasthan. Precambrian Research 65:1-23

Argles T, Foster G, Whittington A, Harris N, George M (2003) Isotope studies reveal a complete Himalayan section in the Nanga Parbat syntaxis. Geology 31:1109-1112

Arita K (1983) Origin of the inverted metamorphism of the Lower Himalayas, central Nepal. Tectonophysics 95:43-60

Ayer JA, Davis DW (1997) Neoarchean evolution of differing convergent margin assemblages in the Wabigoon Subprovince: geochemical and geochronological evidence from the Lake of the Woods greenstone belt, Superior Province, Northwestern Ontario. Precambrian Research 81:155-178

Beccaluva L, Ohnenstetter D, Ohnenstetter M (1979) Geochemical discrimination between ocean-floor and island-arc tholeiites - application to some ophiolites. Canadian Journal of Earth Sciences 16:1874-1882

Beaumont C, Jamieson RA, Nguyen MH, Lee B (2001) Himalayan tectonics explained by extrusion of a low-viscosity crustal channel coupled to focused surface denudation. Nature 414:738-742

Beaumont C, Jamieson RA, Nguyen MH, Medvedev S (2004) Crustal channel flows: 1. Numerical models with applications to the tectonics of the Himalayan-Tibetan orogen. Journal of Geophysical Research 109. DOI: 10.1029/2003JB002809

Beaumont C, Nguyen MH, Jamieson RA, Ellis S (2006) Crustal flow modes in large hot orogens. In: Law RD, Searle MP, Godin L (eds) Channel Flow, Ductile Extrusion and Exhumation in Continental Collision Zones., Special Publication 268. Geological Society, London, pp 91-145

Bhargava ON (1995) The Bhutan Himalaya: A Geological Account. In, vol Geological Survey of India, Special Publication 39. p 245

Bhattacharyya DS, Das KK (1983) Inversion of metamorphic zones in the lower Himalayas at Gangtok, Sikkim, India. Journal of Geology 91:98-102

Brookfield ME (1993) The Himalayan passive margin from Precambrian to Cretaceous times. Sedimentary Geology 84:1-35

Brunel M (1986) Ductile thrusting in the Himalayas: shear sense criteria and stretching lineations. Tectonics 5:247-265

Brunel M, Kienast J-R (1986) Petrologic and structural study of ductile Himalayan thrust faulting across the Everest-Makalu area, eastern Nepal. Canadian Journal of Earth Sciences 23(8):1117-1137

Burchfiel BC, Chen Z, Hodges KV, Liu Y, Royden LH, Deng C, Xu J (1992) The south Tibetan detachment system, Himalayan orogen: Extension contemporaneous with and parallel to shortening in a collisional mountain belt. In: Geological Society of America Special Paper 269. pp 1-41

Burchfiel BC, Royden LH (1985) North-south extension within the convergent Himalayan region. Geology 13:679-682

Burg JP, Chen G (1984) Tectonics and structural formation of southern Tibet, China. Nature 311:219-223

Carlson RW, Lugmair GW, Macdougall JD (1981) Columbia River volcanism, the question of mantle heterogeneity or crustal contamination. Geochimica Cosmochimica Acta 45:2483-2500

Catlos EJ, Dubey CS, Harrison TM, Edwards MA (2004) Late Miocene movement within the Himalayan Main Central Thrust shear zone, Sikkim, north-east India. Journal of Metamorphic Geology 22:207-226

Catlos EJ, Harrison TM, Manning CE, Grove M, Rai SM, Hubbard MS, Upreti BN (2002) Records of the evolution of the Himalayan orogen from in situ Th-Pb ion microprobe dating of monazite: Eastern Nepal and western Garhwal. Journal of Asian Earth Sciences 20:459-479

Chakraborty S, Ganguly J (1992) Cation diffusion in aluminosilicate garnets: experimental determination in spessartine-almandine diffusion couples, evaluation of effective binary diffusion coefficients, and applications. Contributions to Mineralogy and Petrology 111:74-86

Chakungal J, Dostal J, Grujic D, Ghalley KS (2002) Towards understanding Eohimalayan tectonics: do gabbroic cumulates and ultramafics of the Bhutan Himalaya hold the clues? In: 18th Himalayan Karakorum Tibet Workshop, vol., Ascona, Switzerland, p 30

Condie KC (1994) Archean crustal evolution, vol 11. Elsevier, Amsterdam, pp 1-9

Copeland P, Harrison TM, Hodges KV, Maruejol P, Le Fort P, Pecher A (1991) an early Pliocene thermal disturbance of the Main Central Thrust, central Nepal; implications for Himalayan Tectonics. Journal of Geophysical Research 96:8475-8500

Daniel CG, Hollister LS, Parrish R, Grujic D (2003) Exhumation of the Main Central Thrust from lower crustal depths, Eastern Bhutan Himalaya. Journal of Metamorphic Geology 21:317-334

Dasgupta S (1995) Jaishidanda Formation. In: Bhargava ON (ed) The Bhutan Himalaya: A geological account, vol Special publication No. 39. Geological Survey of India, Calcutta, India, pp 79-88

Dasgupta S, Ganguly J, Neogi S (2004) Inverted metamorphic sequence in the Sikkim Himalayas: crystallization history, P-T gradient and implications. Journal of Metamorphic Geology 22:395-412

Davidson C, Grujic D, Hollister LS, Schmid S (1997) Metamorphic reactions related to decompression and synkinematic intrusion of leucogranite, High Himalayan Crystallines, Bhutan. Journal of Metamorphic Geology 15:593 – 612

Deloule E, Alexandrov P, Cheilletz A, Laumonier B, Barbey P (2002) In situ U-Pb zircon ages for Early Ordovician magmatism in the eastern Pyrenees, France: the Canigou orthogneisses. International Journal of Earth Science (Geologisches Rundschau) 91:398-405

de Sigoyer J, Guillot S, Lardeaux JM, Mascle G (1997) Glaucophane-bearing eclogites in the Tso Morari dome (eastern Ladakh, NW Himalaya). European Journal of Mineralogy 9:1073 – 1083

de Sigoyer J, Chavagnac V, Blichert TJ, Villa IM, Luais B, Guillot S, Cosca M, Mascle G (2000) Dating the Indian continental subduction and collisional thickening in the Northwest Himalaya; multichronology of the Tso Morari eclogites. Geology 28(6):487 - 490

DeCelles PG, Gehrels GE, Najman YMR, Martin A, Carter A, Garzanti E (2004) Detrital geochronology and geochemistry of Cretaceous - Early Miocene strata of Nepal: implications for timing and diachroneity of initial Himalayan orogenesis. Earth and Planetary Science Letters 227:313-330

DeCelles PG, Gehrels GE, Quade J, LaReau B, Spurlin M (2000) Tectonic implications of U-Pb zircon ages of the Himalayan orogenic belt in Nepal. Science 288:497-499

Deloule E, Alexandrov P, Cheilletz A, Laumonier B, Barbey P (2002) In situ U-Pb zircon ages for Early Ordovician magmatism in the eastern Pyrenees, France: the Canigou orthogneisses. International Journal of Earth Science (Geologisches Rundschau) 91:398-405

DePaolo DJ (1988) Neodymium Isotope Geochemistry An Introduction, vol. Springer-Verlag, Berlin, p 187

Dostal J, Baragar WRA, Dupuy C (1986) Petrogenesis of the Natkusiak continental basalts, Victoria Island, Northwest Territories, Canada. Canadian Journal of Earth Sciences 23:622-632

Edwards MA, Harrison TM (1997) When did the roof collapse? Late Miocene N-S extension in the High Himalaya revealed by Th-Pb monazite dating of the Khula Kangri granite. Geology 25:543-546

Edwards MA, Kidd WSF, Li J, Yue Y, Clark M (1996) Multi-stage development of the southern Tibet detachment system near Khula Kangri. New data from Gonto La. Tectonophysics 260:1-19

Edwards MA, Pecher A, Kidd WSF, Burchfiel BC, Royden LH (1999) Southern Tibet Detachment System at Khula Kangri, Eastern Himalaya: A Large-Area, Shallow Detachment Stretching into Bhutan? The Journal of Geology 107:623-631

Fleck RD, Sutter JF, Elliot D (1977) Interpretation of discordant $^{40}Ar/^{39}Ar$ age-spectra of Mesozoic tholeiites from Antarctica. Geochimica et Cosmochimica Acta 41:15-32

Foster G, Kinny P, Prince C, Vance D, Harris N (2000) The significance of monazite U-Th-Pb age data in metamorphic assemblages; a combined study of monazite and garnet chronometry. Earth and Planetary Science Letters 181:327-340

Ganguly J, Dasgupta S, Cheng W, Neogi S (2000) Exhumation history of a section of the Sikkim Himalayas, India: records in the metamorphic mineral equilibria and compositional zoning of garnet. Earth and Planetary Science Letters 183:471-486

Gansser A (1964) Geology of the Himalayas., vol. Wiley-Interscience, London

Gansser A (1983) Denkschriten der Schweizerischen Naturforschenden Gesellschaft., vol.,

Garzanti E (1999) Stratigraphy and sedimentary history of the Nepal Tethys Himalayan passive margin. In: Upreti BN, Le Fort P (eds) Advances on the geology of the Himalaya: focus on Nepal., vol 17. Journal of Asian Earth Sciences., pp 805-827

Gehrels GE, DeCelles PG, Martin A, Ojha TP, Pinhassi G (2003) Initiation of the Himalayan Orogen as an Early Paleozoic thin-skinned thrust belt. GSA Today 13(9):4-9

Godin L, Gleison T, Searle MP, Ullrich TD, Parrish R (2006a) Locking of southward extrusion in favour of rapid crustal-scale buckling of the Greater Himalayan Sequence, Nar Valley, Central Nepal. In: Law RD, Searle MP, Godin L (eds) Channel Flow, Ductile Extrusion and Exhumation in Continental Collision Zones., vol Special Publication. Geological Society London, pp 269-292

Godin L, Grujic D, Law RD, Searle MP (2006b) Channel flow, ductile extrusion and exhumation in continental collision zones: an introduction. In: Law RD, Searle MP, Godin L (eds) Channel Flow, Ductile Extrusion and Exhumation in Continental Collision Zones., vol Special Publications 268. Geological Society London, pp 1-23

Grasemann B, Fritz H, Vannay J-C (1999) Quantitative kinematic flow analysis of the Main Central Thrust Zone (NW Himalaya, India): Implications for a decelerating strain path and the extrusion of orogenic wedges. Journal of Structural Geology 21:837-853

Grasemann B, Vannay J-C (1999) Flow controlled inverted metamorphism in shear zones. Journal of Structural Geology 21:743-750

Grujic D, Casey M, Davidson C, Hollister LS, Kundig R, Pavlis T, Schmid S (1996) Ductile extrusion of the Higher Himalayan Crystalline in Bhutan: evidence from quartz microfabrics. Tectonophysics 260:21 – 43

Grujic D, Hollister LS, Parrish R (2002) Himalayan metamorphic sequence as an orogenic channel: insight from Bhutan. Earth and Planetary Science Letters 198:177 – 191

Guillot S, Lardeaux JM, Mascle G, Colchen M (1995a) A new record of high-pressure metamorphism in the Himalayan Range - the retrogressed eclogites of the Tso Morari Dome (East Ladakh). C R Academic Science Ser II 320(10/2):931 – 936

Guillot S, Mascle G, Lardeaux JM, Colchen M, de Bernardy J (1995b) A new discovery of eclogites from the Himalaya, Tso Morari dome unit (Northeastern India). In: Spencer DA, Burg JP, Spencer-Cervato C eds) 10th Himalaya-Karakoram-Tibet Workshop, vol Abstract Volume. Monte Verita, Ascona, Ticino, Switzerland, p 298

Harris N, Caddick M, Kosler J, Goswami S, Vance D, Tindle AG (2004) The pressure-temperature-time path of migmatites from the Sikkim Himalaya. Journal of Metamorphic Geology 22:249-264

Hauck ML, Nelson KD, Brown LD, Zhao W, Ross AR (1998) Crustal structure of the Himalayan orogen at ~ 90° east longitude from project INDEPTH deep reflection profiles. Tectonics 17(4):481-500

Hawkesworth CJ, Mantovani M, Peate D (1988) Lithosphere remobilisation during Paraná CFB magmatism. In: Menzies MA, Cox KG (eds) Oceanic and Continental Lithosphere: Similarities and Differences., vol. Journal of Petrology Special Issue, pp 205-223

Heaman LM, Parrish R (1991) U-Pb geochronology of accessory minerals. In: Heaman LM, Ludden JN (eds) Applications of Radiogenic Isotope Systems to Problems in Geology, vol. Mineral Association of Canada, Short Course Handbook 19, pp 59-102

Hodges KV (2000) Tectonics of the Himalaya and southern Tibet from two perspectives. GSA Bulletin 112(3):324 – 350

Hodges KV (2006) A synthesis of the Channel Flow-Extrusion hypothesis as developed for the Himalayan-Tibetan orogenic system. In: Law RD, Searle MP, Godin L (eds) Channel Flow, Ductile Deformation and Exhumation in Continental Collision Zones., vol Special Publications 268. Geological Society, London, pp 71-90

Hodges KV, Silverberg DS (1988) Thermal evolution of the Greater Himalaya, Garhwal, India. Tectonics 7(3):683-600

Hodges KV, Bowring SA, Davidek KL, Hawkins D, Krol M (1998) Evidence for rapid displacement on Himalayan normal faults and the importance of tectonic denudation in the evolution of mountain ranges. Geology 26(6)

Hodges KV, Parrish R, Searle MP (1996) Tectonic evolution of the central Annapurna Range, Nepalese Himalayas. Tectonics 15:1264-1291

Holland T, Powell R (1998) An internally consistent thermodynamic dataset for phases of petrological interest. Journal of Metamorphic Geology 16:309-

Hollister LS (1966) Garnet zoning: An interpretation based on the Rayleigh Fractionation Model. Science 154: 1647-1651

Hollister LS (1969) Contact metamorphism in the Kwoiek Area of British Columbia: an end-member of the metamorphic process. Geological Society of Amercia Bulletin 80: 2465-2494

Hollister LS (1982) Metamorphic evidence for rapid (2 mm/yr) uplift of a portion of the central gneiss complex, Coast Mountains, B.C. Canadian Mineralogist 20:319-332

Hollister LS, Grujic D (2006) Pulsed channel flow in Bhutan. In: Law RD, Searle MP, Godin L (eds) Channel Flow, Ductile Extrusion and Exhumation in Continental Collision Zones., vol Special Publication 268. Geological Society, London, pp 415-423

Holm PE (1985) The geochemical fingerprints of different tectonomagmatic environments using hygromagmatophile element abundances of tholeiitic basalts and basaltic andesites. Chemical Geology 51:303-323

Horan MF, Hanson GN, Spencer KJ (1987) Pb and Nd isotope and trace element constraints on the origin of basic rocks in an early Proterozoic igneous complex, Minnesota. Precambrian Research 37:323-342

Hubbard MS (1996) Ductile shear as a cause of inverted metamorphism: example from the Nepal Himalaya. Journal of Geology 104:493-499

Hubbard MS, Harrison TM (1989) 40Ar/39Ar age constraints on deformation and metamorphism in the Main Central Thrust zone and Tibetan Slab, eastern Nepal Himalaya. Tectonics 8:865-880

Irvine TN, Baragar WRA (1971) A guide to the chemical classification of the common volcanic rocks. Canadian Journal of Earth Sciences 8:523-548

Jain AK, Manickavasagam RM (1993) Inverted metamorphism in the intracontinental ductile shear zone during Himalayan collision tectonics. Geology 21:407-410

Jamieson RA, Beaumont C, Medvedev S, Nguyen MH (2004) Crustal channel flows: 2. Numerical models with implications for metamorphism in the Himalayan-Tibetan orogen. Journal of Geophysical Research 109. DOI: 10.1029/2003JB002811

Jamieson RA, Beaumont C, Nguyen MH, Grujic D (2006) Provenance of the Greater Himalayan Sequence and associated rocks: Predictions of channel flow models. In: Law RD, Searle MP, Godin L (eds) Channel Flow, Ductile Extrusion and Exhumation of Lower-mid Curst in Continental Collision Zones., vol Special Publication 268. Geological Society London, pp 165-182

Kesson SE, Ringwood AE (1989) Slab-mantle interactions: 1. Sheared and refertilised garnet peridotite xenoliths; samples of Wadati-Benioff zones? Chemical Geology 78(2):83-96

Kohn MJ, Spear F (2000) Retrograde net transfer reaction insurance for pressure-temperature estimates. Geology 28:1127-1130

Le Fort P (1975) Himalayas: the collided range. Present knowledge of the continental arc. American Journal of Science 275a:1-44

Le Fort P, Debon F, Pêcher A, Sonet J, Vidal P (1986) The 500 Ma magmatic event in Alpine southern Asia, a thermal episode at Gondwana scale. Sciences de la Terre. Mémoire (Nancy) 47:191-209

Leake BE (1964) The chemical distinction between ortho- and para-amphibolites. Journal of Petrology 5:238-254

Lee J, Hacker BR, Dinklage WS, Wang Y, Gans P, Calvert A, Wan J, Chen W, Blythe AE, McClelland W (2000) Evolution of the Kangmar Dome, southern Tibet: structural, petrologic, and thermochronologic constraints. Tectonics 19(5):872-895

Lee J, McClelland W, Wang Y, Blythe AE, McWilliams MO (2006) Oligocene-Miocene middle crustal flow in southern Tibet: geochronology of Mabja Dome. In: Law RD, Searle MP, Godin L (eds) Channel Flow, Ductile Deformation and Exhumation in Continental Collision Zones., vol Special Publications 268. Geological Society, London, pp 445-469

Leech ML, Singh S, Jain AK, Klemperer SL, Manickavasagam RM (2005) The onset of India-Asia continental collision: Early, steep subduction required by the timing of UHP metamorphism in the western Himalaya. Earth and Planetary Science Letters 234:83-97

Luais B, Telouk P, Albarède F (1997) Precise and accurate neodymium isotopic measurements by plasma-source mass spectrometer. Geochimica et Cosmochimica Acta 61(22):4847-4854

Maluski H, Matte P, Brunel M, Xiao X (1988) Ar^{40}- Ar^{39} dating of metamorphic events in the north and high Himalaya belts (southern Tibet-China). Tectonics 7:299-326

Mantovani MSM, Marques LS, deSousa MA, Civetta L, Atalla L, Innocenti F (1985) Trace element and strontium isotope constraints on the origin and evolution of Paraná continental flood basalts of Santa Catarina State (southern Brazil). Journal of Petrology 26:187-209

Martin A, deCelles PG, Gehrels GE, Patchett PJ, Isachsen C (2005) Isotopic and structural constrains on the location of the Main Central thrust in the Annapurna Range, central Nepal Himalaya. Geological Society of America in press.

McDougall I, Harrison TM (1988) Geochronology and Thermochronology by the $^{40}Ar/^{39}Ar$ method., vol. Oxford University Press,

Medvedev S, Beaumont C (2006) Growth of continental plateaus by channel injection: models designed to address constraints and thermomechanical consistency. In: Law RD, Searle MP, Godin L (eds) Channel Flow, Ductile Extrusion and Exhumation in

Continental Collision Zones., vol Special Publication 268. Geological Society, London, pp 147-164

Merrihue C, Turner G (1966) Potassium-argon dating by activation with fast neutrons. Journal of Geophysical Research 71:2852-2859

Metcalfe RP (1993) Pressure, temperature and time constraints on metamorphism across the Main Central Thrust zone and High Himalayan Slab in the Garwhal Himalaya. In: Treloar PJ, Searle MP (eds) Himalayan Tectonics, vol Special Publications, 74. Geological Society, London, pp 485-509

Miller C, Klötzli U, Frank W, Thöni M, Grasemann B (2000) Proterozoic crustal evolution in the NW Himalaya (India) as recorded by circa 1.80 Ga mafic and 1.84 Ga granitic magmatism. Precambrian Research 103:191-206

Miller C, Thöni M, Frank W, Grasemann B, Klötzli U, Guntli P, Draganits E (2001) The early Palaeozoic magmatic event in the Northwest Himalaya, India: source, tectonic setting and age of emplacement. Geological Magazine 138:237-251

Mitchell JG (1968) The ^{40}Ar/^{39}Ar method for potassium-argon age determination. Geochimica et Cosmochimica Acta 32:781-790

Mohan A, Windley BF, Searle MP (1989) Geothermobarometry and development of inverted metamorphism in the Darjeeling-Sikkim region of the eastern Himalaya. Journal of Metamorphic Geology 7:95-110

Molnar P, England PC (1990) Temperatures, heat flux, and frictional stress near major thrust faults. Journal of Geophysical Research 95(B4):4833-4856

Murphy MA, Harrison TM (1999) Relationship between leucogranites and the Qomolangma detachment in the Rongbuk Valley, south Tibet. Geology 27:831-834

Myers RE, Cawthorn RG, McCarthy TS, Anhaeusser CR (1987) Fundamental uniformity in the trace element patterns of the volcanics of the Kaapvaal Craton from 3000 to 2100 Ma: evidence for the lithospheric origin of these continental tholeiites. In: Pharaoh TC, Beckinsale RD, Rickard D (eds) Geochemistry and Mineralization of Proterozoic Volcanic Suites., vol 33. Geological Society of London Special Publication, pp 315-325

Myrow PM, Hughes NC, Paulsen TS, Williams IS, Parcha SK, Thompson KR, Bowring SA, Peng S-C, Ahluwalia AD (2003) Integrated tectonostratigraphic analysis of the Himalaya and implications for its tectonic reconstruction. Earth and Planetary Science Letters 212:433-441

Najman YMR, Garzanti E (2000) Reconstructing early Himalayan tectonic evolution and paleogeography from Tertiary foreland basin sedimentary rocks, northern India. Geological Society of America Bulletin 112:435-449

Neogi S, Dasgupta S, Fukuoka M (1998) High P-T polymetamorphism, dehydration melting, and generation of migmatites and granites in the Higher Himalayan crystalline complex, Sikkim, India. Journal of Petrology 39:61-99

O'Brien PJ (1997) Garnet zoning and reaction textures in overprinted eclogites, Bohemian Massif, European Variscides: A record of their thermal history during exhumation. Lithos 41:119-133

O'Brien PJ (1999) Asymmetric zoning profiles in garnet from HP-HT granulite and implications for volume and grain-boundary diffusion. Mineralogical Magazine 63(2):227-238

O'Brien PJ, Rötzler J (2003) High-pressure granulites: formation, recovery of peak conditions and implications for tectonics. Journal of Metamorphic Geology 21:3-20

Parrish R, Hodges KV (1996) Isotopic constraints on the age and provenance of the Lesser and Greater Himalayan sequences, Nepalese Himalaya. Geological Society of America Bulletin 108:904-911

Pattison DRM (2003) Petrogenetic significance of orthopyroxene-free garnet + clinopyroxene + plagioclase ± quartz-bearing metabasites with respect to the amphibolite and granulite facies. Journal of Metamorphic Geology 21:21-34

Pattison DRM, Chacko T, Farquhar J, McFarlane CRM (2003) Temperatures of Granulite-facies metamorphism: constraints from experimental phase equilibria and thermobarometry corrected for retrograde exchange. Journal of Petrology 44(5):867-900

Pearce JA (1983) Role of the sub-continental lithosphere in magma genesis at active continental margins. In: Hawkesworth CJ, Norry MJ (eds) Continental basalts and mantle xenoliths., vol. Shiva Publishing Limited, Cheshire, UK, pp 230-249

Pearce JA, Cann JR (1973) Tectonic setting of basic volcanic rocks determined using trace element analyses. Earth and Planetary Science Letters 19:290-300

Pearce JA, Norry MJ (1979) Petrogenetic implications of Ti, Zr, Y, and Nb variations in volcanic rocks. Contributions to Mineralogy and Petrology 69(1):33-47

Pêcher A (1989) The metamorphism in the central Himalaya. Journal of Metamorphic Geology 7:31-41

Pognante U, Spencer DA (1991) First report of eclogites from the Himalayan belt Kaghan valley (northern Pakistan). European Journal of Mineralogy 3:613 - 618

Richards A, Argles T, Harris N, Parrish R, Ahmad T, Darbyshire F, Draganits E (2005) Himalayan Architecture constrained by isotopic tracers from clastic sediments. In: 20th Himalayan Karakorum Tibet Workshop, vol., Aussois, France, pp 164-165

Richards A, Parrish R, Harris N, Argles T, Li Z (2006) Correlation of lithotectonic units across the eastern Himalaya, Bhutan. Geology in press.

Ritchie L (2004) Tectonic history of the sole and roof of the Greater Himalayan Sequence: structural and metamorphic observations of garnet-staurolite schists from the Bhutan Himalaya. In: Earth Sciences, vol BSc, Honours. Dalhousie University, Halifax, p 59

Robinson DM, deCelles PG, Patchett PJ, Garzione CN (2001) The kinematic evolution of the Nepalese Himalaya interpreted from Nd isotopes. Earth and Planetary Science Letters 192:507-521

Rowley DB (1996) Age of initiation of collision between India and Asia: A review of stratigraphic data. Earth and Planetary Science Letters 145:1-13

Royden LH (1996) Coupling and decoupling of crust and mantle in convergent orogens: Implications for strain partitioning in the crust. Journal of Geophysical Research 101:17,679-617,705

Royden LH, Burchfied BC, King RW, Chen Z, Shen F, Liu Y (1997) Surface deformation and lower crustal flow in eastern Tibet. Science 276:788-790

Rubatto D, Gebauer D (2000) Use of cathodoluminescence for U-Pb zircon dating by ion microprobe: some examples from the Western Alps. In: Pagel M, Barbin V, Blanc P, Ohnenstetter D (eds) Cathodoluminescence in geosciences., vol. Springer, Berlin, Germany, pp 373-400

Samson SD, Alexander EC (1987) Calibration of the interlaboratory ^{40}Ar/^{39}Ar dating standard, MMhb-1. Chemical Geology 66:27-34

Searle MP, Corfield RI, Stephenson BJ, McCarron J (1997) Structure of the north Indian continental margin in the Ladakh-Zanskar Himalayas: Implications for the timing of obduction of the Spontang ophiolite, India-Asia collision and deformational events in the Himalaya. Geological Magazine 134:297-316

Searle MP, Godin L (2003) The South Tibetan detachment and the Manaslu Leucogranite; a structural reinterpretation and restoration of the Annapurna-Manaslu Himalaya, Nepal. Journal of Geology 111(5):505-523

Searle MP, Law RD, Godin L (2006a) Defining the Himalayan Main Central Thrust. Journal of Asian Earth Sciences 26:160

Searle MP, Law RD, Jessup M (2006b) Crustal structure, restoration and evolution of the Greater Himalaya in Nepal-South Tibet: implications for channel flow and ductile extrusion of the middle crust. In: Law RD, Searle MP, Godin L (eds) Channel Flow, Ductile Extrusion and Exhumation in Continental Collision Zones., vol Special Publications 268. Geological Society London, pp 355-378

Searle MP, Rex AJ (1989) Thermal model for the Zanskar Himalaya. Journal of Metamorphic Geology 7:127-134

Searle MP, Simpsons RL, Law RD, Parrish R, Waters DJ (2003) The structural geometry, metamorphic and magmatic evolution of the Everest Massif, High Himalaya of Nepal-South Tibet. Journal of the Geological Society, London 160:345-366

Searle MP, Waters DJ, Rex DC, Wilson RN (1992) Pressure, temperature and time constraints on Himalayan metamorphism from eastern Kashmir and western Zanskar. Journal of the Geological Society of London 149:753-773

Sheraton JW, Black LP (1981) Geochemistry and geochronology of Proterozoic tholeiite dykes of east Antarctica: evidence for mantle metasomatism. Contributions to Mineralogy and Petrology 78:305-317

Shervais JW (1982) Ti-V plots and the petrogenesis of modern and ophiolitic lavas. Earth and Planetary Science Letters 59:101-118

Singh S, Barley ME, Brown SJ, Jain AK, Manickavasagam RM (2002) SHRIMP U-Pb in zircon geochronology of the Chor granitoid: evidence for Neoproterozoic magmatism in the Lesser Himalayan granite belt of NW India. Precambrian Research 118:285-292

Slagstad T, Culshaw NG, Jamieson RA, Ketchum JWF (2004) Early Mesoproterozoic tectonic history of the south-western Grenville Province, Ontario: constraints from geochemistry and geochronology of high-grade gneisses. Geological Society of America 197:209-241

Spear F (1993) Metamorphic phase equilibria and Pressure-Temperature-time paths., vol. Mineralogical Association of America, Washington, D.C.

Spear F, Kohn MJ, Cheney JT (1999) P-T paths from anatectic pelites. Contributions to Mineralogy and Petrology 134(1):17-32

Spear F, Kohn MJ, Florence FP, Menard T (1991) A model for garnet and plagioclase growth in pelitic schists: implications for thermobarometry and P-T path determinations. Journal of Metamorphic Geology 8:683-696

Stephenson BJ (1997) The tectonic and metamorphic evolution of the Main Central Thrust zone and High Himalaya around the Kishtwar and Kulu windows, northwest India. In: Department of Earth Sciences, vol Doctor of Philosophy. University of Oxford, Oxford, England, p 216

Stephenson BJ, Searle MP, Waters DJ, Rex DC (2001) Structure of the Main Central Thrust zone and extrusion of the High Himalayan deep crustal wedge, Kishtwar-Zanskar Himalaya. Journal of the Geological Society of London 158(4):637-652

Stephenson BJ, Waters DJ, Searle MP (2000) Inverted metamorphism and the Main Central Thrust: field relations and thermobarometric constraints from the Kishtwar Window, NW Indian Himalaya. Journal of Metamorphic Geology 18(5):571-590

Stüwe K, Foster D (2001) $^{40}Ar/^{39}Ar$, pressure, temperature and fission track constraints on the age and nature of metamorphism around the Main Central Thrust in the eastern Bhutan Himalaya. Journal of Asian Earth Sciences 19:85-95

Sun SS, McDonough WF (1989) Chemical and isotopic systematics of oceanic basalts; implications for mantle composition and processes. In: Saunders AD, Norry MJ (eds) Magmatism in the ocean basins, vol 42. Geological Society Special Publications, pp 313-345

Swapp SM, Hollister LS (1991) Inverted metamorphism within the Tibetan slab of Bhutan: evidence for a tectonically transported heat-source. Canadian Mineralogist 29:1019 – 1041

Tanaka T, Togashi S, Kamioka H, Amakawa H, Kagami H, Hamamoto T, Yuhara M, Orihashi Y, Yoneda S, Shimizu H, Kunimaru T, Takahashi K, Yanagi T, Nakano T, Fujimaki H, Shinjo R, Asahara Y, Tanimizu M, Dragusanu C (2000) JNdi-1: a neodymium isotopic reference in consistency with LaJolla neodymium. Chemical Geology 168(3-4):279-281

Theide RC, Arrowsmith JR, Bookhagen B, McWilliams MO, Sobel ER, Strecker MR (2005) From tectonically to erosionally controlled development of the Himalayan orogen. Geological Society of America 33(8):689-692

Thompson RN, Morrison MA, Dickin AP, Hendry GL (1983) Continental flood basalts...arachnids rule OK? In: Hawkesworth CJ, Norry MJ (eds) Continental basalts and mantle xenoliths, vol. Shiva Publishing Limited, Cheshire, UK, pp 158-185

Tracy RJ (1982) Compositional zoning and inclusions in metamorphic minerals. In: Ferry JM (ed) Characterization of Metamorphism through Mineral Equilibria, vol 10. Reviews in Mineralogy, pp 355-397

Van de Kemp PC (1964) Bulletin of the Geological Society of America 81:1127-1136

Vance D, Harris N (1999) Timing of prograde metamorphism in the Zanskar Himalaya. Geology 27(5):395-398

Vannay J-C, Grasemann B, Rahn M, Frank W, Carter A, Baudraz V, Cosca M (2004) Miocene to Holocene exhumation of metamorphic crustal wedges in the NW Himalaya: Evidence for tectonic extrusion coupled to fluvial erosion. Tectonics 23:TC1014, doi:1010.1029/2002TC001429

Vannay J-C, Hodges KV (1996) Tectonometamorphic evolution of the Himalayan metamorphic core between the Annapurna and Dhaulagiri, central Nepal. Journal of Metamorphic Geology 14:635-656

Vannay J-C, Sharp ZD, Grasemann B (1999) Himalayan inverted metamorphism constrained by oxygen isotope thermometry. Contributions to Mineralogy and Petrology 137:90-101

Watters BR, Pearce JA (1987) Metavolcanic rocks of the La Ronge Domain in the Churchill Province, Saskatchewan: geochemical evidence for a volcanic arc origin. In: Pharaoh TC, Beckinsale RD, Richard D (eds) Geochemistry and mineralization of Proterozoic volcanic suites., vol Special Publication, 33. Geological Society, pp 167-182

Weaver BL, Tarney J (1981) The Scourie dike suite: petrogenesis and geochemical nature of the Proterozoic sub-continental mantle. Contributions to Mineralogy and Petrology 78:175-188

Wiesmayr G, Edwards MA, Meyer M, Kidd WSF, Leber D, Hausler H, Wangda D (2002) Evidence for steady fault-accommodated strain in the High Himalaya: progressive fault rotation of the southern Tibet detachment system in NW Bhutan. In: de Meer S, Drury MR, de Bresser JHP, Pennock GM (eds) Deformation mechanisms, Rheology and Tectonics: Current Status and Future Perspectives., vol 200. The Geological Society of London, London, pp 371-386

Williams ML, Buick IS, Cartwright I (1996) An extended episode of early Mesoproterozoic metamorphic fluid flow in the Reynolds Range, central Australia. Journal of Metamorphic Geology` 14:29-47

Wilkinson JFG, Maitra RW (1987) Upper mantle amphibolites and micas and TiO_2, K_2O, and P_2O_5 abundances and 100 Mg (Mg^+ Fe^{2+}) ratios of common basalts and andesites: Implication for model metasomatism and undepleted mantle composition. Journal of Petrology 28:37-73

Winchester JA, Floyd PA (1977) Geochemical discrimination of different magma series and their differentiation products using immobile elements. Chemical Geology 20:325 - 343

Wu C, Nelson KD, Wortman G, Samson SD, Youngjun Y, Juxiang L, Kidd WSF, Edwards MA (1998) Yadong cross structure and South Tibetan detachment in the east central Himalaya (89°-90° E). Tectonics 17:28-45

Yardley BWD (1989) An introduction to metamorphic petrology, vol. Longman Scientific & Technical, London

Yardley BWD, Valley JW (1997) The petrologic case for a dry lower crust. Journal of Geophysical Research 102(B6):12,173-112,185

Zeitler PK (1985) Cooling history of the northwestern Himalaya, Pakistan. Tectonics 4:127-151

APPENDIX A

Bhutan 2000 (Djordje Grujic)

#	LAT	LON					
39	28°04'00.8"	89°37'48.3"	3720 m	Bt-Ga-Sill migmatite	Sf 087/20	Lstd 179/02	BH 165
					Shear band: ~ 320/52 t-t-t-south	Lfa 032/15	
40	28°03'55.0"	89°39'02.6"		Approx the core of the Gansser's synform			
41	28°03'45.3"	89°39'55.7"	3745 m	Migmatite	Sf 304/17 328/24		
42	28°03'47.1"	89°40'13.9"	3805 m	Migmatite & Ga gneiss	Sf 016/21, 019/10		
43	28°03'55.4"	89°41'43.3"	3865 m	Banded migmatite Anastomosing leucosome	Sf 254/24 249/35 250/19 290/21		BH 166
44	28°04'10.8"	89°42'11.0"	ridge	Sf 322/02 121/17			
45	28°03'47.2"	89°40'15.2"	3825 m	Migmatite, boudinaged sills of leucogranite	Sf 335/25 225/25 345/22 356/12-sample		BH 167
49	28°01'29.0"	89°43'32.6"	3335 m	Shear zone with strongly sheared tu leucogranite	Sf mylonitic 160/76	Lstr 093/55	BH 168
50	28°01'01.8"	89°43'42.5"	3295	Strongly foliated migmatitic gneiss +Ga +sill	Sf 039/42 039/46	Lstd 001/42	
				Internal boudinage w/ leucosome	Sf 007/47	Lstr 045/40 029/44 L boudin 026/24	
51	28°00'51.2"	89°43'46.5"	?	Migmatite, less foliated Leucosome in elongated pods	Sf 058/22 359/45 007/50		
52	28°00'40.5"	89°43'56.0"	bridge	Leucogranite Sheared, mylonitised	Sf-myl 156/57 159/52	Lstr 116/42 119/44	
53	28°00'24.2"	89°44'01.1"	Before the ascent	Gneiss, and migmatite w/ internal boudinage	Sf 003/14 312/26 343/22 S shear band 150/50 t-t-t-south		

Bhutan 2000 (Djordje Grujic)

Stop GPS #									
62	27°43'21.0"	89°45'22.0"	1474 m	22-OCT-00	Migmatite (Bt, Ga) + “Schlieren”	Sf 312/10, 004/12, 332/12		Sample B170	S vergent folds
63	27°42'40.7"	89°45'53.6"	1470 m	22-OCT-00	Migmatite (Bt, Ga ± Sil) Strong foliation	Sf 347/21, 318/20	Lst (Sil) 330/19, 343/20		
64	27°41'34.6"	89°46'14.9"	1440 m	22-OCT-00	Migmatite. Leusosome (aplitic) veins strongly folded into ptygmatic folds with axial planes II main foliation. Sub-horizontal pegmatite veins cross cut all structures	Sf 004/14		Sample B171 [apatite FT age by I. Coutand 2.3 ± 0.5 Ma	t-t-S shear bands 176/48
65	27°40'34.4"	89°46'25.6"	1380 m	22-OCT-00	Migmatite	Sf 318/12, 335/19		Sample B172	
66	27°38'36.3"	89°47'16.6"	1330 m	22-OCT-00	Migmatites (like stop 64) Beneath Ga amphibolites with Bt schist & quartzite	Sf 339/26, 338/20, 006/21	Lstr 330/21, 342/20	Sample B173 Sample B173a Sample B 173q	

Bhutan May 2002
Joyia Chakungal
*****NOTE: All planar measurements are presented as dip direction and dip angle.*****

Station	Date	Co-ordinates	sample	S	L
006	08. 05.	No	291 ?	Shear bands tt S 148/ 33	Lstr 137/37
007		028 01 311 089 43 550 3227 m	289 ?		
1		028 08 054 089 47 295 4070 m		Sf 116/15 Ssb: 162/75	Lstr 146/15 Lboudin: 094/22
		To the S	201	S1 254/63 Sap in boudin: 356/46	Lfa in boudin: 296/33
2		dj	202	Sf 312/10 Sap(isocl) 328/14, 295/10 Sf 127/25	Lstr(augen) 290/05 Lfa(isocl) 286/20, 316/05 Lstr. 306/02, 308/20
3		dj		Ssb344/35 ttS Sf 316/30	
4		028 08 270 089 47 471 4133 m		Sf 072/32 Fault 312/62, 314/72	Lsl 310/70 Lis 105/27
			203	Ssb 328/30 Sf 128/20	Lfa(isocl) 146/12
5		Dj #13		Sf 111/33, 082/15,	Lstr (sillm) 151/25,

				010/30	Lis 102/15 Lfa 147/15
6		dj		Joints: 332/80, 325/90, 232/48 Fault: 336/90	Lsl 068/59
7		028 08 848 089 47 717 4218 m			
8		028 08 980 089 47 924 4125 m		Fault 156/66, 168/49	Lsl 153/66 ttSE, 143/43 normal
9		028 09 050 089 47 956 4123 m		Sf 025/52, 057/10 Fault 156/70	Lstr 118/07 Lsl 134/65 normal, ttSE
10		028 09 098 089 47 999 4137 m	204 205 206 207	Fault 170/60 Sf 034/35	Lsl 130/55 + tourmaline Lfa 085/02
11		028 09.148 089 48.024 4190 m	208	Sf 033/33	
12		028 09.226 089 48.065 4202 m		Sf 036/34	
13		028 09.300 089 48.037 4277 m		Sf 048/18	
14		dj		Sf 020/60, 080/37?	
15	14. 05.	028 10.307	209	Sf 005/55, 000/55	

		089 48.363 4289 m	210 211 212 213a 213b		
15		028 10.304 089 48.368 4419 m		Sf 039/30	
16 wpt 22		028 10.304 089 48 368 4419 m		Sf 039/30	
17		028 10.321 089 48.364 4447	214	Mylonitised! Sf 042/40 Au.gneiss 012/27 restite	
18		028 10.344 089 48.377 4476 m	215	Sf 009/28 Sf 032/33	
19		028 10.367 089 48.408 4479 m	216 a,b,c 217 a,b	Sf 040/65	
20	15. 05.	028 07.849 089 47.057 4144	218	Sf 212/20, 165/48 Fault 314/68 Sf 155/12 Fault 321/68	Lstr-bt 168/28 Lsl 288/68, Rev. ttSW Lsl 263/55
21		028 07.988 089 46.905 4425	219 220 221	Fault 170/59 Sf 145/42, 152/26, 154/21	Lsl 130/54 normal Lstr(Sill) 152/25

				Fault 145/50 Joints: 062/80, 067/83 Sf 287/40 173/20	Lsl 103/58 Lstr(sill) 161/21
22		028 08.044 089 47.274 4358 m		Sf 146/33	
→ Toma La	16. 05.	028 11.243 089 49.231 4490/4470am			
Halt	17. 05.				
New camp	18. 05.				
23	19. 05.	028 10.558 089 48.712 4411 m		Sf 076/24 109/40 020/35	Lboudin 016/10 Lstr(sill) 152/30 Lstr(hbl) 120/18
			222	Sf 039/15	Lmin 324/07
24		028 10.518 089 48.686 4386	223	Sf 055/34, 058/35 Sf 013/83 in m.bou Sf 063/25	Lboudin 093/13 Lboudin 350/40 ? Lstr(sil)155/15
25		028 10.473 089 48.604 4375	224A 224B 224C 224D	Sf around boud: 044/76 Sf 005/50	

	20. 05	Wagye La 028 13 421 089 52.032 5430 m /am 5291 m /GPS			
26		028 12.356 089 51.474 4913 m	226	S3 292/24 C in a S/C fabrics	
27	21. 05.	028 11.082 089 50.351 4728 m	227 228 229	S3? 356/15 Sf 268/15, 266/20 ? Sf 238/00	
28?		dj	230	S3 344/17	
29		028 10.070 089 50.464 4790		Sf 068/13, 000/32	Lstr(fsp) 042/12 Lstr 342/07 dyke
New camp Kuluka	22. 05.				
30	23. 05.	028 06.238 089 45.225 3980 m		Sf 167/20 Ssb 153/37 2 sets Fault 178/90	Lstr 145/37 s.book Lsl 092/60
31		dj		Ssb 149/51, 145/45 Sf 256/15, 230/15	ttS
			243-258		

New camp	24. 05.	028 03.702 089 42.714 3419 m			
32	25. 05	028 03.745 089 43.014 3743 m		Sf 198/34 Fault 172/84 Sf 235/20	Lsl 095/60 ttSE Foliation drag
33		dj		Sf 276/17, 281/13 Fault 163/84	Lsl 094/67
34		028 04.256 089 43.244 4014 m	259	Sf 241/263/14	
35		028 04.376 089 43.332 4047m	260	Sf 319/41, 262/15? Fault 169/90 Sf 312/30 264/10? 302/32 Sf 264/10 Fault 164/83	TdtSE Lsl 089/57
			261-267		
Laya	26. 05.				
Laya	27. 05.				
New camp	28. 05.	028 08.089 089 42.329			

		3874m			
36	29. 05.	028 09.596 089 41.672 4187 m	268 269	Sf 052/20 357/12, 344/17 Sf 028/10	Lmin(sill)333/15
37		028 09.589 089 41.906 4214 m	270	Sf 023/40, 033/20 Fault 169/85 Fault/contact: 163/60, 160/50	Lsl 090/55
38		028 09.097 089 41.996 4068 m		Sf 001/41, 050/40, 037/20, 358/23, 037/20 Fault 168/61	Lsl 097/29
39	30. 05.	028 03.843 089 43.053 4076 m		Sf 028/40 ga/amf Sf 353/60, 062/42 Fault 152/70	Lsl 083/50 + Riedels, s.book Lmin(amf) 322/13, 181/15
40		028 08.884 089 43.139 4089 m		Sf 026/47, 050/43, 000/53	
41		028 09.005 089 43.310 4127 m	275-280	Sf 025/30, 034/20	Lmin(sill) 325/17
42	31. 05.	028 08.574			Limin(sill) 335/30,

		089 42.451 4114 m		Sf 300/30, 341/23 Sf 029/28 Fault 301/69 Sf 338/41, 010/55, 030/47	331/19 Lboudin 322/13 Lstr(m.agr) 334/22 Lsl 283/64 tdNW Lstr(sill) 343/30
43		dj		Sf 022/23, 024/34, 040/52, 035/48, 040/45, 028/36	Lstr/min344/27, 328/23, 346/38, 338/24 Lfa 116/20
44		028 08.435 089 42.542 3839 m		Sf 358/22, 355/35 Fault 344/76	Lis 353/21 Lsl 255/17
45		028 08.033 089 42.552 3833 m		Fracture ? 297/65 Sf 019/20, 057/37, 042/32, 056/40	
			271- 274 281		
45	01. 06.	028 08.354 089 43.018 3926 m	282	Sf 296/50, 066/33 Joints: 290/76, 293/83, 294/82 Fault 298/85	Lstr(Kfs) 332/47 Lsl 022/57?
46		028 08.472 089 43.124 3923 m		Fracture cleavage 252/32 Sf 044/35, 042/42	
47		028 08.669		Sf 061/28, 004/37?	

		089 43.389 4088	283 284	Joints 326/63 Sf 035/30, 049/38 Sf 326/55 Sf 005/30 Sf 319/28	
48		028 08.980 089 43.599 4186 m	285 286	Sf 032/52	
49	02. 06.	028 06.569 089 41.378 3755	287	Sf 200/45, 234/53, 224/35 Sf 205/73, 240/60, 219/65 Sf 224/38, 224/35, 215/50	Lstr(sill) 329/24 Lis 122/10
	03. 06.				
	04. 06.		288		
			289 290 291		
	05. 06.				
50	06. 06.	027 39.487 089 47.371 1380 m	173A 292		

Bhutan
September - November 2004

** PLANAR STRUCTURES HAVE BEEN PRESENTED AS DIP DIRECTION AND DIP ANGLE

Date	Station #	GPS co-ords	GPS Elevation (m)	Sample #	Sample Description	S' features	L' features
Northeastern Bhutan: HIGHER STRUCTURAL LEVEL							
27/09/04	1	see D's notes	2,760	—	—	—	—
	2	see D's notes	2,745	BH-248	sand for fission track	—	—
	3	see D's notes	—	BH-249	sand for fission track	—	—
	4	see D's notes	2,550	—	—	—	—
29/09/04	Shumpha Camp	27°39.521'N 090°12.520'E	1,160	—	—	—	—
30/09/04	Durgang Camp	27°41.254'N 091°14.510'E	1,317	—	—	—	—
1/10/04	Yunglapung Camp	27°44.309'N 091°16.338'E	2,048	—	—	—	—
2/10/04	Chikang gong Camp	27°49.470'N 091°18.722'E	2,557	—	—	—	—
3/10/04	Thangkarma Camp	27°53.476'N 091°19.472'E	2,947	—	—	—	—
5/10/04	5	27°'58.395'N 091°18.223'E	3,850	BH-250	migmatite for fission track	s.f: 330/50 328/50 336/65	—
6/10/04	6	27°'58.419'N 091°17.441'E	3,865	BH-352	gnt-bt gneiss for fission track	s.f: 000/15 236/45 340/25 006/28	s.l: 352-05 f.a: 270-30
	7	27°57.300'N 091°16.682'E	4,200	BH-353	bt+tour leucogranite	s.f: 270/40 302/35 048/80 sh.pl: 312/60	—
	8	27°57.341'N 091°18.005'E	3,718	—	—	s.f: 033/32 056/35	—
10/10/04	—ringthang Camp	see D's notes?	4,280	—	—	—	—
	9	27°59.402'N 091°17.919'E	4,227	BH-355	bt-tour granite for fission track		—
				BH-356	oriented bt+gnt+sill gneiss.	s.f: 260/58(?) 005/40	—
	10	27°59.163'N 091°17.878'E	4,045	BH-357	leucogranite for fission track	s.f: 020/70	—

12/10/04	11	27°00.598'N 091°16.954'E	4,818	BH-359	oriented (on bottom) bt gneiss	s.f: 025/45 023/43	—
13/10/04	12	27°58.567'N 091°22.261'E	3,540	BH-360	tour+gnt qtzite	D's notes	D's notes
				BH-361	bt+sill+gnt gneiss	D's notes	D's notes
				BH-362		D's notes	D's notes
14/10/04	Romethang Camp	27°57.740'N 091°21.538'E	3,440	—	—	—	—
15/10/04	13	27°58.567'N 091°22.261'E	3,545 (or 3,645?)	BH-263	ms+tour leucogranite for fission track	massive?	—
18/10/04	Khomakang Camp	27°45.582'N 091°16.624'E	2,005	—	—	—	—
	14	27°40.963'N 091°16.355'E	1,565	BH-367	bt+gnt+sill+ms gneiss	s.f: 314/15 a.pl: 048/44	s.l: 002-30 (// to f.a. and min. lin)
				BH-368	bt+sill+/-ms gneiss	s.f: 030/40	—
19/10/04	Khoma Camp	27°41.284'N 091°13.520'E	1,290	—	—	—	—
	Shumpha Camp	27°39.426'N 091°12.572'E (why so different from sept measure??)	1,115	—	—	—	—
20/10/04	15	27°39.939'N 091°12.287'E	1,165	—	—	s.f: 084/45 070/57 071/60	—
	16	27°39.879'N 091°12.523'E	1,192	BH-371	oriented bt+gnt+ms schist	s.f: 060/33 052/35 054/50	—
		27°39.881'N 091°12.538'E	1,194	BH-372	graphite schist	s.band: 030/56	—
		see D's notes	see D's notes	BH-373	bt quartzite	—	—
		see D's notes	see D's notes	BH-374	ky+gnt+bt+ms gneiss	s.f: 049/44	—
	17	27°39.901'N 091°12.769'E	1,214			s.f: 060/57 063/60	m.ln:128-40
	18	27°40.160'N 091°13.060'E	1,228	BH-375A BH-375B	ky+gnt+bt+ms gneiss A: boulder B: oriented	s.f: 008/50	—
	19	27°36.140'N 091°12.875'E	1,104	BH-376	bt+ms+/-gnt ultramylonite	s.f: 050/56 034/27	—

21/10/04	20	27°35.616'N 091°12.911'E	1,127	BH-377	bt+/-ms+/-gnt schist	s.f: 340/44 310/55	—
	21	27°31.700'N 091°10.853'E	1,117	BH-378	plag porphry dyke	s.f: 076/30	—
24/10/04	22	27°23.027'N 091°31.081'E	1,278	BH-396	plag porphry dyke intruding into Checkha	s.f: 350/20 s.f2: 320/59	—
25/10/04	24?	see D's notes	see D's notes	BH-297	bt+gnt+ms gneiss	—	—

Surey/Jigmecholing Section: LOWER STRUCTURAL LEVEL

29/10/04	1	26°59.692'N 090°32.984'E	1,223	BH-1	bt+gnt+ms+/-sill granite gneiss. Oriented on bottom	s.f: 020/30 014/23	—
		26°59.572'N 090°33.005'E	1,224	—	—	s.f: 044/25	—
	2	26°58.908'N 090°33.393'E	1,252	—	—	s.f: 034/31 a.pl: 344/55 347/53	f.a: 270-07 (chevron fold)
	3	26°58.735'N 090°33.404'E	1,239	BH-2A	oriented bt+gnt gneiss (intercalated w/ quartzite)	s.f: 003/90 347/45	m.ln:317-43
				BH-2B	oriented bt+gnt+ms gneiss	s.f: 232/67 213/85	f.a: 195-85 (crenulation)
	4	26°58.260'N 090°32.701'E	1,148	BH-3	bt+musc+/-gnt+/-sill gneiss	s.f: 077/35	—
	5	26°58.213'N 090°32.718'E	1,142	BH-4	bt+gnt+ms gneiss	s.f: 028/05	m.ln:026-05
				BH-5	mylonitized augen gneiss	s.f: 044/25	—
	6	26°58.260'N 090°32.701'E	1,136	BH-6	bt+gnt+mus+k-spar augen granite(?) gneiss	s.f: 070/60 079/63	—
	7	26°58.247'N 090°33.164'E	1,106	BH-7	oriented gnt+mica schist	s.f: 069/57	—

	8	26°58.082'N 090°33.436'E	1,097	BH-8 BH-9A BH-9B BH-9C	quartzite layer in gnt+bt+ms gneiss oriented bt+gnt+ms gneiss boulder of ky bearing quartz vein boudine foliated granite	s.f: 083/83 032/57	—
	9	26°57.999'N 090°33.455'E	1,083	BH-10	oriented bt+gnt+ms mylonite granite gneiss	s.f: 049/50	—
	10	26°57.835'N 090°33.349'E	1,074	BH-11	mylonitic mica+qtz schist	s.f: 042/70 053/65	m.ln: 162-60
30/10/04	11	26°57.028'N 090°32.825'E	771	—	—	s0&s.f: 037/45 014/57 031/72 024/57 j.p: 184/33	—
	12	26°57.232'N 090°33.307'E	865	—	—	s0&s.f: 048/77 042/58	—
	13	26°57.635'N 090°33.579'E 26°57.589'N 090°33.448'E	964	BH-12 BH-12B	white mica schist (phyllite) gnt+mica schist	s0&s.f: 072/30 s.f: 056/52	—
	14	26°57.633'N 090°33.260'E	1,017	BH-13	gnt+mica schist	s.f: 097/25	—
	15	26°58.333'N 090°32.773'E	1,173	BH-14A BH-14B	mica schist mylonitized gnt+mica+tm granite gneiss	s.f: 042/43 053/40	—
	16	27°00.635'N 090°34.877'E	915	BH-15	gnt+mica schist of GHS	s.f: 352/40	—
	17	27°01.176'N 090°36.919'E	1,615	BH-16	granite gneiss w/ xenoliths of augen gneiss	s.f: 302/45	—
	18	—	—	BH-17	gnt+mica schist intercalated w/ quartzites	a.p: 302/45 (// to s.f)	f.a: 145-10
	19	26°58.589'N 090°33.096'E	1,231	—	gnt+mica granite	massive	—

	20	26°58.496'N 090°32.785'E	1,192	BH-18	gnt+mica schist	s.f: 052/40	—
31/10/04	Gelephu	26°52.098'N 090°29.187'E	197 (map says 210)	—	—	—	—

Sarpang - Damphu Section: LOWER STRUCTURAL LEVEL

31/10/04	21	26°52.098'N 090°29.187'E	997	—	—	s.f: 320/60	—
	22	26°55.123'N 090°12.339'E	1,022	BH-19	gnt+mica schist	s.f: 341/32 342/40	—
	23	26°55.395'N 090°12.326'E	1,056	BH-20	gnt+mica psammite	s.f: 002/47 004/46	—
	24	26°55.517'N 090°12.418'E	1,078	BH-21	oriented gnt+mica granite	s.f: 349/42 345/52	m.ln:346-47
				BH-21B	oriented gnt+mica granite for geochron		
	25	26°55.587'N 090°12.438'E	1,096	BH-22	granite gneiss also for geochron	s.f: 341/40 348/35	—
	26	26°55.729'N 090°12.477'E	1,112	BH-23A	oriented? Gnt+mica mylonitized augen? gneiss	s.f: 346/47 008/50 020/50	m.ln:352-47
				BH-23B	oriented? Gnt+mica augen gneiss (seems more mylonitic than 23A)		
	27	26°55.604'N 090°12.588'E	1,140	BH-24	gnt+mica augen gneiss	s.f: 314/60	—
	28	26°55.469'N 090°12.571'E	1,158	BH-25	gnt+mica schist	s.f: 346/53 348/42 012/50	—
	29	26°55.500'N 090°12.966'E	1,215	—	gnt+mica augen gneiss	—	—
	30	26°55.583'N 090°13.076'E	1,228	—	gnt+mica augen gneiss (of GHS)	s.f: 326/52 332/55	—
	31	26°55.812'N 090°13.289'E	1,274	—	gnt+mica augen gneiss (of GHS)	s.f: 324/32	—

	32	26°56.220'N 090°13.286'E	1,329	BH-26	gnt+mica gneiss (of GHS)	s.f: 005/64 017/44	m.ln:354-43
1/11/04	33	27°00.567'N 091°04.293'E	287	BH-27	medium grained sand for fission track	—	—
	waypoint #123	27°04.133'N 090°04.250'E	355	—	GHS migmatites	dipping to NE	—
	waypoint #124	27°05.772'N 090°04.452'E	526	—	Checkha quartzites. contact b/w GHS and Checkha is just below this	s0: 058/37 (// to s.f.)	—
	Way—yter Checkpost (Wangdue-Tsirang border)	27°09.027'N 090°04.330'E	432	—	Checkha quartzites.	s0: 012/52 010/32 (// to s.f.)	—
	waypoint #126	27°13.360'N 090°04.109'E	818	—	GHS migmatites	s.f: 180/75	—
	waypoint #127	27°14.842'N 090°03.100'E	703	—	btm contact of massive leucognt intruding Checkha	—	—
	waypoint #128	27°16.599'N 090°01.476'E	647	—	upper contact of massive leucognt intruding Checkha	—	—
	waypoint #129	27°16.794'N 090°00.744'E	662	—	last o/c of Checkha dipping to the S-SE	—	—
	waypoint #130	27°23.102'N 089°54.469'E	1,139	—	GHS migmatites	s.f: 142/40	—
	waypoint #133	27°24.331'N 089°54.178'E	1,196	—	GHS migmatites	s.f: 000/20	—
	waypoint #134	27°25.598'N 089°54.144'E	1,209	—	GHS migmatites	dips to NE	—

APPENDIX B